Development of organic-inorganic perovskite solar cells via thermal evaporation and spin-coating

Towards a fully thermally evaporated perovskite solar cell

Mels Kerklaan

MSc Thesis Report

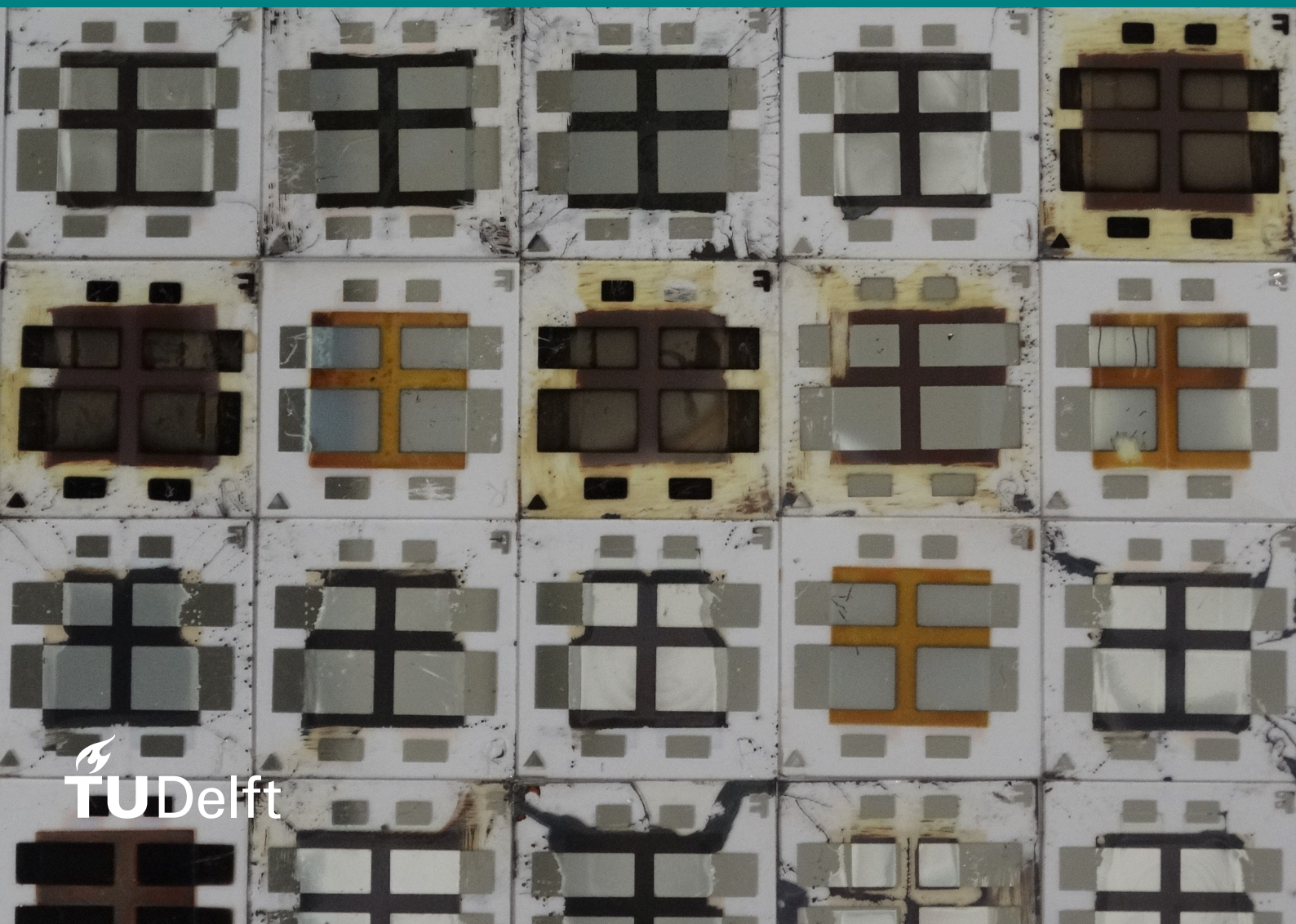

TU Delft

Development of organic-inorganic perovskite solar cells via thermal evaporation and spin-coating

Towards a fully thermally evaporated perovskite solar cell

by

Mels Kerklaan

to obtain the degree of Master of Science
at the Delft University of Technology,
to be defended publicly on Thursday July 28, 2022 at 1:30 PM.

Student number:	4491610	
Project duration:	November 22, 2021 – July 28, 2022	
Thesis committee:	Dr. L. Mazzarella	TU Delft (PVMD), supervisor
	Dr. T.J. Savenije	TU Delft (OM)
	Dr. S.W.H. Eijt	TU Delft (FAME)

An electronic version of this thesis is available at `http://repository.tudelft.nl/`.

TU Delft

Abstract

Perovskite solar cells (PSCs) are an emerging and promising photovoltaic technology that have demonstrated impressive power conversion efficiencies exceeding 25% after only fourteen years of development. This rapid progress can mostly be attributed to the development and optimisation of PSCs fabricated by solution-based methods, because of their easy processing and inexpensive equipment. However, to commercialise PSCs, alternative methods are required. Among these methods, the vacuum-based technique thermal evaporation is a suitable candidate. In thermal evaporation, solid precursors are evaporated and deposited onto a substrate in a high vacuum chamber. Thermal evaporation is a mature technique in the semiconductor industry to fabricate pinhole-free and highly uniform thin films at a large scale on different types of substrates. To date, the efficiency of PSCs by thermal evaporation is lagging behind their solution-based counterpart, partly due to limited research on vacuum deposited PVK films and several challenges unique to thermal evaporation.

In this MSc thesis project, organic-inorganic metal halide perovskite absorbers based on thermally evaporated $FA_xCs_{1-x}Pb(I_yBr_{1-y})_3$ and spin-coated $MAPbI_3$ have been developed together with the additional supporting layers for device fabrication. Several PSCs with different p-i-n architectures have been fabricated and characterised. The device comprises of: ITO as front electrode, spiro-TTB, spiro-OMeTAD and/or MoO_x as hole transport layer, PVK absorber layer, C60 as electron transport layer, BCP as buffer layer, and silver and aluminium as metallic back electrode. The goal of this work is to develop and optimise the structural and opto-electronic properties of different device layers and demonstrate a working perovskite solar cell.

PVK engineering is carried out on both thermally evaporated and spin-coated PVK thin films with the aim at obtaining perovskite that possesses desirable opto-electronic properties. For $FA_xCs_{1-x}Pb(I_yBr_{1-y})_3$ fabricated by sequential layer thermal evaporation, the uniformity and tooling factors were optimised to grow layers with a correct precursor ratio showing a high crystallinity and absorptance. No clear effect of post-annealing could be detected for the temperatures and times tested in this work. Achieving the target thickness and obtaining a satisfactory reproducibility were not fully reached. For spin-coated $MAPbI_3$, it was found that increasing the precursor solution concentration helped to achieve a desirable thickness for PSCs. Moreover, an adequate bandgap, diffractogram and absorptance were measured. However, based on the small crystal size determined with SEM, and poor device performance, further improvement is needed.

Transport, contact, and buffer layers were successfully fabricated by developing new deposition recipes for silver, BCP, and spiro-TTB. Furthermore, spectrophotometry measurements show that thermally evaporated HTLs (MoO_x and spiro-TTB) exhibit much lower parasitical absorption losses compared to spin-coated spiro-OMeTAD. An optical model to fit spectroscopic ellipsometry data measured on spiro-TTB thin films is created to determine its thickness and optical properties. Moreover, time resolved microwave conductivity results indicate that C60 effectively extracts electrons from $MAPbI_3$. In contrast, spiro-TTB films did not appear to possess any hole extracting abilities. Strong quenching of the steady-state PL signal is observed for bi-layers of $MAPbI_3$ with either C60, spiro-OMeTAD and MoO_x. This quenching is possibly caused by extraction of either electrons or holes and/or enhanced non-radiative recombination at the interface.

The optimised films were combined in complete PSCs with most layers fabricated by thermal evaporation through metal masks structuring cells with active areas of 0.16 and 0.36 cm^2. Solar cells were characterised in the dark and under illumination using a solar simulator integrated with a glove box to prevent degradation. A wide range of J-V characteristics are identified and classified: (1) ohmic responses, possibly caused by poor quality PVK absorber layers with pinholes filled with thermally evaporated metal, (2) S-shaped curves under illumination, possibly caused by a mismatch in energy band alignment or increased non-radiative recombination at the MoO_x/$MAPbI_3$ interface, (3) diode behaviour in the dark, and (4) a high series resistance and low shunt resistance, possibly caused by low mobility, non-optimal thicknesses, internal currents, and mismatches in band alignment. The most promising PSC featuring the ITO (200 nm)/Spiro-OMeTAD/MoO_x (5 nm)/$MAPbI_3$/C60 (20 nm)/BCP (4 nm)/Ag (150 nm) architecture, had a short circuit current of 10.0 mA/cm^2 and an open circuit voltage of 0.67 V.

The experiments carried out in this MSc thesis project supported the development of several steps of PSC fabrication process. This work contributes towards understanding thermal evaporation processes of perovskite films and fabricating fully evaporated devices with high efficiency and a large area.

Preface

This MSc thesis project was conducted to fulfill the last requirements to obtain the degree Master of Science in Applied Physics at the Delft University of Technology. The project was carried out as a cooperation between two research groups: the Photovoltaic Materials and Devices group (PVMD) and the Opto-electronic Materials group (OM). Being part of these groups enabled me to work with a wide variety of experimental setups, which is something I am really grateful for. Although the results of my work are not what I was initially aiming for, I hope to have contributed to the development of perovskite solar cells within these groups.

There are some people I would like to express my gratitude to. Firstly, my daily supervisor Jin Yan. I want to thank you for all the help throughout the project and I very much enjoyed working together on the countless depositions we carried out. Secondly, my responsible supervisor Luana Mazzarella. I want to thank you for guiding me through this project and providing me with helpful feedback. I very much appreciate that you were always available to answer questions or provide me with help. Thirdly, Tom Savenije. I want to thank you for giving me the opportunity to work on this project within the OM group and for the useful advise on the device fabrication that you gave me during the year. Finally, I would like to thank fellow master students, PhD students and technicians of both research groups who helped me with experimental setups, theoretical understanding and moral support during the project.

Mels Kerklaan
Delft, July 2022

Contents

1 Introduction **1**
1.1 The need for renewable energy sources . . . 1
1.2 Photovoltaic technologies . . . 1
1.3 Perovskite solar cells . . . 2
1.4 Research objectives . . . 3
1.5 Report structure . . . 4

2 Theoretical Background **5**
2.1 Solar cell operational principles . . . 5
2.1.1 Semiconductor behaviour . . . 5
2.1.2 Recombination mechanisms . . . 6
2.1.3 Semiconductor junctions . . . 7
2.1.4 Solar cell parameters . . . 10
2.2 Hybrid organic–inorganic metal halide perovskites . . . 11
2.2.1 Crystal structure . . . 11
2.2.2 Opto-electronic properties . . . 12
2.2.3 Stability issues . . . 13
2.3 Perovskite solar cells . . . 13
2.3.1 Architectures and operating mechanism . . . 13
2.3.2 S-shaped J-V curves . . . 15
2.3.3 Hole transport layers . . . 16
2.3.4 Electron transport layers . . . 17
2.3.5 Transparent conductive oxides . . . 18
2.3.6 Buffer layers . . . 18

3 Experimental Methods **21**
3.1 Substrate preparation, storage and PSC fabrication . . . 21
3.1.1 Substrate preparation and sample storage . . . 21
3.1.2 Mask design . . . 22
3.1.3 Device fabrication . . . 23
3.2 Deposition methods . . . 24
3.2.1 Thermal evaporation . . . 24
3.2.2 One-step spin-coating . . . 29
3.2.3 Radio frequency sputtering . . . 30
3.3 Characterisation techniques . . . 32
3.3.1 X-ray diffraction . . . 32
3.3.2 UV/Vis/NIR spectrophotometry . . . 33
3.3.3 Photoluminescence spectroscopy . . . 35
3.3.4 Time resolved microwave conductivity . . . 35
3.3.5 Scanning electron microscopy . . . 36
3.3.6 Stylus profilometry . . . 36
3.3.7 Spectral ellipsometry . . . 37
3.3.8 Four-point probe method . . . 39
3.3.9 Solar simulator . . . 40

4 Development of Perovskite Absorber Layers **43**
4.1 Managing thermal evaporation of $FA_xCs_{1-x}Pb(I_yBr_{1-y})_3$ thin films . . . 43
4.1.1 Control on uniformity of depositions . . . 43
4.1.2 Compositional engineering of perovskite thin films . . . 46
4.1.3 Technical obstacles . . . 54

4.2 Characterisation of spin-coated $MAPbI_3$ films for device application . . . 55
4.2.1 Structural characterisation and thickness optimisation . . . 55
4.2.2 Opto-electronic characterisation. . . . 58

5 Optimisation of Transport and Contact Layers 63
5.1 Front and back electrode fabrication and characterisation . . . 63
5.1.1 Structural characterisation of indium tin oxide . . . 63
5.1.2 Opto-electronic characterisation of indium tin oxide . . . 65
5.1.3 Development of a thermal evaporation recipe for silver . . . 67
5.2 Fabrication and characterisation of transport and buffer layers . . . 68
5.2.1 Development of buffer and electron transport layers . . . 68
5.2.2 Optical characterisation of buffer and electron transport layers . . . 68
5.2.3 Development of hole transport layers . . . 69
5.2.4 Optical characterisation of hole transport layers . . . 70
5.2.5 Charge carrier dynamics of $MAPbI_3$-transport layer combinations . . . 74

6 Device Development and Testing 79
6.1 Devices with a thermally evaporated perovskite layer . . . 79
6.1.1 Investigation of possible silver electrode corrosion . . . 81
6.2 Devices with a spin-coated perovskite layer . . . 84
6.2.1 Spin-coating issues with spiro-TTB as underlying layer . . . 84
6.2.2 Looking for a suitable interface for spin-coating of $MAPbI_3$ . . . 86
6.2.3 Diode behaviour and S-shaped J-V curves . . . 87
6.2.4 Comparison and explanations of observed J-V characteristics . . . 95

7 Conclusion and Recommendations 99
7.1 Conclusion . . . 99
7.2 Recommendations . . . 101

A Appendix 103
A.1 Different device architectures . . . 103
A.1.1 Devices with thermally evaporated perovskite . . . 103
A.1.2 Devices with spin-coated perovskite . . . 104
A.2 Matlab script to calculate nominal thicknesses for thermally evaporated PVK . . . 105
A.3 Deposition recipe for aluminium and C60 . . . 106
A.4 Diffractogram and spectrophotometry spectra for a quartz substrate . . . 107
A.5 Correction factors and Matlab code four-point probe method . . . 108
A.6 Development of ellipsometry model for spiro-TTB . . . 109

Bibliography 113

1 Introduction

1.1. The need for renewable energy sources

By 2050 the global energy consumption is expected to increase with nearly 50% with respect to 2020 [1]. In the same period, if current technology and policy trends continue, the CO_2 emissions related to energy are expected to increase by 5% in OECD countries and 25% in non-OECD countries [1]. It is estimated that CO_2 emissions are responsible for 64% of the total amount of greenhouse gas emissions [2]. Greenhouse gas emissions lead to global warming and climate change, which cause extreme weather patterns and a rising sea level [3]. These numbers do not sketch a bright future, however, alternatives like renewable energy sources, are being developed and implemented at an increasing rate. The share of renewables in the total energy mix is expected to grow from 15% in 2020 to 27% in 2050, as can be seen in Fig. 1.1 [1]. Among these RES, solar energy is considered the most promising. Harvesting all energy from the sun that reaches the earth's surface for only 1.5 hours, would be enough to cover the global energy consumption for a full year [4]. This calculation underlines the huge potential of solar energy. Among the different techniques used to harvest energy from the sun, the photovoltaic (PV) technology is the largest and fastest growing. The energy generation from PV increased with 156 TWh in 2020 to a total of 821 TWh, representing an increase of 23% with respect to 2019 [5].

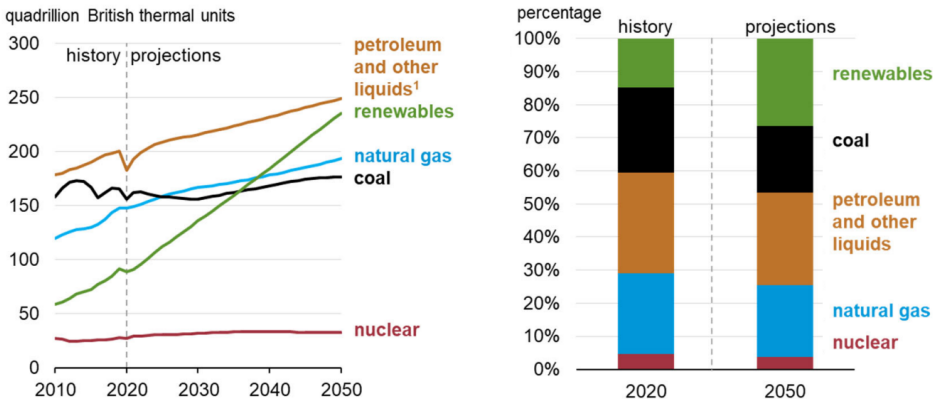

Figure 1.1: Left: primary global energy consumption by source. Right: share of primary global energy consumption by source [1].

1.2. Photovoltaic technologies

The most dominant technology on the PV market, is represented by solar modules based on crystalline silicon (c-Si). The c-Si solar cell has been developed for over 60 years, making it a very mature technology [6]. Two types of c-Si solar cells can be distinguished: mono-crystalline silicon (mono-Si) solar cells, with a record efficiency of 26.7%, and multi-crystalline silicon (multi-Si) solar cells, with a record efficiency of 24.4% [7]. Other commercially available solar cells are thin film solar cells, such as copper indium gallium selenide

(CIGS) and cadmium telluride (CdTe) solar cells. In 2020, mono-Si solar cells were dominating the total PV energy generation with a share of 80%, leaving 15% for multi-Si and 5% for thin film solar cells [7].

The efficiency of single-junction solar cells is limited by several loss mechanisms such as the inability to convert photons because the photon energy is smaller than the bandgap and thermalisation of photons that exceed the band gap. Due to these losses there is a maximum conversion efficiency for single-junction solar cells, known as the Shockley-Queisser limit [8]. For c-Si, this limit is determined to be 29.43% [9]. In addition, c-Si is an indirect bandgap semiconductor with relatively low absorption, which means that thick wafers of high quality are needed for the fabrication. This need influences the costs, considering that fabricating high quality c-Si material is already a costly process. In order to reduce costs, thin film solar cells have been proposed as an interesting alternative. However, most of them still suffer from relatively low power conversion efficiencies (PCEs) [10].

For the above described reasons, solar cell research is driven towards techniques that can potentially be more cost-effective, reduce material consumption and/or reach higher efficiencies than state-of-the-art technologies. One of the promising techniques is the hybrid organic-inorganic metal halide perovskite solar cell (PSC).

1.3. Perovskite solar cells

Hybrid organic-inorganic metal halide perovskites were first used to sensitize TiO_2 for visible light conversion in dye-sensitized solar cells (DSSCs), yielding an efficiency of 3.8% in 2009 [11]. In 2011, perovskites were used as sensitizer for quantum-dot-sensitized solar cells reaching an efficiency of 6.5% [12]. These results indicated the potential of using PVK in solar cells, even though stability was limited due to the use of a liquid electrolyte. The first solid-state PSC, using PVK nanoparticles as light harvesters, a mesoporous layer for transport of electrons and a hole transport material, reached a PCE of 9.7% in 2012 [13]. After it was demonstrated that mesostructured charge selective contacts were not needed to achieve a decent efficiency, focus shifted to planar heterostructures. The planar structure proved success when a PSC with a vapor-deposited PVK layer achieved a PCE of 15% in 2013 [14]. In the years that followed, there was a tremendous increase in efficiency of PSCs, with a current world record efficiency of 25.8% achieved by researchers from the UNIST institute in South-Korea in 2021 [15]. This achievement makes PSCs comparable to c-Si solar cells on a laboratory scale. Note that the record cell was fabricated with solution-based methods.

The rapid increase in power conversion efficiency since its first appearance, is a result of excellent optoelectronic properties that perovskite possesses. These are a low defect density, high carrier mobility, long charge carrier lifetime and long charge carrier diffusion length [16]. Another interesting property of PSCs is the tunable bandgap, which can be altered by incorporation of different halides. This property makes PVK an ideal material to be applied as a top cell in a c-Si tandem solar cell. This is one of the opportunities for the PV community to overcome the theoretical predicted limit for c-Si solar cells [17]. Despite the tremendous progress made in device performance, the biggest issues for PSCs are the limited stability and upscaling. Even though use of multi-cation and multi-halide PVK thin films enhances the stability, it remains a big issue until today. The issue concerning upscaling is illustrated by Fig. 1.2, where we see that the efficiency for larger areas is still far behind [18]. Another disadvantage is the toxicity of lead present in most PVK thin films. Research is carried out to replace lead by more environmentally benign alternatives.

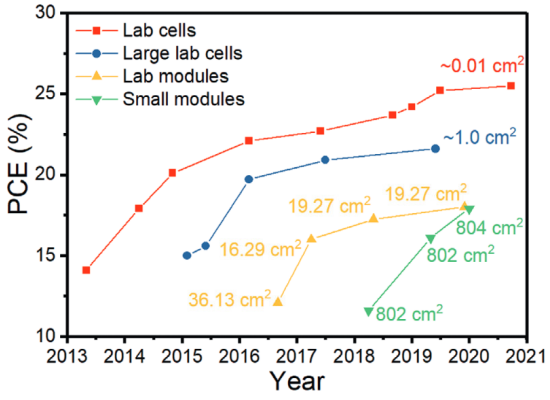

Figure 1.2: Certified record PCEs for lab cells, large lab cells, lab modules and small modules [18].

The different techniques available to fabricate PVK thin films can be classified into solution-based and vacuum-based methods. Advantages of solution-based methods are simple processing, low investment costs (easy to start), low-temperature processing and easy adjustment of film thickness. Disadvantages are dependence on solubility of elements, hazardous solvent usage, requirement of a substrate with good wettability, poor thickness uniformity and pinhole formation. Advantages of vacuum-based methods are good thickness uniformity, conformal growth on different substrates, scalability and no use of solvents. Disadvantages are limited control over deposition of organic components, difficulties in controlling the production of multi-cation and multi-halide PVK thin films, slow production and complex equipment. Interestingly, most research on PVK thin film deposition techniques has been focused on solution-based methods, predominantly due to the low costs. Much less research has been done on vacuum-based methods, even though this is seen as the best method to realise upscaling and therefore commercialisation [19],[20].

1.4. Research objectives

This MSc thesis project is partly conducted under the wings of the Photovoltaic Materials and Devices group (PVMD) and partly with the Opto-electronic Materials group (OM). Therefore, several research activities have taken place at the Else Kooi Laboratory (EKL clean room) and Electrical Sustainable Power Lab (ESP lab) of the faculty of electrical engineering, mathematics and computer science, and several research activities at the laboratories of the faculty of applied sciences of the Delft University of Technology.

Perovskite solar cells have been produced at research facilities all around the world. However, production of a PSC at the Delft University of Technology, has yet to be achieved. Therefore, the main goal of this project is to develop a working PSC by combining the knowledge of the PVMD group on complete solar cell fabrication with the knowledge of the OM group on perovskite crystals and their properties.

Our attempt to produce a working PSC starts from a concept on the device architecture, prior knowledge on some of the individual layers and a design. From this, entire devices are built by combining multiple layers, i.e. a transparent front electrode, hole transport layer (HTL), perovskite absorber layer, electron transport layer (ETL), metallic back electrode and possibly a buffer layer (BL). The long term aim is to produce a fully thermally evaporated perovskite solar cell with an inverted p-i-n architecture, as shown in Fig. 1.3.

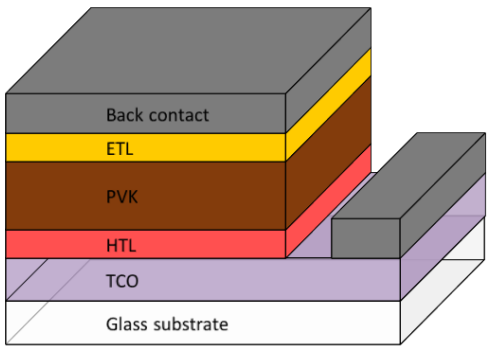

Figure 1.3: Concept for a fully thermally evaporated PSC with an inverted p-i-n architecture.

Eventually, over the duration of the project, additional layers are produced which add on to the total device architecture or replace layers of the original concept. An indium tin oxide (ITO) layer on top of a glass substrate acts as the front electrode and is fabricated by radio frequency sputtering. As hole transport layer, molybdenum oxide (MoO_x), spiro-TTB (both deposited by thermal evaporation) and spiro-OMeTAD (deposited by spin-coating) are tested. The perovskite absorber layer is either fabricated by thermal evaporation ($FA_xCs_{1-x}Pb(I_yBr_{1-y})_3$) or spin-coating ($MAPbI_3$). For the electron transport layer, Buckminsterfullerene (C_{60}) deposited by thermal evaporation, is used. For a buffer layer, bathocuproine (BCP) is deposited between the ETL and the metallic back electrode by thermal evaporation. Finally, silver or aluminium is deposited as a metallic back electrode by thermal evaporation.

Next to attempting to fabricate a full device, this research project includes additional development on indi-

vidual layers and combinations of them. Therefore, the following research goals are set to support the main goal and hopefully contribute towards the future development of our PSCs:

1. Development of PVK thin films via sequential layer thermal evaporation and spin-coating with optical and photo-electrical quality suitable for integration in a solar cell.
2. Optimising the delicate evaporation parameters using three source precursors to obtain multi-cation and multi-halide PVK. Control the film composition and the the effect of post-annealing on the structural and optical properties.
3. Implement and optimise deposition processes for transport layers, including determining the thickness and absorption spectra of such thin films, and development of a fitting model procedure to analyse ellipsometry data.
4. Evaluate the photo-electronic properties of several device layers and combinations of them. This includes charge carrier dynamics of neat spin-coated PVK absorber layers and bi-layers (combination of PVK and a transport layer). Furthermore, this includes measurements on the sheet resistance of ITO.
5. Fabricate complete PSCs and address pitfalls encountered in the development process to evaluate the limiting (bi-)layers in the device and where possible take action to solve shortcomings.

1.5. Report structure

In chapter 1, a general introduction about (perovskite) photovoltaics and this MSc thesis project is given. Subsequently, an overview of the relevant theory needed to understand and support this work is given in chapter 2. This includes a recap on solar cells, after which the focus shifts to PVK, PSCs and materials used in this work. Next up is the experimental method, where the substrate preparation, flowchart for the production of devices, different synthesis methods and setups used to do all kinds of characterisation measurements will be described (chapter 3). Then an evaluation of the results and corresponding discussion will be presented over three chapters, with in chapter 4, the development and characterisation of thermally evaporated and spin-coated PVK layers, in chapter 5, the development and characterisation of the transport, buffer and contact layers, and in chapter 6, the fabrication and testing of complete devices. At the end, a conclusion and recommendations are given in chapter 7.

2

Theoretical Background

2.1. Solar cell operational principles

2.1.1. Semiconductor behaviour

The operation of a semiconductor device depends on the transport and concentration of charge carriers inside the material, i.e. electrons and holes. In a semiconductor at thermal equilibrium, an electron can absorb thermal energy and break free from its covalent bond leaving a hole behind. At the same time, electrons can recombine with holes via a variety of mechanisms. Generation and recombination occur at the same rate. Since formation and loss of electron-hole pairs happens in pairs, the concentration of electrons is equal to the concentration of holes and known as the intrinsic carrier concentration n_i [21].

In many semiconductor devices such as c-Si solar cells, the concentration of electrons and holes is manipulated by introducing dopant impurities, which replace some of the semiconductor atoms. Donor impurities increase the concentration of free electrons n making the semiconductor material n-type, whereas acceptor impurities enhance the concentration of holes p making the semiconductor p-type. Moreover, doping affects the Fermi energy E_F. For n-type semiconductors, E_F moves closer to the conduction band (CB), and for p-type semiconductors, E_F moves towards the valence band (VB). When the concentration of impurity atoms is really low, a semiconductor is referred to as an intrinsic semiconductor [21].

Illumination of a semiconductor disturbs the thermal equilibrium state. Propagating light through a semiconductor material can be partially absorbed if the photons have an energy higher than the bandgap energy (E_G) of the semiconductor. In that case, electrons are excited from the VB to the CB while creating holes in the VB. The process of creating electron-hole pairs is known as photo generation. The total concentration of free electrons in the CB and holes in the VB increases with the excess carrier concentrations (Δn and Δp). The excitation of charge carriers is accompanied by recombination of them. Different mechanisms of recombination occur and the relevance of each mechanism can differ between different semiconductor materials [21]. Different recombination mechanisms are described in subsection 2.1.2.

Under operational conditions, a net electrical current can flow through a semiconductor device. The currents are generated by the transport of electrons and holes via two transport mechanisms: drift and diffusion. Drift is the motion of a charged particle in response to an electric field $\vec{E}$. When an electric field is present, the positively charged holes are accelerated in the direction of the electric field, whereas the electrons are accelerated against the direction of the electric field. Due to interactions with the lattice and impurity atoms, the motion can be described with an average drift velocity $\vec{v}$. The drift velocity is proportional to the electric field strength, with proportionally factor μ, known as the mobility. The mobility is a measure of how easily electrons and holes can move through a semiconductor material. The total drift current $\vec{J}_{drift}$ is given by the following equation:

$$\vec{J}_{drift} = q(p\mu_p + n\mu_n)\vec{E} = \sigma\vec{E} \tag{2.1}$$

in which q is the elementary charge, μ_p the hole mobility, μ_n the electron mobility and σ the total conductivity. The other transport mechanism, diffusion, is the process where particles spread from regions of high particle concentration to regions with a low particle concentration. The driving force is a gradient in concentration. The currents resulting from diffusion of electrons and holes are proportional to the gradients in electron and hole concentration (∇n and ∇p). The total diffusion current $\vec{J}_{diff}$ is given by the following equation:

$$\vec{J}_{diff} = q(D_n \nabla n - D_p \nabla p) \tag{2.2}$$

in which D_p is the diffusion constant for holes and D_n the diffusion constant for electrons. Moreover, the diffusion constants are related to the mobilities via the Einstein relation:

$$\frac{D_n}{\mu_n} = \frac{D_p}{\mu_p} = \frac{k_B T}{q} \tag{2.3}$$

in which k_B is the Boltzmann constant and T the temperature [21].

2.1.2. Recombination mechanisms

After the generation of charge carriers, different recombination processes can occur. Important parameters that describe the recombination of excess charge carriers, are the charge carrier lifetime τ and the diffusion length L. The charge carrier lifetime is defined as the average time a carrier can spend in an excited state after it is generated, and is related to the different recombination mechanisms. The more recombination mechanisms present and the more effective they are, the shorter the lifetime. The diffusion length is interpreted as the typical distance carriers can diffuse before they recombine. It is given by the following equation:

$$L = \sqrt{D\tau} \tag{2.4}$$

The first recombination process described in this subsection is direct recombination. In this process, an electron in the CB combines with a hole in the VB while releasing a photon with an energy equal to E_G. Since this process depends on both the electron and hole concentration, it is a second-order process. Another type of recombination occurs when the energy released by the recombination of an electron and hole is transferred to a different electron in the CB or hole in the VB. Either an electron is raised higher into the CB or a hole is pushed deeper into the VB. Due to thermalisation the electron (or hole) relaxes back to CB edge (or VB edge). This is a non-radiative process known as Auger recombination [22]. A schematic of direct recombination and Auger recombination is shown in Fig. 2.1a,b.

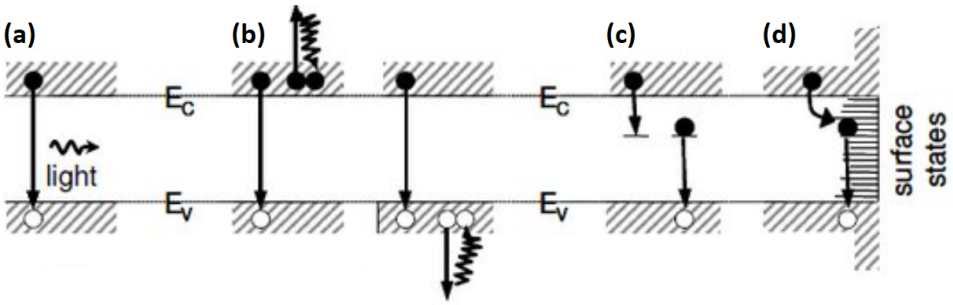

Figure 2.1: Different recombination mechanisms. (a) Direct recombination. (b) Auger recombination. (c) Shockley-Read-Hall recombination. (d) Surface recombination [23].

Furthermore, recombination can be facilitated by defects in the lattice such as vacancies, interstituals and dislocations. This type of recombination is known as Shockley-Read-Hall (SRH) recombination. The defects, which can act as recombination centres, can introduce energy levels within the bandgap, known as trap states. As an example, if an electron gets trapped in such a trap state, it can subsequently recombine with a

hole in the VB. This process is typically non-radiative (see Fig. 2.1c). Two different type of traps can be identified: donor-type traps, which are neutral when they contain an electron and positively charged when they do not, and acceptor-traps, which are negatively charged when they contain an electron and neutral when they do not. Another distinction can be made between shallow and deep trap states. If the energy difference between the trap state and the band edge is smaller than $k_B T$, it is a shallow trap state, otherwise, it is a deep trap state. Deep trap states are more detrimental to the performance of a solar cell than shallow trap states. A large trap density N_T has a negative effect on the lifetime of charge carriers [22].

The recombination mechanisms discussed so far are occurring in the bulk of the semiconductor material. However, recombination can also occur at the surface of a semiconductor (surface recombination). At the surface, many single occupied orbitals, that want to form a bond, are present. These are called dangling bonds and introduce many trap states within the bandgap, which induce SRH recombination (see Fig. 2.1d). In order to reduce surface recombination, the density of surface trap states N_{sT} can be lowered by passivation. Passivation implies that a thin layer of suitable material is grown on top of the semiconductor surface. Due to this layer, the dangling bonds can be satisfied by formation of covalent bonds [22].

2.1.3. Semiconductor junctions

Several different types of junctions exist in solar cells. Firstly, the p-n junction, which is created by bringing an n- and p-type semiconductor together. A schematic of the n- and p-type semiconductor and their band diagrams before they are brought together is shown in the left of Fig. 2.2. Remember that in the n-type semiconductor, the concentrations of free electrons is high, and in the p-type, it is the concentration of holes that is high. Both are electrically neutral due to the charge of the donor and acceptor atoms [21].

When the n- and p-type are brought together, the difference in electron concentration causes a diffusion current from the n- to p-region. Similarly, holes diffuse in the opposite direction. Due to this process, the region close to the junction becomes depleted of free charge carriers. This region is known as the depletion or space-charge region. The space-charge region gives rise to an electric field (due to background dopant atoms) which forces the electrons and holes to move in the opposite direction as the concentration gradient does. Eventually, drift and diffusion compensate each other and no current flows through the junction. This process is shown in the right of Fig. 2.2. The concentration of holes in the n-type region and electrons in the p-type region are referred to as minority carrier concentrations [21].

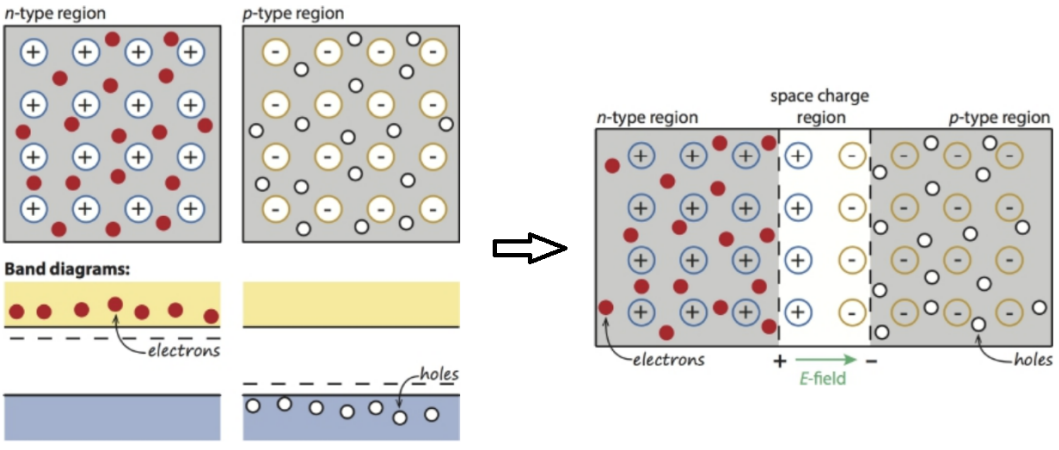

Figure 2.2: Left: schematic of n-type and p-type semiconductor and their band diagram before they are brought together. Right: formation of the space-charge region when the n-type and p-type are brought together [21].

When analysing the energy band diagram of a p-n junction, E_F is constant throughout the junction. If this would not be the case a current would be flowing. In addition, the band energies of the CB edge E_c and valence band edge E_v and vacuum energy E_{vac} should be continuous. This leads to band bending indicating the presence of an electric field in the space-charge region. Note that the vacuum energy level represents the energy to which an electron can be elevated so that it is not under the influence of the atom anymore. The electric field creates an electrostatic potential difference across the space-charge region. This important

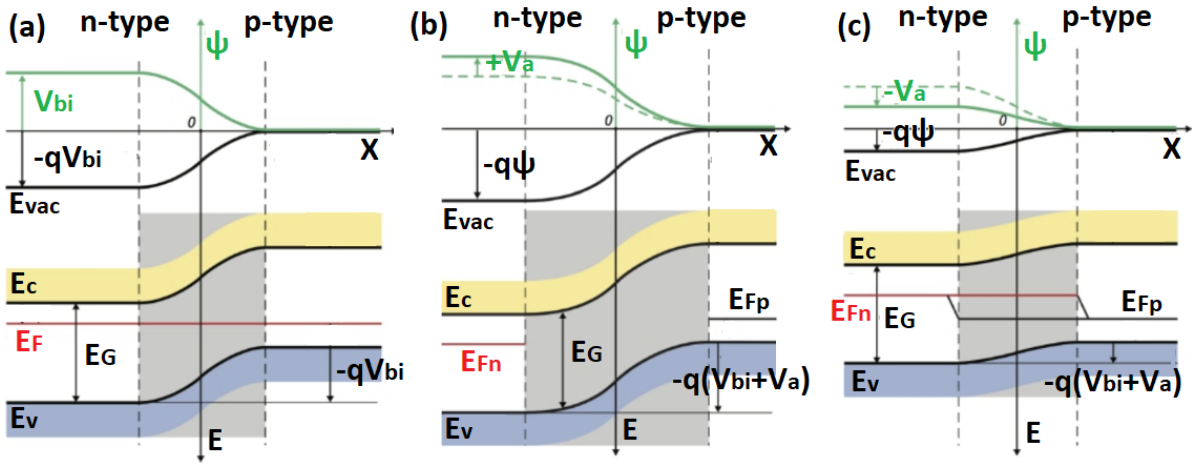

Figure 2.3: (a) Band alignment of a p-n junction and profile of the electrostatic potential ψ. (b) Band alignment and profile of the electrostatic potential ψ under the influence of a reverse-bias voltage. (c) Band alignment and profile of the electrostatic potential ψ under the influence of a forward-bias voltage [21].

parameter of a junction is known as the built-in voltage V_{bi}. The resulting band diagram of a p-n junction including the profile of the electrostatic potential ψ is shown in Fig. 2.3a [21].

In case an externally applied voltage V_a is put over the p-n junction, the electrostatic potential over the space-charge region will be affected. If the applied voltage is negative with respect to the p-type region, the potential difference will increase. This is referred to as a reverse-bias, which leads to an increase in size of the space-charge region (see Fig. 2.3b). The p-n junction is no longer in equilibrium and the concentration of electrons and holes is described by the quasi-Fermi energies E_{Fn} for electrons and E_{Fp} for holes. If the applied voltage is positive with respect to the p-type region, the potential difference across the space charge region will decrease. This is referred to as a forward-bias leading to a smaller space-charge region (see Fig. 2.3c). Decreasing the potential difference increases the minority carrier concentration at the edges of the space-charge region. The gradient in concentration that arises from this, leads to a so-called recombination current J_{rec} (since the minority carriers recombine with majority carriers in the bulk). Under the equilibrium condition (no bias), the recombination current is compensated by a thermal generation current J_{gen} caused by drift of minority carriers. If forward voltage V_a is applied, J_{rec} increases with the Boltzmann factor $\exp(\frac{qV_a}{k_BT})$, whereas J_{gen} does not change. The total current density at V_a can be written as:

$$J = J_{rec} - J_{gen} = J_0 \left[\exp(\frac{qV_a}{k_BT}) - 1 \right] \tag{2.5}$$

in which J_0 is the saturation current density. Ideally, J_0 is as small as possible. Due to recombination of the majority carriers with the minority carriers, majority carriers flow from the electrodes into the semiconductor and a net current flows through the p-n junction. The described principle is the working mechanism of a diode and solar cell in the dark [21].

When a solar cell is illuminated, additional electron-hole pairs are generated. Due to this, the concentration of holes in the n-type region and the concentration of electrons in the p-type region strongly increases. These minority carriers flow across the space-charge region (electrons from p to n and holes from n to p) causing a photogenerated current density J_{ph}. If we would now connect a load between the electrodes of the illuminated solar cell, only part of J_{ph} would flow through the external circuit. This is due to the fact that the voltage drop over the load, lowers the electrostatic potential over the space-charge region, resulting in an increase of J_{rec}. Note that J_{rec} flows in the opposite direction as J_{ph}. The voltage drop over a load can be simulated by applying a forward-bias voltage over the junction. The total current density can then be written as:

$$J = J_{rec} - J_{gen} - J_{ph} = J_0 \left[\exp(\frac{qV_a}{k_BT}) - 1 \right] - J_{ph} \tag{2.6}$$

The characteristics of a solar cell are found in its J-V curve. The J-V curves for a solar cell in the dark and under

illumination are depicted in Fig. 2.4. The relevant solar cell parameters shown in this figure will be further explained in subsection 2.1.4 [21].

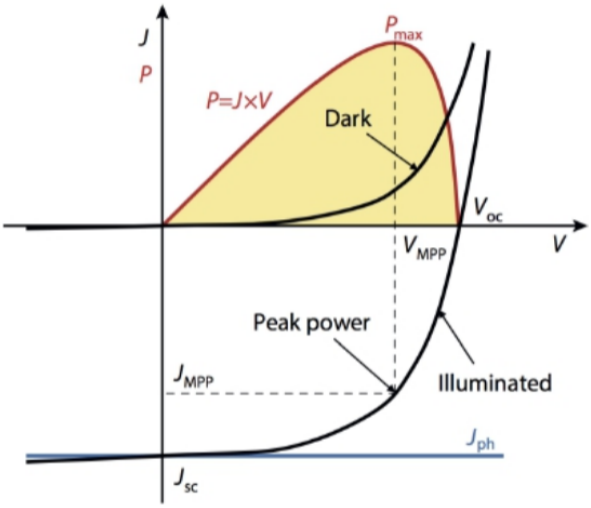

Figure 2.4: J-V curve of a p-n junction under illumination and in the dark [21].

Another relevant junction is the metal-semiconductor junction (m-s junction), which is present at the back and front of a solar cell. This junction is important to properly connect a solar cell to an external circuit. Two types of m-s junctions can be distinguished. These are the rectifying type and the non-rectifying type (ohmic) [21]. The band diagram of a metal and n-type semiconductor before and after they make contact, for a rectifying junction is depicted in Fig. 2.5a. Important parameters are the metal work function ϕ_m, the semiconductor work function ϕ_s, and the electron affinity χ of the semiconductor. In case ϕ_m is larger than ϕ_s, the Fermi level of the semiconductor is above the Fermi level of the metal before they make contact. In order for E_F to become constant throughout the system after contact, electrons from the semiconductor flow into the lower energy states of the metal and positive donors remain in the semiconductor. This creates a space-charge region that is fully located in the semiconductor. The barrier ϕ_{B0} is the potential barrier seen by electrons in the metal that try to move into the semiconductor. This barrier, known as the Schottky barrier, can be determined with the following equation:

$$\phi_{B0} = \phi_m - \chi \tag{2.7}$$

On the side of the semiconductor, electrons that try to move into the metal experience the built-in potential barrier V_{bi}. It is given by:

$$V_{bi} = \phi_{B0} - \phi_n \tag{2.8}$$

in which ϕ_n is the distance between E_c and E_F. Similar to the p-n junction, if we apply a forward-bias voltage (positive voltage with respect to the metal) the barrier is lowered and electrons can flow easier from the semiconductor into the metal. The current flow is caused by majority carrier electrons. Without a forward-bias, there is not net current from the semiconductor to the metal [24].

On the other hand, for non-rectifying contacts, ϕ_m is smaller than ϕ_s. The band diagram of a metal and n-type semiconductor before and after they make contact, for a non-rectifying junction is depicted in Fig. 2.5b. To achieve thermal equilibrium in this junction, electrons from the metal flow into the semiconductor making the semiconductor surface more n-type. A positive voltage applied to the metal induces a flow of electrons from the semiconductor into the metal since there is no barrier. When a positive voltage is applied to the semiconductor, the barrier height for electrons to flow from the metal into the semiconductor is equal to ϕ_n. In practice this is relatively small if the semiconductor is sufficiently doped. To sum up, this junction is a low resistance junction providing conduction of electrons in both directions and is therefore called an ohmic

contact. A similar discussion can be held for the contact between an electrode and a p-type semiconductor. However, in that case ϕ_m has to be larger than ϕ_s in order to form an ohmic contact [24].

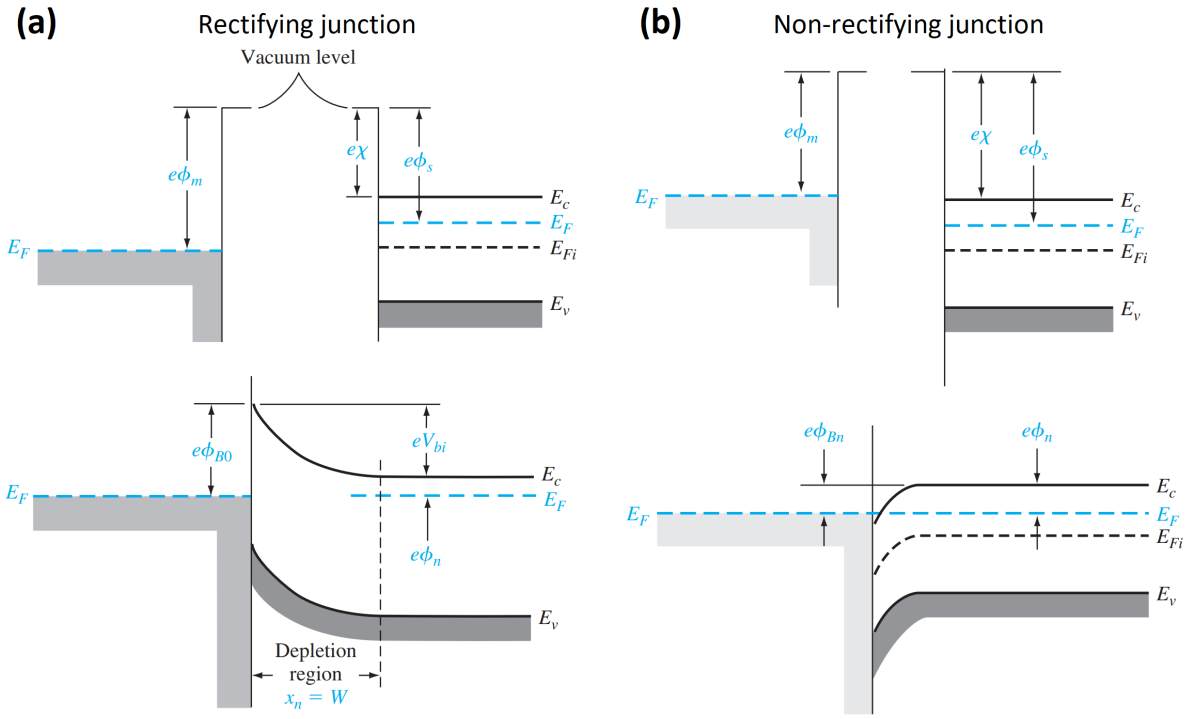

Figure 2.5: (a) Rectifying junction. Top: band diagram of metal and n-type semiconductor before contact. Bottom: band diagram after contact. (b) Non-rectifying junction. Top: band diagram of metal and n-type semiconductor before contact. Bottom: band diagram after contact. E_F, E_c, E_v, intrinsic Fermi level E_{Fi}, work functions as energy ($e\phi_m$, $e\phi_s$), potentials as energy (ϕ_n, eV_{bi}), electron affinity as energy $e\chi$ and width of depletion region W (or x_n) are indicated [24].

2.1.4. Solar cell parameters

Several important parameters that are characteristic for a solar cell can be derived from the J-V curve under illumination. These are the peak power P_{max}, the short circuit current density J_{sc}, the open circuit voltage V_{oc} and the fill factor FF. The short circuit current density is defined as the external current through the circuit when the electrodes are short circuited. In this case, J_{ph} flows entirely through the external circuit and there is no change of the electrostatic potential barrier. J_{sc} depends among others on the incoming photon flux, absorption, reflection, the diffusion length of minority charge carriers, and surface passivation. The open circuit voltage is defined as the voltage at which no current flows through the external circuit. This corresponds to a forward-bias voltage at which J_{rec}, J_{gen} and J_{ph} compensate each other [21]. In equation:

$$V_{oc} = \frac{k_B T}{q} \ln\left(\frac{J_{ph}}{J_0} + 1\right) \tag{2.9}$$

From this equation we can see that V_{oc} depends on J_{ph} and J_0. Since J_0 depends on recombination processes, the V_{oc} is a measure for the recombination in a device. The fill factor FF is defined at the ratio between P_{max} and the product of J_{sc} with V_{oc}. The operating point where the power is maximum is known as the maximum power point. Its corresponding voltage and current density are V_{mpp} and J_{mpp}. In general, a high fill factor is desired in solar cells. Since FF depends on J_{sc} and V_{oc} it has the same dependencies as those parameters have. In practice, FF is lowered due to parasitic resistance losses. Furthermore, with all relevant parameters described, the PCE can be calculated with the following equations:

$$\text{PCE} = \frac{P_{max}}{I_{in}} = \frac{V_{mpp} J_{mpp}}{I_{in}} = \frac{J_{sc} V_{oc} FF}{I_{in}} \tag{2.10}$$

in which I_{in} is the incoming light intensity [21].

The J-V curve of an illuminated solar cell can be described by an equivalent circuit containing a diode and a current source in parallel. As mentioned before, in practice the FF is affected by parasitic resistance losses. These can be represented by a series resistance R_s and a shunt resistance R_{sh}. When these resistances are included in the equivalent model, we obtain the circuit shown in Fig. 2.6a. The J-V curve for this equivalent circuit is described by the following equation:

$$J = J_0 \left[\exp\left(\frac{q(V - AJR_s)}{k_B T}\right) - 1 \right] + \frac{V - AJR_s}{R_{sh}} - J_{ph} \tag{2.11}$$

The series resistance is caused by movement of current through the semiconductor, contact resistance with the electrodes, and the resistance of the electrodes. Ideally, R_s is as low as possible. The effect of an increasing R_s on the J-V curve is shown in Fig. 2.6b. R_s can be found from the inverse of the slope of the J-V curve at the open circuit point. The shunt resistance represents alternative current paths for J_{ph} in a solar cell, which leads to power losses. Ideally, R_{sh} is as high as possible. The effect of a decreasing R_{sh} is shown in Fig. 2.6c. R_{sh} can be found from the inverse of the slope of the J-V curve at the short circuit current point [25].

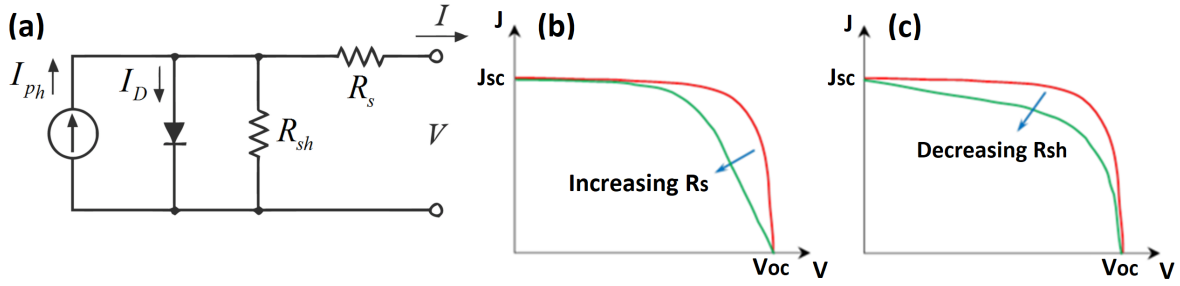

Figure 2.6: (a) Equivalent circuit of an illuminated solar cell with current source, diode, shunt resistance and series resistance. (b) Change of J-V curve due to an increasing series resistance. (c) Change of J-V curve due to a decreasing shunt resistance [26],[27].

2.2. Hybrid organic–inorganic metal halide perovskites

2.2.1. Crystal structure

Materials that are considered to be perovskites have the same crystal structure as calcium titanade ($CaTiO_3$), which is the first-discovered PVK crystal. The general chemical formula of perovskite is ABX_3. For hybrid organic-inorganic perovskites, the A is a monovalent cation such as methylammonium (MA^+), formamidinium (FA^+) and/or cesium (Cs^+); B is a divalent metal cation such as lead (Pb^{2+}) or tin (Sn^{2+}); and X is a halide such as iodide (I^-), bromide (Br^-) and/or chloride (Cl^-). Using mixtures of different cations and/or halides, known as compositional engineering, can change the properties of a perovskite. Note that $MAPbI_3$ is the archetype hybrid organic-inorganic perovskite. The generic representation of the crystal structure is depicted in Fig. 2.7. The cations in the B-sites are located inside connected octahedrons formed by the X-site halides. Eight connected octahedrons form cubic voids in which the A-site cations are located. The function of the A-site cations is to fill the voids and neutralise the charge of the octahedrons [20].

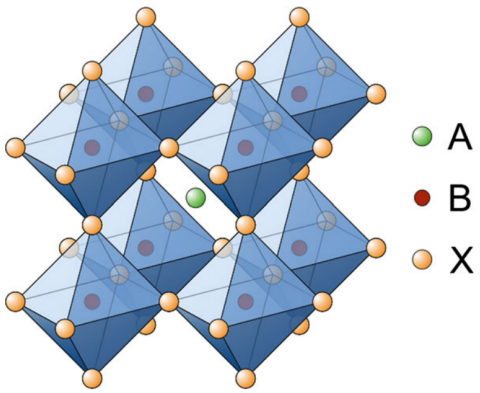

Figure 2.7: Crystal structure of ABX_3 hybrid organic–inorganic metal halide perovskites [28].

The general crystal structure of perovskite is cubic (known as α phase). In order to determine in which crystal phase a specific perovskite can exist at room temperature, the Goldschmidt tolerance factor t can be used. It is calculated with the following equation:

$$t = \frac{r_A + r_X}{\sqrt{2}(r_B + r_X)} \tag{2.12}$$

in which r_A, r_B and r_X are the ionic radii of the A cation, B cation and X halide. If t is in the range between 0.89 and 1, a cubic PVK can exist. If t is lower, PVK is intended to form a less symmetric structure such as tetragonal (β phase) or orthorhombic (γ phase) perovskite [20]. For the purpose of this research, we are interested in the perovskites $MAPbI_3$ and $FA_xCs_{1-x}Pb(I_yBr_{1-y})_3$. Due to the relatively large radius of I^-, $MAPbI_3$ has a tetragonal structure at room temperature. $FA_xCs_{1-x}Pb(I_yBr_{1-y})_3$ has a cubic structure at room temperature if the Cs content is sufficiently high.

2.2.2. Opto-electronic properties

Perovskite has drawn a great deal of attention in the PV community as semiconductor material, since it exhibits some great opto-electronic properties and can be fabricated with relative ease via solution-based methods. In $MAPbI_3$, the bandgap originates from sp^3d^2 hybridization of $6s^26p^05d^0$ orbitals of lead ions with $5p^6$ orbitals of iodide ions [20]. The bandgap is believed to be direct and located between 1.5 and 1.6 eV [29]. The bandgap of lead perovskites can be tuned by incorporation of multiple halides at the X-sites and subsequently by varying the content ratio among them. Considering $FA_xCs_{1-x}Pb(I_yBr_{1-y})_3$, the bandgap is equal to 1.56 eV for the y=1 (only I) and 2.07 eV for y=0.17 (around 83% Br). Incorporating more bromide, so decreasing the I:Br ratio, leads to an increase in the bandgap [16]. This bandgap tunability makes PVK an ideal candidate for multi-junction solar cells. Furthermore, PVK is proven to be an excellent absorber with a high absorption coefficient α. The absorption coefficient is a measure of how far light of a particular wavelength can penetrate into a material before it is absorbed [24]. A comparison of α as a function of energy for $MAPbI_3$ ($CH_3NH_3PbI_3$) and other semiconductor materials used in solar cells is shown in Fig. 2.8 [30]. A high absorption coefficient allows the usage of thin films.

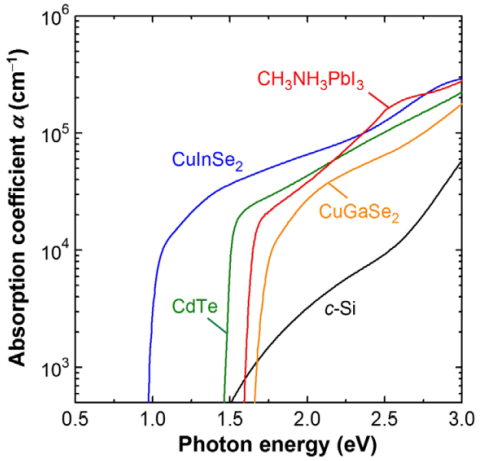

Figure 2.8: Absorption coefficient as a function of photon energy for different semiconductor materials: $MAPbI_3$ ($CH_3NH_3PbI_3$) (red), CdTe (green), c-Si (black), $CuInSe_2$ (blue) and $CuGaSe_2$ (yellow) [30].

Perovskite possesses great electronic properties. First of all, the effective mass for electrons and holes is relatively low, which results in a higher mobility [31]. Note that the effective mass replaces the normal mass in semiconductor physics, by taking into account the effect of both the particle mass and the effect of internal forces [24]. In addition, PVK shows relatively low defect densities which have a positive effect on the mobility as well. Based on these arguments, it can be concluded that PVK has a high electron and hole mobility. Furthermore, the relatively low defect density is responsible for a long charge carrier lifetime (sometimes larger than 1 μs) [32]. As we have seen in equations (2.3) and (2.4), all relevant properties are related, which implies that a high mobility and long lifetime leads to long charge carrier diffusion lengths [20].

2.2.3. Stability issues

Nowadays, one of the big issues hindering commercialisation of PSCs is the poor stability. The most important problem is the instability of the PVK absorber layer itself. However, stability problems caused by other layers in a device arise as well [33]. Four key factors can be identified that are causing degradation processes of PVK thin films. These are oxygen, moisture, UV light and thermal instabilities. PVKs are highly sensitive to water and tend to hydrolyse in the presence of it. The PVK decomposes into its original precursors which can further decompose under the influence of oxygen and UV light [34].

$MAPbI_3$ is the organic–inorganic hybrid metal halide perovskite that has been used since the beginning of PSC development. Therefore, the degradation processes were firstly experienced with this type of PVK. Research on enhancing the stability has shown that using mixtures of different cations and/or halides, can be a successful route to improve stability. Using FA and Cs to replace MA in $MAPbI_3$, leads to PVKs with interesting bandgaps for photovoltaic applications. However, both $FAPbI_3$ and $CsPbI_3$ have a non-perovskite δ phase together with the photoactive α phase at room temperature [35]. With annealing, a transition to the α phase can be assured. However, at room temperature the reverse process occurs leading to unstable device operation [36]. Stabilising the α phase is possible by using mixtures of different cations (such as FA and Cs) and/or halides (such as I and Br). This leads to the fabrication of PVKs such as $FA_xCs_{1-x}Pb(I_yBr_{1-y})_3$. However, implementing halide mixtures might lead to phase segregation under light exposure. In this process, I- and Br-rich domains are created in the PVK, which reduces performance [36].

2.3. Perovskite solar cells

2.3.1. Architectures and operating mechanism

Since hybrid organic-inorganic metal halide perovskites were initially used as sensitizer for DSSCs, the first solid-state PSCs were fabricated with a mesoporous film to facilitate electron transport. The mesoporous layer is often made of titanium(IV) oxide (TiO_2). In the mesoporous structure, a thick compact ETL (TiO_2) is deposited on a TCO. This layer is then covered with a mesoporous layer (again TiO_2) and filled with perovskite. On top of this, an HTL and metal electrode are deposited to complete the cell (see left of Fig. 2.9) [17]. A complete filling of all the pores in the mesoporous scaffold is important to prevent leakage currents, increase absorption of photons and enhance charge carrier collection [37]. These aspects makes the thickness of this layer relevant. The mesoporous structure is still widely used to fabricate high performance solar cells [17].

Due to the long charge carrier diffusion lengths for both electrons and holes in perovskites, it was realised that charge carriers can be transported to their electrodes without the need of a mesoporous layer [38]. For this reason, research shifted towards a planar device architecture, in which the PVK absorber layer is deposited directly on a compact transport layer. Two types of planar architectures can be distinguished. These are the conventional n-i-p architecture and the inverted p-i-n architecture. In the n-i-p architecture, the solar cell is illuminated through the ETL, whereas with a p-i-n architecture, the cell is illuminated through the HTL (see middle and right of Fig. 2.9). Based on conventions in the solar cell industry, the n-i-p architecture is referred to as conventional and the p-i-n structure is referred to as inverted [17].

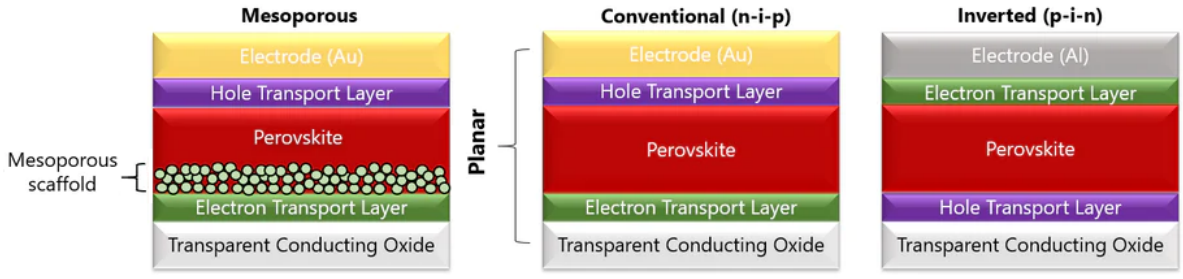

Figure 2.9: Different PSC architectures. Left: mesoporous configuration with TCO/ETL/mesoporous scaffold and PVK/HTL/electrode. Middle: conventional n-i-p configuration with TCO/ETL/PVK/HTL/electrode. Right: inverted p-i-n configuration with TCO/HTL/PVK/ETL/electrode [39].

The working mechanism of PSCs can be best compared to p-i-n solar cells, such as amorphous silicon. In p-i-n solar cells, an intrinsic absorber layer is sandwiched between a p- and n-doped layer, whereas in PSCs, the PVK layer is sandwiched between the HTL and ETL [21]. It is assumed that the PVK layer is intrinsic which implies that it is almost free of charge carriers initially. The transport layers must satisfy a proper band alignment with the PVK layer. For the ETL this means that it should have its lowest unoccupied molecular orbital (LUMO) and highest occupied molecular orbital (HOMO) lie lower than the CB and VB edge of the PVK layer respectively. For the HTL this means that it should have its LUMO and HOMO lie higher than the CB and VB edge of the PVK layer respectively [31]. This band alignment can be seen in Fig. 2.10a. When the layers are not in contact, E_F of the ETL is located more towards the LUMO, whereas E_F of the HTL is located closer to its HOMO. When the layers are brought in contact, E_F equilibrates along the device under dark and thermal equilibrium conditions [21]. This equilibration creates a slope over the electronic band of the PVK layer producing a built-in potential V_{bi} (see Fig. 2.10b). The slope reflects a built-in electric field [40].

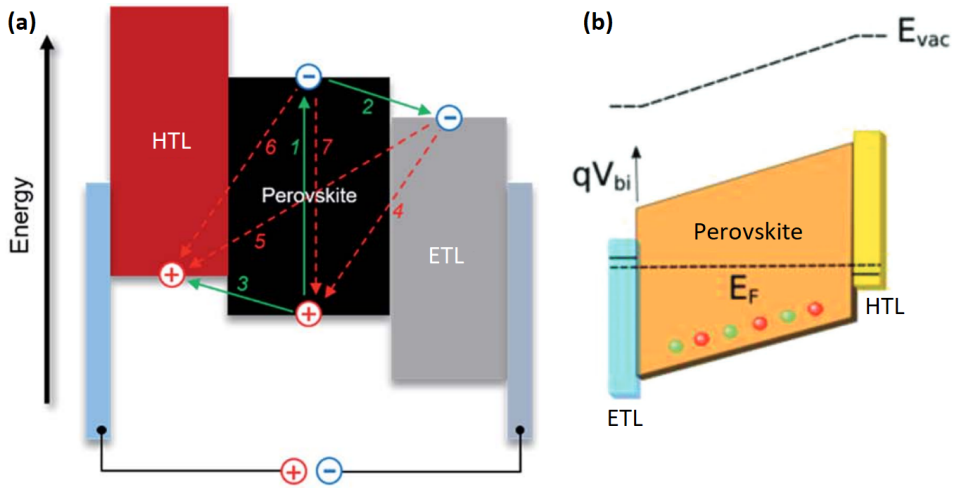

Figure 2.10: (a) Energy band alignment for HTL, PVK and ETL. Green arrows representing generation, hole extraction and electron extraction, red arrows representing recombination at the interfaces and the bulk [41]. (b) Continuous E_F under thermal equilibrium creating an electric field. Slope over the electronic band equal to $q \cdot V_{bi}$ [42].

Upon illumination, excitons are generated. An exciton is a bound state of an electron and a hole attracted to each other by the Coulomb force. Since excitons in PVK have a relatively low binding energy, the excitons dissociate in electron-hole pairs at room temperature (electron to the CB and hole to the VB) [31]. The charge carriers separate under the influence of the built-in electric field; the electrons will move towards the ETL and then to the cathode and the holes will move to the HTL and then to the anode [31]. The injection of electrons and holes happens quite efficiently due to the high charge carrier diffusion lengths. In the end, holes and electrons recombine at the anode closing the circuit. The generation and separation of charge carriers are represented by the green arrows in Fig. 2.10a. However, undesirable recombination processes take place as well. For PSCs this is mainly non-radiative trap-assisted recombination occurring at the ETL/PVK and HTL/PVK interface and in the bulk of the perovskite layer. This recombination is represented by the red arrows in Fig. 2.10a [41].

When the PSC is forward-biased and in the dark, electrons from the ETL and holes from the HTL are injected in the PVK layer where they recombine resulting in a recombination current. Under illumination (which generates J_{ph}) and by varying the forward-bias voltage (which changes J_{rec}) J-V curves similar to those for c-Si solar cells are obtained. Equations similar to (2.5) and (2.6) for the current under dark and illuminated conditions are valid again [31].

The open circuit voltage is equal to the the difference between the work functions of the ETL and HTL. If the band alignment would be perfect, and E_F of the HTL coincides with the VB while the E_F of the ETL coincides with the CB, V_{oc} would be equal to the bandgap of the PVK layer [42].

It is important to mention that other research suggests that the electrical potential distribution in PSCs is actually forming a p-n junction at the ETL/PVK interface. This implies that similar to c-Si solar cells, operation of the solar cell is determined by minority carrier drift and diffusion rather than the operation mechanism of a p-i-n solar cell as described above [43].

It is interesting to have a look at the device performance for the perovskites under investigation in this thesis. PSCs with thermally evaporated $FA_xCs_{1-x}Pb(I_yBr_{1-y})_3$ absorber layers have been reported with a J_{sc} in the range of 19 to 23 mA/cm^2, a V_{oc} in the range of 1.06 to 1.08 V and a PCE between 16 and 18% [35],[44]. PSCs with a spin-coated $MAPbI_3$ absorber layer have been reported with a J_{sc} up to 24 mA/cm^2, a V_{oc} in the range of 1.06 to 1.08 V and a PCE of 21% [45]. Note that these numbers are for PSCs with an inverted p-i-n configuration and similar transport layers as we are using. The thickness of the PVK absorber layer in PSCs is typically around 500 nm [35]. However, in practice solar cells with an absorber layer thickness ranging from 300 nm to of 1 μm have been fabricated [46].

The energy levels with respect to the vacuum level of all materials used in this work are depicted in Fig. 2.11. Note that the rectangles represent the bandgap of the material.

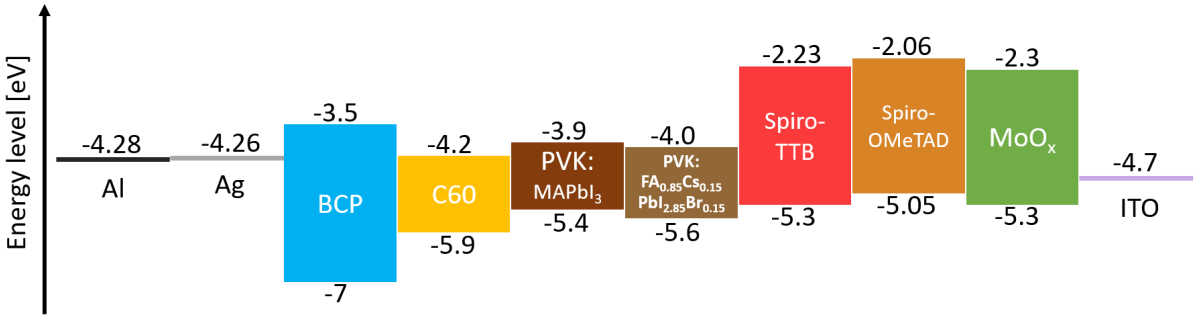

Figure 2.11: Energy levels with respect to E_{vac} for all materials used in this work. Rectangles represent the bandgap of a material [24],[16],[47],[48],[49].

2.3.2. S-shaped J-V curves

When a solar cell is not operating as intended, it shows a J-V curve under illumination that may differ from the theoretical shape (Fig. 2.4). In some cases, the J-V curve shows an S-shape, as can be seen in Fig. 2.12. S-shaped J-V characteristics are a frequently occurring hurdle in the development of solar cells when using new materials or device architectures. The S-shape indicates that there is a problem with the extraction of charge carriers at an interface between two adjacent materials. As we have seen with the description of the equivalent model, R_s and R_{sh} can provide a more realistic description of a solar cell. However, putting a value to these resistances cannot explain the S-shape. Due to the S-shape, J_{sc} and V_{oc} can be significantly reduced [50].

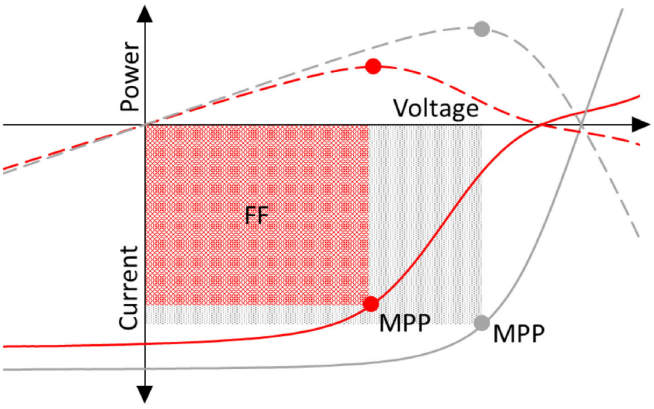

Figure 2.12: J-V curve for a well functioning solar cell (gray) and for a solar cell exhibiting S-shape behaviour (red). Solid lines representing J-V and dashed lines representing power-voltage [50].

The S-shape, indicative of a charge transport bottleneck, can have several explanations. Firstly, a high concentration of interfacial trap states. Secondly, extraction or injection barriers due to a mismatch in band alignment. Thirdly, presence of layers with a very low electron and/or hole mobility, which leads to a low conductivity. These layers then function as insulating layers [50]. Fourthly, a big difference in hole mobility

in the HTL and electron mobility in the ETL. This can result in charge accumulation and the formation on an interface dipole [49]. Finally, there could be an issue in the physical contact between layers [51].

2.3.3. Hole transport layers

Hole transport layers play a crucial role in the extraction of holes from the PVK layer that are generated under illumination. After extraction, holes should be transported to the electrode. The band alignment of the HTL is important. The HOMO (or VB edge) of the HTL should be higher in energy than the the VB of the PVK, and the LUMO (or CB edge) of the HTL should be higher than the CB of the PVK layer. If the latter is the case, electrons are effectively rejected from moving towards the anode [52].

Other desirable properties of HTLs include a high conductivity (high concentration of holes and hole mobility), good interface with perovskite in order to reduce surface recombination as much as possible, and a good interface with the electrode by forming an ohmic contact [52]. In general, the decision of which transport layer to use is dictated by electrical properties, but also optical ones. In our case, when the HTL is used in an inverted p-i-n configuration, a high transparency in the UV-Vis region is desired.

Both inorganic and organic options for an HTL are available. Inorganic HTLs include NiO_x, VO_x and MoO_x. Organic HTLs include spiro-OMeTAD, spiro-TTB, P3HT, PTTA and PEDOT:PSS [52].

Spiro-TTB and spiro-OMeTAD

Spiro-TTB (2,2',7,7'-tetra(*N*,*N*-di-tolyl)amino-9,9-spirobifluorene) and spiro-OMeTAD (2,2',7,7'-Tetrakis[*N*,*N*-di(4-methoxyphenyl)amino]-9,9'-spirobifluorene) are conjugated small organic molecules based on a spiro unit (see Fig. 2.13). These materials have proven to be effective HTLs, since the production of the first solid-state PSC, in which spiro-OMeTAD was used. The properties of spiro-linked molecules originate from their rigid structure. They possess a good thermal stability and appropriate energy levels for transfer of holes and blocking of electrons [47].

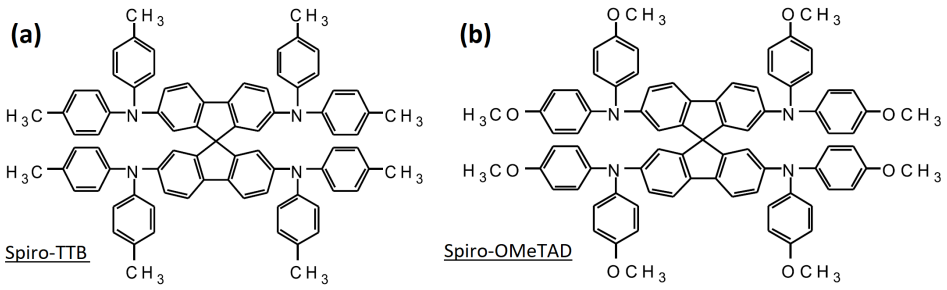

Figure 2.13: (a) Chemical structure of spiro-TTB. (b) Chemical structure of the spiro-OMeTAD [47].

Spiro-linked molecules have been used mainly in n-i-p PSCs. Thick layers up to 200 nm were required to fully cover the PVK. In addition, doping of the spiro-based layer is required to achieve a high enough conductivity and obtain a good device performance. Without doping, these layers show a low conductivity, resulting in a larger series resistance. Doping is usually done with inorganic salt molecules or other small molecules. On the other hand, doping can have a negative effect on the long-term stability of PSCs and increase the fabrication costs. Note that spiro-based molecules are already relatively expensive [47]. In order to overcome the problems doping can induce, undoped spiro-TTB and spiro-OMeTAD layers have been shown to work well in p-i-n PSCs reaching high hole mobilities and a PCE up to 18% [47].

Spiro-OMeTAD is commonly produced by solution-based methods. A disadvantage of this is that the layer is rather thick leading to high parasitic absorption losses in p-i-n PSCs. On the other hand, spiro-TTB is commonly produced by vacuum-based methods, which allows fabrication of much thinner films with lower parasitic absorption losses. This is an advantage spiro-TTB has over spiro-OMeTAD [53].

Molybdenum oxide

Molybdenum oxide (MoO_x) is a transition metal oxide that can serve as an inorganic HTL in several types of solar cells. In general, MoO_3 is used. However, the oxidation state is subject to change in the deposition

process, either on purpose or unintentionally. The oxidation state is therefore somewhere in between MoO_3 and MoO_2, which is also denoted as MoO_3 with x < 3. For more information, see subsection 3.2.1. MoO_x thin films can be fabricated by both vacuum-based and solution-based deposition [54].

An advantage of MoO_x is that it has a relatively high hole mobility, can enhance stability in PSCs (since it is inorganic), is relatively cheap and has a very small valence band offset with the frequently used PVK $FA_{0.83}Cs_{0.17}PbI_{1.5}Br_{1.5}$ [54]. Especially blocking of moisture penetration to the active layers can drastically improve stability if a MoO_x layer is present. In addition, MoO_x attracted attention to be used as a supportive layer for charge extraction in several types of solar cell due its low optical losses (high transparency) [55]. MoO_x has also been used as buffer layer between the HTL and TCO or gold (Au) electrodes. In one study, MoO_x was co-evaporated with the Au film [56].

Despite the beneficial properties that MoO_x possesses, several studies show that in practice several issues occur leading to poor device performances. First of all, we should mention that hole extraction by a MoO_3 layer happens between the VB of the PVK and the low lying CB of the MoO_3 layer. An occurring problem was that the energy levels of both PVK and MoO_3 changed after deposition on top of each other. For the PVK layer, the bands shifted downwards, whereas the bands of MoO_3 shifted upwards. This shift leads to a barrier for hole extraction. In addition, it has been shown that a chemical reaction (MoO_3 to MoO_2) occurs at the PVK/MoO_3 interface. This reaction leads to an increase in surface recombination. The addition of a thin passivation layer between PVK and MoO_x has been suggested to overcome this problem [57].

2.3.4. Electron transport layers

Electron transport layers play a key role in the extraction of photogenerated electrons from the PVK absorber layer. Subsequently, they are responsible for the transport of the electrons to the electrode. Moreover, ETLs simultaneously serve as a hole blocking layer which leads to a reduction in recombination. The most relevant property of an ETL is its energy band alignment. The LUMO (or CB edge) of the ETL must lie equal with or underneath the CB of the PVK, and the HOMO (or VB edge) of the ETL must lie under the VB edge of the PVK layer. If this is the case, electrons will be transported to the ETL since they can move to a lower energy level, whereas holes will be blocked [58].

Other relevant properties of ETLs are the electron mobility, presence of trap states, stability, morphology and interfacial properties. All these properties influence each other and determine the performance of the ETL in a PSC. In general, a relatively high electron mobility is desired to efficiently transport electrons through the ETL. Since the mobility is related to the defects, a low number of defects and thus trap states is desired. Especially optimization of the PVK/ETL and ETL/electrode interfaces are relevant to reduce surface recombination as much as possible. In view of that, a proper morphology of the ETL is needed to improve the contact with the PVK layer [59].

Inorganic materials such as TiO_2, Al_2O_3 and ZrO_2 are often used as ETL in PSCs with a mesoporous architecture. On the other hand, organic molecules such as C60 and derivatives of C60 (e.g. PCBM and ICBM) are often used in PSCs with an inverted p-i-n architecture. If the ETL is used in an n-i-p configuration, a high transparency in the UV-Vis region is desired [59].

C60

Buckminsterfullerene is a type of fullerence with chemical formula C_{60}. C60 is a material that efficiently extracts electrons from the PVK film, has a suitable energy level alignment, decent electron mobility and can be fabricated at low temperatures [59]. Solution-based methods turn out to be not practical for the fabrication of C60, as it is a hydrophobic molecule. In addition, spin-coating of a hydrophilic PVK precursor solution on top of C60 is difficult. For this reason, C60 is often used in inverted p-i-n architectures where it is deposited one top of the PVK layer by vacuum-based methods [60].

Incorporation of C60 as ETL, showed to reduce the phenomenon of hysteresis in PSCs. This result is possibly due to the excellent electron extraction of the C60 layer [59]. Note that hysteresis is the phenomenon where the J-V curve looks different depending on the scan direction (from forward-bias to reverse-bias or reversed). This phenomenon is not observed in other types of solar cells and the exact physical process behind hysteresis is still under debate [17].

The debate on the optimal thickness for the C60 layer is still ongoing. Some research suggests that a 1 nm

thick layer of C60 is already enough to achieve a high device performance [49]. In other research, a thickness of 15 nm turned out to give the best performance [61]. When the layer is too thick, it becomes harder for electrons to transport through it, which leads to an increase of the series resistance and recombination in the PSC. The optimal thickness could differ between different devices depending on the used PVK layer.

2.3.5. Transparent conductive oxides

Generated charge carriers in the absorber layer are collected at the front and back electrodes of the cell. If we assume the ETL to be at the back of the cell, the back electrode collects the electrons and covers the entire cell surface. On the other hand, at the front of the cell (hole collection), a metal electrode could only cover a very small portion of the surface, as shading losses would become too high. Since perovskite and transport layers have a relatively poor lateral conductivity due to growth direction of the materials during deposition, a transparent layer with good lateral conductivity at the front of the cell is required. This function is fulfilled by a transparent conductive oxide layer (TCO). A TCO is a metal oxide mixture with a wide bandgap [62].

Since TCO acts as front electrode, it should be both highly conductive and highly transparent (to minimise parasitic absorption losses). The wavelength range where the TCO layer should have a high transparency depends on the active wavelength range of the absorber material. For short wavelengths, the transparency is low due to high absorption of light with energies higher than the bandgap of the TCO. For wavelengths in the visible range, the transmission is very high, which is relevant for solar cell applications. Beyond a wavelength known as the plasma wavelength λ_p, the absorption and reflection of a TCO layer increase. However, this does not cause a problem if the wavelength belonging to the bandgap of the absorber layer is smaller than λ_p [21]. The conductivity of TCOs depends on the concentration of free charge carriers and their mobility. For this reason, possible doping of the TCO, size of crystalline grains, and presence of defects influence the conductivity. This property makes the deposition method, doping techniques, and post annealing treatment relevant for optimisation of TCO thin films [62].

For all TCOs, a trade-off has to be made between conductivity and transparency when it comes to the thickness of the TCO layer. An increasing layer thickness leads to a higher concentration of charge carriers and therefore increases the conductivity. At the same time, an increase in thickness would decrease the transparency of the layer [63].

Indium tin oxide

ITO is a solid mixture of indium(III) oxide (In_2O_3) and tin(IV) oxide (SnO_2). It typically consists of 90% In_2O_3 and 10% SnO_2 (percentages by weight). Currently, ITO is the best and most widely used TCO due to its high electrical conductivity and optical transparency [63]. The high conductivity of ITO is related to the presence of shallow impurity states close to the conduction band edge of In_2O_3. The shallow impurity states are produced by Sn^{4+} present at In^{3+} positions and by the presence of oxygen vacancies in In_2O_3. Due to thermal ionization of electrons from these shallow states to the CB at room temperature, the concentration of free electrons in the conduction band increases. When the content of SnO_2 is sufficient (enough doping with Sn^{4+}), a big population of free electrons, known as an electron gas, exists in the ITO. Most importantly, the In_2O_3 bandgap stays intact and the material remains transparent in the visible region [64]. A disadvantage of ITO is that indium has a very low abundance in the earth's crust (0.05 ppm) [21].

2.3.6. Buffer layers

A buffer layer is one of the possible inter-layers that can be added to the PSC architecture with the goal to enhance device efficiency and stability. Other inter-layers include passivation layers, placed at the PVK/ETL and/or PVK/HTL interfaces, and seed layers, used to assist the vertical growth of perovskite crystals on top. In the inverted p-i-n structure, buffer layers are generally used to improve the interface between the ETL and the metal electrode. Materials such as bathocuproine (BCP), LiF, polyethylenimine (PEIE) and aluminum/zinc oxides are often used to prevent as much recombination between the ETL and electrode as possible [65].

Desirable properties of a buffer placed on the electron transport side include blocking of holes and improving the extraction of electrons. In addition, a buffer layer should provide a better shunt protection and in general protect the cell from influences hindering the stability of the PSC [66]. It is known that optimizing the thickness of the buffer layer is relevant to improve the PCE. On the other hand, other guidelines for buffer layers in

PSCs remain unclear [65]. Note that buffer layers can also be used at the interface between the HTL and TCO. This could be in both n-i-p or p-i-n architectures. MoO_x is sometimes used in this position.

Bathocuproine

Bathocuproine (2,9-dimethyl-4,7-diphenyl-1,10-phenanthroline) is an organic molecule that is often used as a buffer layer by being placed at the C60/Ag or PCBM/Ag interface in p-i-n PSCs. BCP has even been shown to enhance the efficiency when used as passivation layer at both the HTL/PVK and PVK/ETL interfaces at the same time [67]. BCP layers can be fabricated with both solution-based and vacuum-based techniques.

Several studies have investigated the effect of adding a BCP layer between the C60/Ag or PCBM/Ag interfaces. When Ag is placed in direct contact with PCBM or C60, a Schottky barrier is formed, as can be seen in the left of Fig. 2.14a. This barrier leads to charge accumulation and a larger series resistance, and can eventually degrade the solar cell [68]. Note that the barrier height is relatively low. When a BCP layer is placed in between the ETL and electrode, BCP prevents contact between the ETL and electrode. This improves the interface to a good ohmic contact, leading to a decrease of the series resistance. In addition, charge accumulation is eliminated and the shunt resistance becomes larger due to a decrease of interfacial recombination (see middle of Fig. 2.14a) [65],[68]. However, as the BCP layer thickness increases, the series resistance increases due to the low conductivity of BCP. Moreover, the shunt resistance decreases due to the enhanced electron-hole recombination that emerges from charge accumulation at the ETL/BCP interface. Most of this recombination tends to occur at the PVK/ETL interface, as can be seen in the right of Fig. 2.14a [65]. Considering the above, multiple studies suggest that a thickness around 5 nm for the BCP layer is optimal to enhance efficiency and stability of PSCs [65],[68].

BCP molecules are able to make a chemical bond with Ag atoms, as depicted in Fig. 2.14b. This bond suppresses the diffusion of Ag towards the other layers of the PSC. Since electrode diffusion has been identified as one of the causes of device degradation, the BCP layer can improve stability [69]. In addition, due to the good hydrophobicity of BCP, it can reduce water and oxygen erosion of the PVK layer [67]. On the other hand, some research postulates that since BCP is an organic molecule, it is not stable against UV light and cannot act as a effective protection layer against other influences [70].

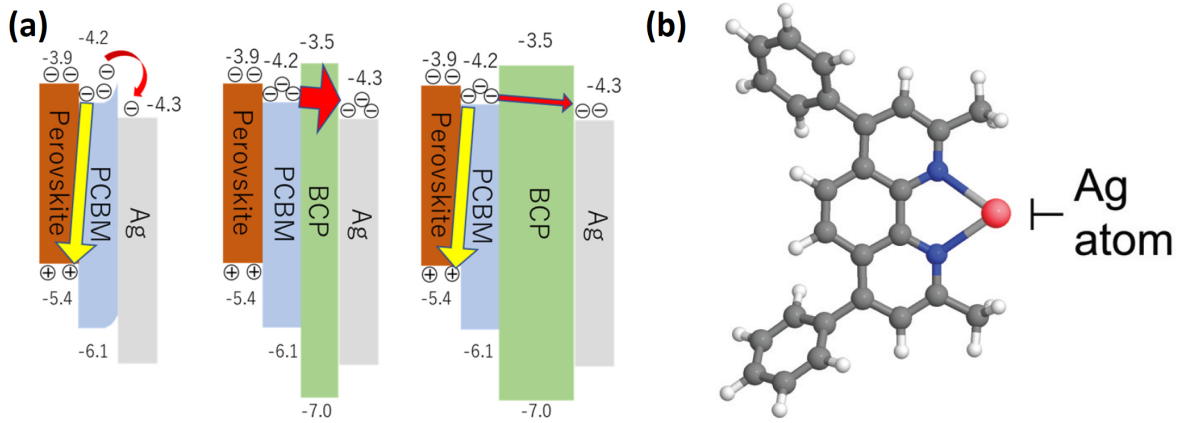

Figure 2.14: (a) Energy band diagram and charge transfer in PVK, PCBM, BCP and Ag stack. Left: No BCP, forming of Schottky barrier. Middle: thin layer BCP, forming of ohmic contact. Right: thick BCP layer, causing recombination [65]. (b) Structure of BCP that coupled with an Ag atom (red). H atoms in white, N atoms in blue and C atoms in grey [69].

3

Experimental Methods

3.1. Substrate preparation, storage and PSC fabrication

3.1.1. Substrate preparation and sample storage

Four different types of substrates are used in this work depending on the material deposited and the type of characterisation. These are:

- Microscope glass slides, which are used as a substrate to deposit thermally evaporated PVK on and to carry out a variety of tests on the deposited films.
- A piece of silicon wafer, which is used as a substrate to deposit FAI on.
- Quartz substrates, which are used as a substrate for different thermally evaporated materials and for spin-coated PVK. More specifically, most of the characterisation of individual layers and combination of layers is done with thin films deposited on top of quartz substrates.
- Corning glass substrates, which are used for the production of devices. The Corning glass, with initial dimensions of 10 cm x 10 cm and a thickness of 0.7 mm, is cut with a diamond blade dicer to achieve the required dimensions for production of devices (2.5 cm x 2.5 cm).

A variety of methods are used to clean the substrates. Among these methods, an ultrasonic bath and a UV-ozone cleaner are used in sequence. In an ultrasonic bath, high-frequency sound waves are transmitted through a liquid. This agitates the liquid and creates microscopic bubbles which implode on the substrate surface to remove contaminants [71]. UV-ozone cleaning relies on UV light with specific wavelengths of 184 nm and 254 nm. Upon irradiation with the 184 nm light, oxygen present in the air can form radicals which can react further to molecules of ozone. In the meantime, the 254 nm light excites organic contamination present on the substrate surface to increase its reactivity. The reaction of excited contamination with ozone results in the formation of volatile molecules which easily leave the surface. This results in a clean substrate surface [72].

Before spin-coating, quartz substrates are cleaned extensively. Firstly, a 15 min treatment in the ultrasonic bath with acetone, followed by 15 min with ethanol. Next, the samples are dried with a nitrogen gun and placed in the UV-ozone cleaner for 5 min. UV-ozone treatment increases the wettability which plays an important role in the spin-coating process. Substrates used for the deposition of thermally evaporated thin films are cleaned less extensively. Firstly, substrates are cleaned by wiping a tissue with acetone over the surface, followed by ethanol. Finally, the samples are placed in the UV-ozone cleaner for 1 to 5 min. For the production of devices, the extensive cleaning procedure is applied. After this, the substrates are transported to the EKL clean room where they are rinsed with acetone and isopropanol and subsequently dried with a nitrogen gun. After the deposition of the ITO layer, the samples are cleaned again before the deposition of the first transport layer. Again the extensive method with the ultrasonic bath is used. However, use of the UV-ozone cleaner is omitted since this can raise the work function of ITO [73].

Since PVK and the organic layers degrade when they are exposed to oxygen and water, samples are stored in a glove box filled with nitrogen (see Fig. 3.1a). A metal tube is used to transport samples between different glove boxes or buildings to prevent exposure to the ambient atmosphere (see Fig. 3.1b).

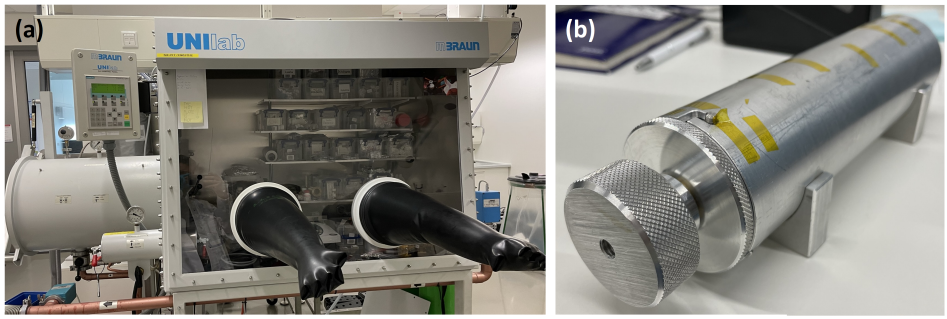

Figure 3.1: (a) Glove box filled with nitrogen for storage of samples. (b) Metal tube to transport samples.

3.1.2. Mask design

In order to produce a full PVK device, stainless steel masks are used to deposit patterned layers with the correct dimensions. The masks used for the ITO, HTL, thermally evaporated PVK, ETL, BL and back electrode are shown in Fig. 3.2. Note that for spin-coated PVK layers the mask is not used. Instead, a knife and cotton swab are use to remove any spin-coated PVK from the edges. The glass substrates are aligned with the masks as precise as possible and connected to the masks with heat resistant tape.

Eventually, four cells can be produced per 2.5 cm x 2.5 cm glass substrate: two larger cells with an active area of 0.6 x 0.6 = 0.36 cm^2 and two smaller cells with an active area of 0.4 x 0.4 = 0.16 cm^2. For more details on the mask design see Ref. [74].

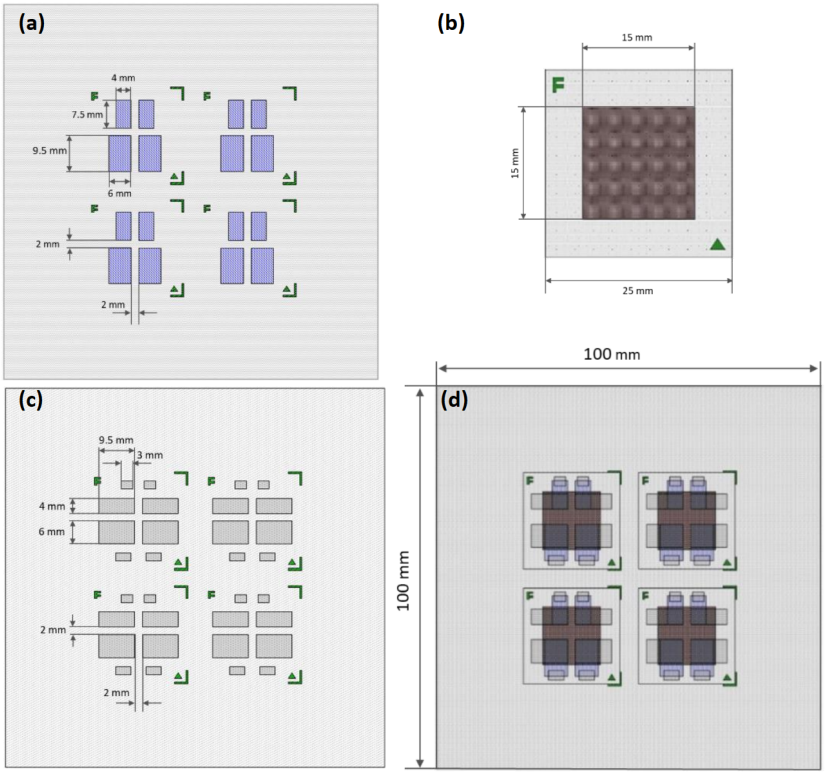

Figure 3.2: Set of metal masks used to produce PSCs: (a) mask for ITO, (b) mask for HTL, PVK, ETL and BL (c) mask for metallic back electrode and (d) result of all layers on top of each other [74].

3.1.3. Device fabrication

The process of creating a PSC consists of several steps. A flowchart representing this process is shown in Fig. 3.3. The deposition techniques used for each step will be further explained in the next section. An overview of all different fabricated devices is shown in Fig. A.1-A.11 in the appendix.

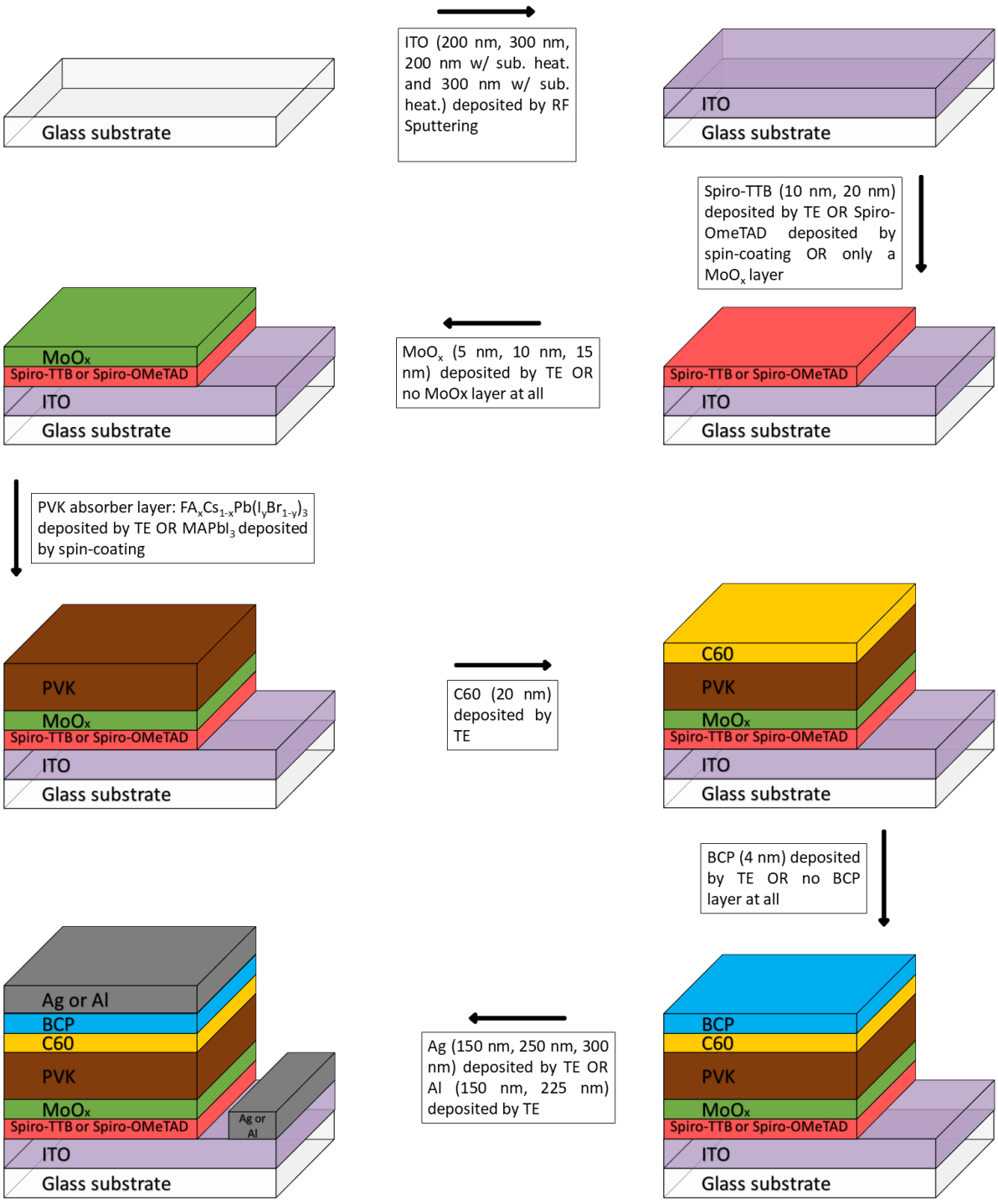

Figure 3.3: Flowchart depicting the PSC fabrication process. Deposition techniques and different materials with their thicknesses are addressed. TE = thermal evaporation.

3.2. Deposition methods

3.2.1. Thermal evaporation

Thermal evaporation (TE) is a physical vapor deposition (PVD) method in which the temperature of a material is raised until it melts and evaporates (or sublimes). In order to assure deposition on a substrate, the mean free path should be longer than the source-substrate distance. For this reason, the process is executed under a high vacuum to prevent collisions with background gas molecules as much as possible [75].

Resistive heating is the most commonly used method for TE. The source material, in powder or pellet form, are evaporated by a resistively heated filament or boat. The filament or boat are often made of metals such as molybdenum or tungsten, because of their high melting temperatures and the fact that they do not interact with or contaminate the intended evaporated material. Often crucibles made of quartz, boron nitride or alumina are used to hold material in powder form. These are then placed in a tungsten wire basket [76]. The temperature is slowly raised by increasing the direct current through the resistive element until the required deposition rate is reached. Next, a shutter is opened and the vapor particles travel towards a substrate where they condense on the surface forming a thin layer [75].

It is desirable to have a good thickness uniformity across the entire film. During deposition, substrates are rotated to increase this uniformity. Considering the situation shown in Fig. 3.4a,b, it is possible to derive an equation for the thickness with respect to the position on a substrate. From experiments it is known that the evaporating flux density follows a $\cos^n(\phi)$ relation. When the simplest model, $\cos(\phi)$ (Knudsen distribution), is used, the mass deposited per unit area is given by:

$$\frac{dM_s}{dA_s} = \frac{M_{tot}\cos\phi\cos\theta}{\pi r^2} \tag{3.1}$$

in which M_{tot} is the total evaporated mass by a source in a certain time, dM_s is the amount of mass deposited on substrate area dA_s. In addition, ϕ is the emission angle, θ the receiving angle and r the distance between the source and substrate. Note that the projected area of dA_s on the evaporation cone is equal to dA_c [75], [77].

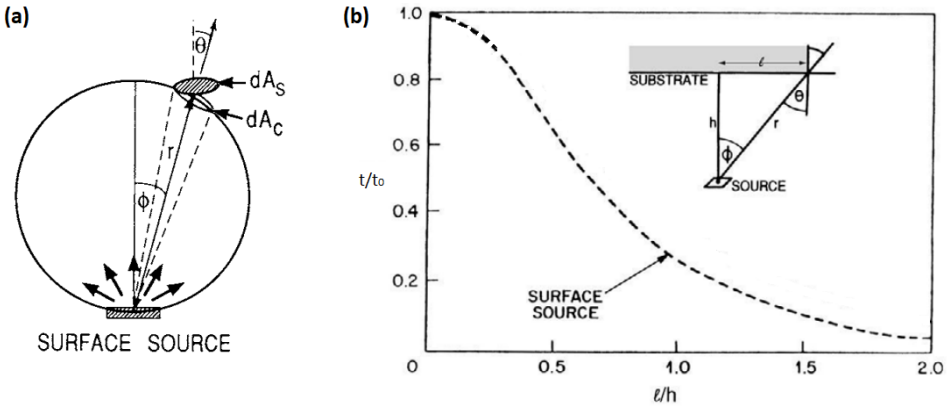

Figure 3.4: (a) Schematic of evaporation from a surface source. (b) Uniformity of normalized film thickness (t/t_0) for a surface source for different values of the l/h ratio. Insert (b): geometry of evaporation onto a parallel plane substrate [77].

Next, the thickness t can be calculated as a function of the source-substrate distance h and the position on the substrate l. The result is given by:

$$t = \frac{1}{\rho}\frac{dM_s}{dA_s} = \frac{M_{tot}\cos\phi\cos\theta}{\rho\pi r^2} = \frac{M_{tot}}{\rho\pi r^2}\frac{h^2}{r^2} = \frac{M_{tot}h^2}{\rho\pi(h^2+l^2)^2} \tag{3.2}$$

in which ρ is the material density. Note that $\cos\theta = \cos\phi = h/r$ and $r = (h^2+l^2)^{1/2}$ have been used to arrive at this result. When the thickness is normalized with the maximum possible thickness t_0 at ϕ is equal to zero, the thickness distribution, as shown in Fig. 3.4b, is obtained [77].

The deposition rate, measured in units of Å/s or nm/s, and deposited thickness are monitored by a quartz crystal microbalance sensor (QCM sensor). QCM sensors have a finite lifetime and must be replaced once in a while depending on the total amount of material deposited on it. Due to the piezoelectric effect, the quartz crystal can mechanically oscillate at a certain frequency when an AC voltage is applied to it via small metal electrodes. The resonance frequency is affected by the addition of small amounts of mass onto the sensor surface. More precisely, in 1959, Sauerbrey showed that the change in frequency of the oscillating quartz is linearly related to the change of mass on its surface [78]. By monitoring the frequency change, the deposition rate and thickness can be determined in real time. In order to do so, the QCM sensor needs some input information about the material that is being deposited. The input consists of the material density, Z-ratio and tooling factor (TF) [79].

The Z-ratio is a parameter that corrects the frequency change to deposition rate/thickness calculation for the effects of acoustic impedance mismatch between the quartz crystal and the deposited material. It can be calculated with the following equation:

$$\text{Z-ratio} = \frac{Z_{quartz}}{Z_{material}} \tag{3.3}$$

in which Z_{quartz} is the acoustic impedance of quartz ($8.834 \cdot 10^5$ g/cm^{2}s) and $Z_{material}$ the acoustic impedance of the evaporated material [79].

Another important term in TE is the tooling factor. This is the correction needed between the thickness deposited on the QCM sensor and the thickness of the actual deposited film on the substrate. The TF depends on the substrate position, sensor position, source position, geometry of the chamber and the material evaporated. The tooling factor is calculated as the ratio of the actual thickness t_{actual} to the thickness measured by the sensor t_{sensor}. In equation:

$$\text{TF} = \frac{t_{actual}}{t_{sensor}} \tag{3.4}$$

By measuring the actual thickness and reading the value of the sensor, the TF is calculated. Sometimes, this result can be put in the thermal evaporation program to have the sensor read the actual thickness. When an initial tooling factor is already in place, it should be multiplied with the ratio of t_{actual} and t_{sensor} to get the new TF. Note that sometimes the TF is presented as a percentage [80].

For the purpose of this research, three different thermal evaporation systems have been used. These are described below.

Perovskite deposition

The AJA ATC orion 4 thermal evaporator is used in an attempt to obtain $FA_xCs_{1-x}Pb(I_yBr_{1-y})_3$ based perovskite. PVK thin films are produced by sequential deposition of three precursors: PbI_2, FAI and CsBr. These materials undergo sublimation when sufficient heat is supplied. Each precursor is placed in one of the three available source positions in the vacuum chamber of the evaporator (see Fig. 3.5b). The evaporation source consists of a quartz crucible placed in a Knudsen cell (see Fig. 3.5c,d). The Knudsen cell is used to form the evaporation beam and consists of resistive windings, heat shielding and a thermocouple [81]. Each source position has its own small shutter. In the middle above the sources, a QCM sensor is located. Since there is only one sensor, it is not possible to accurately perform co-evaporation in this specific setup. Above the sensor a big shutter, which can move sideways, is present. The big shutter allows measurement of the deposit rate before any deposition on the substrate has happened. The substrate holder can rotate and is placed at the top of the chamber facing downwards. The height of the substrates can be adjusted manually. A schematic is shown in Fig. 3.5e.

Each source is controlled from its own control panel. In addition, there is one central controller with a display. The system as a whole allows control over several important aspects such as controlling the temperature, opening and closing of shutters, selecting an evaporation source and adjusting the target thickness. Note that a specific target thickness, measured by the QCM sensor, is given as input to the system for each source.

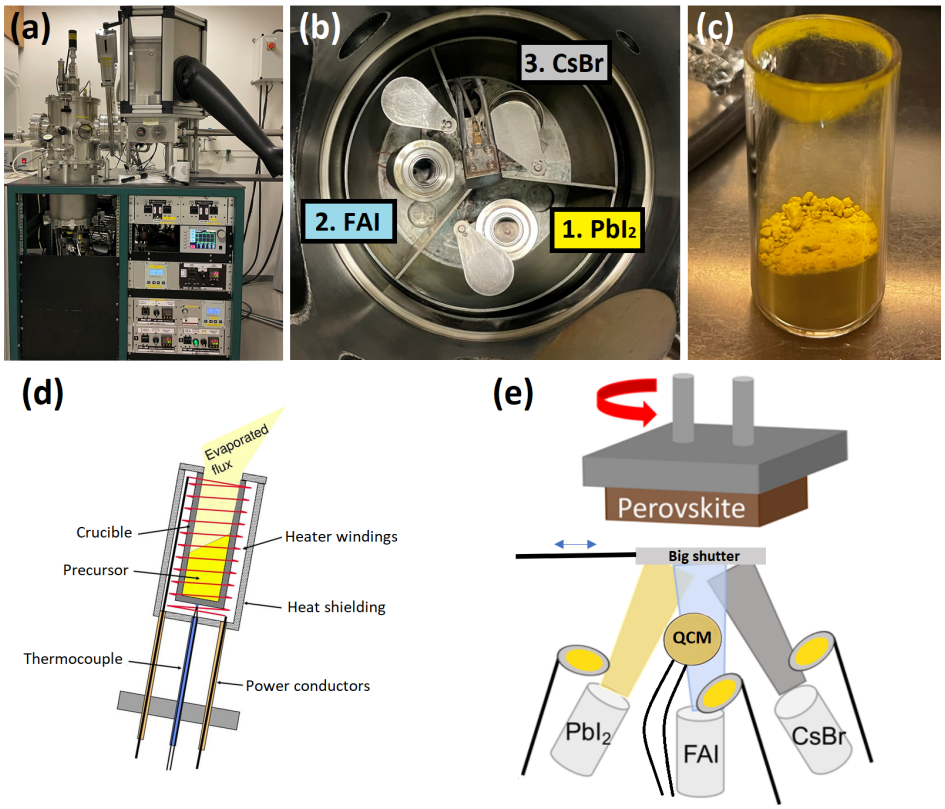

Figure 3.5: (a) AJA evaporator. (b) View of the evaporation chamber from the top with precursor at each source location indicated. (c) Quartz crucible filled with PbI_2. (d) Knudsen cell [82]. (e) Schematic of relevant parts inside the vacuum chamber [35].

To determine the amount of material n (in moles) that gets deposited on a substrate the following equation is used:

$$n = \frac{\rho A t}{M} \tag{3.5}$$

in which A is the surface area of the substrate, t the film thickness and M the molar mass. The required real thickness for each individual layer depends on the desired molar ratio, $n_{\mathrm{FAI}}{:}n_{\mathrm{PbI_2}}{:}n_{\mathrm{CsBr}}$, and the total target thickness of the PVK film. When a specific molar ratio and total target thickness are chosen, the following system of equations can be solved to find the thickness of each individual layers:

$$\begin{cases} \dfrac{n_{\mathrm{PbI_2}}}{n_{\mathrm{FAI}}} = \dfrac{t_{\mathrm{PbI_2}} \cdot \rho_{\mathrm{PbI_2}} / M_{\mathrm{PbI_2}}}{t_{\mathrm{FAI}} \cdot \rho_{\mathrm{FAI}} / M_{\mathrm{FAI}}} \\ \dfrac{n_{\mathrm{PbI_2}}}{n_{\mathrm{CsBr}}} = \dfrac{t_{\mathrm{PbI_2}} \cdot \rho_{\mathrm{PbI_2}} / M_{\mathrm{PbI_2}}}{t_{\mathrm{CsBr}} \cdot \rho_{\mathrm{CsBr}} / M_{\mathrm{CsBr}}} \\ t_{\mathrm{total}} = t_{\mathrm{PbI_2}} + t_{\mathrm{FAI}} + t_{\mathrm{CsBr}} \end{cases} \tag{3.6}$$

Unfortunately, the TF for each material/source position cannot be provided as input in the control panel. Therefore, the calculated thicknesses from the system of (3.6) have to be divided by the TFs to obtain the thicknesses that are used as input to the system (t_{sensor}). A Matlab script has been written to execute all the calculations described above (see A.2 in the appendix). In this script, the desired ratio, total target thickness and TFs can be adjusted.

When the thickness is calculated and used as input for the deposition program for a specific source, the process starts by increasing the temperature until the target temperature is reached. One should be careful for overshooting of the temperature as the target temperature approaches. Next, the deposition rate is checked by opening the small shutter. When the rate has stabilised around the desired value, the big shutter can be

opened and the actual deposition on the substrate starts. During the deposition, the rate is kept as close as possible to the desired rate by manually increasing the temperature. In practice, this means that constant attention is required during the depositions. Once the target thickness is reached, the big and small shutter automatically close and the next source can be selected. The deposition is carried out in a high vacuum ranging from $6.00{\cdot}10^{-7}$ to $3.00{\cdot}10^{-6}$ mbar and with substrate rotation of 20 rpm. Relevant deposition parameters are given in table 3.1.

Table 3.1: Relevant parameters for the three precursors: PbI_2, FAI and CsBr. Material density, molar mass, Z-ratio, temperature range where deposition happens and target deposition rate are given. An * indicates that the material's Z-ratio is not known (a value of 1.000 is used).

	Density [g/cm^3]	**Molar mass [g/mol]**	**Z-ratio [-]**	**Temp. range [°C]**	**Dep. rate [Å/s]**
PbI_2	6.16	461.01	1.000*	180-220	0.50
FAI	2.31	171.97	1.000*	85-105	0.50
CsBr	4.46	212.81	1.410	385-405	0.15

For the purpose of this research, depositions with a different target thickness, ratio and annealing procedure are carried out. Another variation is the execution of a so called multi-layer deposition. In this case, sequential deposition is carried out from each source to get a certain thickness, this is then repeated N times (see Fig. 3.6). As an example, a total target thickness of 400 nm is attempted by depositing a 100 nm PVK layer four times. In case $N = 1$, we refer to it as a single-layer deposition.

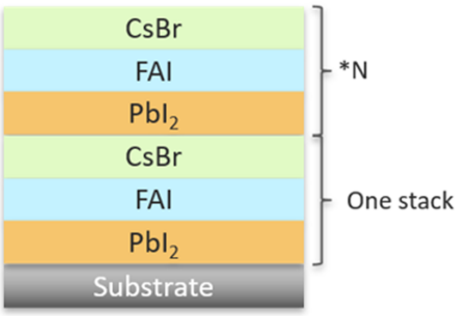

Figure 3.6: Visualisation of a multi-layer deposition process (drawing made by Jin Yan).

After a certain amount of depositions, the chamber is opened and cleaned with tissues covered in acetone or ethanol. This cleaning is important to avoid any influence of contamination on the depositions. In addition, the crucibles are taken out and extensively cleaned with acetone and ethanol in the ultrasonic bath. Next, the crucibles are filled with new powder and put back in chamber. The QCM is replaced when its lifetime drops below 90%.

An advantage of this evaporator is that substrates can be loaded in and out without exposing them to the air and without having to vent the vacuum chamber. In order to do so, substrates are firstly connected to the substrate holder with a metal bar and screws or with tape. Next, the holder is placed in the compartment shown in the top right of Fig. 3.5a which can be filled with nitrogen. When the O_2 level in this compartment has dropped down to about 50 ppm, the load lock is vented. The substrate holder is then placed in the load lock and put under a vacuum. Next, the port between the load lock and chamber is opened and the substrate holder is moved in via a movable arm. After connecting the substrate holder to the top of the chamber and putting it at the right height, the movable arm is retrieved and the port is closed. The steps are reversed when samples are loaded out. A small container is used to transport samples from the evaporator to the glove box.

MoO_x deposition

The Provac Pro 500S high vacuum PVD coating system is used for the thermal evaporation of MoO_x and located in the EKL clean room. This system is capable of performing both thermal evaporation and electron beam evaporation. Images of the outside and inside of the system are shown in Fig. 3.7a,b. Substrates are taped to a mask (Fig. 3.2b) and connected to the substrate holder with alligator clamps at the top of the

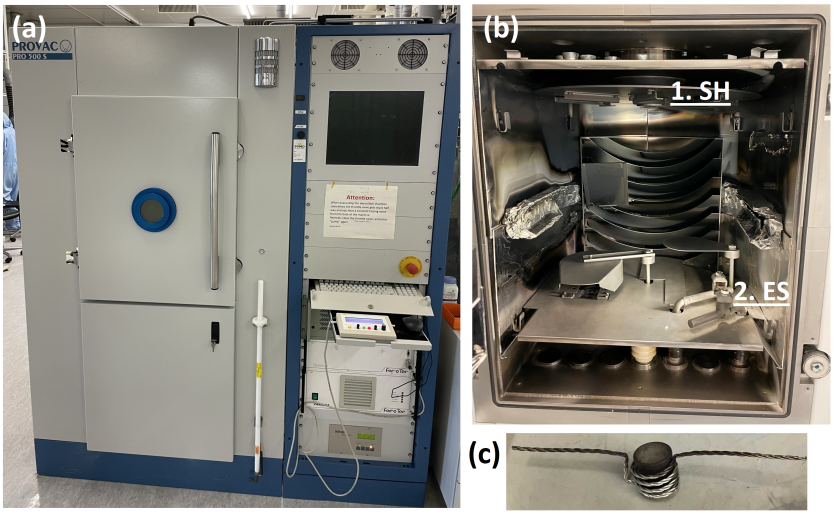

Figure 3.7: (a) Provac evaporator. (b) Side view of the evaporation chamber with location of substrate holder (1. SH) and evaporation source (2. ES) indicated. (c) Tungsten basket with alumina crucible used for MoO_x deposition.

chamber. A tungsten basket with alumina crucible is used as thermal evaporation source for MoO_x (see Fig. 3.7c). After loading of the samples and evaporation source, a recipe is used in which the deposition parameters are specified. The TF is set to 97.5%, substrate rotation to 10 rpm, Z-ratio to 1.000, density to 4.700 g/cm^3 and required chamber pressure to $5.00 \cdot 10^{-6}$ mbar. It takes about two hours to reach the required vacuum.

In addition, the recipe specifies the ramping up of power to the eventual deposition power, which is expressed as a percentage of the maximum power of 3.2 kW. The deposition goes as follows:

1. Power increase to 25% with ramp time of 20 s and hold time of 10 s
2. Power increase to 35% with ramp time of 20 s and hold time of 60 s
3. Power increase to 45% with ramp time of 60 s and hold time of 90 s
4. Opening of shutter and deposition on substrate

The deposition is carried out with a rate of 0.1 nm/s monitored by a QCM sensor. Since we are evaporating only thin layers of MoO_x (5, 10 or 15 nm) the actual deposition time is only a few minutes.

A disadvantage of the Provac is that loading in and out of samples does not happen under inert conditions. This implies that samples are exposed to the ambient atmosphere. The evaporated powder, originally molybdenum trioxide (MoO_3), is not stored under inert conditions. In addition, the evaporation process influences the stoichiometry. For this reason, the true oxidation state is unknown. Therefore, MoO_3 will be named MoO_x ($x < 3$) in this report.

Spiro-TTB, C60, BCP, silver and aluminium deposition

The Mantis Hex evaporator is a thermal evaporator incorporated in a glove box. This allows us to make PSCs without exposure to the ambient atmosphere. In addition, organic powders evaporated with this evaporator, can be placed and removed from the vacuum chamber without exposure. Unfortunately, opening the vacuum chamber induces an increase to 10-40 ppm O_2 in the glove box due to a small leak at one of the source positions. An image of the outside and inside of the chamber and the different used evaporation sources is shown in Fig. 3.8. The system contains three source positions. One is used for the deposition of silver pellets, one for aluminium pellets and the other one for C60, spiro-TTB and BCP by swapping out the crucible in the tungsten basket.

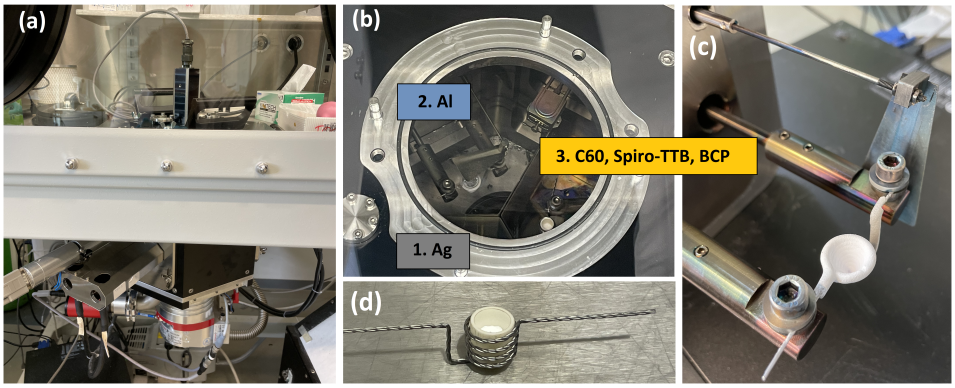

Figure 3.8: (a) Mantis Hex evaporator inside glove box. (b) Top view of the evaporation chamber with materials indicated. (c) Tungsten basket with alumina crucible used for spiro-TTB, C60 and BCP deposition and alumina coated tungsten basket used for Ag and Al deposition.

The required material (crucible with powder or Ag/Al pellet) is carefully placed in the evaporation source with tweezers. Next, samples are taped to the corresponding mask and substrate holder. The substrate holder is connected to the lid of the vacuum chamber. Subsequently, the system is evacuated. It takes about 30 minutes to reach a pressure around $3.00 \cdot 10^{-6}$ mbar after which the deposition program is started. Each materials has its own deposition program that consist of a few steps. Firstly, the material density, TF and acoustic impedance of the material $Z_{material}$ are specified as input for the QCM sensor. Next, the power supply for the corresponding source position is turned on and the substrate rotation is set to the required value. With this evaporator, the deposition is controlled by the current setting. Subsequently, the voltage limit is set to 6 V and the current through the source is slowly ramped up to a specified value. After the required current has been reached, the shutter is opened manually and the rate and thickness are monitored by the QCM sensor. During the deposition it is possible to increase (or decrease) the current to increase (or decrease) the deposition rate. When the target thickness is reached, the shutter is closed manually and the current is ramped down to 0 A in a specified time. Finally, the rotation is stopped and power supply turned off.

Existing programs are used for the evaporation of Al and C60. Details on these programs can be found in A.3 in the appendix. As one of the goals of this project, new programs are developed for the evaporation of Ag, BCP and spiro-TTB. More details on the developed programs and accompanying deposition rates can be found in subsections 5.1.3, 5.2.1 and 5.2.3.

3.2.2. One-step spin-coating

Spin-coating is the most used method to produce PVK thin films. Precursors are weighed according to the desired molar ratio and dissolved in a solvent. The precursor solution is then spread on a substrate to completely wet the surface and spun at high speeds. The centripetal force and surface tension of the liquid create and even covering. Next, the solvent evaporates partly during the spinning process and partly by a subsequent annealing process. This process, known as one-step spin-coating, results in the synthesis of a thin PVK film [83].

Some important factors have to be taken into account during synthesis. Firstly, the wettability which depends on the surface tension of the solution and the surface energy of the substrate. A good wettability implies that the precursor solution spreads easily on the surface. This is characterised by a low contact angle. UV-ozone cleaning increases the surface energy and therefore increases the wettability. Secondly, dust and other contaminants can cause pin hole formation. This stresses the importance of the cleaning procedure. Thirdly, many factors can influence the consistency of the process. For example, the evaporation rate is influenced by the ambient conditions. To decrease these influences, spin-coating is performed inside a glove box. Finally, the thickness of a spin-coated layer depends on the spin speed, concentration of the precursor solution and solvent evaporation rate [83].

The process starts with the preparation of the precursor solution. The precursor solution consists of methyl ammonium iodide (MAI), lead acetate trihydrate ($Pb(Ac)_2 \cdot 3H_2O$) and *N*,*N*-dimethylformamide (DMF). Two different precursor solutions are made with a different concentrations. The recipes are shown in table 3.2.

Table 3.2: Recipe for the precursor solution with normal concentration and higher concentration.

	MAI [g]	MAI [mmol]	$Pb(Ac)_2{\cdot}3H_2O$ [g]	$Pb(Ac)_2{\cdot}3H_2O$ [mmol]	DMF [mL]	Concentration [mol/L]
Normal con. pre. sol.	0.480	3	0.379	1	1.55	0.65
High con. pre. sol.	0.576	3.6	0.455	1.2	1.55	0.77

Firstly, the powders are precisely weighed with a scale and dissolved in the solvent. The precursor solution is then stirred overnight with a rotation speed of 250 rpm. Next, the precursor solution is filtered with a PTFE membrane with a pore size of 0.22 μm after which it is ready for the spin-coating process.

$MAPbI_3$ thin films are obtained with an SPS Polos spin-coater inside a glove box. Firstly, the substrate is placed in the middle of the spin-coater where a vacuum chuck secures the substrate firmly. Subsequently, the precursor solution is spread over the substrate with a pipette. To be more precise, 50 μL of precursor solution is used on quartz substrates and 150 μL is used for the production of devices. Next, the substrate is rotated at 2000 rpm for 45 s. The rotation speed increases/decreases with 500 rpm/s at the beginning/end of the process. Finally, the sample is left to dry for 3 to 4 min before it is placed on a hot plate. On the hot plate samples are annealed for 5 min at 100 °C. An image of the setup and other attributes is shown in Fig. 3.9.

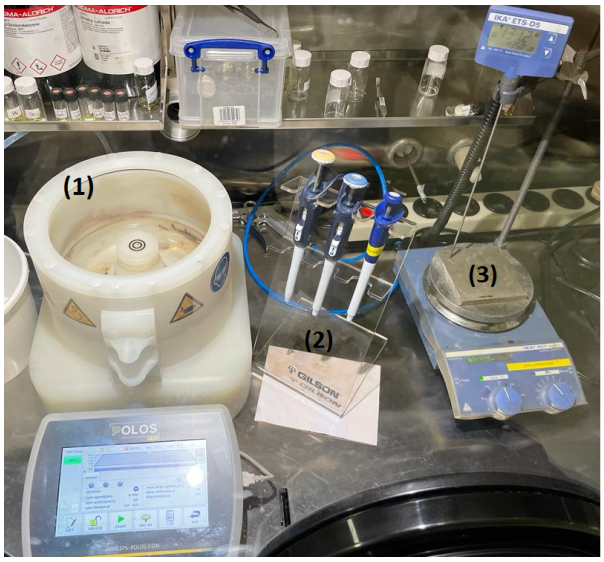

Figure 3.9: Spin-coating setup with (1) Polos spin-coater, (2) pipettes and (3) hot plate.

$MAPbI_3$ thin films are produced on top of glass/ITO/TL interface for the production of devices and on quartz to obtain results on its structural and opto-electronic properties. In total five batches of $MAPbI_3$ thin films are produced during different stages of this project. Some of these batches are produced solely on quartz, some solely for device purposes and some for both. In the latter case, the characterisation results directly tell something about the properties of the PVK layer in the device.

Next to spin-coated PVK, spin-coating is used to deposit Spiro-OMeTAD. Firstly, 75 mg of Spiro-OMeTAD is dissolved in 1 ml chlorobenzene and stirred for one hour with a rotation speed of 300 rpm. Next, the precursor solution is filtered with the same type of filter as used for PVK. Subsequently, 100 μL precursor solution is spread on a substrate and rotated at 3500 rpm for 45 s. The high rotation speed is used to get a thin layer. The rotation speed increases/decreases with 500 rpm/s at the beginning/end of the process. Finally, samples are annealed at 60 °C for one hour.

3.2.3. Radio frequency sputtering

Radio frequency or RF sputtering is a PVD method used to perform all kinds of depositions in the semiconductor industry. In this research, the technique is used to sputter ITO, which functions as the transparent front electrode of the PSCs. The process takes place in a vacuum chamber at a certain base pressure. A heavy inert gas, such as argon, is passed through the chamber between two electrodes (anode and cathode).

The electric field between the electrodes accelerates free electrons from the cathode to the anode. On its way, electrons collide with neutral argon atoms which undergo ionization. This results in the formation of a plasma. The argon atoms accelerate under the influence of the electric field towards the cathode where the source material (or ITO target) is present. Bombardment of the ITO target by argon ions causes atoms to be sputtered off into the plasma. This happens when the transferred energy is greater than the binding energy of the target atoms. The atoms diffuse towards the anode side and are deposited when they condense as a thin film on the substrate present there. A schematic of this process is shown in Fig. 3.10. The electrical potential between the electrodes is alternated at an RF of 13.56 MHz. This prevents positive charge to build up on the target material. During the positive cycle, electrons get attracted by the target. During the negative cycle, the argon ions and electrons move in their normal direction again and the sputtering continues [84].

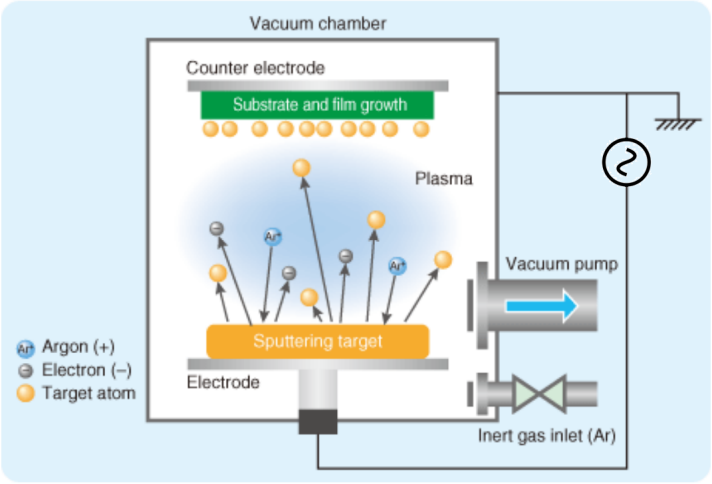

Figure 3.10: Schematic of the RF sputtering process. Directions of electrons, target atoms and argon ions during the negative part of the cycle are shown [85].

RF sputtering of the ITO layer is done in a Polyteknic cluster tool called '*Zorro*'. The machine is located in the EKL clean room. The recipe used for the sputtering of ITO consists of five steps during which the base pressure is kept at $2.00{\cdot}10^{-2}$ mbar. These steps include heating up, ramping up the deposition power (to 130 W), target cleaning, the actual deposition and ramping down the deposition power. The deposition time is set to 2872 s to obtain an ITO layer with a target thickness of 200 nm and 4308 s to obtain a target thickness of 300 nm. In addition, the argon flow is set to 34.875 sccm (standard cubic centimeters per minute), the 1% O_2 – 99% Ar flow to 10.125 sccm and the substrate rotation to 10 rpm for the entire deposition. Moreover, there is an option to heat the substrate during the process. The relation between the temperature set in the recipe T_{set} and the actual substrate temperature T_{sub} is given by:

$$T_{set} = -0.0005 \cdot T_{sub}^2 + 2.1721 \cdot T_{sub} - 26.785 \tag{3.7}$$

Note that this option was only available for a short time during this project. Substrate heating has been used for one batch with T_{set} = 250 °C and T_{sub} = 131 °C.

Four different ITO layers have been produced:

- Target thickness 200 nm without substrate heating.
- Target thickness 200 nm with substrate heating.
- Target thickness 300 nm without substrate heating.
- Target thickness 300 nm with substrate heating.

The only post-deposition annealing process performed on the ITO layer is the annealing process after the spin-coating of the PVK layer (5 min at 100 °C). ITO is deposited on glass for the production of devices and on quartz to obtain results on its structural and opto-electronic properties.

3.3. Characterisation techniques

3.3.1. X-ray diffraction

X-ray diffraction (XRD) is a technique that can be used to identify the phase (3D arrangement of atoms) in crystalline materials. Moreover, it can be used to determine physical properties of crystalline materials, such as unit cell parameters, crystal shape and presence of disorder [86]. When a collimated and monochromatic X-ray beam strikes a crystalline sample, X-rays scatter from the the different lattice planes. In case the scattered X-rays are in phase they can interfere constructively. This happens when Bragg's law is obeyed:

$$n\lambda = 2d\sin(\theta) \tag{3.8}$$

in which λ is the wavelength of the incoming X-rays, n is an integer, d is the spacing between a specific set of lattice planes and θ is the incident angle [87]. A schematic of this phenomenon is shown in Fig. 3.11a. When Bragg's law is obeyed, the measured reflection results in a peak in the diffractogram with a specific position and intensity. A lot of information is contained in the peaks and their features. Firstly, the peak position depends on the set of crystallographic planes (with a certain d) that generates the reflection and on the unit cell parameters. Secondly, the intensity of the peak depends on the unit cell content, the crystal size and symmetry. Finally, the full width at half maximum (FWHM) of a peak depends on the crystal size and the presence of disorder. The average crystal size can be determined from the FWHM with the Scherrer equation:

$$L = \frac{k\lambda}{\beta\cos(\theta)} \tag{3.9}$$

in which L is the average crystal size, k is the shape factor and β the FWHM (in radians) [87].

Families of lattice planes can be identified by the Miller indices, which describe a specific direction in reciprocal space. Since XRD measures the scattering of X-rays from lattice planes, each peak in a diffractogram can be associated to a certain set of Miller indices [86].

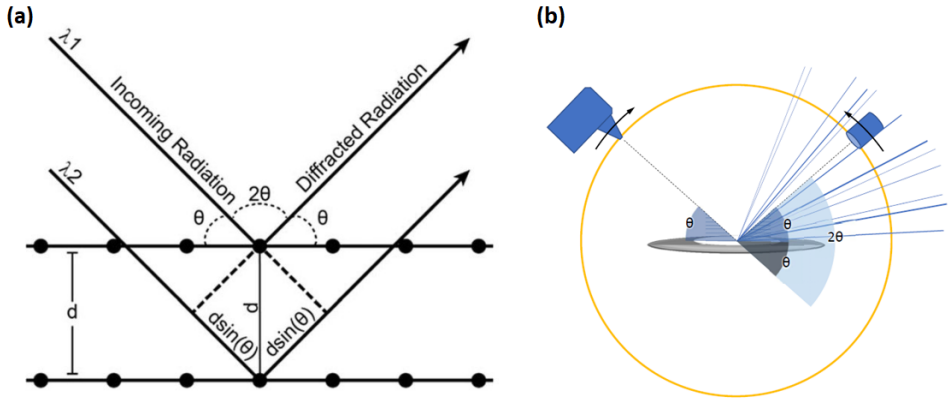

Figure 3.11: (a) Principle of XRD where incident X-rays hit a sample under an angle θ. Constructive interference occurs when the longer path length, $2d\sin(\theta)$, of $\lambda 2$ is equal to an integer number times the wavelength [88]. (b) Movement of the X-ray tube and detector according to the Bragg-Brentano geometry [86].

For the purpose of this research, the technique is used firstly to determine the crystal phases of spin-coated and thermally evaporated PVK. The peak positions, intensities and widths of the peaks are analysed to get a better understanding of the crystallinity of our depositions. This provides information on the quality of the PVK layer in the devices. Secondly, once problems were encountered with the thermal evaporator, XRD was used to determine if any PVK could be obtained after changing something. Thirdly, XRD spectra of thermally evaporated PVK with C60 and Ag are recorded. Finally, the technique is used to analyse the crystallinity of ITO depositions that differ in thickness and substrate heating.

Diffractograms are measured using a Bruker D8 Advance-ECO with Bragg-Brentano geometry. Firstly, X-rays are generated by an X-ray tube (Cu Kα radiation with a wavelength of 1.5418 Å). Next, incident-beam optics,

including a divergence slit, are used to condition the X-ray beam before it hits the sample. A goniometer is responsible for the movement of the source and detector according to the Bragg-Brenanto geometry. After the X-rays encounter the sample, optics on the receiving side are used to condition the X-ray beam. Finally, a Lynxeye-XE-T position sensitive detector counts the number of X-rays scattered from the sample and a diffractogram is obtained [87].

Measurements are done in a 2θ range from 5° to 60°, with a step time of 0.1 s/step for a total of 5334 steps. Moreover, the slit opening changes during a measurement to keep the sample illumination length (3 mm) constant. It is important to place the thin film substrate at the same height as the sample holder. Otherwise, a wrong peak position and intensity are obtained.

Since the thin films are deposited on quartz substrates, the amorphous phase of the quartz is seen as a background in all measurements. As a reference, the diffractogram of a quartz substrate only is shown in A.4 in the appendix.

3.3.2. UV/Vis/NIR spectrophotometry

UV/Vis/NIR spectrophotometry is a quantitative technique that is used to determine the absorption, transmission or reflection of a material as a function of wavelength. For the purpose of this research, the technique is used to determine the optical properties of thin film substrates, i.e. the different layers in the PSC.

When a medium is illuminated with light, the light can be returned (reflectance), pass through the medium (transmittance) or be absorbed by the medium (absorptance). Reflection can occur at the boundary between two different media (surface reflection) or at the inside of a medium (volume reflection). Moreover, the total reflection can be categorised as specular reflection, i.e. direct reflection from a smooth surface, and diffuse reflection, i.e. reflection of rough surfaces and reflection from scattering within a medium. Similarly, the transmission can be either direct or diffuse [89]. Absorption is the process where an incident photon is absorbed leading to the transition of an electron to a higher energy level. For semiconductor materials, this happens when the photon energy is equal to or larger than the bandgap of the material. An electron is then excited from the VB to the CB [24]. In accordance with the above, the following equation is valid:

$$1 = \frac{I_A + I_T + I_R}{I_0} = F_A + F_T + F_R \tag{3.10}$$

in which I_0 is the incident light intensity, I_A, I_T and I_R are the intensity of the absorbed, transmitted and reflected light and F_A, F_T, and F_R represent the fractions of the light that are either absorbed, transmitted or reflected. Note that F_A includes both the absorptance of the thin film and the absorptance of the quartz substrate. In practice, the absorptance of the quartz substrate is zero. In addition, F_R includes the reflectance of the thin film, the reflectance between the interface of the thin film and the substrate and the reflectance of the back of the substrate. As a reference, F_A and F_R of a quartz substrate only are shown in A.4 in the appendix.

Transmittance and absorptance spectra are measured using a Perkin Elmer Lambda 1050 spectrophotometer with a 150 mm integrating sphere [90]. The system uses two light sources, a deuterium lamp for the UV range and a tungsten lamp for the Vis/NIR range. Next, a monochromator is used to select only light with a specific wavelength at a given time. By rotating the grating of the monochromator, the spectra can be recorded wavelength by wavelength. The next important part is the chopper which divides the beam in a beam to illuminate the sample and a reference beam [91].

The sample beam is targeted at the integrating sphere where samples can be placed at different positions depending on the measurement goal. More precisely, F_T, F_A and F_R can be determined by placing the sample in front, inside or on the back of the integrating sphere respectively. Usage of an integrating sphere allows measurement of the total reflectance and transmittance including the diffuse components. Due to its geometrical shape and Lambertian reflectance of the inner surface, the light to be detected is evenly spread over the entire surface of the sphere [92]. A schematic of the setup for the integrating sphere is shown in Fig. 3.12.

After illuminating the sample, the light is detected by a photomultiplier tube (PMT) for the UV/Vis range and a Peltier-controlled InGaAs detector for the NIR range. By comparison of the detected signal with the reference beam, the required spectrum can be determined. Finally, the system consists of a set of mirrors, attenuators and (de)polarizers to regulate the correct illumination [91].

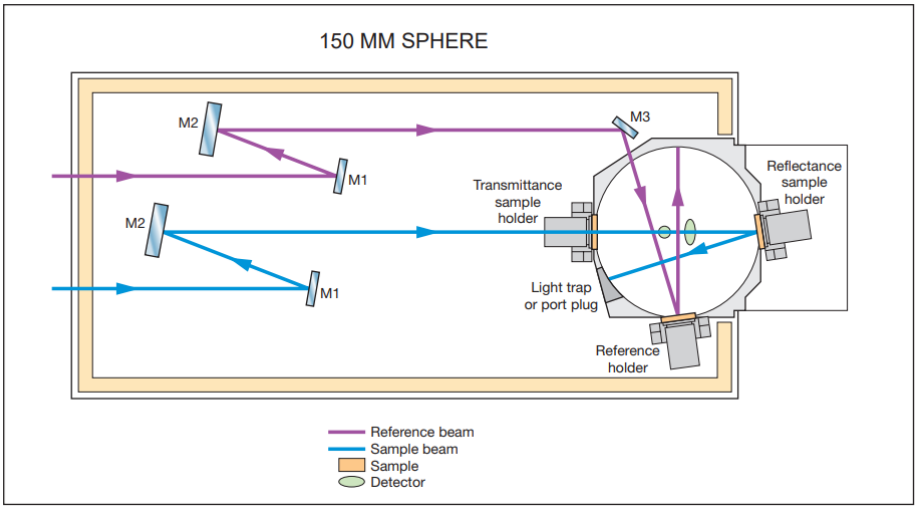

Figure 3.12: Drawing of the 150 mm integrating sphere setup in the Lambda 1050. Sample beam, reference beam, sample holders and detectors are shown [90].

Measurements are done in percent transmittance units (%T mode) from 850 (or 800 nm) to 250 nm with a data interval of 1 nm and a scan speed of 266.75 nm/min. Before measuring, a 100%T/0A and 0%T (blocked beam) baseline correction are carried out.

To determine F_A, samples are placed inside the integrating sphere at an angle of 12°. In this case, the total reflectance and transmittance, $F_{T,R}$, are measured and F_A is calculated with:

$$F_A = 1 - F_{T,R} \tag{3.11}$$

From equation (3.11) and the measurement of F_T in front of the integrating sphere, F_R can be determined with:

$$F_R = 1 - F_A - F_T \tag{3.12}$$

Spectrophotometry measurements can be used to determine the bandgap of PVK films. In order to do so, the Tauc method is applied [93]. Firstly, the absorption coefficient α is needed. The absorption coefficient determines how far into a material light of a particular wavelength can penetrate before it is absorbed [24]. It can be calculated from the transmission spectrum by using:

$$\frac{I_T}{I_0} = F_T = e^{-\alpha d} \tag{3.13}$$

in which d is the thickness of the sample [94]. Equation (3.13) is valid for samples with negligible reflection. However, since PVK films are quite reflective, equation (3.13) is adjusted by taking into account F_R [94]. The absorption coefficient can then be calculated with:

$$\alpha = -\frac{1}{d} \ln\left(\frac{F_T}{1 - F_R}\right) \tag{3.14}$$

Subsequently, the wavelength (in nm) is converted to photon energy ($h\nu$) (in eV) via:

$$h\nu = \frac{1240}{\lambda} \tag{3.15}$$

in which h is the Planck constant and ν the frequency. Next, a Tauc plot is made by plotting $(\alpha h\nu)^{\frac{1}{n}}$ versus the photon energy ($h\nu$). In this case $n = 1/2$ since we are dealing with direct allowed transitions. The curve of

the Tauc plot contains a linear part. If extended to the x-axis, the x-intercept of this linear part gives the value for the bandgap.

Absorptance and transmittance spectra are recorded for spin-coated and thermally evaporated PVK samples. From these results, the above described method is applied to firstly determine the absorption coefficient and then the bandgap via a Tauc plot. Moreover, absorptance and transmittance spectra are recorded for other layers in the device, i.e. ITO, spiro-TTB, spiro-OMeTAD, MoO_x, C60, BCP, and combinations of layers. For spiro-TTB, the absorption coefficient and bandgap are determined as well.

3.3.3. Photoluminescence spectroscopy

Photoluminescence spectroscopy (PL) is a technique that can be used to measure emission spectra. An emission spectrum is the wavelength distribution of an emission that is produced after excitation at a specific wavelength. In semiconductor materials, excitation can lead to the promotion of an electron from the VB to the CB while leaving behind a hole in the VB. Subsequently, emission can occur if the electron and hole undergo second-order band-to-band recombination. The energy emitted in this radiative process relates to the energy difference between the CB and VB. This type of measurement is known as steady-state PL [95].

PL spectra are recorded with an Edinburgh Instruments FLS980 Photoluminescence spectrometer. The setup contains a 450 W xenon lamp that is used as the light source for excitation. An excitation wavelength of 650 nm is selected by the excitation monochromator. Next, the thin film is excited by this specific wavelength, resulting in PL emission. Subsequently, the emission monochromator scans the desired range of wavelengths (700-850 nm) and the lights get detected by a PMT. The PMT is sensitive in the UV/Vis range and cooled down to -22 °C For both monochromators slit widths can be selected. A small slit width results in a high resolution, but gives a lower intensity. On the excitation side a slit width of 2 or 3.5 mm and on the emission side a slit width of 2.5 or 4 mm are chosen. Emission spectra are recorded in steps of 1 nm and with a dwell time of 0.2 s. Two scans are performed per sample to get a higher signal [96].

For the purpose of this research, steady-state PL spectra are recorded for a variety of samples. These include, spin-coated PVK samples on quartz for different precursor solution concentrations and spin-coated PVK in combination with a transport layer (C60, spiro-TTB, spiro-OMeTAD and MoO_x) on quartz. A comparison is made between the single layer (spin-coated PVK) and bi-layer (spin-coated PVK and transport material). This measurement is done in order to observe the occurrence of quenching, which is the process that leads to a reduction in the PL intensity.

3.3.4. Time resolved microwave conductivity

Time resolved microwave conductivity (TRMC) is a technique that is used to study the charge carrier dynamics in semiconductor materials. The technique is based on the interaction between mobile charge carriers and the electric field component of microwaves [97].

Electrons are excited from the VB to the CB by illumination of a sample with pulsed laser light (Nd:YAG laser). Neutral density filters are used to vary the photon fluence from the laser from 10^9 to 10^{14} photons/cm^2. This affects the total number of free charge carriers. The creation of free electrons and holes leads to an increase of the electrical conductivity σ and a change in photoconductance ΔG. ΔG is defined as an increase in the electrical conductivity as a result of incident illumination. In the meanwhile, a voltage-controlled oscillator produces microwaves in the GHz regime which are send through the sample. Due to the interaction of microwaves with free charge carriers, there is a reduction in microwave power (ΔP) on the detector. From the normalized reduction in microwave power, the change in photoconductance times a sensitivity factor K can be determined [97]. In equation:

$$\frac{\Delta P}{P} = -K\Delta G \tag{3.16}$$

As explained in section 2.1.2, charge carrier generation in a PVK layer is followed by recombination of charge carriers. This can be either direct band-to-band recombination or trap-assisted recombination. Since ΔG is proportional to the number of free charge carriers, probing ΔG with microwaves over time shows the effect trap-assisted recombination due to defects in the material. Therefore, extensive analysis of TRMC data provides insight in the recombination mechanisms and defect densities.

Samples are placed in a gold-plated cavity cell at $\frac{3}{4}$ of the cell's length. This specific position ensures that the electric field component of the microwaves is a maximum when it interacts with the sample. The cavity cell has an instrumental response time of 18 ns. Note that the technique probes the total integrated change in conductivity over the entire film thickness.

For the purpose of this research, the technique has been used to determine the charge carrier dynamics in spin-coated PVK layers and presence of charge carrier extraction by transport layers. Studied samples are spin-coated PVK, PVK/C60 and PVK/Spiro-TTB.

3.3.5. Scanning electron microscopy

Scanning electron microscopy (SEM) is a technique where a focused electron beam is projected and scanned over a surface to make an image [98]. To produce electrons, a tungsten filament is heated by applying a current until its electrons have enough energy to escape. A high voltage is applied between the tungsten filament (cathode) and an anode which accelerates the electrons in the right direction [99]. Next, the electron beam is passed through a set of magnetic lenses and apertures to focus the electron beam. A magnetic lens is a coil through which a current passes to produce a magnetic field. The magnetic field interacts with the electron beam and allows bending or focussing of the beam. Subsequently, the electron beam is scanned over the sample surface and interacts with it. Different interaction events are happening which are detected by different detectors. The detected signals come from a different penetration depth [98]. In this study, secondary electrons, which are a result of inelastic interactions between the electron beam and the electrons of the sample, are relevant. Secondary electrons originate from atoms close to the sample surface and are detected by a secondary electron detector (SED). The process to make an image from this is known as secondary electron imaging (SEI) [100].

For the purpose of this research, SEM images are made to study the morphology of spin-coated PVK thin films. In addition, the SEM is used to have a look at the ITO layer and the spiro-TTB on top of the ITO layer. Thirdly, the scanning electron microscope is used to make an image of the cross section of a thermally evaporated FAI film with the goal to determine its thickness.

SEM images are made with a JEOL 6010 SEM. This type of SEM is capable of reaching a resolution of 5 nm. Samples are taped to the holder by a piece of conductive carbon tape and placed at a distance of 10 mm from the detector inside the SEM. For the settings, images are made with accelerating voltages of 5-8 kV, magnifications up to 30,000x and a spot size, which is the diameter of the electron bundle by which the surface is scanned, of 50 nm up to a magnification of 5,000x and 30 nm for higher magnifications. To increase the conductivity, samples are coated with a thin layer of gold with a Jeol JFC-1300 auto fine coater.

3.3.6. Stylus profilometry

Stylus profilometry is a technique that is used to measure all kinds topographical features such as roughness and vertical profile. In addition, it can be used to measure thin film thicknesses. The technique is based on the mechanical contact between a stylus probe and the thin film surface. The stylus probe moves physically along the surface over a specified distance with a specified contact force. Meanwhile, changes in the vertical position of the stylus probe are recorded and the surface can be reconstructed [101].

For the purpose of this research, the technique is firstly used to determine the thickness of thermally evaporated PbI_2, CsBr, Ag, spiro-TTB and BCP. This allows the determination of the tooling factor for the evaporation process of these materials. Secondly, the technique is used to determine the thickness of thermally evaporated PVK and spin-coated PVK thin films. These results can be used in equation (3.14) to determine α and provide information about the thickness of the absorber layer in the PSCs.

Thickness measurements are carried out with a Veeco Dektak 8 Stylus Profiler. Measurements are done in 'Hills and Valleys' mode for a duration of 25 s (45 s for organic films) with a stylus radius of 12.5 μm and a stylus force of 3 mg (29.4 μN) for PbI_2, CsBr and PVK thin films, 5 mg (49.1 μN) for Ag films and 1 mg (9.8 μN) for spiro-TTB and BCP. The scan length is varied between 800 and 1200 μm by making a different scan routine for each measurement.

In order to measure the thickness, a small scratch on a sample has to be made (see Fig. 3.13a). For this tweezers with a sharp end are used. After a measurement, the software leveling is used to obtain a profile similar to the one shown in Fig. 3.13b. The thickness is determined by placing the M cursor at the lowest

point of the valley. Eventually, the average thickness is determined from multiple measurements along the scratch(es).

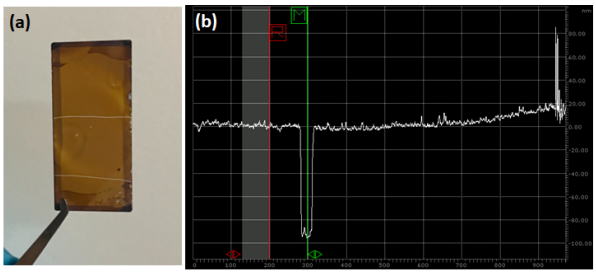

Figure 3.13: (a) Example of a quartz/PVK thin film with scratches near the centre and edge. (b) Result after software leveling that allows measuring the thickness.

3.3.7. Spectral ellipsometry

Spectral ellipsometry (SE) is an optical technique that can be used to determine the refractive index n and extinction coefficient k of a sample based on the change in the polarization state upon light reflection. In addition, other film properties, such as thickness, uniformity, surface roughness and bandgap can be determined after proper modeling of measured data [102].

The basic principle of SE is shown in Fig. 3.14. It starts with the illumination of polarized light on a sample. When light is polarized, its electric field component is oriented in a specific direction. The electric field vector can be decomposed in a component parallel to the incident plane (p-polarization) and a component perpendicular to the incident plane (s-polarization). From Fresnel's equations it is known that the s and p components show different behaviour upon reflection. More precisely, the amplitude of the p- and s-polarized components and the phase between them change depending on the optical constants and thickness of the sample. As can be seen in Fig. 3.14, the reflected p- and s-polarization are no longer consistent and the total electric field vector rotates around the propagation direction (elliptical polarized light). Eventually, two parameters are measured: the amplitude ratio Ψ and phase difference Δ. They are defined as:

$$\tan(\Psi) = \frac{|r_p|}{|r_s|} \tag{3.17}$$

$$\Delta = \delta_p - \delta_s \tag{3.18}$$

in which $|r_p|$ and $|r_s|$ represent the amplitude ratio of the incident and reflected p- and s-polarized waves respectively and δ_p and δ_s represent the phase difference between the incident and reflected p- and s-polarized waves respectively [102].

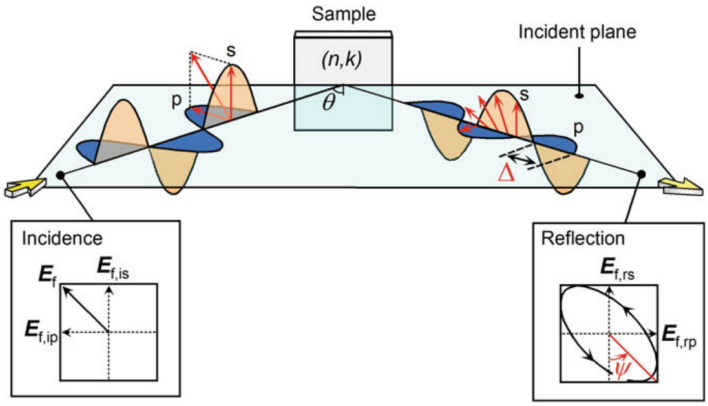

Figure 3.14: Principle of spectral ellipsometry. Incoming light, with electric field component E_f decomposed in p- and s-polarized waves, incident on sample at angle θ. Due to interaction with the sample (optical properties n and k), the polarization of the reflected wave changes characterised by Ψ and Δ [102].

The first part of SE consists of the measurement of Ψ and Δ with an M-2000DI ellipsometer (J. A. Woollam Co., Inc.). An extensive procedure is followed to align the lamp and detector before doing measurements. The system is equipped with a deuterium and a quartz tungsten halogen lamp to cover photon energies in the range of 0.75 eV to 6.5 eV. Before the sample is illuminated, it goes through a polarizer. Subsequently, the sample is illuminated and measurements are taken from different angles (55° to 70° with steps of 5°). At each angle, Ψ and Δ are measured for the whole range of photon energies. Since the thin films are deposited on quartz or glass, magic tape is put at the backside of the substrate to avoid back reflection. The elliptically polarized reflected light goes through a rotating compensator and a spectrograph. This allows simultaneous measurement of 700 wavelengths. A high speed CCD detector is used to collect all data.

The second part of SE consists of fitting an optical model to the measured data. The development and use of these fitting models is done with the CompleteEASE software. The model is used to retrieve the optical constants and other sample properties. Two common descriptions for the optical constants of a material are the complex dielectric function (ϵ) and the complex refractive index (N). They are given by:

$$\epsilon = \epsilon_1 - i\epsilon_2 \tag{3.19}$$

$$N = n - ik \tag{3.20}$$

in which ϵ_1 and ϵ_2 describe the response of a material to electric fields, n is the index of refraction and k is the extinction coefficient. The extinction coefficient is a measure of how strongly a material absorbs light. It is related to the absorption coefficient by:

$$\alpha = \frac{4\pi k}{\lambda} \tag{3.21}$$

The complex dielectric function and complex refractive index are related by:

$$\epsilon = N^2 \tag{3.22}$$

Not every model that matches the SE data represents a physical model. Negative values for parameters such as ϵ_2 or thickness are examples of non-physical results. In order to limit the possible optical models to only those which are physically plausible the Kramers-Kronig relations (KK) are used. The KK relations establish a physical connection between ϵ_1 and ϵ_2 [102].

In order to carefully build up the analysis several different models are used. Firstly, the Cauchy model is used. This is an empirical model represented by the following dispersion relation:

$$n(\lambda) = A + \frac{B}{\lambda^2} + \frac{C}{\lambda^4} + ... \tag{3.23}$$

$$k(\lambda) = 0 \tag{3.24}$$

in which A sets the amplitude of the refractive index and B and C add curvature to produce normal dispersion. This model is widely used for transparent materials. Therefore, we use it to model the substrate material. This acts as the basis on which we continue to build the rest of the model. In addition, the Cauchy model is used to model the transparent region present in some thin films.

Secondly, a b-spline model is used to model the thin layers on top of the substrate. The b-spline model represents a curve-fitting approach and produces a smooth curve over the spectrum by varying the optical constants independently. The model sums individual basis functions to construct a final curve. Each individual basis function is constructed from multiple polynomials and is only valid for a local region associated to a node. The spacing between nodes can be adjusted to control the shape of the b-spline curve. In this research, a node spacing of 0.03 eV is used.

From equation (3.22) we know that in reality the optical constants are not independent from each other. Therefore, the b-spline model does not have a physical background. In order to overcome this, the model

contains an option to introduce KK consistency and force ϵ_2 to be positive. In this way, ϵ_1 is defined by the KK transform of ϵ_2 and the basis functions become KK consistent. In addition, for materials with a transparent region, it is important to enforce the nodes for ϵ_2 to be equal to zero in this region.

Due to the non-physical origin of the b-spline model it is sometimes preferred to parameterize it to generic oscillators that do represent specific absorption peaks. For this, the software's generic oscillator approach is used with the Tauc-Lorentz model for the oscillators. This model works well for organic materials with resonant absorption peaks in the UV range. In practice, multiple oscillators are fitted to follow the shape of the peaks of the imaginary part of the dielectric function ϵ_2. The Tauc-Lorentz dispersion equations, which assume only absorption of light above the bandgap, are given by the following equations:

$$\epsilon_2(E) = \frac{AE_0C(E-E_G)^2}{(E^2-E_0^2)^2+C^2E^2}\cdot\frac{1}{E} \text{ if } E > E_G \tag{3.25}$$

$$\epsilon_2(E) = 0 \text{ if } E \leq E_G \tag{3.26}$$

in which A the amplitude, E_0 the central peak energy, C the broadening and E_G the bandgap energy represent the fitting parameters for an oscillator. After the fitting for ϵ_2 is optimised, ϵ_1 can be determined via the KK relations. Finally, after obtaining the dielectric function, the optical constants n and k can then be determined.

For the purpose of this research, existing SE models have been used to determine the thickness of thermally evaporated PVK and C60. In addition, a new model has been developed for spiro-TTB.

3.3.8. Four-point probe method

The four-point probe method is a technique that is used to determine the sheet resistance (R_{sq}) of a thin film. R_{sq} quantifies the ability for charges to travel in the lateral direction in thin uniform films. For PSCs, low sheet resistance materials are desired [103]. For the purpose of this research, the method is used to determine the R_{sq} for different ITO depositions. Eventually, this method, in combination with UV/Vis/NIR spectrophotometry, can be used to optimise the ITO layer in the PSC.

The sheet resistance represents the resistance between two opposite sides of a square on a thin film with a nominally uniform thickness. Therefore, it is expressed in units of $\Omega/\square$. The resistance of a square is always the same irrespective of its size (width and length the same in law of Pouillet). Therefore, the following equation is valid:

$$R_{sq} = \frac{\rho}{t} \tag{3.27}$$

in which ρ is the resistivity and t the thickness of the thin film [104].

The four-point probe consists of four electrical probes with equal spacing between each of the probes as shown in Fig. 3.15. A current, I, is injected through the first probe and collected at the fourth probe. Meanwhile, the voltage, V, is measured between the second and third probe. Note that the contact resistance of the probes does not influence the result. The injected current travels away from the probe in cylindrical shells and the following equation can be derived:

$$R_{sq} = \frac{\pi}{\ln(2)}\frac{V}{I} = 4.5324\frac{V}{I} \tag{3.28}$$

Equation (3.28) is valid for samples with infinite dimensions [103]. In practice, the result should be multiplied with a correction factor (CF) due to the proximity of the edges of the sample, which limits the possible current pathways. The correction factor depends on the dimensions of the sample (a and d) and the distance between the probes (S) (see Fig. 3.15) [104]. A table with values of 4.5324·CF for different values of d/S and a/d, is shown in table A.1.

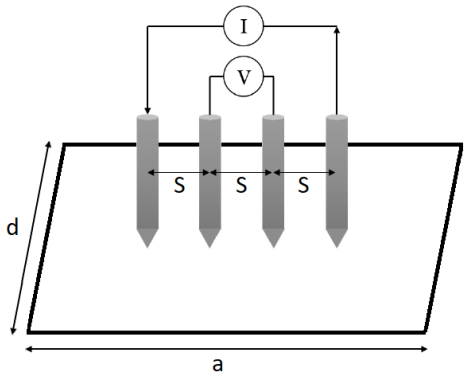

Figure 3.15: Schematic of the four-point probe method with two current carrying probes and two voltage measuring probes with probe distance S, sample length a and sample width d.

Measurements are done with a CMT-SR2000PV instrument with a probe distance of 1 mm. The studied samples are ITO depositions on 2.5 cm x 2.5 cm glass substrates fabricated with the mask of Fig. 3.2a. Since, not all d/S and a/d values are available from the table, a cubic spline interpolation method has been used to determine the correction factor for the different ITO sample sizes used in this research [103].

3.3.9. Solar simulator

A solar simulator is a setup that can be used to test solar cells by mimicking the illumination of natural sunlight. Testing of solar cells is done under a fixed set of standard test conditions (STC). In this way, a fair comparison between different solar cells all around the world can be made. The STCs include a cell temperature of 25 °C, illumination with an intensity of 100 mW/cm^2 according to an AM1.5 spectrum and a four point probe to remove the contact resistances [25].

To characterise a solar cell, its I-V curve is measured. This can be in the dark (dark I-V) or under illumination (light I-V). All kinds of parameters can be derived from the light I-V curve. These are the V_{oc}, I_{sc}, V_{mpp}, I_{mpp}, Fill factor, R_{sh}, R_s and efficiency. An I-V curve is measured by applying a series of voltages to the cell. Subsequently, the current flowing through the device at each voltage is measured [105].

The solar simulator used is a OAI Tri-Sol AAA solar simulator. The natural sunlight is mimicked by a xenon lamp in combination with an AM1.5 filter. The device is placed under a glove box and illuminates the cells through a window at the bottom of the glove box. Measuring inside the inert atmosphere of the glove box prevents degradation of the PSCs. The voltage and current are measured by a Keithley 2602B multimeter. Cells are placed on a platform which can be adjusted in height. The platform contains a reference cell, several openings and holders for the probes. Before measuring, the height of the platform is adjusted until the I_{sc} of the reference cell reads a value of about 143.5 mA. The temperature controller is not installed, therefore, measurements are not done at a constant temperature of 25 °C. In addition, only two probes are used.

Both dark and light I-V curves have been recorded for all the different produced devices. A mask cut out from black paper is used to illuminate only one cell at a time. Measurements are done over a varying voltage voltage range between -2.0 and 2.0 V, with a step size of 0.008 V and a frequency of 50 Hz. The compliance settings (voltage and current limits) for the light I-V measurement are set to 0.009 A for small cells and 0.01 A for larger cells. For the dark I-V measurements, the compliance is set to 0.02 A. The voltage limit is set to the maximum of the voltage range for that specific measurement. It is important to keep the compliance settings as close as possible to the expected values so the Keithley uses the correct sensitivity level.

The solar simulator setup has not been used a lot over the past years. To verify its ability to be used for this research, light I-V curves for four interdigitated back contact (IBC) cells (see Fig. 3.16a) have been measured with a reference solar simulator at the ESP lab and the OAI Tri-Sol AAA solar simulator. The results are shown in Fig. 3.16b.

To obtain an I-V curve in the first quadrant, the probes should be connected to the correct sides of a cell. To find out which probe belongs to the n-side and which probe belongs to the p-side, a n-type IBC solar cell is used. For an n-type IBC cell, the p-region is wider than the n-region. This implies that the wider fingers on

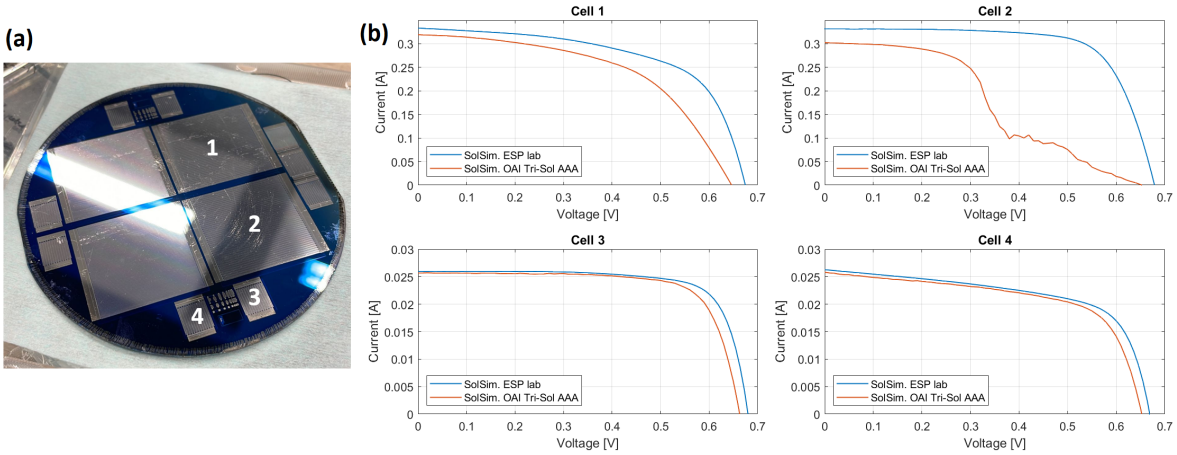

Figure 3.16: (a) IBC device that contains the four measured cells. (b) Light I-V curves of the four devices measured with a reference solar simulator at the ESP lab (blue) and the OAI Tri-Sol AAA solar simulator at the applied sciences building (red).

the back of the cell belong to the p-side. By tracing the fingers to the busbar, and connecting the probes in such a way that an I-V curve in the first quadrant is obtained, the correct probes for the n- and p-side are determined.

4

Development of Perovskite Absorber Layers

4.1. Managing thermal evaporation of $FA_xCs_{1-x}Pb(I_yBr_{1-y})_3$ thin films

4.1.1. Control on uniformity of depositions

At the start of this project, a problem hindering the thickness uniformity of deposited thin films was present. The uniformity problem is best illustrated by the image shown in Fig. 4.1a in which depositions of solely PbI_2 were carried out from source position two (see subsection 3.2.1, Fig. 3.5b) with substrate rotation. In this figure, we observe a round area in the centre of the substrate, which is an optical effect given by a higher thickness in the centre. The circular shape in the centre emerges, when part of the substrate is not covered by the evaporation flux coming of a source (in this case the edge of the substrate is not covered) and substrate rotation is on. PbI_2 was used, because this allowed us to do fast depositions with clear results (yellow coloured films). The described problem was only encountered for source position two.

Our thermal evaporation process for the fabrication of PVK is rather slow (due to low deposition rates). As an example, depositions with a target thickness of 400 nm, take about eight hours. In addition, the substrate holder only has place for a limited number of quartz substrates (used for most of the characterisation). In order to do proper characterisation measurements on samples from a certain deposition and be able to compare different depositions, it was deemed important that all samples in one deposition have the same composition. For these reasons, more tests were carried out to find the root of the uniformity problem.

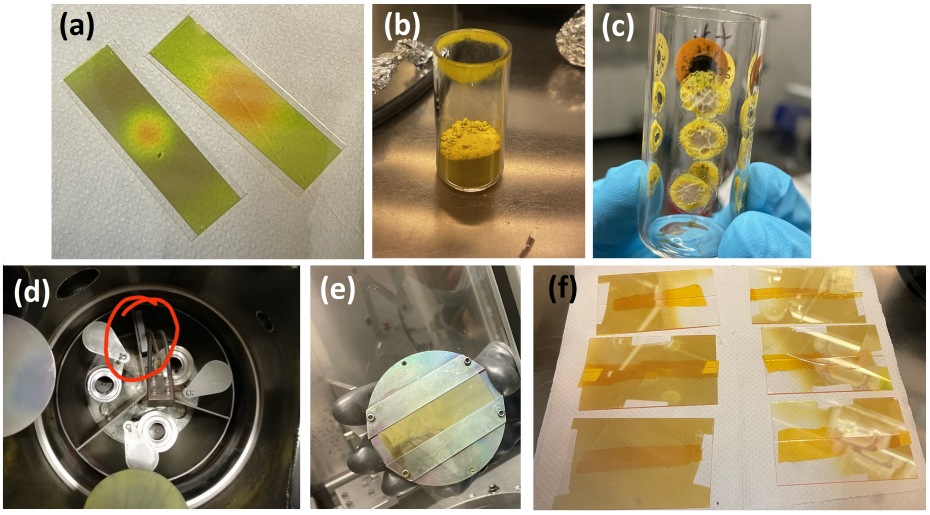

Figure 4.1: (a) Non-uniformity of depositions seen as a circle in the middle of the PbI_2 film deposited on microscope glass slides. (b) Crucible with increased powder level (three times higher than usual). (c) Thermal stickers on the inside of a crucible. (d) Metal block (circled in red) to move the sensor to the side. (e) Fully covered substrate after a deposition with the metal block in place. (f) PbI_2 depositions to find a suitable position for the sensor.

Three possible causes of the problem were suggested and investigated:

- Powder fill level too low: it was thought that the powder fill level in the crucibles was too low, which would contribute to hinder the flux towards the substrate. Increasing the powder fill level (three times higher than usual), as can be seen in Fig. 4.1b, resulted in a similar film thickness distribution as the one depicted in Fig. 4.1a.
- Temperature distribution: it was thought that the temperature distribution around the crucible in the Knudsen cell was not uniform. It was reasoned that if this would be the case, powder not properly heated on one side of the crucible would not contribute to the evaporation flux and could cause the uniformity problem. A test with thermal indicator stickers on the inside of the crucible was carried out (see Fig. 4.1c). Note that the middle of the sticker turns black when a certain temperature threshold is passed. The outcome of the test was that stickers with temperature thresholds of 121°C and 177°C all turned black after setting the source temperature to 150°C. From this result we learned that all sides of the crucible were sufficiently heated, and therefore, this is not the cause of the uniformity problem. In addition, we learned that the real temperature is higher than than the temperature measured by the thermocouple, which is displayed on the temperature controller.
- Blocking of the evaporation flux: it was thought that the QCM sensor located in the middle above the evaporation sources, was blocking part of the evaporation flux coming from source position two. A deposition was carried out in which the sensor was temporarily blocked away from source two, forced by a small metal block (see Fig. 4.1d). The result of this deposition can be seen in Fig. 4.1e. The entire substrate is covered uniformly, from which we concluded that blockage by the sensor was the cause of the uniformity problem.

After identifying the cause of the problem, a workable situation was sought after. By repeatedly opening the chamber, moving the sensor to a new location and do a quick deposition, the ideal sensor location was searched for. Note that moving the sensor is not trivial, since the sensor holder is connected to the bottom of the chamber by a rigid metal tube. Moreover, moving the sensor away from one position can create the same problem for the other two source positions. Eventually, after repeatedly carrying out depositions with different sensor positions from all three sources, the best workable situation was found. These depositions were done on microscope glass slides taped on the substrate holder without substrate rotation (see Fig. 4.1f). The horizontal and vertical position of the sensor, which were deemed the best workable location, were measured in reference to the walls and metal shield (between sources) of the evaporation chamber. The measurements are shown in Fig. 4.2. It turned out to be impossible to find a position for the sensor in which blocking of the evaporation flux from any of the sources could be completely eliminated. From then on, we decided to keep substrates as close as possible to the middle of the sample holder. Note that this is not an ideal situation. To sum up, an improved thickness uniformity was obtained compared to what we initially started with. However, in hindsight this took too much time, which should have been spend on optimising PVK depositions.

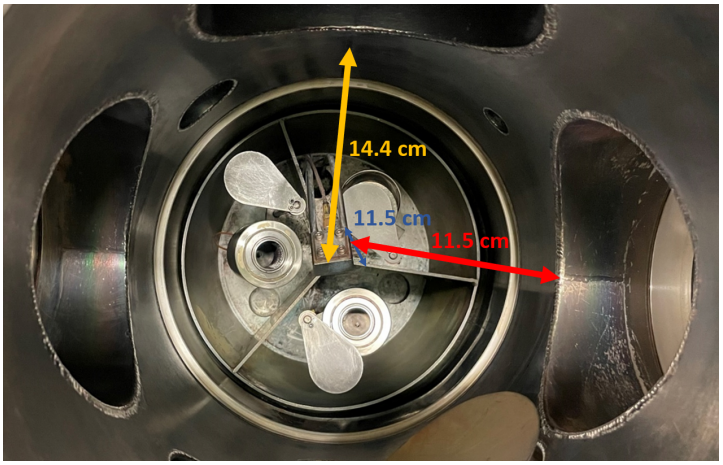

Figure 4.2: Top view of the evaporation chamber with distances between the sensor and sensor walls indicated after optimisation. The yellow arrow represents the distance between the sensor and the middle of the back wall, the red arrow represents the distance between the right side of the sensor and the right chamber wall and the blue arrow represents the height of the top left corner of the sensor to the metal shield separating the source areas.

Due to movement of the sensor, new tooling factors had to be determined. In order to determine the TFs, a single-layer deposition from each source was carried out. For PbI_2, a deposition with t_{sensor} = 100 nm was carried out on top of a microscope glass slide (2.5 cm x 7.5 cm). Note that this substrate covers the whole width of the sample holder. The average thickness at the centre of the substrate was 39.4 nm (ten measurements) and the average thickness at the edge was 34.8 nm (five measurements). In addition, a PbI_2 deposition with t_{sensor} = 300 nm was carried out on top of a microscope glass slide. The average thickness at the centre was 103.3 nm (six measurements) and the average thickness at the edge was 83.5 nm (four measurements). Since we planned to place samples in the middle of the substrate holder, equation (3.4) to calculate the TF, is applied using the centre thickness. The TF for PbI_2 was calculated to be 0.394 for the 100 nm target and 0.344 for the 300 nm target. For the depositions presented in the next section, the used TF for PbI_2 will be mentioned. In hindsight, the TF determined for the 300 nm target thickness is probably more certain, because measuring thicker layers with the profilometer is possibly more reliable.

For CsBr, a deposition with t_{sensor} = 100 nm was carried out on top of a microscope glass slide. The average thickness at the centre was 92.2 nm (six measurements) and the average thickness at the edge was 81.8 nm (six measurements). From the centre thickness, the TF was calculated to be 0.922.

For FAI, a deposition with t_{sensor} = 300 nm was carried out on top of a piece of silicon wafer. Since the thickness could not be measured with profilometry, cross sectional SEM images were taken (top row of Fig. 4.3). The average thickness was estimated to be 250 nm. From the average thickness, the TF was calculated to be 0.833. Furthermore, top view SEM images depict the morphology of the FAI film (bottom row of Fig. 4.3). Even though the FAI seems to cluster together in small islands, the uniformity is good and the islands are rather close to each other. Note that in the sequential deposition of our PVK thin films, FAI is deposited on top of PbI_2 on which it might grow different due to the different nature of the underlying layer. The SEM images are consistent with similar reports [106].

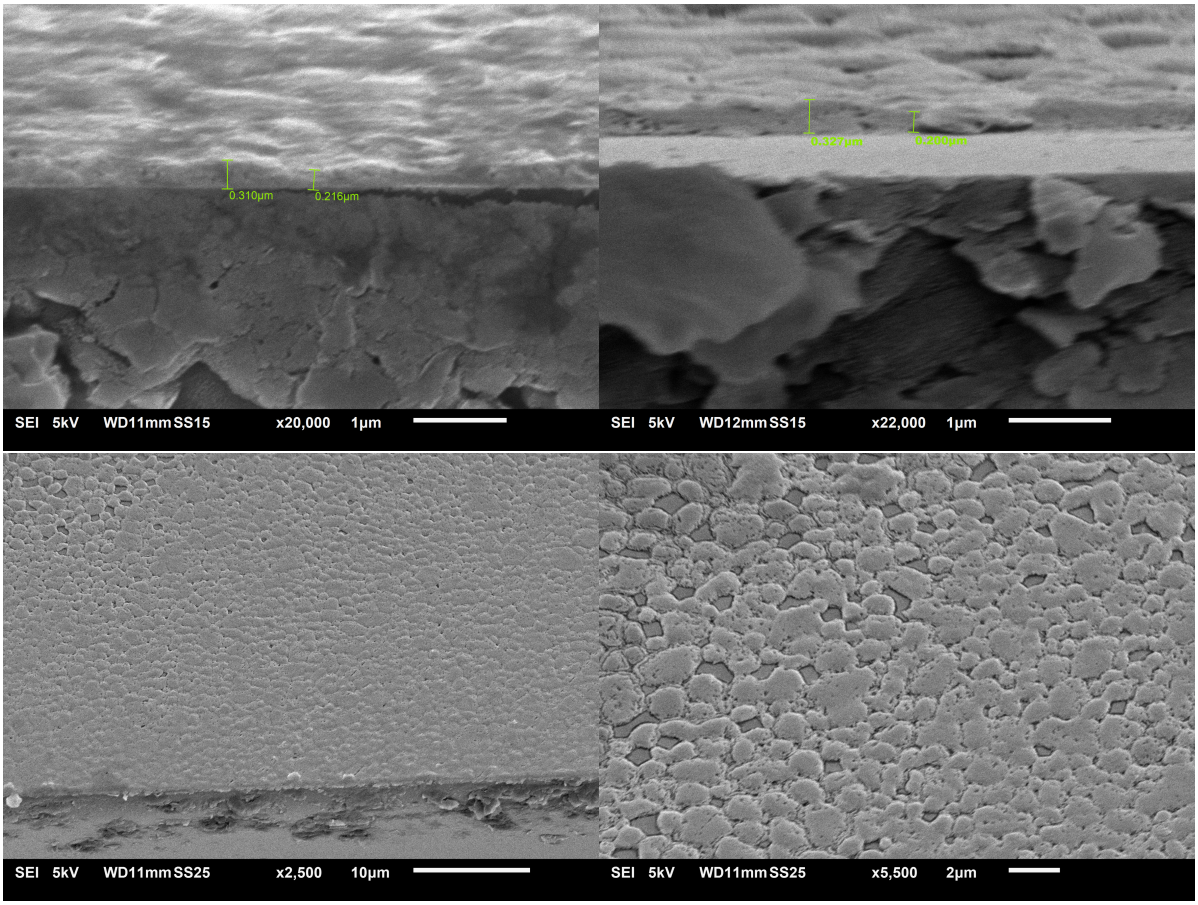

Figure 4.3: SEM images of FAI deposited on a silicon wafer. Top left: cross section of FAI with magnification 20,000x. Thickness measurements: 310 nm and 216 nm. Top right: cross section of FAI with magnification 22,000x. Thickness measurements: 327 nm and 200 nm. Bottom left: top view of FAI with magnification 2,500x. Bottom right: top view of FAI with magnification 5,500x.

4.1.2. Compositional engineering of perovskite thin films

The fabrication of thermally evaporated $FA_xCs_{1-x}Pb(I_yBr_{1-y})_3$ thin films, turned out to be a steep learning process. Occasionally, depositions of high quality PVK were obtained, but on other moments there were setbacks. Consistent results for a longer period of time were not obtained. In hindsight, different choices could have possibly led to better results.

In this subsection, three experiments are described that explain some of the attempts that have been carried out with the goal to optimise our depositions. The goal was to obtain multi-cation and multi-halide PVK of the form $FA_{0.85}Cs_{0.15}PbI_{2.85}Br_{0.15}$. In case annealing of a sample is mentioned, in most cases it was carried at 100°C for 10 min. The temperature was based on experiments carried out prior to the start of this thesis. In addition, the temperature and duration were kept rather low, considering the device fabrication that was going to be carried out later. For the devices, it was believed that a high annealing temperature and/or duration could have a detrimental effect on the TL underneath the PVK layer.

Effect of FAI content on structural and optical properties

After establishing the best workable situation and measurement of the TF for PbI_2 and CsBr, three depositions with a varying FAI content were carried out. Note that at that time, the TF for FAI was still unknown because the thickness was not measurable with the profilometer. For this reason, we tried an empirical approach by assuming values for the FAI tooling factor. The goal of this experiment was to determine with which assumed TF, the best PVK could be obtained. The PVK films were examined using XRD and absorption measurements.

Single-layer depositions with order PbI_2-FAI-CsBr were carried out. The perovskite target thickness for each deposition was 60 nm and the molar ratio between the different precursors was set to n_{FAI}:n_{PbI_2}:n_{CsBr} = 0.85:1.1:0.15. This ratio implies that a small excess of PbI_2 was chosen, since it has been reported that this can provide passivation [35]. Recall that when the desired molar ratio and PVK target thickness are known, equation (3.6) helps us to calculate the desired thickness for each individual precursor. Equation (3.6) gives: t_{PbI_2} = 32 nm, t_{FAI} = 25 nm and t_{CsBr} = 3 nm. Next, the nominal thickness that we provide as input for the controller (t_{sensor}), is based on the tooling factor for each source/material combination. For PbI_2 and CsBr we used the measured TFs of 0.394 and 0.922 respectively. For FAI, this is the point where we apply the assumed TFs, which lead to different nominal thicknesses. Therefore, the only variable that was varied, is the nominal FAI thickness provided as input for the controller. No post-deposition annealing process was executed.

An overview containing the assumed TF for FAI, nominal thickness as input for the controller for each precursor (t_{sensor}), PVK target thickness and PVK actual thickness is shown in table 4.1. Note that the latter is measured with the profilometer. Surprisingly, t_{actual} does not increase with increasing FAI content. However, measurements with the profilometer on samples that are this thin are not very reliable.

Table 4.1: Deposition parameters for three depositions named Dep.1, Dep.2 and Dep.3. Assumed TF for FAI, nominal thickness as input for controller for PbI_2, FAI and CsBr, target and actual PVK thickness are given.

	Assum. TF FAI	t_{sensor} **PbI_2 [nm]**	t_{sensor} **FAI [nm]**	t_{sensor} **CsBr [nm]**	t_{target} **PVK [nm]**	t_{actual} **PVK [nm]**
Dep. 1	0.6	82	41	3	60	41
Dep. 2	0.5	82	50	3	60	33
Dep. 3	0.4	82	62	3	60	30

The XRD results for the three depositions with different FAI content are shown in Fig. 4.4. All samples show a similar diffractogram with three peaks that belong to α phase PVK. These are two more intense peaks belonging to the (001) and (002) reflection, located around 2θ = 14.0° and 28.3°, and one less intense peak belonging to the (003) reflection, located around 2θ = 43.0°. The occurrence of these peaks around the given values for 2θ, is consistent with values reported in literature for the same type of PVK [44]. In addition, all samples show three other peaks which can be related to PbI_2 (2θ = 12.6°, 25.4° and 38.6°) [107]. These peaks indicate the presence of unreacted PbI_2.

The (001) PVK reflection and main PbI_2 peak (2θ = 12.6°), are further analysed to make a comparison between the three depositions. The 2θ angle, intensity and FWHM for the (001) PVK reflection are given in table 4.2 for all three depositions. In addition, the intensity of the main PbI_2 reflection is given as well.

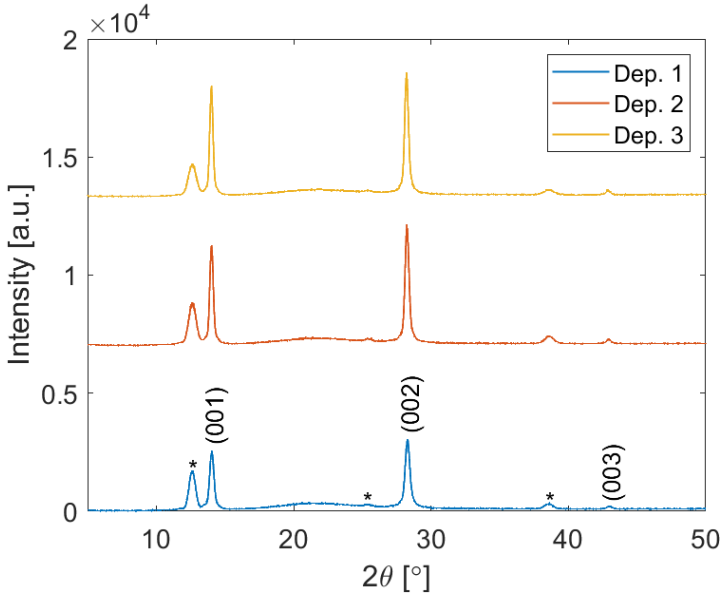

Figure 4.4: Diffractogram for three different depositions with varying FAI content (see table 4.1). From low to high FAI content: deposition 1 (blue), deposition 2 (red) and deposition 3 (yellow). PVK reflections indicated with Miller indices and PbI_2 reflections indicated with a * symbol.

Table 4.2: The peak position, peak intensity and FWHM for the (001) PVK reflection and peak intensity for the main PbI_2 reflection for all three depositions (see table 4.1).

	Peak pos. PVK [°]	**Peak int. PVK [a.u.]**	**FWHM PVK [°]**	**Peak int. PbI_2 [a.u.]**
Dep. 1	14.04	2547	0.37	1726
Dep. 2	14.03	4265	0.30	1847
Dep. 3	14.02	4695	0.29	1415

The peak position of the (001) reflection shifts from 14.04° for deposition 1 to 14.02° for deposition 3. This shift towards smaller angles for an increasing FAI content can possibly be explained by the fact that an iodide ion is larger than a bromide ion. Increasing the FAI content increases the I:Br ratio leading to an increase of the lattice spacing and therefore a shift to a smaller angle [108]. Note that measurement errors or uncertainty in the angle could also cause this observation.

The intensity of the (001) reflection is highest for deposition 3. Recall that this was the deposition with the lowest assumed TF and therefore the highest FAI content (table 4.1). This result implies that deposition 3 has the highest crystallinity, which is the degree of structural order in a solid. In addition, the crystal size in the (001) direction is largest. However, we should mention that the differences are rather small. In general, the intensity of the peaks is not very high when we compare it to depositions done prior to this thesis.

Next, equation (3.9) (Scherrer equation) is used to calculate the average size of the crystalline domains. In order to do so, the peak position and FWHM (converted to radians) from table 4.2 are used. In addition, λ = 0.15418 nm (Cu Kα) and the shape factor k = 0.94 [109]. The average crystal sizes were found to be $L_{Dep.1} \approx$ 23 nm, $L_{Dep.2} \approx$ 28 nm and $L_{Dep.3} \approx$ 30 nm. Note that we do not take these numbers as completely reliable, but merely as an indication of the relative average crystal sizes.

The intensity of the PbI_2 peak is not a measure for the PbI_2 content (by mass) in a sample. Instead, it is rather a measure of the crystallinity and crystal size (in direction belonging to the reflection) of PbI_2 present in a sample [110]. Considering table 4.2, the intensity of the main PbI_2 peak is lowest for deposition 3. This result suggests that PbI_2 has a poorer crystallinity and smaller crystal size in deposition 3 compared to the other samples. Based on the small excess of PbI_2 that was imposed in the molar ratio, PbI_2 peaks were expected. On the other hand, from the SEM images of the cross section of FAI, we learned that the real TF is around 0.833. This observation implies that for these depositions, with an assumed TF of 0.6, 0.5 and 0.4, there is actually more FAI than stoichiometrically needed. Therefore, the presence of PbI_2 could mean that the reaction to

form PVK did not fully happen. In hindsight, annealing could have possibly led to dissolution of PbI_2, leading to an improved crystallinity of the PVK phase as suggested in [109]. Note that since none of the samples were annealed, we are still able to compare them to each other, but, the crystallinity of the PVK phase might be lower than it would have been with annealing.

Finally, absorption spectra were measured for all three depositions. The results are shown in Fig. 4.5. F_A is rather low over the entire wavelength range. However, this is as expected, since the films have a very low thickness. There is not a big difference between the three depositions. Determining the bandgap is difficult since the absorptance is so low. It is estimated to be around 1.56 eV for all three samples. This value is a bit lower than expected [16].

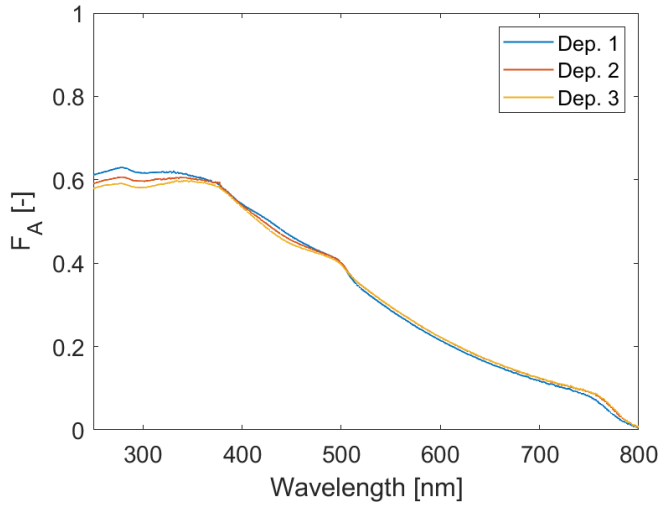

Figure 4.5: F_A as a function of wavelength for three different depositions with varying FAI content (see table 4.1). From low to high FAI content: deposition 1 (blue), deposition 2 (red) and deposition 3 (yellow).

Based on the peak intensity and average crystal size determined with XRD, the assumed TF for FAI of deposition 3 was deemed best. For this reason, 0.4 was chosen as FAI tooling factor for a multi-layer PVK deposition that ended up in the first two PSC devices fabricated in this project. The outcome of this multi-layer deposition and performance of the devices can be found in section 6.1. In hindsight, the FAI TF was actually equal to 0.833. Therefore, it is strange that TF = 0.4 turned out to give the best results in this experiment.

Comparison of single- and multi-layer depositions based on the tooling factors

After the TFs were measured for all source/material combinations, a single-layer and multi-layer deposition ($N = 1$ and $N = 4$ respectively) were carried out. Recall that the multi-layer deposition implies, carrying out sequential deposition from all three sources repeated four times (see Fig. 3.6). The goal of these depositions was to see how properties of single-layer deposited perovskite differ from the multi-layer counterpart. We were hoping to keep the same PVK quality repeating the single-layer four times with the goal to apply this deposition for a batch of devices.

The depositions were carried out with order PbI_2-FAI-CsBr. The perovskite target thickness for the single- and multi-layer deposition, was 100 nm and 400 nm respectively. The molar ratio between the different precursors was set to n_{FAI}:n_{PbI_2}:n_{CsBr} = 0.85:1.05:0.15. The ratio implies that a small excess of PbI_2 was chosen hoping to achieve passivation [35]. Equation (3.6) helps us to calculate the desired thickness for each individual precursor in a single-layer. Equation (3.6) gives: t_{PbI_2} = 53 nm, t_{FAI} = 42 nm and t_{CsBr} = 5 nm ($N = 1$). Next, the nominal thickness that we provide as input for the controller, is based on the tooling factor for each source/material combination. For PbI_2, FAI and CsBr we used the measured TFs of 0.394, 0.833 and 0.922 respectively. The nominal thickness (t_{sensor}) of a single-layer provided as input for the controller was set to 134 nm for PbI_2, 51 nm for FAI and 5.2 nm for CsBr ($N = 1$). Again, for the multi-layer deposition this implies that a deposition of a single-layer (one PVK stack) is repeated four times. For the multi-layer deposition, a dark brown film colour was detected righ after deposition (see Fig. 4.6). Based on the visual inspection, these samples are considered high quality perovskite.

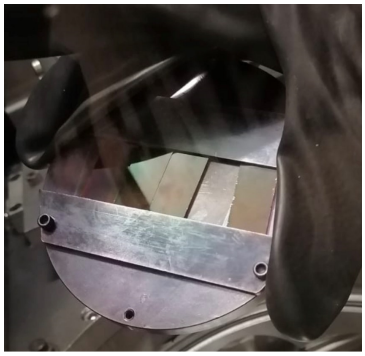

Figure 4.6: Image of samples of the multi-layer deposition directly after fabrication.

The XRD results for the multi- and single-layer deposition are shown in the left of Fig. 4.7. In addition, the multi-layer sample was annealed (130°C, 5 min) after measurement of the XRD spectrum and subsequently measured again (yellow spectrum in right of Fig. 4.7). The multi- and single layer deposition both show peaks belonging to the (001), (002) and (003) reflection of α phase PVK [44]. In addition, the multi-layer deposition shows two additional α phase PVK reflections belonging to the (012) and (022) plane [44]. Next to reflections belonging to α phase PVK, the diffractogram of both depositions shows three peaks that can be related to PbI_2 (2θ = 12.6°, 25.4° and 38.6°) [107]. These peaks indicate the presence of unreacted PbI_2. Note that the intensities of the PbI_2 peaks are quite high for the single-layer deposition. The XRD spectrum of the multi-layer deposition after annealing, shows the first PbI_2 peak and the (001) and (002) reflection of PVK. Note that this measurement was only carried out until 2θ = 30°. The XRD result indicates a reduced crystallinity after annealing. The reduced crystallinity could be caused by the annealing procedure itself. However, it is more likely that the sample was degraded by the glove box atmosphere where the annealing took place. The glove box, where annealing is carried out usually, was unavailable. Therefore, annealing was done in a glove box where all different kinds of chemicals including solvents are used. For this reason, the possibly contaminated glove box atmosphere could have had a detrimental effect on the sample, and therefore, a clear conclusion about the effect of annealing cannot be drawn.

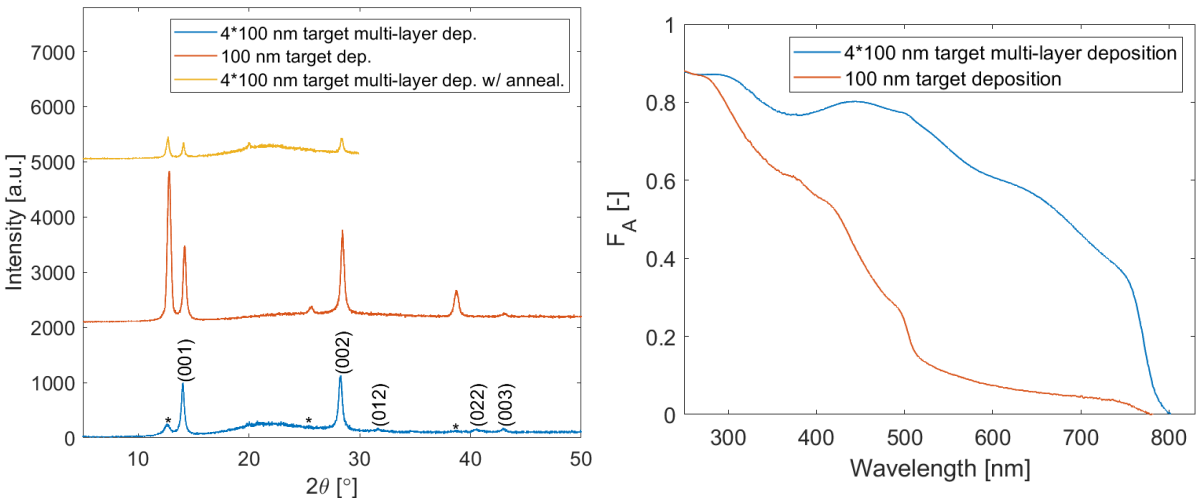

Figure 4.7: Left: diffractogram for the multi-layer deposition (blue), single-layer deposition (red) and multi-layer deposition with annealing (yellow). PVK reflections indicated with Miller indices and PbI_2 reflections indicated with a * symbol. Right: F_A as a function of wavelength for the multi-layer deposition (blue) and single-layer deposition (red).

The (001) PVK reflection is further analysed to make a comparison between the single- and multi-layer deposition (both without annealing). The 2θ angle, intensity and FWHM for the (001) PVK reflection are given in table 4.3.

Table 4.3: The peak position, peak intensity and FWHM for the (001) PVK reflection for the multi-layer and single-layer deposition without annealing.

	Peak pos. PVK [°]	**Peak int. PVK [a.u.]**	**FWHM PVK [°]**
Multi-layer deposition	14.03	992	0.36
Single-layer deposition	14.20	1370	0.33

The intensity of the (001) reflection is slightly higher for the single-layer deposition than for the multi-layer deposition. This result implies that the single-layer deposition has a higher crystallinity. In addition, the crystal size in the (001) direction is a bit larger for the single-layer deposition. Next, equation (3.9) (Scherrer equation) is used to calculate the average size of the crystalline domains. In order to do so, the peak position and FWHM (converted to radians) from table 4.3 are used. The average crystal sizes were found to be L_{Multi} ≈ 24 nm and L_{Single} ≈ 26 nm. Note that we do not take these numbers as completely reliable, but merely as an indication of the relative average crystal sizes.

The occurrence of the (012) and (022) plane of α phase PVK for the multi-layer deposition, indicates that the multi-layer deposition has a lower preferred orientation than the single-layer deposition [86]. In general, the intensity of the perovskite peaks is rather low, whereas especially for the single-layer deposition, PbI_2 crystal domains with a relatively high crystallinity are present. The reaction to form PVK could be enhanced by annealing or with a better optimisation of the precursor ratio [109].

Absorption spectra were measured for both the single- and multi-layer deposition. The results are shown in the right of Fig. 4.7. F_A is very low over the entire wavelength range for the single-layer deposition. On one hand, a low absorptance is expected, since it is a relatively thin film. On the other hand, the absorptance is even lower compared to the spectra measured for a varying FAI content (see Fig. 4.5). Note that the samples with the varied FAI content were even thinner. The low absorptance can be explained by the relatively large crystalline PbI_2 domains present. Around a wavelength of 500 nm, a steep decline of F_A can be seen, which is exactly where the bandgap of PbI_2 is located [107]. F_A for the multi-layer deposition is relatively high considering the quality we are able to obtain with this evaporator. This is in accordance with the dark brown film colour we observed. The bandgap for the multi-layer deposition is determined to be 1.57 eV. In addition, the bandgap for the single-layer deposition is determined to be 1.60 eV. E_G for the multi-layer deposition is lower than expected, whereas E_G for the single-layer deposition comes close to the expected value [16].

The average actual thickness of the multi-layer deposition was determined to be 220 nm (five measurements). Moreover, the average actual thickness of the single-layer deposition was determined to be 75 nm (six measurements). Recall that the target thickness for the multi-layer deposition was 400 nm, and for the single-layer depositions 100 nm. Therefore, in both depositions, the target thickness was not achieved. The relative difference between the actual thickness and the target thickness, is highest for the multi-layer deposition. For this reason, it can be concluded that the deposited thickness and thus the growth of PVK is influenced by the presence of the earlier deposited layers. It also shows the big challenge present to fabricate a thick absorber layer around 500 nm that would be desired in a PSC [35].

Deposition order, annealing and stability analysis

Based on the findings of the comparison between the single- and multi-layer deposition, a set of experiments was designed (depositions with N = 1, 2, 3 and 4) to dive into the observed phenomena. In addition, we wanted to learn something about the influence of annealing, deposition order and stability. However, due to encountered setbacks with the evaporator, only part of these experiments could be executed. More on the technical obstacles can be found in subsection 4.1.3. Eventually, two single-layer depositions were carried out. One with the usual deposition order (PbI_2-FAI-CsBr) and one with a different deposition order (PbI_2-CsBr-FAI). In addition, effects of annealing and exposure to the ambient atmosphere were investigated for the deposition with the usual deposition order.

The perovskite target thickness for both depositions was 100 nm and the molar ratio between the different precursors was set to n_{FAI}:n_{PbI_2}:n_{CsBr} = 0.85:1:0.15. Equation (3.6) helps us to calculate the desired thickness for each individual precursor. Equation (3.6) gives: t_{PbI_2} = 51.5 nm, t_{FAI} = 43.5 nm and t_{CsBr} = 5 nm. Next, the nominal thickness that we provide as input for the controller, is based on the tooling factor for each source/material combination. For PbI_2, FAI and CsBr we use the measured TFs of 0.344, 0.833 and 0.922 respectively. Note that this time the TF for PbI_2 is different then in previous depositions. The one used now,

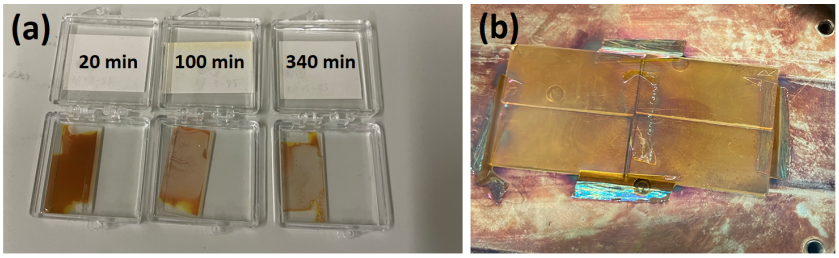

Figure 4.8: (a) Image of samples from deposition with usual deposition order after exposure to the atmosphere for 20, 100 and 340 min. (b) Image of samples from deposition with different deposition order directly after fabrication.

was determined on the 300 nm target PbI_2 layer (see subsection 4.1.1). The actual thickness could possibly be closer to the target thickness by applying TF = 0.344. The nominal thickness t_{sensor} provided as input for the controller was set to 149 nm for PbI_2, 52 nm for FAI and 5.4 nm for CsBr.

For the deposition with the usual deposition order, XRD spectra were recorded after exposure of a sample to the ambient atmosphere (lab environment) for 20, 60, 100 and 340 min. Absorption spectra were recorded on the same sample after exposure of 20 and 340 min. In addition, a sample of this batch was annealed at 100°C for 10 min, and subsequently, XRD spectra and absorption measurements were recorded. For the deposition with the different deposition order, XRD spectra and absorption measurements were recorded. Images of samples from the deposition with usual order for different exposure times, and samples from the deposition with different order are shown in Fig. 4.8. From a visual inspection, the film colour for the first deposition looks a bit reddish, whereas the film colour of the second deposition looks more yellow/gold.

The XRD results for the usual order deposition for different exposure times to the ambient atmosphere are shown in the Fig. 4.9. All diffractograms show peaks belonging to the (001) and (002) reflection of α phase PVK [44]. In addition the (003) reflection can be seen for measurements after exposure of 20, 60 and 100 min. There are no PbI_2 peaks present in the diffractogram which indicates that there is no unreacted PbI_2. Therefore, the reaction to form PVK happened either stoichiometrically or with a small deficit of PbI_2. Considering the intensity of the peaks, the intensity of the (001) reflection for the 20 min exposure, is the highest found out of all depositions done in this project. Therefore, the samples possess a relatively high crystallinity. The intensity stays roughly the same even after the sample was exposed to the ambient atmosphere for 100 min. Therefore, we can conclude that the stability of our fabricated PVK film is relatively good. After exposure of 340 min, the intensity of the XRD peaks is much lower, which indicates that the film degraded.

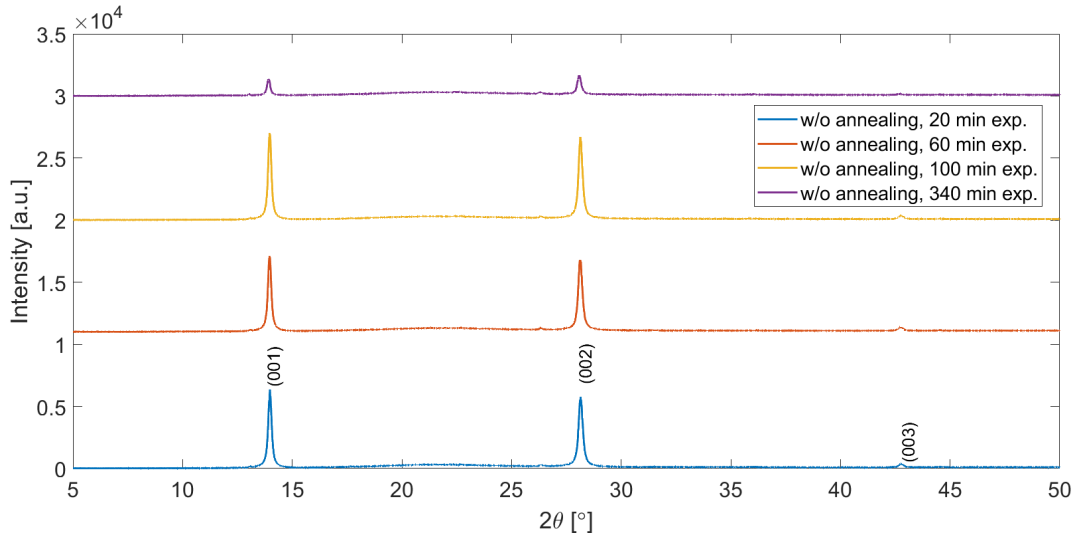

Figure 4.9: Diffractogram of the same sample after exposure to the ambient atmosphere for different durations. From short to long exposure times: 20 min (blue), 60 min (red), 100 min (yellow) and 340 min (purple). PVK reflections indicated with Miller indices.

The XRD results for the usual order deposition with and without annealing are shown in the left of Fig. 4.10. In addition, the XRD results for the usual deposition order and different order (FAI last) are shown in the right of Fig. 4.10. Note that the blue diffractogram of Fig. 4.9 and Fig. 4.10 is the same measurement. All diffractograms show similar peaks belonging to the (001), (002) and (003) reflection of α phase PVK [44]. Furthermore, the deposition with different deposition order shows three peaks that can be related to PbI_2 (2θ = 12.6°, 25.4° and 38.6°) [107]. These peaks indicate the presence of unreacted PbI_2.

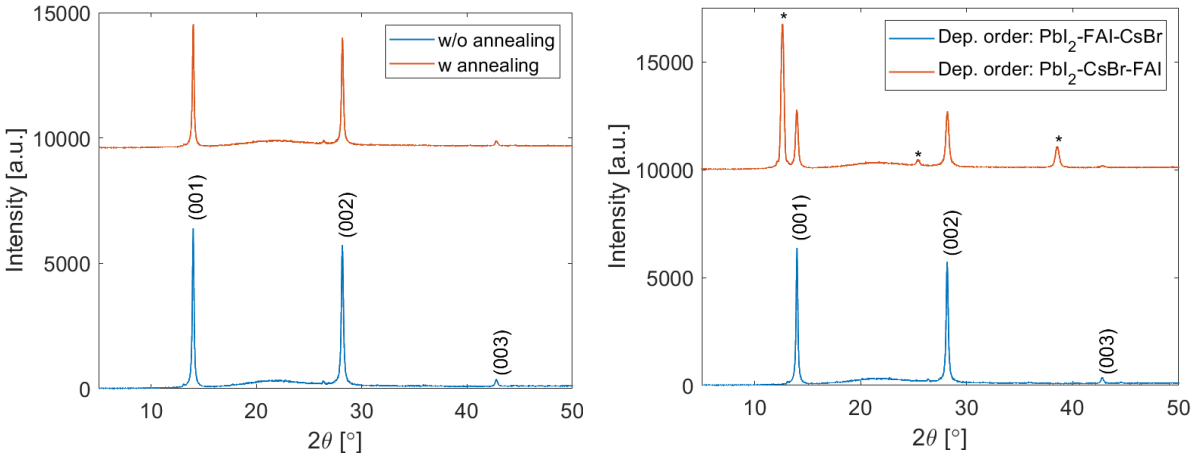

Figure 4.10: Left: diffractogram of two samples from the same deposition without annealing (blue) and with annealing (red). Right: diffractogram of two samples from depositions with a different deposition order. PbI_2-FAI-CsBr (blue) and PbI_2-CsBr-FAI (red). PVK reflections indicated with Miller indices and PbI_2 reflections indicated with a * symbol.

The (001) PVK reflection is further analysed to make a comparison between the different spectra of Fig. 4.10. The 2θ angle, intensity and FWHM for the (001) PVK reflection are given in table 4.4.

Table 4.4: The peak position, peak intensity and FWHM for the (001) PVK reflection for the deposition with usual deposition order (with and without annealing) and the deposition with different deposition order (PbI_2-CsBr-FAI).

	Peak pos. PVK [°]	**Peak int. PVK [a.u.]**	**FWHM PVK [°]**
Dep. order PbI_2-FAI-CsBr w/o annealing	13.98	6375	0.19
Dep. order PbI_2-FAI-CsBr w annealing	13.99	4947	0.18
Dep. order PbI_2-CsBr-FAI w/o annealing	13.96	2767	0.29

The intensity of the (001) reflection is highest for the usual deposition order without annealing. This result implies that this deposition has the highest crystallinity. Upon annealing the intensity drops a bit. The intensity for the deposition with different deposition order is significantly lower. The presence of high PbI_2 peaks indicates the presence of unreacted PbI_2, which could be the result of the different deposition order. Possibly, CsBr on top of the PbI_2 functioned as a barrier for the diffusion of FAI into the PbI_2 film. It should be noted that around this time problems with the evaporator started to occur (see subsection 4.1.3). These problems could have possibly affected the deposition with the different order. We conclude that the usual deposition order (PbI_2-FAI-CsBr) gives a higher quality PVK.

Next, equation (3.9) (Scherrer equation) is used to calculate the average size of the crystalline domains. In order to do so, the peak position and FWHM (converted to radians) from table 4.4 are used. In addition, λ = 0.15418 nm (Cu Kα) and the shape factor k = 0.94 [109]. The average crystal sizes were found to be $L_{norm.ord.}$ ≈ 46 nm, $L_{w/anneal.}$ ≈ 49 nm and $L_{diff.ord.}$ ≈ 30 nm. This result shows that even though the difference is small, the average crystal size increased upon annealing.

Spectral ellipsometry was used to determine the thickness of the film with usual deposition order. The thickness was found to be 99 nm, which is almost the same as the target thickness of 100 nm. Therefore, with this sample it is confirmed that 0.344 as TF for PbI_2 is correct and the target thickness was achieved.

Absorption and transmission spectra were measured for the deposition with usual order for a sample without annealing, without annealing and exposure of 340 min, and with annealing. In addition, the same measurements were done for the deposition with different order (PbI_2-CsBr-FAI). From the absorption and trans-

mission spectra, the fraction of light that gets reflected was calculated. Next, equation (3.14) was used to determine the absorption coefficient. A film thickness of 100 nm was assumed for all films. F_A, F_R and α all as a function of wavelength are depicted in Fig. 4.11 for the four studied samples.

Taking a closer look at F_A (top left in Fig. 4.11), a few interesting aspects can be noticed. Firstly, for the deposition with usual deposition order, both the annealed and unannealed variant (blue and yellow) show a relatively high absorptance considering the relative thin thickness. In addition, the absorptance for the annealed sample is larger than for the sample without annealing. It can be concluded that annealing had a positive effect on the optical properties. Secondly, a detrimental effect on F_A can be seen for the sample that has been exposed for 340 min to the ambient atmosphere. This observation is in agreement with the image depicted in Fig. 4.8a; the disappearance of film colour results in a poor absorptance. Finally, for the deposition with different deposition order, F_A is rather low. The poor absorptance can be explained by the relatively large crystalline PbI_2 domains present. Around a wavelength of 500 nm, a steep decline of F_A can be seen. It turns out that this is exactly where the bandgap of PbI_2 is located [107]. Moreover, this sample also turned out to have the largest F_R, as can be seen in the top right of Fig. 4.11.

Taking a closer look at the absorption coefficient, similar aspects as for F_A are noticed. These are a high absorption coefficient for the deposition with usual order (with and without annealing), poor absorption coefficient for the exposed sample, and a decline at a wavelength of 500 nm for the absorption coefficient of the deposition with different order. The absorption coefficient for the usual order deposition without exposure is consistent with reports in literature [111]. The bandgaps are determined to be 1.55 eV for the usual deposition (without annealing, with annealing, exposed) and 1.59 eV for the deposition with different order. The former bandgap is a bit lower than expected, whereas the latter comes close to the expected value [16].

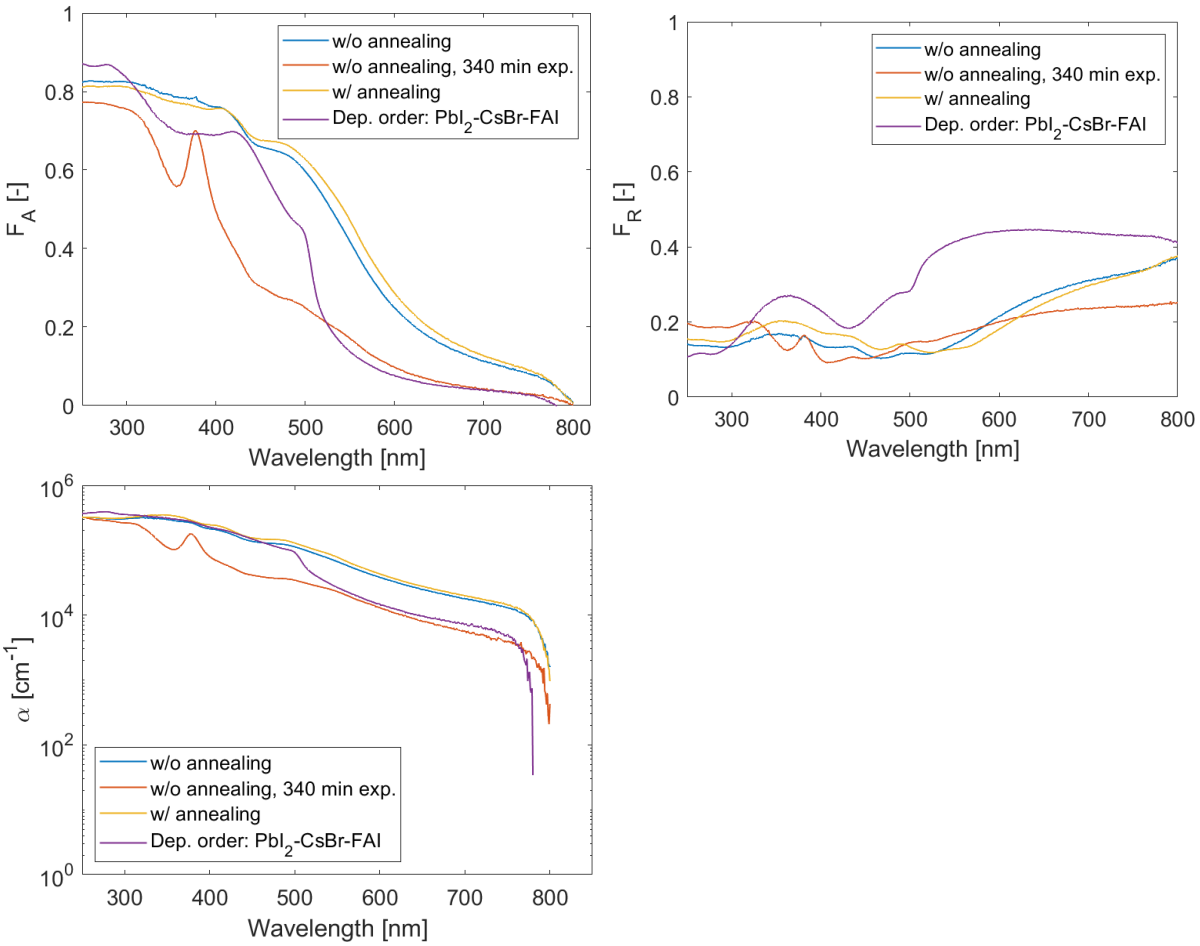

Figure 4.11: F_A (top left), F_R (top right) and α (bottom left) as a function of wavelength for thermally evaporated PVK samples from two different depositions. Usual deposition order without annealing (blue), usual deposition order without annealing and after exposure to the ambient atmosphere for 340 min (red), usual deposition order with annealing (red), and second deposition with a different deposition order (purple).

4.1.3. Technical obstacles

From one day to another, obtaining high quality perovskite with the thermal evaporator became impossible, as can be seen in the blue XRD spectrum shown in Fig. 4.12. Note that this is an XRD measurement for a sample with a similar stoichiometry and with the same TFs as depositions done before. No PVK reflections are observed for this sample. Only three peaks corresponding to PbI_2 are occurring.

Several reasons behind the disappearance of the PVK phase were suggested:

- A leak in the vacuum chamber: it was thought that there was a small leak at the side of the chamber where the big shutter is connected. The reason behind this, is that the disappearance of the PVK peaks from the diffractogram had been encountered before, and at that time a leak at the big shutter connection was the root of the problem. In order to test this possible cause, the big shutter was removed from the chamber and the place where it enters was properly sealed. Next, a PVK deposition was carried out and the XRD recorded. The XRD spectra without and with annealing (100°C, 10 min) are shown in Fig. 4.12. Note that the same stoichiometry, target thickness and TFs were used as the deposition corresponding to the blue diffractogram. We observe the appearance of the (001), (002) and (003) PVK α phase reflections. The intensity of these peaks gets higher upon annealing. Therefore, we can conclude that removing the big shutter did have a positive influence on the deposition. However, comparing this result to a similar deposition done a few weeks before (inset in Fig. 4.12), the intensity of the (001) reflection is almost eight times lower. Eventually, the suggestion of a leak was dismissed since the pressure in the chamber was still able to reach very low values up to $4.00{\cdot}10^{-7}$ mbar. If there would have been a leak, reaching such a low pressure would not be possible.
- Fluctuating deposition rate for FAI: it was observed that it was harder to obtain a stable deposition rate for FAI. The target rate of 0.5 Å/s was hard to reach and when it was reached, the rate would drop towards 0.1-0.2 Å/s in a fast manner. In addition, the setting for the temperature controller required to achieve the target rate, was a lot higher as compared to previous depositions. Previously, a temperature around 100°C was enough to achieve a stable rate around 0.5 Å/s for a long time, whereas this time heating up to even 114°C resulted in unstable rates, which dropped towards 0.1-0.2 Å/s. Based on these observations, it was thought that there was a degradation problem with the FAI powder or a problem with the temperature controller of source position two. We also thought that if something else in the evaporator would be wrong, FAI would probably be affected first since it is an organic material. Eventually, replacing the FAI powder with freshly bought powder did not make any difference. In addition, checking the temperature distribution with thermal indicator stickers did not show any problem.

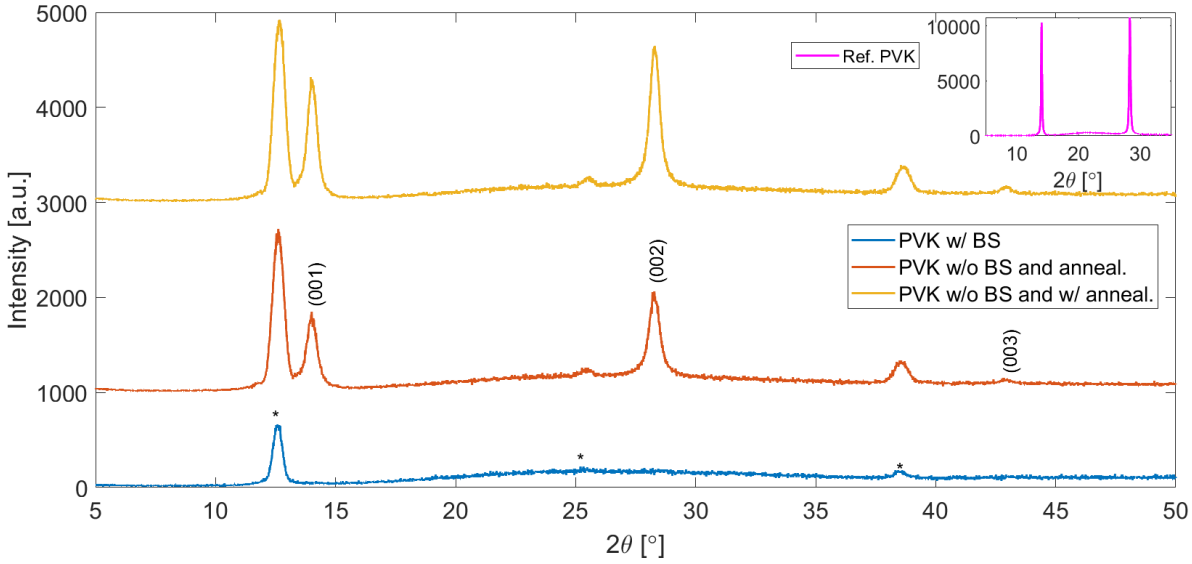

Figure 4.12: Diffractogram of three samples from two depositions with the same ratio: one deposition with big shutter in place (blue) and one deposition without big shutter (without annealing (red) and with annealing (yellow)). BS in legend stands for big shutter. Inset is an example of a diffractogram obtained before problems occurred (pink). PVK reflections indicated with Miller indices and PbI_2 reflections indicated with a * symbol.

Since the problem could not be resolved, the focus shifted towards the fabrication of spin-coated $MAPbI_3$ thin films. These were subsequently used as absorber layer in our PSCs. Eventually, it turned out that replacing the PbI_2 powder with freshly bought powder would solve the thermal evaporation problem. In addition, swapping the thermal controller of source two and three led to a more stable FAI deposition. Unfortunately, these things were discovered too late in regard to this project.

4.2. Characterisation of spin-coated $MAPbI_3$ films for device application

$MAPbI_3$ was prepared via spin-coating following the fabrication procedure described in Ch.3 subsection 3.2.2. In total five batches were prepared. Some of these batches were produced solely on quartz, some solely for device purposes and some for both. Characterisation of the samples on quartz, helps us to get a better understanding of the PVK layer in devices. An overview, containing the precursor solution concentration M, type of characterisation, produced bi- or tri-layers for PL and TRMC (Ch. 5, subsection 5.2.5), usage in a device, and date is shown in table 4.5. Batch numbers will be used in the following subsections. Spin-coated PVK films were fabricated with two different precursor solution concentrations: 0.65 mol/L, referred to as 'normal concentration', and 0.77 mol/L, referred to as 'high concentration' (see subsection 3.2.2, table 3.2). Note that a bi- or tri-layer is a stack of PVK and transport layer(s).

Note that during the fabrication of batch 4 and 5, precursor solution was used for the fabrication of devices as well. Therefore, all results in this section that concern batch 4 and 5, tell us something about the PVK absorber layer that ended up in the set of devices further explained in subsections 6.2.2 and 6.2.3.

Table 4.5: Overview of different spin-coated $MAPbI_3$ batches. The concentration, used characterisation techniques, bi- and tri-layers, usage in a device, and date are given.

	***M* [mol/L]**	**Char. technique quartz substrates**	**Bi- and tri-layers on quartz for PL or TRMC**	**Used in device**	**Date**
Batch 1	0.65	XRD, UV/Vis/Nir, PL, TRMC, SEM, Profilometry	Quartz/PVK/Spiro-TTB (20 nm) Quartz/PVK/C60 (20 nm) Quartz/Spiro-TTB (20 nm)/PVK	No	7-4-22
Batch 2	0.65	-	-	Yes (subs. 6.2.1)	13-4-22
Batch 3	0.65	XRD, UV/Vis/Nir, PL, SEM, Profilometry	Quartz/PVK/MoO_x (5, 15 nm) Quartz/PVK/C60 (20 nm) Quartz/PVK/Spiro-OMeTAD	No	12-5-22
Batch 4	0.77	XRD, UV/Vis/Nir, PL, TRMC, SEM, Profilometry	Quartz/PVK/MoO_x (5,15 nm) Quartz/PVK/C60 (20 nm) Quartz/PVK/Spiro-OMeTAD	Yes (subs. 6.2.2)	12-5-22
Batch 5	0.77	PL	Quartz/PVK/C60 (20 nm) Quartz/MoO_x (5, 15 nm)/PVK Quartz/Spiro-TTB (15 nm)/MoO_x (5, 15 nm)/PVK Quartz/Spiro-OMeTAD/MoO_x (5, 15 nm)/PVK	Yes (subs. 6.2.3)	16-6-22

4.2.1. Structural characterisation and thickness optimisation

In order to characterise the structural properties of spin-coated PVK, three techniques were used: XRD, SEM and profilometry. The XRD results can be seen in Fig. 4.13 for batch 1, batch 3 and batch 4. The reason to do measurements on this many batches with the same PVK composition, was to learn something about the reproducibility and quality of our depositions in regard to the fabrication of devices. All depositions show similar diffractograms with two intense peaks belonging to the (110) and (220) reflection of β phase PVK, located around 2θ = 14.1° and 28.4°, and one less intense peaks belonging to the (330) reflection, located around 2θ = 43.2°. In addition, less intense peaks belonging to the (200), (211), (202), (310) and (224) reflection of PVK can be observed. These peaks are located around 2θ = 20.0°, 23.0°, 24.5°, 41.8°, 31.9° and 40.6°. Note that all the latter peaks are most intense in the diffractogram of batch 1. The occurrence of these peaks around the given values for 2θ, is consistent with values reported in literature for the same type of PVK [112]. In addition, batch 1 shows a peak that can be related to PbI_2 (2θ = 12.6°) [107]. This peak indicates the presence of unreacted PbI_2. Three more peaks can be seen in the diffractogram of batch 1 (indicated with a ? symbol). These are located at 2θ = 7.7°, 11.5° and 19.2°. Unfortunately, the origin of these peaks could not be retrieved.

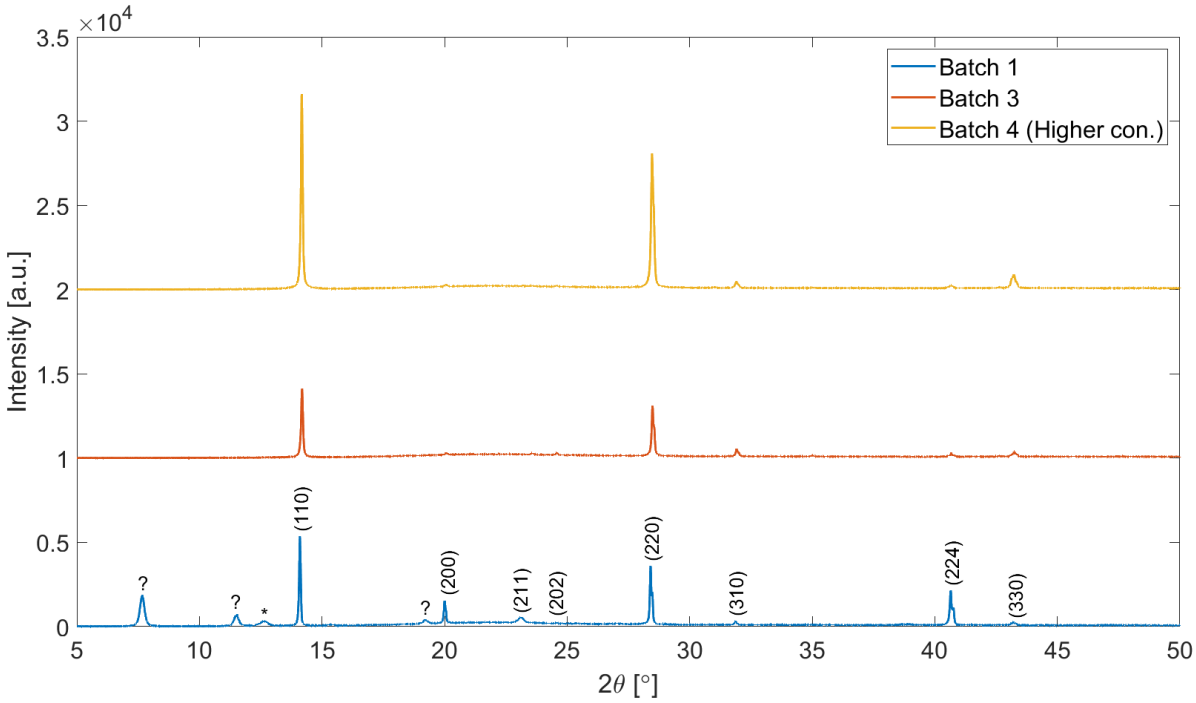

Figure 4.13: Diffractogram of three samples from three different batches of spin-coated $MAPbI_3$: batch 1 (blue), batch 3 (red) and batch 4 (yellow, higher concentration precursor solution) (see table 4.5). PVK reflections indicated with Miller indices, PbI_2 reflections indicated with a * symbol and unspecified reflections indicated with a ? symbol.

The (110) PVK reflection is further analysed to make a comparison between the different spectra of Fig. 4.13. The 2θ angle, intensity and FWHM for the (110) PVK reflection are given in table 4.6.

Table 4.6: The peak position, peak intensity and FWHM for the (110) PVK reflection for batch 1, batch 3 and batch 4.

	Peak pos. PVK [°]	**Peak int. PVK [a.u.]**	**FWHM PVK [°]**
Batch 1	14.10	5349	0.083
Batch 3	14.19	4110	0.083
Batch 4 (Higher con.)	14.18	11570	0.083

The intensity of the (110) reflection is highest for batch 4 (higher precursor concentration). This result implies that this deposition has the highest crystallinity. Next, equation (3.9) (Scherrer equation) is used to calculate the average size of the crystalline domains. In order to do so, the peak position and FWHM (converted to radians) from table 4.6 are used. In addition, $\lambda = 0.15418$ nm (Cu Kα) and the shape factor $k = 0.94$ [109]. The average crystal sizes were found to be $L_{Batch1} \approx 104$ nm, $L_{Batch3} \approx 104$ nm and $L_{Batch4} \approx 104$ nm. It can be concluded that the average length of the crystalline domains in the (110) direction is roughly the same for all batches. Note that we do not take these numbers as completely reliable, but merely as an indication of the relative average crystal sizes.

A table with the results of the average thickness t_{avg} measured for the same batches as analysed with XRD, is shown in table 4.7. We see that with a higher concentration, a thicker layer was obtained, which is desired for the absorber layer in a PSC [35]. Therefore, we did achieve our goal to obtain a thicker PVK absorber layer. There was no difference in thickness found between the edge and centre of the thin film on the quartz substrate.

Table 4.7: Average thickness measured for batch 1,3 and 4. Average calculated over twelve, six and ten measurements for batch 1, 3 and 4 respectively.

	High/normal con.	t_{avg} **[nm]**
Batch 1	Normal	273
Batch 3	Normal	334
Batch 4	High	495

The final characterisation on the structural properties of spin-coated PVK thin films was performed with scanning electron microscopy. SEM images of batch 1, batch 3 and batch 4 with different magnifications are shown in Fig. 4.14. The images depict the morphology of spin-coated $MAPbI_3$ thin films. In general, the morphology looks quite different when we compare the three batches with each other. For batch 1, most crystal grains have a size in the range from 100 to 200 nm. For batch 3, the PVK crystals seem to have clustered together in connected islands, leading to a rough surface. The crystal grain size is around 100 nm. For batch 4, most crystal grains have a size in the range from 90 to 210 nm. Again, groups of PVK crystals seem to cluster together which might lead to a rough surface. The crystal grain sizes are low compared to reports on the same PVK produced with similar spin-coating recipes (DMF and $Pb(Ac)_2{\cdot}3H_2O$). Grain sizes that are ten times as large as the ones found for our batches, are reported [113].

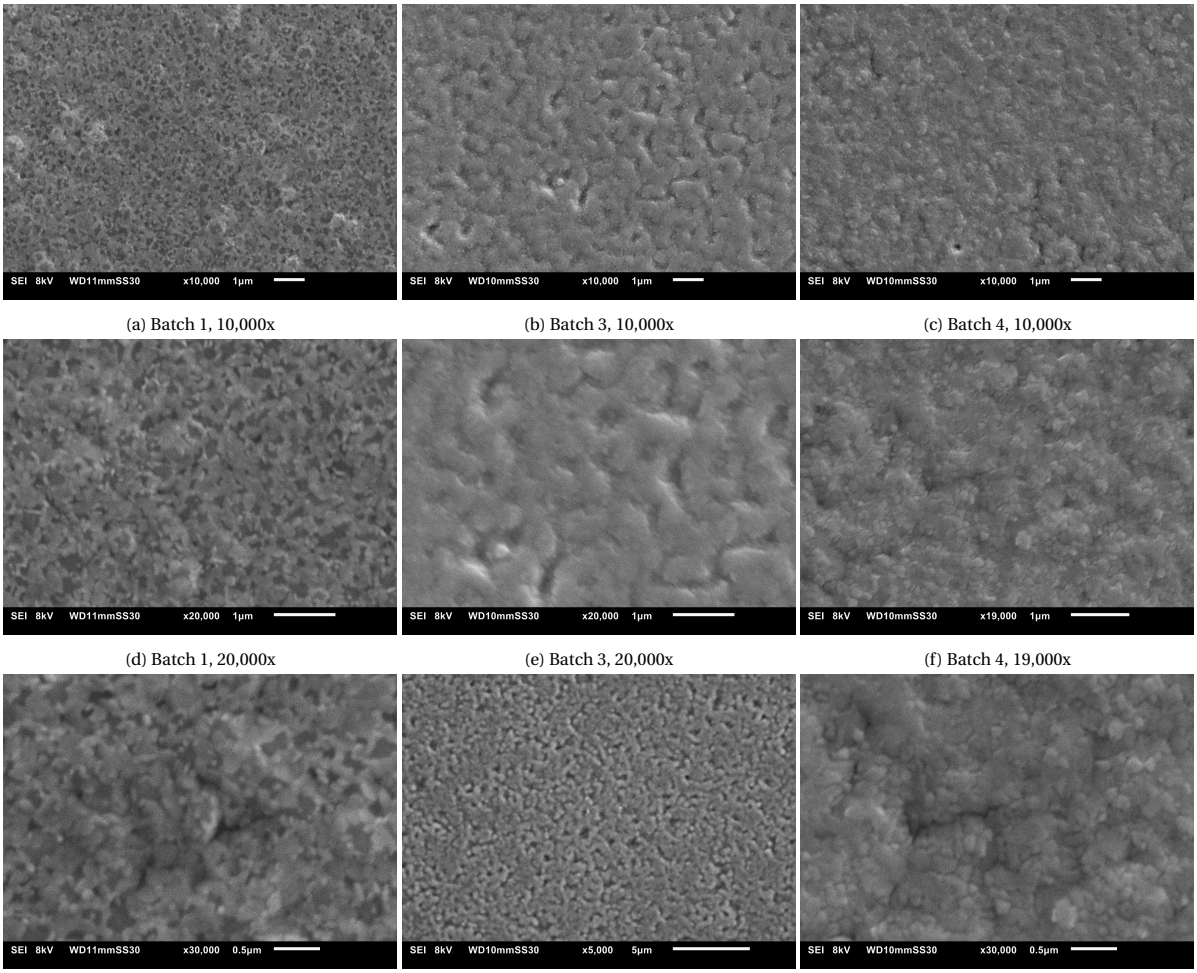

(a) Batch 1, 10,000x (b) Batch 3, 10,000x (c) Batch 4, 10,000x

(d) Batch 1, 20,000x (e) Batch 3, 20,000x (f) Batch 4, 19,000x

(g) Batch 1, 30,000x (h) Batch 3, 5,000x (i) Batch 4, 30,000x

Figure 4.14: SEM images of spin-coated PVK for different batches (see table 4.5). (a), (d) and (g) SEM images of batch 1 with magnifications 10,000x, 20,000x and 30,000x. (b), (e) and (h) SEM images of batch 3 with magnifications 10,000x, 20,000x and 5,000x. (c), (f) and (i) SEM images of batch 4 with magnifications 10,000x, 19,000x and 30,000x.

4.2.2. Opto-electronic characterisation

To assess the optical properties of our spin-coated $MAPbI_3$, absorption and transmission spectra were measured for batch 1, batch 3 and batch 4 (higher concentration) (see table 4.5). From the absorption and transmission spectra, the fraction of light that gets reflected was calculated. Next, equation (3.14) was used to determine the absorption coefficient. The film thicknesses, as depicted in table 4.7, were used to calculate α. Subsequently, the Tauc method was applied to accurately determine the bandgap. F_A, F_R and α all as a function of wavelength, and the Tauc plot, are depicted in Fig. 4.15 for all studied batches.

Taking a closer look at F_A (top left in Fig. 4.15), a few interesting aspects can be noticed. Firstly, batch 3 and 4 follow the same shape and have the same absorption onset. This similarity was expected, since these batches were produced on the same day, which implies that glove box conditions and solvents were the exact same. Note that the diffractogram for these batches is very similar as well (see Fig. 4.13). Secondly, the absorptance of batch 4 is higher than that of the other batches in the wavelength range from 500 to 800 nm. This result can be attributed to the thicker layer obtained for batch 4 with a more concentrated precursor solution. Finally, the absorptance of batch 1 is lower compared to the other batches, which is in agreement with the poorer diffractogram shown in Fig. 4.13, characterised by the occurrence of unknown diffraction peaks.

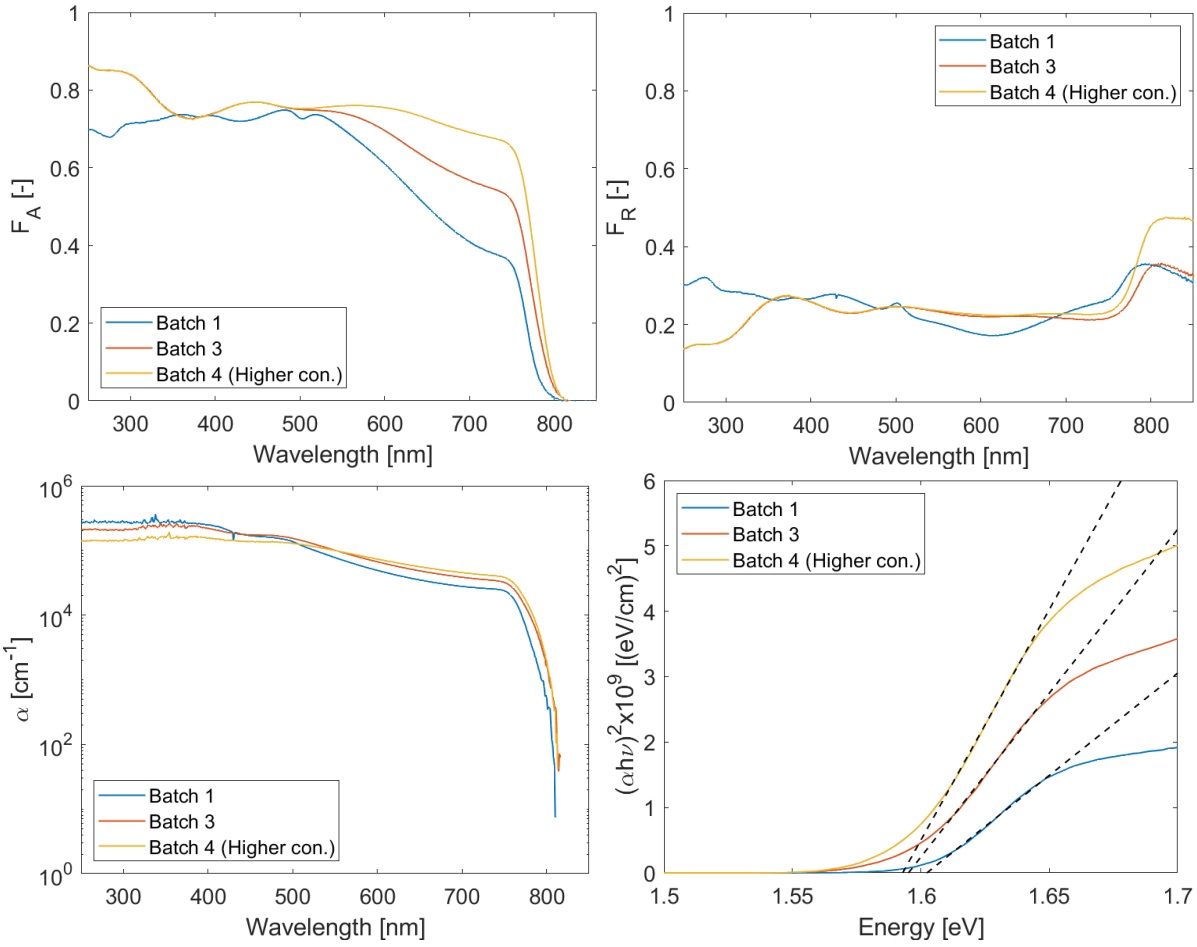

Figure 4.15: F_A (top left), F_R (top right) and α (bottom left) as a function of wavelength for spin-coated PVK from batch 1 (blue), 3 (yellow) and 4 (red) (see table 4.5). Tauc plot for batch 1,3 and 4. (bottom right), linear part is extended to the x-axis (black).

Taking a closer look at the absorption coefficient (bottom left in Fig. 4.15), a similar trend as for F_A is noticed. The absorption coefficient is highest for batch 4 in the wavelength range from 500 to 800 nm. Below a wavelength of 500 nm, α for batch 1 is highest, which is caused by F_R being higher in this wavelength range. Note that we take F_R and F_T into account for the calculation of α. In general, the samples possess a high absorption coefficient, which is in accordance to reports in literature [114]. The Tauc method is used to accurately determine the bandgaps for the different batches. Recall that the bandgap is found at the intercept with the

x-axis. For batch 1 we get E_G = 1.60 eV, for batch 3 we get E_G = 1.59 eV and for batch 4 we get E_G = 1.59 eV. The bandgap values are consistent with literature [29].

Next, photoluminescence spectra were recorded for depositions belonging to batch 1, batch 3, batch 4 and batch 5 (see table 4.5). Note that batch 1, batch 3 and batch 4 have been studied in the previous experiments as well. Batch 5 was produced with the high concentration precursor solution and used for the final batch of eight different devices (see subsection 6.2.3). The PL signal as a function of wavelength for the mentioned batches can be seen in Fig. 4.16.

The PL signal is produced by emission of photons after direct recombination of electrons and holes. From the PL signal, several aspects can be derived for the studied batches. Firstly, the PL spectra show a single peak which coincides with the optical absorption onset and therefore with the bandgap. For batch 1, the peak is located at a wavelength of 771 nm, which corresponds to a bandgap energy of 1.61 eV. For batch 3, the peak is located at a wavelength of 776 nm, which corresponds to a bandgap energy of 1.60 eV. For batch 4, the peak is located at a wavelength of 782 nm, which corresponds to a bandgap energy of 1.59 eV. These results are in good agreement with the bandgaps found from the Tauc plot and differ by maximal 0.01 eV. Moreover, for batch 5, the peak is located at a wavelength of 783 nm, which corresponds to a bandgap energy of 1.58 eV.

Secondly, when we look at the PL signal intensity, a few aspects can be derived. The PL signal for batch 3 and 4 is much lower than for batch 1. A low PL signal could indicate that the non-radiative recombination of electrons and holes is relatively high [115]. Therefore, it can be concluded that probably the non-radiative recombination, caused by lattice defects, is much higher for batch 3 and 4 than for batch 1. Note that these measurements have been taken with an excitation slit width of 3.5 mm and an emission slit width of 4 mm. For this reason, the intensities can be compared.

Finally, batch 5 shows a high intensity PL signal. Note that this measurement has been carried out with an excitation slit width of 2 mm and an emission slit width of 2.5 mm. The lower slit widths were required, since the intensity would otherwise become too high and be harmful for the detector. For this reason, it is likely that the photoluminescence of batch 5 is the most intense. These results provides us with information on the PVK absorber layer present in our devices.

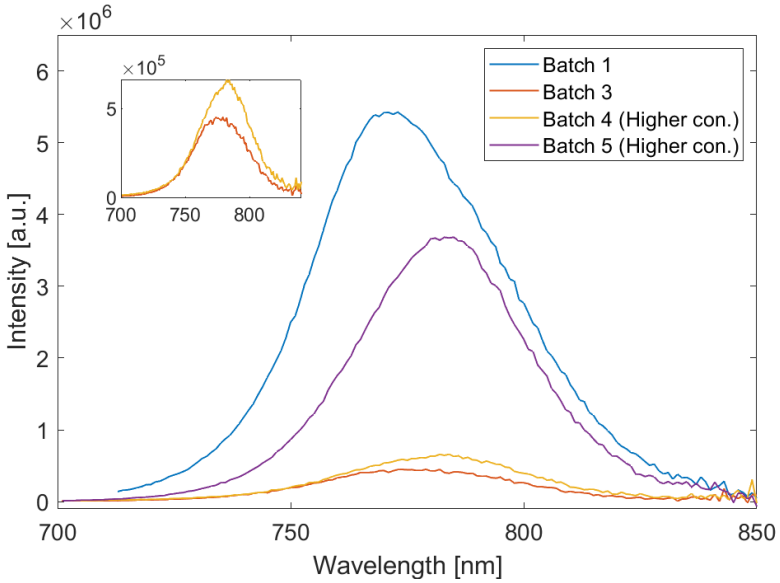

Figure 4.16: PL signal of spin-coated PVK for batch 1 (blue), 3 (red), 4 (yellow) and 5 (purple). The inset is an enlarged version of the results for batch 3 and 4. Batch 1, 3 and 4 are measured with Ex SW = 3.5 mm and Em SW = 4 mm, batch 5 is measured with Ex SW = 2 mm and EM SW = 2.5 mm.

The final characterisation carried out on spin-coated $MAPbI_3$ thin films is TRMC. Samples from two batches are compared: batch 1 (normal concentration precursor solution) and batch 4 (higher concentration). Recall that for batch 4, a very low PL signal was detected compared to batch 1. TRMC signals for batch 1, after excitation with a laser pulse of 650 nm with different photon intensities, are depicted in Fig. 4.17 for short and longer timescales. For batch 4, TRMC signals are depicted in Fig. 4.18 for short and longer timescales.

The y-axis shows the photoconductance normalised by the photon intensity I_0 and geometrical factor β of the microwave guide. Note that the photoconductance is not corrected for F_A.

Recall that the TRMC signal shows us what happens with moving charge carriers that exist after excitation by the laser pulse. As we can see in all TRMC results, initially there is a big increase in normalised photoconductance due to the excitation of charge carriers. After generation, the TRMC signal decays due to recombination and trapping of charge carriers. Increasing the photon intensity, should lead to a reduction of the normalised photoconductance peak and a faster decay of charge carriers. This phenomenon is caused by direct recombination (which is a second-order process) becoming more dominant than SRH recombination. In addition, due to the response time of 18 ns, this results in a lower photoconductance peak for higher photon intensities [97]. When we look at the TRMC signals obtained for batch 1 and 4, a reduction in normalised photoconductance peak for higher intensities, is observed for most traces. In addition, with higher photon intensities, there is a faster decay, as can be seen clearly in the bottom graph in Fig. 4.17. When a decrease in normalised photoconductance and faster decay are not observed upon an increase of intensity, it indicates that electron and hole traps are still being filled [94].

When we compare the TRMC traces of batch 1 to those of batch 4, several observations can be made. Firstly, the maximal normalised photoconductance signal for batch 4 ($\approx$ 6 cm^2/(Vs)) is much lower than for batch 1 ($\approx$ 27 cm^2/(Vs)). If we assume that each photon generates one electron-hole pair (exciton binding energies are low), the low normalised photoconductance of batch 4 indicates that the hole and electron mobility is relatively low [97]. Secondly, the decay of charge carriers for batch 4 is much faster as for batch 1. This observation implies that the charge carrier lifetime for batch 4 is really low. Possibly, trap-assisted recombination happens with a high rate in batch 4. This conclusion is in agreement with the low PL signal detected for this deposition. In addition, it can be concluded that a high crystallinity, thickness and absorptance is no guarantee for good electrical properties. Moreover, it can be concluded that differences found between different batches, can be attributed to uncertainties in the spin-coating procedure, such as glove box conditions (oxygen and moisture level).

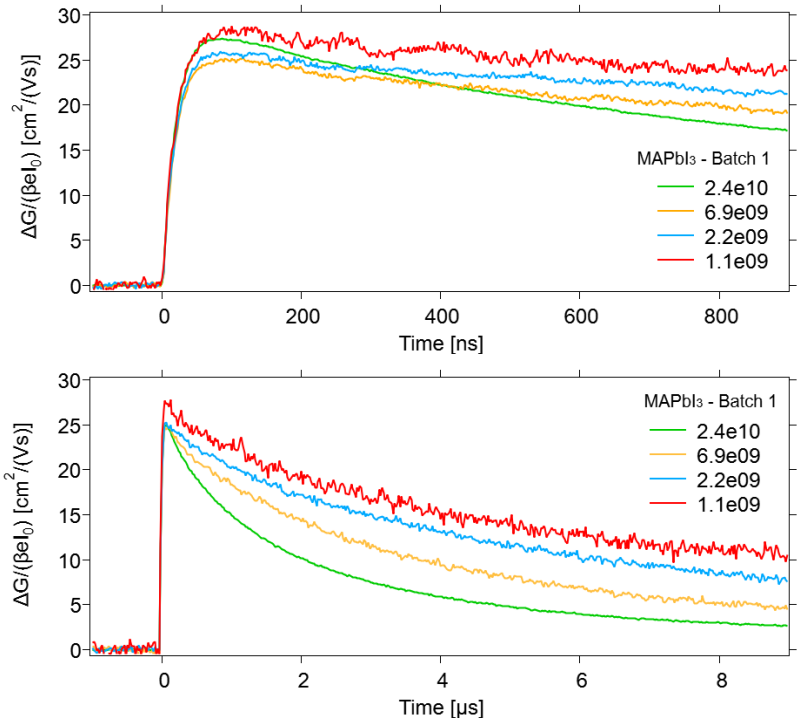

Figure 4.17: TRMC traces for a $MAPbI_3$ sample from batch 1 recorded at laser intensities ranging from 10^9 to 10^{10} photons/cm^2. Excitation at 650 nm. Top: short timescales. Bottom: long timescales.

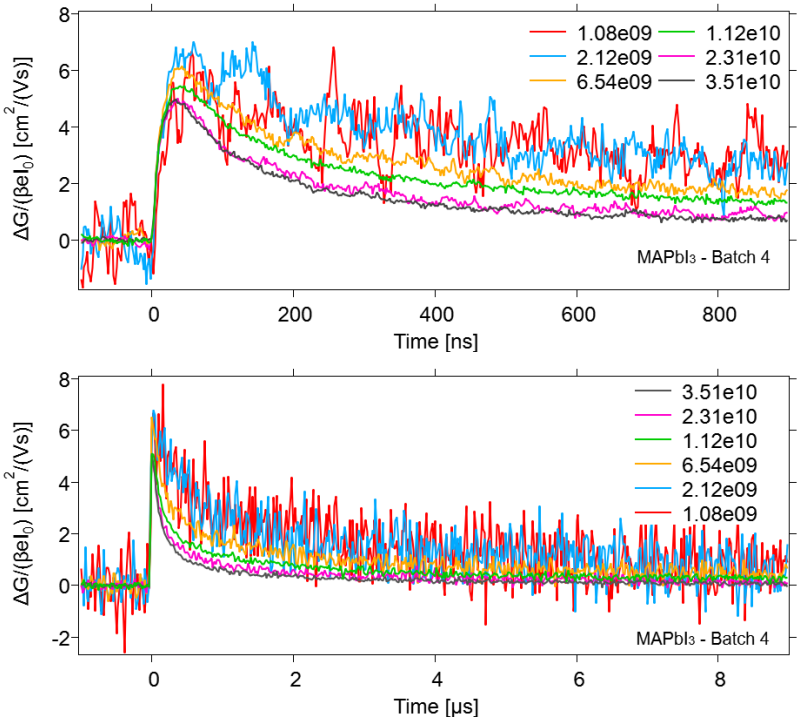

Figure 4.18: TRMC traces for a $MAPbI_3$ sample from batch 4 recorded at laser intensities ranging from 10^9 to 10^{10} photons/cm^2. Excitation at 650 nm. Top: short timescales. Bottom: long timescales.

5

Optimisation of Transport and Contact Layers

5.1. Front and back electrode fabrication and characterisation

5.1.1. Structural characterisation of indium tin oxide

Indium tin oxide was selected as TCO layer. Several different ITO depositions have been carried out, which differ in thickness and/or presence of substrate heating at 131°C during the RF sputtering process. Depositions have been carried out on either quartz substrates (for XRD, UV/Vis/Nir and SEM) or on 2.5 cm x 2.5 cm Corning glass substrates (for the four-point probe method and device fabrication). An overview of different depositions relevant for this section, is given in table 5.1. Moreover, the types of characterisation carried out on a certain deposition and fabrication date are given as well. An image of an ITO layer, deposited through a metal mask for the production of a device, is shown in Fig. 5.1.

Table 5.1: Overview of different ITO depositions. Sample name, thickness, presence of substrate heating, used characterisation techniques and date are shown.

Sample name	***t* [nm]**	**Sub. heat.**	**Char. tech.**	**Date**
ITO 200 nm w/ sub. heat.	200	Yes	XRD, UV/Vis/NIR, SEM, Four-point probe	25-4-22
ITO 300 nm w/ sub. heat.	300	Yes	Four-point probe	25-4-22
ITO 200 nm	200	No	XRD, UV/Vis/NIR, Four-point probe	9-5-22
ITO 300 nm	300	No	XRD, UV/Vis/NIR, Four-point probe	9-5-22
ITO 200 nm (different batch)	200	No	Four-point probe	18-3-22
ITO 300 nm (different batch)	300	No	Four-point probe	18-3-22

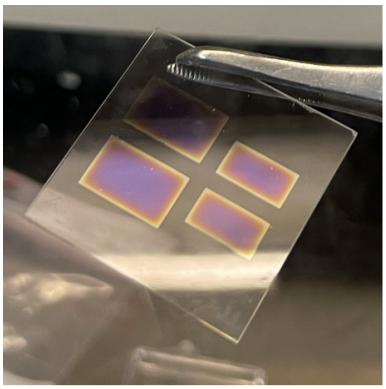

Figure 5.1: Image of a 2.5 cm x 2.5 cm Corning glass substrate coated with a 300 nm thick ITO layer. Note the presence of rectangular pattern obtained using a metal mask during deposition.

In order to characterise the structural properties, XRD measurements were carried out. The diffractograms can be seen in Fig. 5.2 for the 200 nm ITO with substrate heating and 200 and 300 nm ITO without substrate heating. For the latter two, one intense peak belonging to the (222) reflection of ITO, located around 2θ = 30.6°, can be seen. In addition, less intense peaks belonging to the (211), (400), (411), (332), (431), (440) and (611) reflections of ITO can be observed. These peaks are located around 2θ = 21.6°, 35.5°, 37.8°, 41.8°, 45.7°, 51.0° and 56.0°. The occurrence of these peaks around the given values of 2θ is consistent with values reported in literature [116]. The diffractogram for the 200 nm deposition with substrate heating shows two small peaks located at the 2θ angle belonging to the (222) and (400) reflection. Note that no post-deposition annealing was carried out on these samples.

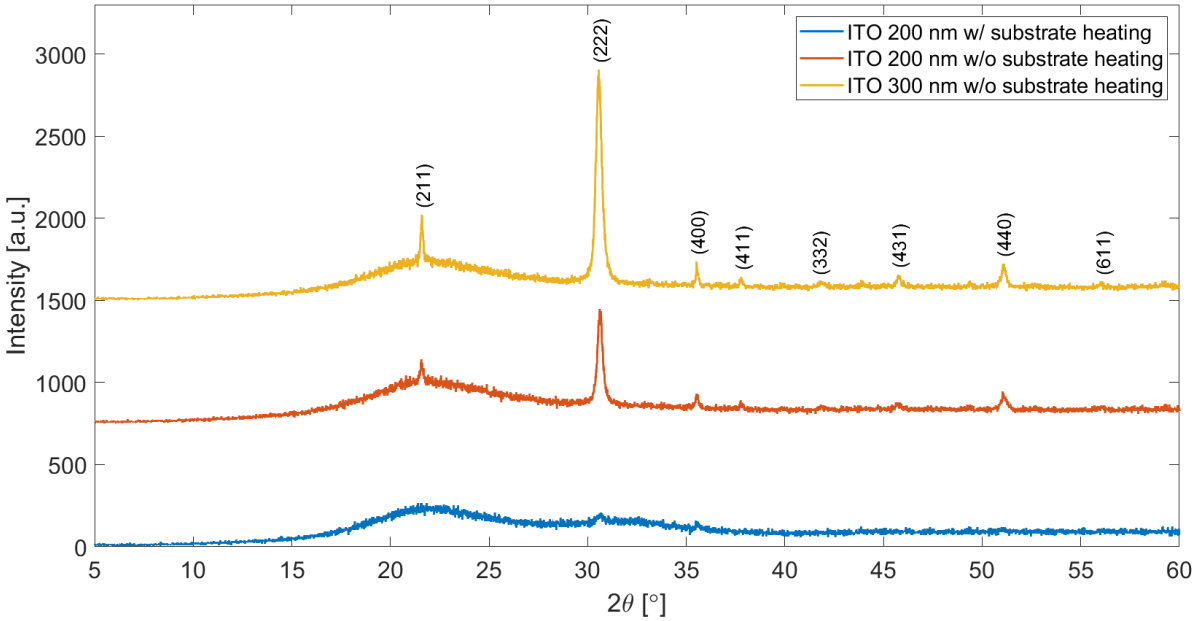

Figure 5.2: Diffractogram of different ITO deposited on quartz: 200 nm with substrate heating during deposition (blue), 200 nm without substrate heating (red) and 300 nm without substrate heating (yellow) (see table 5.1). ITO reflections indicated with Miller indices.

The intensity of the (222) reflection is highest for the 300 nm ITO deposition which indicates that this deposition possesses the highest crystallinity. The 200 nm deposition with substrate heating shows a peak for the (222) reflection with a very low intensity. Apparently, heating the substrate to 131°C is detrimental for the crystallinity. This effect of substrate heating that we encountered, was found to be contradicting with other reports in which it was shown that substrate heating, even at 100°C, has a beneficial effect on the crystallinity [117].

The average crystal sizes in the (222) direction for the 200 and 300 nm ITO film deposited without substrate heating were calculated with equation (3.9) (Scherrer equation). In order to do so, the peak position and FWHM were determined. In addition, λ = 0.15418 nm (Cu Kα) and the shape factor k = 0.94 [118]. The average crystal size for the 200 nm deposition was found to be 28 nm, whereas the average crystal size for the 300 nm deposition was found to be 26 nm. In comparable research, average crystal sizes around 35 nm were found for as-deposited ITO films with a thickness of 200 nm [118]. The same research found that the crystallinity and average crystal size increase upon annealing, with the best result achieved at an annealing temperature of 550°C [118]. Annealing of our depositions could possibly increase the crystallinity as well. The average crystal size for the 200 nm deposition with substrate heating could not be determined reliably.

SEM images of the 200 nm ITO deposition with substrate heating are shown in Fig. 5.3. Note that a thin layer of spiro-TTB was deposited on top of the ITO. However, since this layer is very thin, it does not influence the SEM images. The images depict the morphology of the ITO film.

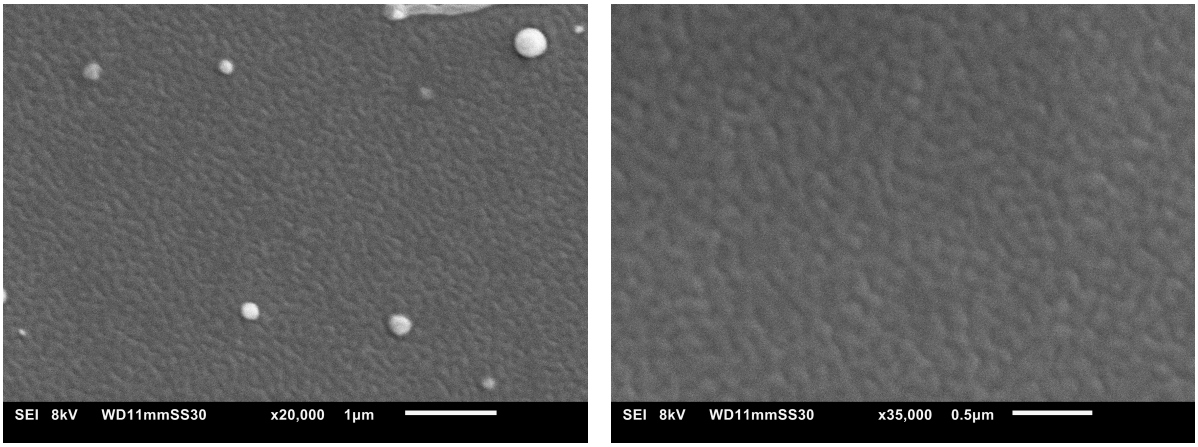

Figure 5.3: SEM images of ITO 200 nm with substrate heating with 30 nm of spiro-TTB on top. Left: 20,000x. Right: 35,000x.

5.1.2. Opto-electronic characterisation of indium tin oxide

In order to characterise the optical properties of the ITO depositions, absorption and transmission spectra were measured. The results are shown in Fig. 5.4 for the 200 nm ITO with substrate heating, and 200 and 300 nm ITO without substrate heating. The goal of these measurements is twofold. Firstly, to determine which ITO has the highest transmittance, and secondly, to get an idea of the parasitic absorption losses due to the ITO layer in our devices.

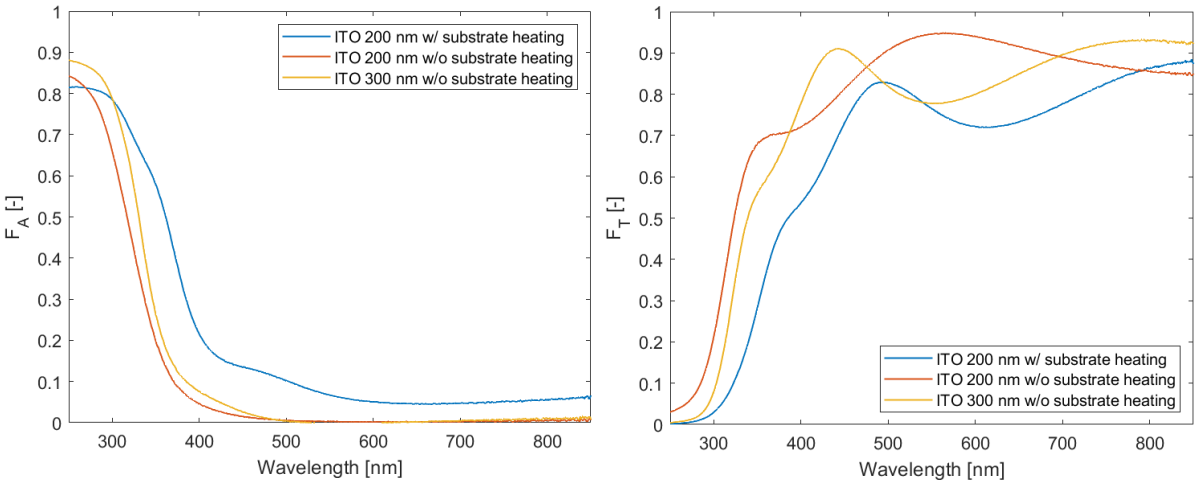

Figure 5.4: F_A (left) and F_T (right) as a function of wavelength for different ITO samples: 200 nm with substrate heating during deposition (blue), 200 nm without substrate heating (red) and 300 nm without substrate heating (yellow) (see table 5.1).

When looking at F_A (left in Fig. 5.4), a few interesting aspects can be noticed. Firstly, for the 200 nm and 300 nm ITO film deposited without substrate heating, F_A is around 0 in the wavelength range of 500 to 850 nm, which means that in this part of the wavelength range no light is parasitically absorbed. Secondly, for wavelengths below 500 nm, F_A starts to increase slowly until around a wavelength of 370 nm, after which there is a steep increase. The steep increase is caused by absorption of photons with an energy higher than the bandgap of ITO. Thirdly, F_A for the 300 nm ITO film is larger than for the 200 nm ITO film (both without substrate heating), which is as expected considering the difference in thickness. Fourthly, for the 200 nm ITO deposition with substrate heating, F_A is non-zero over the entire wavelength range, and higher than that of the other depositions over almost the entire wavelength range. Finally, for wavelengths above 700 nm, the absorptance for all depositions increases slightly as an effect of free carrier absorption [119].

When looking at F_T (right in Fig. 5.4), we obtain an idea about the fraction of light that passes through the ITO layer and substrate. Recall that F_T is measured in front of the integrating sphere. F_T shows interference fringes for all depositions. These fringes are induced by constructive and destructive interference of

the incident light at the air/ITO and ITO/quartz interfaces [120]. When comparing the 200 nm ITO and 300 nm ITO both without substrate heating, the interference fringes are shifted and change shape among them. This observation is expected based on the different thicknesses [120]. On the other hand, when both 200 nm ITO depositions (with and without substrate heating) are compared, we observe that their shape is different as well, and the interference fringes do not align. This observation is unexpected as these samples should have a similar thickness. Furthermore, we see that the 200 nm ITO deposition with substrate heating has the poorest performance because it has the lowest F_T over the entire wavelength range. The recorded spectra for the 200 and 300 nm ITO deposition without substrate heating are consistent with results found in other research for non-annealed depositions [118]. Possibly, post-deposition annealing could have led to a higher transmittance as reported in literature [118].

To get more insights on the electronic properties of the ITO depositions, the sheet resistance has been measured for each of the four rectangular areas on a substrate (see Fig. 5.5). In total six samples with each four cells have been investigated (samples listed in table 5.1). Note that the six samples are deposited on three different occasions during the past months. The correction factors for both small and larger cells have been calculated with the cubic spline interpolation method (Matlab model shown in A.5 in the appendix). The outcome is a correction factor of 3.8028 for a large cell ($d/S = 6$ and $a/d = 1.583$) and 3.2191 for a smaller cell ($d/S = 4$ and $a/d = 1.875$). The measurements can now be corrected for the dimensions of the ITO layer. The results are shown in table 5.2.

Table 5.2: R_{sq} values for different ITO depositions measured in units of Ω/□. Measurements are done on all four cells deposited on a substrate. Note that 'ITO 200 nm w/ sub. heat.' and 'ITO 200 nm w/ sub. heat.' are deposited on 25-4-22, 'ITO 200 nm' and 'ITO 300 nm' on 9-5-22, and 'ITO 200 nm (different batch)' and 'ITO 300 nm (different batch)' on 18-3-22.

	ITO 200 nm w/ sub. heat.	**ITO 300 nm w/ sub. heat.**	**ITO 200 nm**	**ITO 300 nm**	**ITO 200 nm (different batch)**	**ITO 300 nm (different batch)**
Large cell 1	42.9	27.5	97.9	76.7	83.5	61.6
Large cell 2	42.9	29.7	99.2	75.2	88.0	56.7
Small cell 1	39.2	27.1	105.6	78.9	93.1	53.9
Small cell 2	39.2	24.5	102.4	82.0	94.5	59.3

R_{sq} is found to be lower for ITO layers with a thickness of 300 nm compared to their 200 nm counterpart. Note that this observation is based on comparison of the 200 and 300 nm ITO with substrate heating, comparison of the 200 and 300 nm ITO without substrate heating, and comparison of the 200 and 300 nm ITO without substrate heating from a different batch (see table 5.2). The lower sheet resistance for a thicker ITO layer is as expected and consistent with literature [63]. In a thicker layer, the concentration of free charge carriers is higher leading to a higher conductivity and lower resistivity.

The 200 and 300 nm ITO depositions with substrate heating have a much lower sheet resistance than the other depositions. On one hand, this result was not expected based on the diffractogram in which the deposition with substrate heating showed a much poorer crystallinity compared to the depositions without substrate heating. Usually, a higher crystallinity leads to a smaller value for R_{sq} [118]. On the other hand, the lower electrical losses with substrate heating are in accordance with literature [121]. It can be concluded that in our case, for ITO films deposited with substrate heating, the parasitic absorption losses are higher but the electrical losses are lower compared to the films fabricated without substrate heating.

Interestingly, when we compare depositions carried out with the same recipe but on a different day, different values for the sheet resistance are found. We can observe this when we compare the 200 and 300 nm ITO without substrate heating, with the 200 and 300 nm ITO without substrate heating from a different batch (see table 5.2). Note that these depositions were done two months apart from each other. The reason behind the difference in sheet resistance could possibly be related to the depletion of the ITO target. A depleted ITO target results in a high sheet resistance. Once the ITO target is depleted, it is replaced by the EKL clean room technicians. Possibly, the ITO target was closer to the end of its lifetime for the depositions carried out on 9-5-2022 than for those carried out on 18-3-2022 (table 5.1). Note that this could also be the reason behind the low values for R_{sq} found for the depositions with substrate heating.

An uncertainty in the four-point probe method has to be addressed. In practice, it turned out to be difficult to place the probes exactly in the middle of the rectangular area. This difficulty is visualised in Fig. 5.5. Note that placing the probes in the middle of the rectangular area is required, since the correction factors

are determined for that specific position. Furthermore, the edges of the ITO film have different properties, due to the presence of the mask that causes shading. In fact, the film tends to have a different colour at the edges suggesting a thinner layer. Therefore, we can also expect that the material composition is different in proximity of the edges. This difference could possibly have an effect on the paths for the injected current during a measurement. Even though each measurement is subject to these uncertainties, the obtained results are consistent. Therefore, it is not likely that the measurement uncertainties influence the conclusions drawn about our ITO depositions.

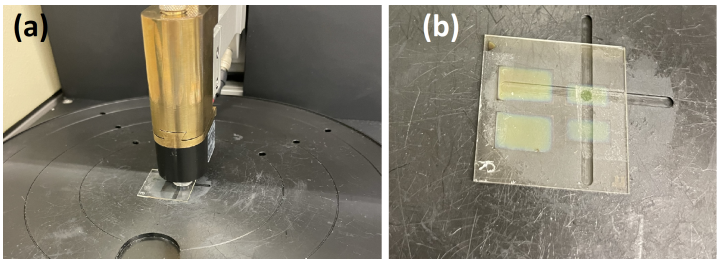

Figure 5.5: (a) Four-point probe on a sample during a measurement. (b) Careful placement of the cell area in the middle of the device.

5.1.3. Development of a thermal evaporation recipe for silver

In order to deposit Ag, a new recipe was developed. After the installation of the alumina covered tungsten basket, a test deposition was carried out with a program similar to the existing program for Al. The current was ramped up to 20 A and manually increased further. Eventually, a rate of 1.3 Å/s was reached at 30 A. Next, the evaporation source was checked and the shutter was found to be covered in a thick layer of Ag. This led to the conclusion that the shutter, which was supposed to open automatically, was closed during the entire deposition. For source position 1 the shutter cannot be opened manually, for this reason the shutter was removed and all of the following Ag depositions are performed without a shutter in place.

Next, a deposition was performed where the tooling factor was varied during the deposition (between 100% and 500%, current to 24 A). The goal was to see the effect on the rate measured by the QCM sensor. From this we learned that increasing the TF simply results in a multiplication of the rate by five. This deposition with t_{sensor} = 68 nm, turned out to have an actual thickness of 213 nm (average of nine measurements). This result led to the conclusion that the TF had to be a lot higher than the value currently set.

In order to determine the TF, a deposition with t_{sensor} = 100 nm and initial TF = 300% was carried out. The average actual thickness, which is the average of eleven measurements, was determined to be 440.2 nm. From this we learned to set the TF to 1250% for the next deposition. Subsequently, a deposition with t_{sensor} = 200 nm and initial TF = 1250% was carried out. The average actual thickness, which is the average of fourteen measurements, was determined to be 223 nm. Subsequently, the TF was set to 1121% in the program.

With the correct TF in place, depositions were performed at a current of 23/24 A, resulting in an increasing rate up to 7 Å/s. Later it was decided that a lower rate, especially at the beginning, would be better for the PSCs [122]. Therefore, depositions are done at a current of 21.5 A and start with a rate of about 0.1 Å/s after which the rate steadily increases until 3.0 Å/s. To sum up, the ideal recipe for Ag was determined to be the following:

1. Set QCM values for Ag:
    - Acoustic impedance: $16.68 \cdot 10^5$ g/cm^{2}s
    - Material density: 10.50 g/cm^3
    - TF: 1121%
2. Rotation to 15 rpm and switch on power supply 1
3. Ramp up current to 21.5 A in 700 s
4. No shutter installed, deposition starts with a low rate (0.1 Å/s)
5. Rate increases steadily to 3 Å/s, wait until target thickness is almost reached

6. Decrease current manually a bit before the target is reached to avoid ending up with a layer thickness higher than the target
7. Ramp down current to 0 A in 800 s
8. Turn off power supply 1 and rotation to 0 rpm

5.2. Fabrication and characterisation of transport and buffer layers

5.2.1. Development of buffer and electron transport layers

Development of bathocuproine deposition recipe

In order to deposit BCP, a new recipe was developed. To determine the deposition parameters, the current was ramped up to 10 A and slowly increased in steps of 1 A. It turned out that a rate started appearing at 19 A. At 19 A, the rate increases to about 0.25 Å/s in 5 minutes. When the current is further increased to 20 A, the rate increases rapidly to over 4 Å/s. From the experiment, it was decided to set the current limit to 19 A. At 19 A, the voltage is around 0.79 V resulting in a deposition power around 15 W.

In order to determine the TF, a deposition with t_{sensor} = 150 nm and initial TF = 120% was carried out. The average actual thickness, which is the average of five measurements, was determined to be 218.6 nm. From the thickness measurement we learned that the TF should be set to 175%. Thickness measurements with the profilometer required a scan time of 60 s in order to acquire a reliable result.

To sum up, the following recipe was developed and has been applied for the thermal evaporation of BCP:

1. Set QCM values for BCP:
   - Acoustic impedance: $1.0773 \cdot 10^5$ g/cm^{2}s
   - Material density: 1.24 g/cm^3
   - TF: 175%
2. Rotation to 10 rpm and switch on power supply 3
3. Ramp up current to 19 A in 500 s
4. Manually open shutter, deposit until target thickness is reached, manually close shutter
5. Ramp down current to 0 A in 700 s
6. Turn off power supply 3 and rotation to 0 rpm

BCP buffer layers were fabricated with deposition rates ranging from 0.1 to 0.3 Å/s. These rates are similar to what is being used in other research [123],[124].

Fabrication of C60 layer

The thermal evaporation of the C60 electron transport layer was carried out with an existing recipe given in A.3 in the appendix. Note that for some depositions the current was increased by 1 or 2 A to achieve a higher rate. In addition, no abnormalities were noticed during the fabrication of C60 layers during this project.

5.2.2. Optical characterisation of buffer and electron transport layers

In order to characterise the optical properties of BCP and C60, absorption and transmission spectra were measured. The spectra for a 20 nm layer of C60 and a 4 nm layer of BCP, are depicted in Fig. 5.6. We chose these specific thicknesses because they are applicable to our PSCs. In addition, in a lot of research, these layers are used with similar thicknesses. Note that we use the ETL and BL in a p-i-n configuration for all of our devices. Therefore, absorption by these layers is not very relevant for us. However, it does allow us to make an assessment of the parasitic absorption losses if these layers were used in an n-i-p configuration.

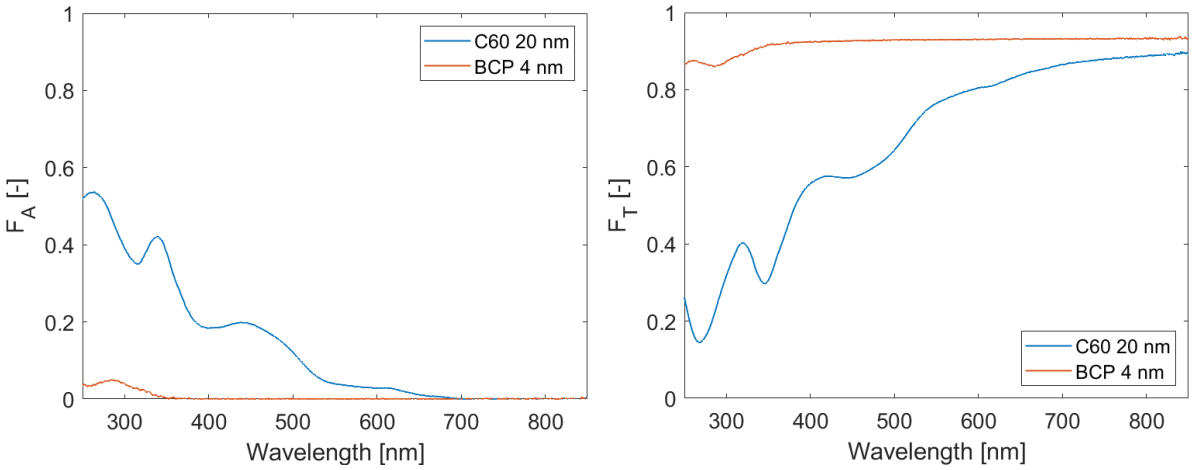

Figure 5.6: F_A (left) and F_T (right) as a function of wavelength for a 20 nm C60 layer (blue) and a 4 nm BCP layer (red).

Taking a closer look at F_A (left in Fig. 5.6), we see that the absorptance for the 4 nm BCP layer is close to 0 over the entire wavelength range. This observation is as expected since the layer is really thin. For wavelengths smaller than 356 nm, F_A increases slightly due to absorption of photons with an energy higher than the bandgap. This absorption onset corresponds to an energy of 3.48 eV and is in agreement with literature [68]. For the 20 nm C60 layer, the absorptance starts increasing for wavelengths smaller than 700 nm. This absorption onset is consistent with literature [125]. When we look at F_A over the entire wavelength range, it increases to relatively high values from a low photon energy. Therefore, using C60 in between the TCO and PVK absorber layer would lead to significant parasitic absorption losses. When we look at F_T (right in Fig. 5.6), we obtain an idea about the fraction of light that passes through the layers and the quartz substrate. Recall that F_T is measured in front of the integrating sphere. As expected, the transmittance is high for the BCP layer. The reason F_T is not equal to 1 for the biggest part of the energy range is due to reflection of the quartz substrate. For C60, we see quite a large decrease in transmittance for lower wavelengths as expected from the absorptance spectrum.

5.2.3. Development of hole transport layers

Development of spiro-TTB deposition recipe

In order to deposit spiro-TTB, a new recipe was developed. To start things off, a program similar to the one used for C60 was applied. The current was ramped up to 21 A. After opening of the shutter, a rate larger than 5 Å/s was measured. From this experiment we learned that the current should be set a lot lower. In the second test, the current was ramped up to 10 A and increased with 1 A every 5 minutes. A non-zero deposition rate was first measured at 15 A. In 10 minutes the rate slowly increased from 0.039 to 0.104 Å/s. At 16 A the rate increased in 3 minutes from 0.1 to 0.4 Å/s. In later depositions, we learned that the rate increases further to at least 1 Å/s in about 5 minutes.

From the experiment, it was decided to set the current limit to 15.5 A. In practice, this implies that after the current limit has been reached, one should wait 5 to 10 minutes before a stable deposition rate of about 0.1 Å/s is reached. At 15.5 A, the voltage is around 0.65 V resulting in a deposition power around 10 W. In some depositions, the current was manually increased to 16.5 A to obtain a higher rate (keeps increasing slowly to at least 1 Å/s).

In order to determine the TF, a deposition with t_{sensor} = 150 nm and initial TF = 120% was carried out. The average actual thickness, which is the average of five measurements, was determined to be 128.2 nm. From the thickness measurement we learned that the TF should be set to 102%. Thickness measurements with the profilometer required a scan time of 45 s in order to acquire a reliable result.

To sum up, the following recipe was developed and has been applied for the evaporation of spiro-TTB:

1. Set QCM values for spiro-TTB:
    - Acoustic impedance: $0.5650 \cdot 10^5$ g/cm^{2}s
    - Material density: 1.28 g/cm^3

- TF: 102%

2. Rotation to 10 rpm and switch on power supply 3
3. Ramp up current to 15.5 A in 500 s
4. Wait for 5-10 minutes to achieve a stable rate around 0.1 Å/s OR manually increase the current to 16.5 A to reach the final deposition rate
5. Manually open shutter, deposit until target thickness is reached, manually close shutter
6. Ramp down current to 0 A in 700 s
7. Turn off power supply 3 and rotation to 0 rpm

In general, spiro-TTB depositions were carried out with deposition rates ranging from 0.1 to 0.3 Å/s. These rates are similar to what is being used in other research [126].

Fabrication of molybdenum oxide and spiro-OMeTAD layers

The thermal evaporation of MoO_x was carried out with an existing recipe given in subsection 3.2.1. No abnormalities were noticed during the fabrication of MoO_x layers during this project.

Spiro-OMeTAD layers were fabricated by spin-coating. The recipe for spin-coating and precursor solution preparation, were given in subsection 3.2.2. Note that a high rotation speed was used (3500 rpm) to make sure the layer thickness did not get too high. From the past, it is known that a rotation speed of 1500 rpm results in a layer thickness of 250 nm. Note that the thickness of our spiro-OMeTAD films was not measured. During the spin-coating, a problem with the uniformity was encountered for some depositions directly on quartz. The film did not always fully cover the surface, as can be seen in Fig. 5.7. Possibly, the rotation speed was too high and/or the surface had a poor wettability. For the production of devices, spiro-OMeTAD deposited on the ITO layer seemed to have a better uniformity for most cells. Evidently, the area of the rectangular ITO parts is smaller than the full area of a quartz substrate, and therefore, achieving a high uniformity is easier for the smaller area. Based on the spin-coating that was carried, we cannot conclude if it had to do with the surface itself.

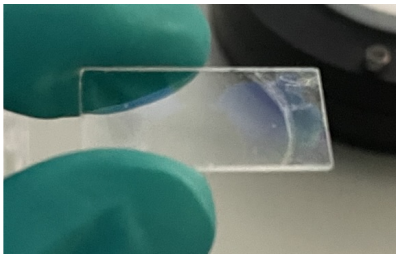

Figure 5.7: Spiro-OMeTAD thin film on a quartz substrate, not uniformly distributed.

5.2.4. Optical characterisation of hole transport layers

In order to characterise the optical properties of the different hole transport layers, absorption and transmission spectra were recorded. The fraction of light that is absorbed or transmitted for 5 and 15 nm MoO_x layers, a 20 nm spiro-TTB layer and a spiro-OMeTAD layer is depicted in Fig. 5.8. We chose these specific thicknesses because they are applicable to our PSCs. Since all of our fabricated devices have a p-i-n configuration, it is relevant to determine parasitic absorption losses due to the HTL.

Taking a closer look at F_A (left in Fig. 5.8), a few interesting aspects can be noticed. Firstly, F_A is equal to 0 for a large part of the wavelength range and takes a non-zero value from a certain point for all HTLs. Note that the increase of F_A from a certain wavelength is caused by absorption of photons with an energy higher than the bandgap of the HTL. For the MoO_x layers, F_A becomes non-zero for wavelengths smaller than 425 nm. This absorption onset corresponds to an energy of 2.92 eV and is in agreement with literature [48]. In addition, the shape of the spectrum is consistent with other reports as well [127]. For the spiro-TTB layer, F_A becomes non-zero for wavelengths smaller than 328 nm corresponding to a bandgap energy of 3.78 eV. This bandgap energy contradicts reports from literature. According to literature, the bandgap of spiro-TTB should be equal to 3.07 eV [128],[47]. The most logical explanation for the difference is that there is a fundamental difference between

used precursor powders. For the spiro-OMeTAD layer, photons are being absorbed for wavelengths smaller than 430 nm corresponding to a bandgap energy of 2.88 eV. This observation is consistent with literature [47]. Secondly, we observe that F_A for the 15 nm MoO_x layer is larger than for the 5 nm MoO_x layer, which is as expected. Thirdly, F_A is much higher for spiro-OMeTAD as for spiro-TTB. This observation is in agreement with what was stated in subsection 2.3.3. Since spiro-TTB is fabricated with thermal evaporation, a much thinner layer could be fabricated with lower parasitic absorption losses compared to the spin-coated Spiro-OMeTAD layer [53]. Finally, even though spiro-OMeTAD has the highest parasitic absorption losses, F_A is still not too high, which indicates that the high rotation speed during spin-coating probably resulted in a relatively thin layer.

When we look at F_T (right in Fig. 5.8), we obtain an idea about the fraction of light that passes through the layers and the quartz substrate. Recall that F_T is measured in front of the integrating sphere. When looking from high to low wavelength, the transmittance for all layers starts off high until the moment the wavelength becomes smaller than the absorption onset, which leads to a decrease in transmittance.

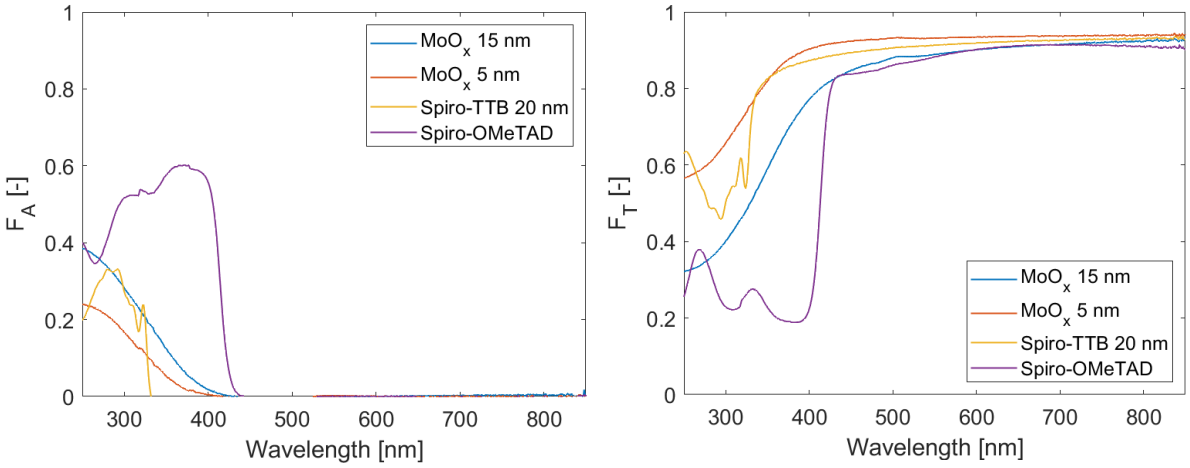

Figure 5.8: F_A (left) and F_T (right) as a function of wavelength for a 15 nm MoO_x layer (blue), a 5 nm MoO_x layer (red), a 20 nm spiro-TTB layer (yellow) and a spiro-OMeTAD layer (purple).

To assess the total impact of parasitic absorption, F_A and F_T were measured for bi-layers of ITO/HTL. The studied bi-layers are ITO 300 nm/MoO_x 15 nm, ITO 200 nm with substrate heating/Spiro-TTB 25 nm and ITO 300 nm/Spiro-OMeTAD. Recall that the 200 nm ITO with substrate heating had a poor transparency compared to the ITO depositions without substrate heating. The results are shown in Fig. 5.9. The recorded spectra do not contain a lot of new information considering that we already analysed the optical properties of the ITO and HTLs separately.

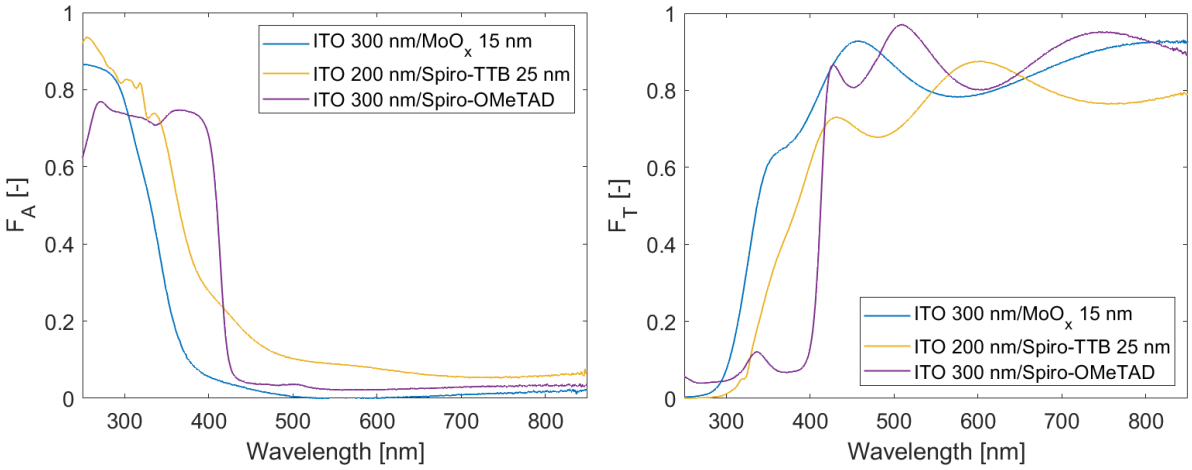

Figure 5.9: F_A (left) and F_T (right) as a function of wavelength for a 300 nm ITO/15 nm MoO_x bi-layer (blue), a 200 nm ITO/20 nm Spiro-TTB bi-layer (yellow) and a 300 nm ITO/Spiro-OMeTAD bi-layer (purple).

Development of an ellipsometry model for spiro-TTB

Spectral ellipsometry is especially useful to determine the thickness for very thin layers where the profilometer is not able to give a reliable result. Therefore, SE and existing optical models have been used throughout the project to determine and verify the thickness of thermally evaporated perovskite and C60 thin films. We wanted to be able to do the same for thermally evaporated spiro-TTB layers. In order to do so, an optical model to fit the measurements of Ψ and Δ had to be developed from scratch. In this subsection, we briefly describe how the model was build and what the outcomes are (n and k data and thickness). Screenshots of the optical model at all intermediate steps can be found in A.6 in the appendix.

In order to carefully build up the analysis several different models are used. Firstly, Ψ and Δ were measured for a quartz substrate only. Next, the Cauchy model was used to fit the measured data. Recall that the dispersion relation of the Cauchy model is given by equation (3.23). The fitted parameters and the mean square error (MSE) are given in table 5.3.

Table 5.3: Fitting parameters of the Cauchy model for a quartz substrate only. A, B, C and MSE are given.

A	1.448
B	0.00361
C	$4.2528{\cdot}10^{-5}$
MSE	1.541

Subsequently, Ψ and Δ were measured for spiro-TTB layers with different thicknesses. We consider two depositions with different layer thickness: a 128 nm spiro-TTB layer (measured with profilometry) and a 26 nm spiro-TTB layer (according to the QCM sensor of the thermal evaporator). As a side note, UV/Vis/Nir spectrophotometry measurements were carried out to determine the absorption coefficient and bandgap (Tauc method) for these two layers. These results are shown in Fig. A.15 in the appendix. Considering the development of the optical model, we start with the 128 nm layer. We continue to build the model by adding a layer on top of the model of the quartz substrate.

From Fig. 5.8 we learned that spiro-TTB has a wide transparent region. Therefore, the transparent part of the wavelength range is selected and analysed with the Cauchy model. Note that the measured ellipsometry data, Ψ and Δ, are a function of wavelength. In order to make an accurate fit, the thickness, A, and B are fitted first. Next, C and the roughness are fitted as well. The results are given in table 5.4. The value obtained for the thickness (129 nm) is very close to the thickness measured with the profilometer. It can be concluded that building the model until this point, is already enough to accurately determine the thickness.

Table 5.4: Fitting parameters of the Cauchy model for the transparent region of a 128 nm spiro-TTB layer on a quartz substrate. A, B, C, the thickness, roughness and MSE are given.

A	1.704
B	0.01206
C	0.00227
Thickness [nm]	129.84
Roughness [nm]	0.62
MSE	1.154

Next, the model is converted to a b-spline model with transparent region, and extended over the entire wavelength range with a wavelength expansion fit. The expansion fit is carried out with an energy resolution of 0.03 eV. The small value for the energy resolution is required to accurately fit all details of Ψ and Δ. With the created b-spline model, a thickness of 129.96 nm, a roughness of 0.88 nm and an MSE of 2.058 were obtained. The relatively low MSE, tells us that the fitting procedure was successful. Note that building the b-spline model in this way, automatically enforces Kramers-Kronig consistency and a positive value for the imaginary part (ϵ_2) of the complex dielectric function. After this procedure, n and k data for the 128 nm spiro-TTB layer were retrieved.

As a final step, the b-spline model was parameterized to generic oscillators with the generic oscillator (gen. osc.) approach. Note that the fitting of oscillators is carried out on ϵ_2 found with the b-spline model. The fitting parameters of the Tauc-Lorentz oscillators (amplitude, central peak energy, broadening and bandgap energy) are given in table 5.5. Note that E_G is the same for all oscillators (coupled). Subsequently, the layer was fitted with the new gen. osc. model resulting in a thickness of 129.92 nm, a roughness of 0.64 nm and an MSE of 2.966. After this procedure, n and k data for the 128 nm spiro-TTB layer were retrieved.

Table 5.5: Fitting parameters for the generic oscillator approach for the analysis of a 128 nm spiro-TTB layer on a quartz substrate. Amplitude A, central peak energy E_0, broadening C and bandgap energy E_G are given.

Osc. nr.	***A*** **[-]**	E_0 **[eV]**	***C*** **[eV]**	E_G **[eV]**
1	25.6283	3.830	0.0876	3.557
2	17.5454	3.984	0.183	3.557
3	24.0062	4.190	0.300	3.557
4	10.6510	4.446	0.425	3.557
5	8.0950	5.362	0.573	3.557
6	9.8101	6.155	1.399	3.557

To verify the reliability of the optical model, the k data found with the b-spline model and generic oscillator model, are compared to values for the extinction coefficient calculated from the absorption coefficient (with equation (3.21)). Recall that α was determined with UV/Vis/NIR spectrophotometry (see Fig. A.15). The extinction coefficient as a function of wavelength for the different methods is given in the left of Fig. 5.10. n and k data directly retrieved from the software for both models is shown in Fig. A.21 in the appendix.

For the analysis of the 26 nm sample, the b-spline model created for the 128 nm layer can be applied directly or a new model following the same steps as before can be created. Choosing for the former, after fitting with the b-spline model, a thickness of 36.27 nm, a roughness of 0.75 nm and an MSE of 3.695 were obtained. After this procedure, n and k data for the 26 nm spiro-TTB layer were retrieved. The difference for the thickness between the model and QCM sensor is quite large (10 nm). More iterations are needed to figure out which of the two is correct. Again, the b-spline model was parameterized to Tauc-Lorentz oscillators. The results for the amplitude, central peak energy, broadening and bandgap energy are given in table 5.6. Subsequently, the layer was fitted with the new gen. osc. model resulting in a thickness of 34.40 nm, a roughness of 2.09 nm and an MSE of 4.591. After this procedure, n and k data for the 26 nm spiro-TTB layer were retrieved.

Table 5.6: Fitting parameters for the generic oscillator approach for the analysis of a 26 nm spiro-TTB layer on a quartz substrate. Amplitude A, central peak energy E_0, broadening C and bandgap energy E_G are given.

Osc. nr.	***A*** **[-]**	E_0 **[eV]**	***C*** **[eV]**	E_G **[eV]**
1	16.4617	3.829	0.0976	3.556
2	9.3931	3.988	0.187	3.556
3	15.5720	4.208	0.314	3.556
4	7.9462	4.475	0.424	3.556
5	5.6472	5.415	0.554	3.556
6	8.1290	6.232	1.296	3.556

Again, the results of the models were compared to measurements for the extinction coefficient determined with UV/Vis/NIR spectrophotometry (see right of Fig. 5.10). n and k data directly retrieved from the software for both models is shown in Fig. A.21 in the appendix.

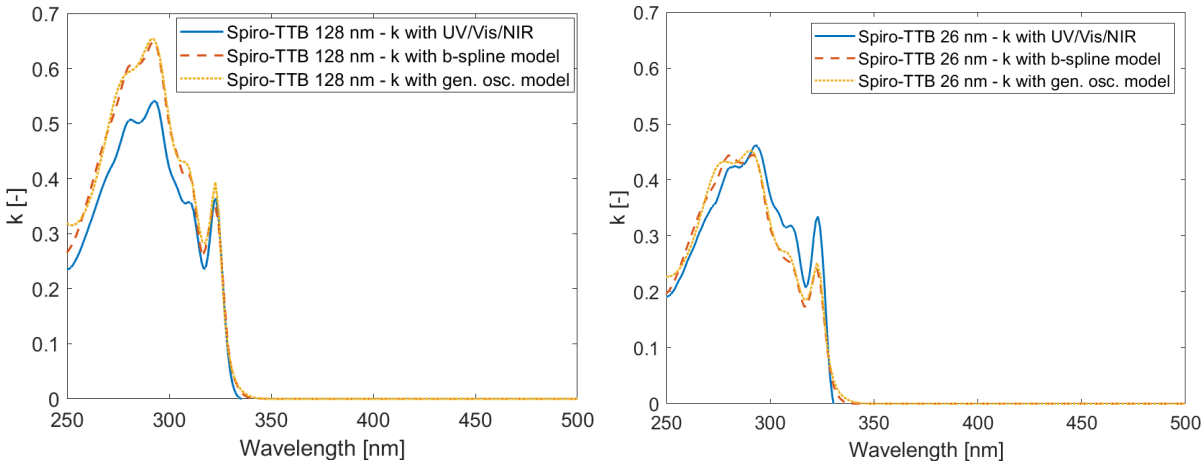

Figure 5.10: Extinction coefficient as a function of wavelength determined with UV/Vis/NIR spectrophotometry (blue), the b-spline model (red) and generic oscillator model (yellow). Left: 128 nm spiro-TTB on quartz. Right: 26 nm spiro-TTB on quartz.

For both thicknesses, the optical models give a similar shape for k compared to the one determined with spectrophotometry. In addition, the result for the thickness of the 128 nm layer was validated with profilometry. From these results, it can be concluded that the optical model works well. However, there are still some differences, such as the absolute value of k at certain wavelengths. It is hard to say whether the differences are caused by inaccuracies in the method to determine k from α with spectrophotometry or in the optical model made to fit spectroscopic ellipsometry data. To improve the model, more iterations are needed with thicknesses in between the ones studied in this section. In addition, the Tauc-Lorentz oscillators could be determined more accurately in order to refine the details of k. Furthermore, when we compare the k data of both thicknesses with each other, we find the extinction coefficient to be larger for the 128 nm thick layer. Next to a higher value for k, the 128 nm sample also exhibits larger values for n (see Fig. A.21). This observation could possibly be explained by the thicker layer being more dense than the thinner layer.

An attempt to make a similar ellipsometry model as the one described above was tried for BCP as well. Even though the model could quite accurately give the correct thickness, getting the correct n and k data was not achieved unfortunately.

5.2.5. Charge carrier dynamics of $MAPbI_3$-transport layer combinations

To gain more insight in the charge carrier dynamics of spin-coated $MAPbI_3$ in combination with a transport layer, several bi-layers were investigated with steady-state PL and TRMC. Recall that the fabricated bi-layers for a certain batch of $MAPbI_3$ were indicated in table 4.5. The bi-layers were completed by deposition of a transport layer on top of the PVK or by carrying out spin-coating on top of the transport layer. Steady-state PL spectra for bi-layers containing PVK fabricated in batch 1, 3, 4 and 5 are shown in Fig. 5.11. The PL signals of the neat PVK layers, which were studied in subsection 4.2.2, are depicted as well. For each batch, the PL spectra will be discussed separately.

The measurements were carried out with an excitation wavelength of 650 nm. From Fig. 5.6 and Fig. 5.8 we learn that at a wavelength of 650 nm, $F_A = 0$ for spiro-TTB, spiro-OMeTAD and MoO_x, and $F_A = 0.01$ for C60. Therefore, we can conclude that the results are not influenced by parasitic absorption of the transport layers. Note that the bi-layers are illuminated with the quartz substrate on the back, i.e. the light goes first through the PVK/TL before it reaches the quartz.

For batch 3, four different bi-layers were produced: PVK/Spiro-OMeTAD, PVK/C60 (20 nm) and PVK/MoO_x (5 and 15 nm). Note that the transport layers were deposited on top of the spin-coated $MAPbI_3$ film. The PL emission spectra can be seen in the top left of Fig. 5.11. When we compare the PL signal of the neat $MAPbI_3$ to the PL signal for the bi-layers, we observe a substantial decrease in intensity for the bi-layers. This drop in intensity is known as photoluminescence quenching. The observed quenching is quite strong and found to be highest for the bi-layer with 15 nm MoO_x and least strong for the bi-layer with spiro-OMeTAD. There are several explanations for the phenomenon of quenching. Firstly, it could indicate that charge carriers are being extracted effectively by the transport layer. Due to the extraction of either holes or electrons, direct radiative recombination is blocked, which leads to a decrease of the PL signal [129]. Secondly, quenching could be caused by the introduction of many defects at the PVK/TL interface, which leads to an enhancement of the non-radiative recombination [130]. Finally, it could be possible that during the deposition of the transport layer, the PVK film degraded causing a lower PL signal. In addition, degradation could also be caused by a reaction between the transport layer and the PVK film. Considering the samples with MoO_x, degradation of the PVK layer could possibly be the reason for quenching. To produce these bi-layers, PVK films had to be moved between buildings and were exposed to the ambient atmosphere during loading in and out of the evaporation chamber used for MoO_x. Note that it was tried to minimise exposure by transport in the metal tube, storage in small nitrogen boxes etc. In addition, it has been reported in literature that a chemical reaction can occur between PVK and MoO_x, which could lead to degradation, and enhanced recombination due to trap states at the interface [57]. For the C60 and spiro-OMeTAD bi-layers, the quenching is probably a result of both increased recombination at the interface and extraction of charge carriers.

For batch 4, four different bi-layers were produced: PVK/Spiro-OMeTAD, PVK/C60 (20 nm) and PVK/MoO_x (5 and 15 nm). Note that the transport layers were deposited on top of the spin-coated $MAPbI_3$ film. The PL emission spectra can be seen in the top right of Fig. 5.11. Again, quenching of the PL signal for the bi-layers is observed. The quenching is really strong for the bi-layers with the different MoO_x thicknesses, which is probably caused by degradation of the PVK layer and/or enhanced surface recombination. Quenching for

bi-layers with C60 and spiro-OMeTAD is much weaker. Same as for batch 3, the quenching of the C60 and spiro-OMeTAD bi-layers is probably a result of increased recombination at the interface and extraction of charge carriers.

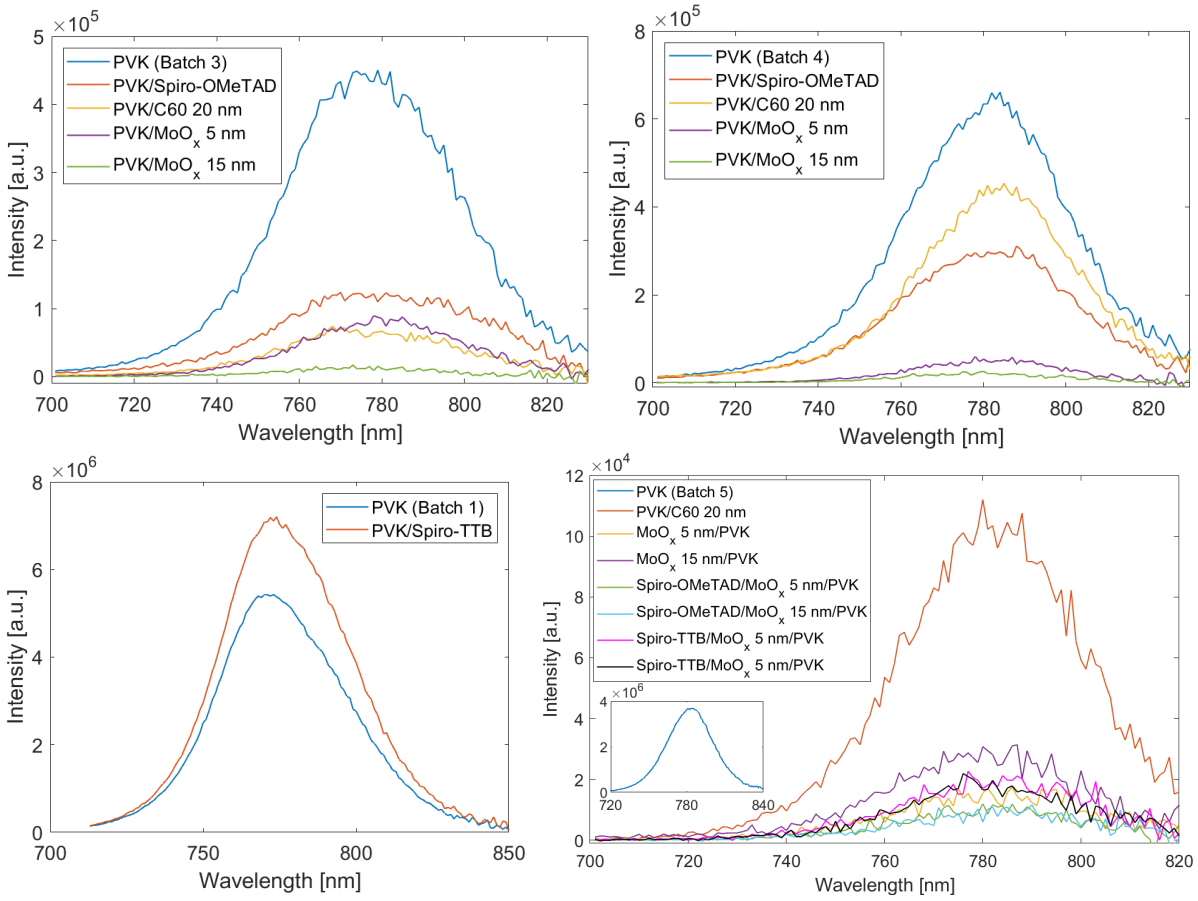

Figure 5.11: PL signal of batch 1, 3, 4 and 5 $MAPBI_3$ with bi-layers. Top left, batch 3: PVK (blue), PVK/Spiro-OMeTAD (red), PVK/C60 20 nm (yellow), PVK/MoO_x 5 nm (purple) and PVK/MoO_x 15 nm (green). Top right, batch 4: PVK (blue), PVK/Spiro-OMeTAD (red), PVK/C60 20 nm (yellow), PVK/MoO_x 5 nm (purple) and PVK/MoO_x 15 nm (green). Bottom left, batch 1: PVK (blue) and PVK/Spiro-TTB (red). Bottom right, batch 5: inset PVK (blue), PVK/C60 (red), MoO_x 5 nm/PVK (yellow), MoO_x 15 nm/PVK (purple), Spiro-OMeTAD/MoO_x 5 nm/PVK (green), Spiro-OMeTAD/MoO_x 15 nm/PVK (light blue), Spiro-TTB/MoO_x 5 nm/PVK (pink) and Spiro-TTB/MoO_x 15 nm/PVK (black).

For batch 1, one bi-layer was studied with steady-state PL: PVK/Spiro-TTB. Note that spiro-TTB was deposited on top of the spin-coated $MAPBI_3$ film. The PL emission spectra can be seen in the bottom left of Fig. 5.11. The intensity is higher for the bi-layer compared to the neat $MAPBI_3$ layer, therefore, no PL quenching is observed. This observation is in contrast with reports from literature, where a very effective quenching was observed for this type of bi-layer [47]. The increase in PL intensity could be explained by a variation in PVK quality in this batch. Since there is no quenching, we conclude that holes are probably not extracted and that spiro-TTB probably does not cause an increase in non-radiative recombination at the interface.

For batch 5, seven different bi- or tri-layers were produced: PVK/C60 (20 nm), MoO_x/PVK (5 and 15 nm MoO_x), Spiro-OMeTAD/MoO_x/PVK (5 and 15 nm MoO_x) and Spiro-TTB/MoO_x/PVK (5 and 15 nm MoO_x). For the bi-layer with C60, the transport layer is deposited on top of PVK. For all other fabricated bi- or tri-layers, the $MAPBI_3$ film is spin-coated on top of the transport layer(s). The PL emission spectra can be seen in the bottom right of Fig. 5.11. Note that the inset is the PL signal for the neat $MAPBI_3$ (much higher intensity). A very strong quenching of the PL signal for the bi- and tri-layers is observed. For the C60 bi-layer, the quenching is probably a result of both increased recombination at the interface and extraction of charge carriers. For the other layers, there could be an additional reason for the strong quenching of the PL signal, namely, a poor growth of the PVK crystal on top of the MoO_x layer. If the $MAPBI_3$ layer possesses a poor crystallinity and many defect states, the PL signal could be significantly reduced due to enhanced SRH re-

combination. In addition, degradation, increased recombination at the interface and possibly extraction of charge carriers could have an influence on the quenching as well.

TRMC measurements on bi-layers have been carried out to determine if the transport layers extract charge carriers from the $MAPbI_3$ film. Three different bi-layers were prepared: PVK/C60, Spiro-TTB/PVK and PVK/Spiro-TTB. The difference between the latter two is the order in which they are deposited on a quartz substrate. All bi-layers contain PVK deposited in batch 1 (see table 4.5). Recall that this batch had a good TRMC result and high PL intensity. Note that the bi-layers are excited from the front (quartz substrate at the back). For PVK/C60 and PVK/Spiro-TTB this implies that the majority of the charge carriers is excited close to the interface, for Spiro-TTB/PVK the majority of the charge carriers is excited further away from the interface. TRMC signals, after excitation with a laser pulse of 650 nm with different photon intensities, for the neat PVK layer and bi-layers are depicted in Fig. 5.12.

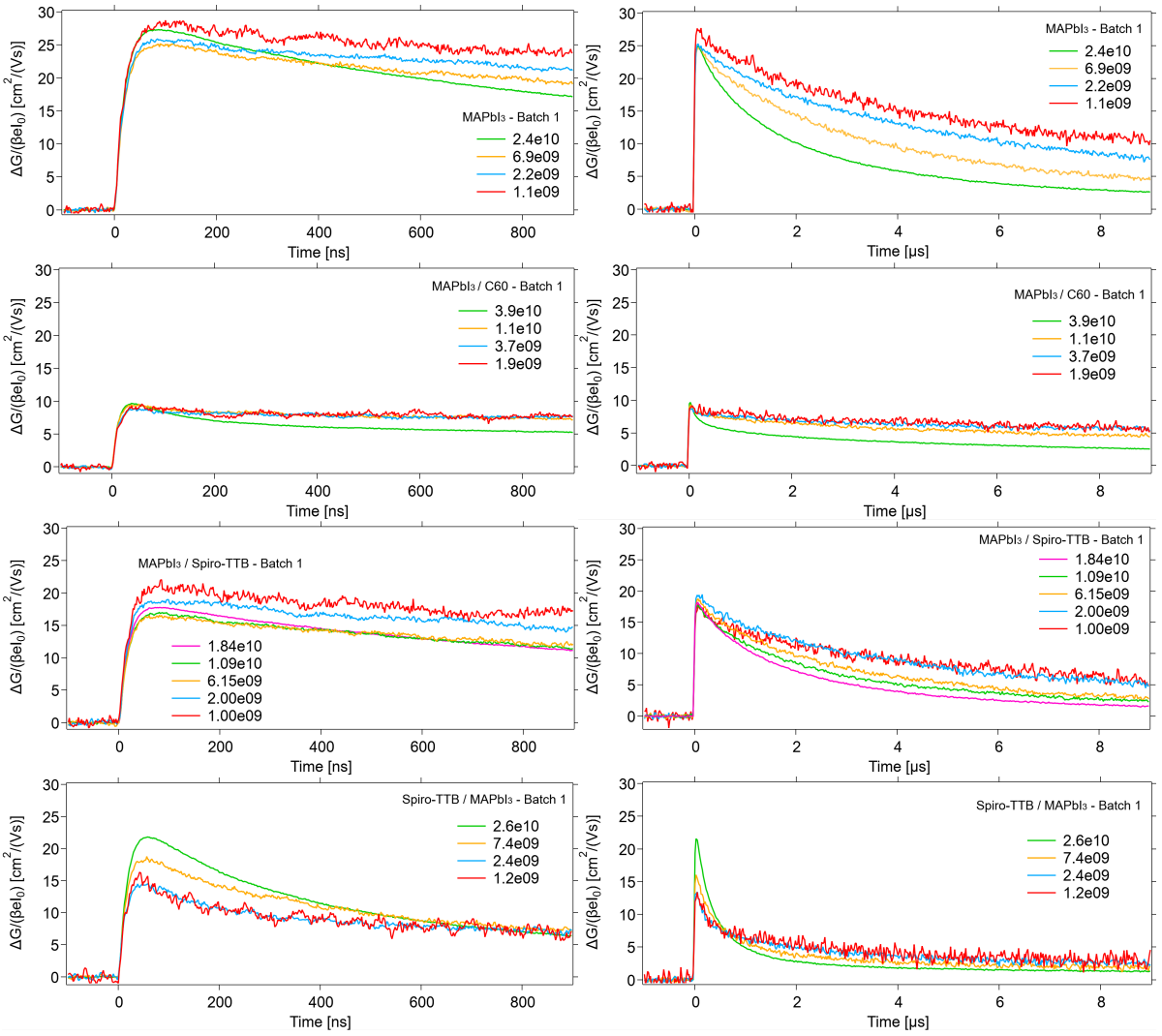

Figure 5.12: TRMC traces for a neat $MAPbI_3$ layer (first row), $MAPbI_3$/C60 (second row), $MAPbI_3$/Spiro-TTB (third row) and Spiro-TTB/$MAPbI_3$ (fourth row) bi-layer from batch 1 recorded at light intensities ranging from 10^9 to 10^{10} photons/cm^2. Excitation at 650 nm.

To determine if extraction of charge carriers by the TLs occurs, a comparison has to be made with the TRMC results for the neat $MAPbI_3$ layer. To make the comparison, two aspects are investigated: the height of the normalised photoconductance peak and the occurrence of a lifetime extension. If the TL does effectively extract either holes or electrons, the photoconductance peak should decrease substantially compared to the neat PVK layer, simply because either electrons and holes are extracted. Note that μ_n and μ_p are much lower

in the organic TLs than in the PVK film, and therefore, extracted holes or electrons do not have a big contribution [97].

Starting with the comparison of the neat $MAPbI_3$ to the bi-layer with C60, we observe that the intensity of the normalised photoconductance peak for the bi-layer is substantially lower than for the neat $MAPbI_3$ layer (≈ 10 $cm^2/(Vs)$ versus ≈ 27 $cm^2/(Vs)$). When looking at the traces, the lifetime of charge carriers is extended for the bi-layer in comparison to the neat layer. Both of these observations lead to the conclusion that C60 probably extracts electrons effectively.

When we compare the neat $MAPbI_3$ to the bi-layer with spiro-TTB on top of the PVK, we observe that the intensity of the normalised photoconductance peak for the bi-layer is lower than for the neat $MAPbI_3$ (≈ 18 $cm^2/(Vs)$ versus ≈ 27 $cm^2/(Vs)$). This result could mean that holes are extracted. However, when looking at the traces, the lifetime is approximately the same for both samples. Based on only these results it is difficult to say whether holes are extracted or not. The lower normalised photoconductance peak could be caused by a variation in this batch or degradation of the PVK layer during deposition of spiro-TTB.

Finally, since we use the HTL below the PVK layer in a device, a bi-layer with spiro-TTB on the bottom was prepared. During the spin-coating of the $MAPbI_3$ layer, difficulties were encountered with the wettability of the spiro-TTB layer. Eventually, a solution was found, however, later it turned out that this led to part of the spiro-TTB layer being washed off. More about this can be found in subsection 6.2.1. When we look at the TRMC result, the intensity of the normalised photoconductance peak is around 22 $cm^2/(Vs)$ for this bi-layer. In addition, the lifetime decreased substantially compared to the neat $MAPbI_3$ layer. From these observations, we conclude that the HTL did not extract any holes and the recombination rate is higher. The higher recombination rate is possibly caused by enhanced non-radiative recombination by interface trap states or trap states in the bulk, possibly introduced by the spin-coating procedure.

6

Device Development and Testing

6.1. Devices with a thermally evaporated perovskite layer

Perovskite solar cells were fabricated following the flowchart shown in Ch.3 subsection 3.1.3. Six devices with a thermally evaporated perovskite layer were prepared in total. The configurations of these devices are given in table 6.1. The numbers in the table will be used to refer to a certain configuration. Note that for configuration 3 and 4, a version with and without annealing (after deposition of the PVK layer) was fabricated. Recall that each device contains four cells: two cells with an active area of 0.16 cm^2 and two cells with an active area of 0.36 cm^2 (see subsection 3.1.2, Fig. 3.2).

Table 6.1: Configuration of fully thermally evaporated devices. Front electrode, HTL(s), PVK absorber layer, ETL, back electrode and annealing are indicated.

Nr.	Front electr.	HTL 1	HTL 2	PVK	ETL	Back electr.	Annealing
1	ITO (200 nm)	MoO_x (10 nm)	Spiro-TTB (10 nm)	$FA_xCs_{1-x}Pb(I_yBr_{1-y})_3$	C60 (20 nm)	Al (150 nm)	w/o
2	ITO (200 nm)	MoO_x (10 nm)	-	$FA_xCs_{1-x}Pb(I_yBr_{1-y})_3$	C60 (20 nm)	Al (150 nm)	w/o
3	ITO (200 nm)	MoO_x (10 nm)	Spiro-TTB (20 nm)	$FA_xCs_{1-x}Pb(I_yBr_{1-y})_3$	C60 (20 nm)	Ag (300 nm)	w/ and w/o
4	ITO (200 nm)	-	Spiro-TTB (20 nm)	$FA_xCs_{1-x}Pb(I_yBr_{1-y})_3$	C60 (20 nm)	Ag (300 nm)	w/ and w/o

Since each layer in a perovskite solar cell has its own function, it does not come as a surprise that if one individual layer does not perform properly, it has a detrimental effect on the entire cell. Considering the layers in our fully thermally evaporated PSCs, the PVK absorber layer turned out to be of inferior quality. Perovskite for the thermally evaporated devices, was fabricated on two occasions described below.

The PVK layers for configuration 1 and 2 of table 6.1, were deposited during the same deposition, which allows for direct comparison. The deposition parameters were based on the results of the experiment that was carried out with the varying FAI content (see subsection 4.1.2). Therefore, the nominal thicknesses required as input for the controller have the same ratio, among the different precursors, as the deposition from the experiment with assumed FAI TF = 0.4. The nominal thicknesses for the different precursors, were adapted to get a single-layer target thickness of 100 nm (instead of 60 nm as used in the FAI experiment). The single-layer was repeated four times making this a multi-layer deposition with $N = 4$. In hindsight, we know that this ratio was far from optimal, because the real TF for FAI turned out to be 0.822. The XRD result for this deposition can be seen in Fig. 6.1. The (001), (002) and (003) reflection of PVK and three peaks related to PbI_2 were found [44],[107]. The intensity of the first PbI_2 peak, is much higher and narrower compared to the intensity of the (001) reflection of PVK. This result indicates that PbI_2 has a good crystallinity and large crystal size in the sample. We conclude that large domains of unreacted PbI_2 are present. In hindsight, annealing could have had an impact on the reaction to form PVK.

The PVK layers for configuration 3 and 4 of table 6.1, were deposited during the same deposition. At that time, we thought to have optimised the thickness ratio between the different precursors. Eventually, this deposition turned out to be the first deposition in which we could not obtain perovskite anymore (see subsection 4.1.3). The PVK layer, which was a multi-layer deposition with target thickness 400 nm, looked light coloured and

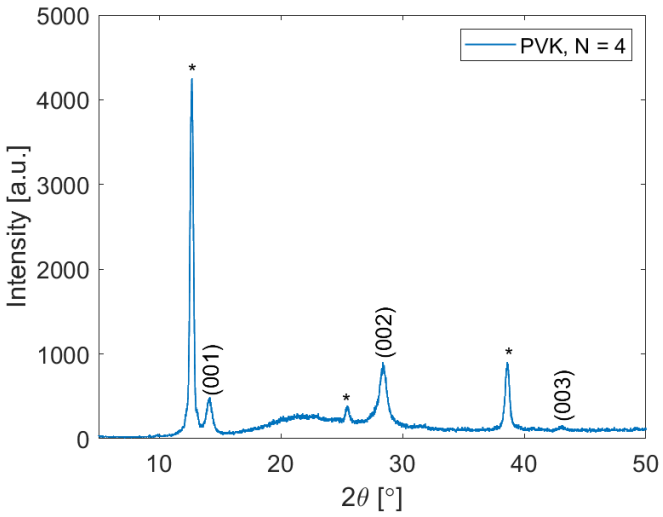

Figure 6.1: Diffractogram for the multi-layer PVK deposition that ended up in device configuration 1 and 2 (see table 6.1). $N = 4$ and the total target thickness is 400 nm. PVK reflections indicated with Miller indices and PbI_2 reflections indicated with a * symbol.

transparent by eye, as can be seen in Fig. 6.2a,b. In an attempt to improve the PVK layer, annealing at 100°C for 10 min was carried out on two devices. At that time, it was not yet known that there was a problem with our thermal evaporation process. Therefore, the devices were completed and tested according to plan.

In addition, it has to be addressed that during the thermal evaporation of the back electrodes, rather high deposition rates were used. For the devices with the aluminium back electrode, the rate was in the range of 1.5 to 6 Å/s, and for devices with the silver back electrode, the rate was in the range of 1 to 5 Å/s. Images of the devices after deposition of the back electrode are depicted in Fig. 6.2c,d. For the devices with a silver back electrode (see Fig. 6.2c), silver on top of the active area was observed to have an unexpected hazy white colour. This observation will be examined in subsection 6.1.1.

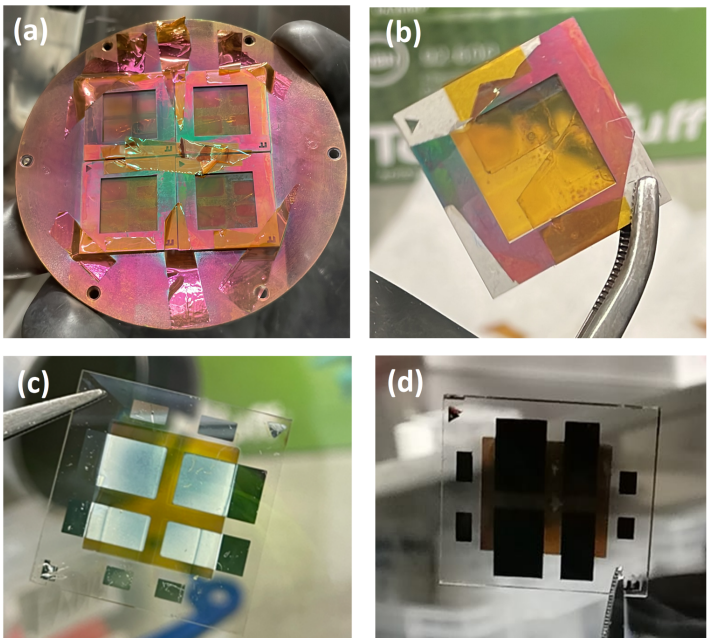

Figure 6.2: (a) Substrate holder with devices of configuration 3 and 4 after deposition of the PVK absorber layer (table 6.1). (b) Device showing the light colour and transparency of the PVK layer. (c) Device with silver back electrode (configuration 3). (d) Device with aluminium back electrode (configuration 1).

After completion of the devices, the solar simulator was used to carry out light and dark J-V curve measurements. The results for four cells each belonging to one of the configurations of table 6.1 are shown in Fig. 6.3. It can be clearly observed that none of these cells show the J-V curve of a working solar cell under illumination (would be expected in the first quadrant). In addition, diode behaviour is not observed for measurements in the dark. Instead, based on the linear relation seen between J and V and the graphs going through the origin, the cells seem to act like resistors. Considering that most of the devices share similar J-V characteristics, only a small selection of the different cells are shown in Fig. 6.3.

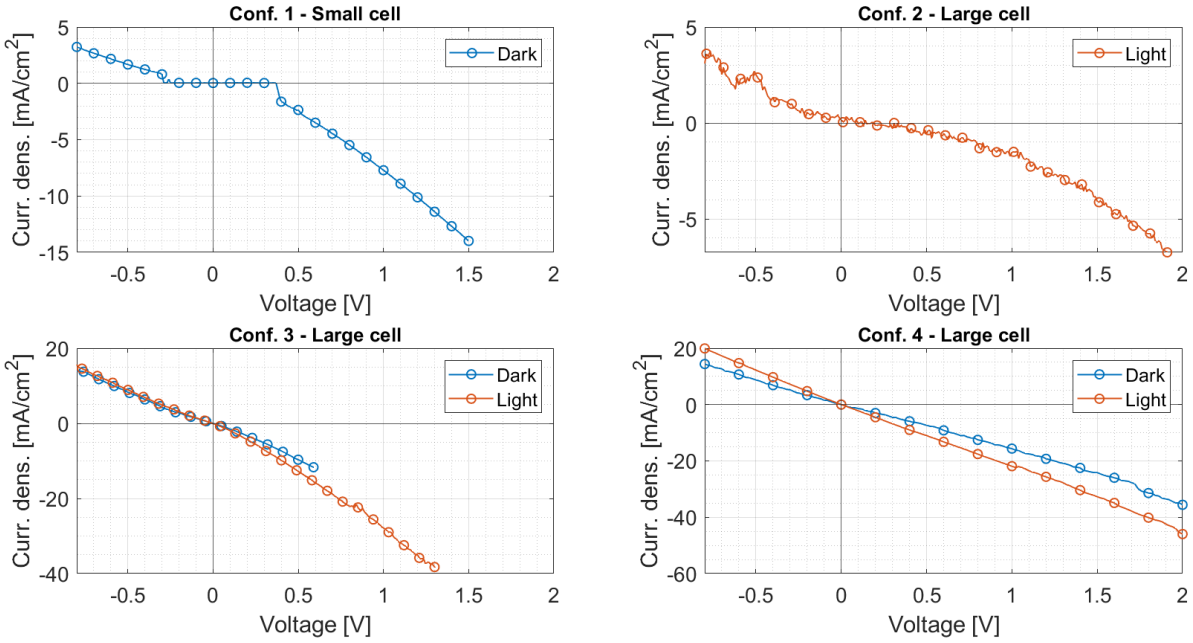

Figure 6.3: Dark J-V curves (blue) and light J-V curves (red) for four cells of the fully thermally evaporated devices (see table 6.1). Top left: configuration 1, small cell. Top right: configuration 2, large cell. Bottom left: configuration 3, large cell. Bottom right: configuration 4, large cell. Note that y-axes show different values.

Based on observations made during the fabrication process, two probable reasons underlying the failure of the cells can be given. Firstly, the poor quality of the PVK absorber layer. It may be clear that if the absorber layer does not even contain crystalline PVK or does not possess the required qualities, the functionality of all other device layers is redundant. Secondly, with the possible presence of pinholes in the PVK absorber layer, the metal (Ag or Al), might penetrate into the open film leading to an electrical short in the cell. In general, pinholes in any layer of the device could result in an increase of the shunt resistance by creating alternative current paths. As mentioned earlier, rather high deposition rates were used for the back electrodes, which could have led to an enhanced interdiffusion of Ag and Al atoms into the layers of the device [122]. The combination of the high deposition rate and the possible presence of pinholes in the PVK layer, could have resulted in a direct electrical connection between the ITO layer and back electrode. This argument could explain the resistive behaviour observed for the cells.

Many more reasons can be proposed to explain the non-ideal J-V characteristics measured. An example is limited or no extraction by a TL. However, based on the results and observations made during the fabrication, it is not possible to be conclusive about this. It should be mentioned that at this point in time our experimental skills for testing PSCs with the solar simulator were rather inadequate. Problems with connection of the probes on the relatively thin layers and poking through the entire cell, when measuring on top of the active area, were some of the issues encountered.

6.1.1. Investigation of possible silver electrode corrosion

As mentioned in the previous section and seen in Fig. 6.2c, samples with silver deposited on the devices' active area showed an unusual appearance. Where a shiny reflective layer as seen during the development of the deposition recipe was expected, we observed a hazy white colour on top of the active area. The difference

is best illustrated by the image depicted in Fig. 6.4a, where the shiny Ag layer is seen on the edges and the white Ag layer on top of the active area.

From literature we learned that the colour change of the silver electrode could be related to a chemical reaction of silver with the halides present at the X-sites of PVK [122],[131]. Degradation of silver into silver iodide (AgI) was found to be significantly faster than the formation of silver bromide (AgBr). The mechanism proposed by researchers, involved migration of iodine containing compounds from the PVK layer, through pinholes in the transport layer, to the silver layer [131]. In the cited research, the formation of AgI was observed after several weeks and was accelerated when devices were kept in ambient conditions due to an increase in the creation of volatile iodine compounds [131].

It was reasoned that the white colour observed for our devices could be related to the formation of AgI, even when we take into account that it was directly observable after the deposition. This reasoning was based on the fact that the absorber layer did probably not contain a stable crystalline perovskite phase but rather a mixture of unreacted precursors containing iodide. In addition, since a high deposition rate (1 to 5 Å/s) was used, and the C60 layer is only 20 nm thick, it was reasoned that silver could have gone through the C60 layer being in direct contact with the absorber layer. To investigate this possibility, a small experiment involving XRD measurements was designed. Six samples were prepared. The first set of samples consisted of three previously deposited PVK samples with either 0, 20 or 40 nm C60, and 300 nm Ag deposited on top. A second set of samples consisted of 0, 20 and 40 nm C60 directly on quartz with 300 nm Ag on top. Images of these samples are depicted in Fig. 6.4b,c. Optically, the silver deposited on C60 coated quartz appears as a shiny reflective layer, as can be seen in Fig. 6.4c. From this observation it can be concluded that the white appearance of the silver is not caused by the C60 layer. For the silver deposited on PVK with 0, 20 and 40 nm C60 in between, the silver appearing as a white layer is most strongly observed for the film without C60 and to a lesser extent for the other two samples (see Fig. 6.4b).

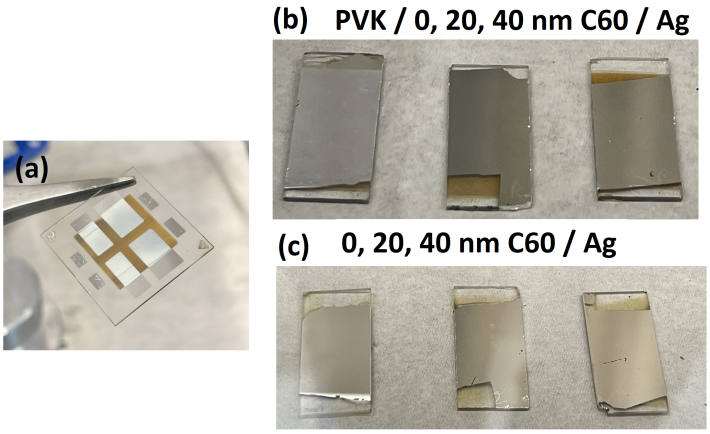

Figure 6.4: (a) PSC device with Ag back electrode. The overlap of Ag with the device area has a white appearance. (b) 1: PVK/Ag, 2: PVK/20 nm C60/Ag, 3: PVK/40 nm C60/Ag. Silver gets more reflective with increasing C60 thickness. (c) 1: Ag, 2: 20 nm C60/Ag, 3: 40 nm C60/Ag. Silver is reflective for all samples.

Fig. 6.5 depicts the diffractograms of the PVK/0, 20 and 40 nm C60/Ag layers, neat PVK before C60 and Ag, and Ag only. These measurements were taken two days after deposition, with the goal to check the presence of AgI. Note that AgI is a crystalline material with expected diffraction peaks at 2θ = 22.3°, 23.8° and 25.3° (hence the inset in the Fig. 6.5) [131]. However, no peaks belonging to AgI were found. Furthermore, for all samples containing silver, two peaks related to Ag can be observed (2θ = 38.1° and 44.3°) [131]. In addition, for all samples containing PVK, the (001), (002) and (003) reflection of α phase PVK can be identified [46]. For the PVK/0 nm C60/Ag sample, two other peaks with 2θ = 11.7° and 29.6° were found. Unfortunately, the origin of these peaks could not be retrieved.

XRD measurements on the PVK/Ag sample were repeated after storage in a glove box for two months. This time, the diffractogram was measured between 20° and 26° (range where we expect to see AgI formation) with 1 s/step (in other measurements we used 0.1 s/step). The result can be seen in Fig. 6.6 where the 2θ angles of AgI reflections are indicated as well [131]. Note that the background signal is caused by the quartz substrate. A few small peaks can be observed at 2θ = 21.9°, 22.8°, 23.7° and 24.5°. The first two of these peaks

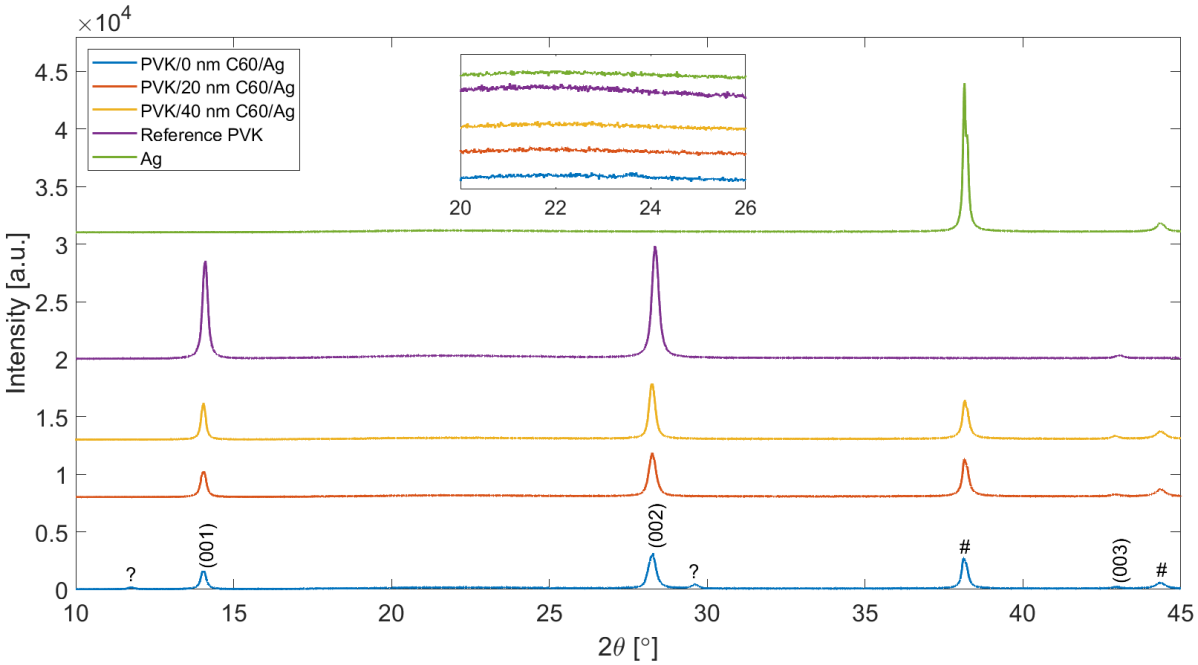

Figure 6.5: Diffractogram of PVK/Ag (blue), PVK/20 nm C60/Ag (red), PVK/40 nm C60/Ag (yellow), reference PVK (purple, before C60 and C60) and Ag (green). Inset is a zoomed version from 20° to 26° where AgI peaks are expected. PVK reflections indicated with Miller indices and Ag reflections indicated with a # symbol and unspecified reflections indicated with a ? symbol.

are most likely related to δ phase $CsPbI_3$ [132],[133]. The peak around 24.5° is most likely related to the (111) reflection of α phase $FA_xCs_{1-x}Pb(I_yBr_{1-y})_3$ or to the δ phase of $FAPbI_3$ [134]. An explanation for the peak at 2θ = 23.7° could not be found and turns out to be quite close to the peak location of the (002) reflection of AgI. Therefore, this peak could possibly indicate the presence of AgI in our sample.

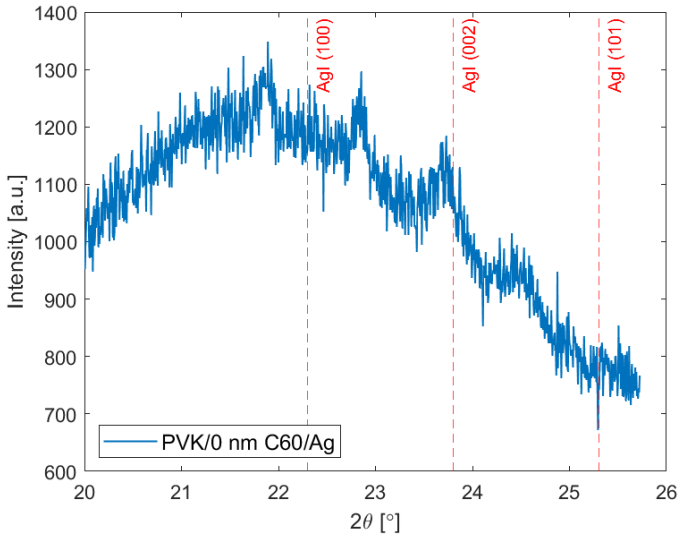

Figure 6.6: Diffractogram of PVK/Ag (blue) with 1 s/step (total measurement time 1512 s). As a reference, location of AgI reflections are shown (22.3°, 23.8° and 25.3°) in red [131].

To complete this section, it should be mentioned that later on during the fabrication of devices with a spin-coated $MAPbI_3$ layer, the same phenomenon was observed. Unlike the thermally evaporated devices, a lower rate for the silver deposition was used and a BCP buffer layer was present in these devices. In conclusion, we think it is more likely that the silver appearing white has a different cause than a chemical reaction with the halides. It could for example be attributed to the surface roughness of the underlying PVK layer. Note that the

surface roughness of our PVK films is not known, but from literature it can be learned that perovskite layers have a surface roughness on a scale of tens of nm [135].

6.2. Devices with a spin-coated perovskite layer

The fabrication of devices with a spin-coated $MAPbI_3$ absorber layer has been a learning process. For this reason, the fabricated devices will be discussed in chronological order in the following subsections.

6.2.1. Spin-coating issues with spiro-TTB as underlying layer

Due to difficulties encountered with the thermal evaporation process for PVK, devices with a spin-coated PVK absorber layer were fabricated. After some practice and characterisation of the first batch of $MAPbI_3$, four devices with three different configurations were produced (see table 6.2). The numbers in the table will be used to refer to a certain configuration. Configuration 3 was fabricated twice. Note that the spin-coated $MAPbI_3$ layers in these devices, correspond to 'batch 2' in table 4.5 of section 4.2. The normal precursor solution concentration was used (0.65 mol/L), which should result in an absorber layer thickness around 300 nm. Moreover, ITO layers with different thicknesses (200 and 300 nm) and both silver and aluminium were used to fabricate these devices. This time, silver and aluminium were deposited with a rate of 0.1 to 1.5 Å/s.

Table 6.2: Configuration of devices with a spin-coated PVK absorber layer. Front electrode, HTL, PVK absorber layer, ETL and back electrode are indicated.

Nr.	**Front electr.**	**HTL**	**PVK**	**ETL**	**Back electr.**
1	ITO (300 nm)	Spiro-TTB (20 nm)	$MAPbI_3$	C60 (20 nm)	Ag (250 nm)
2	ITO (300 nm)	Spiro-TTB (20 nm)	$MAPbI_3$	C60 (20 nm)	Al (225 nm)
3	ITO (200 nm)	Spiro-TTB (20 nm)	$MAPbI_3$	C60 (20 nm)	Al (225 nm)

In practice, it turned out to be challenging to carry out spin-coating on top of the thermally evaporated spiro-TTB layer. It was found that the spiro-TTB had a poor hydrophilicity, which made it difficult to spread the PVK precursor solution on the surface. During the actual rotation, all precursor solution was swept away and the surface remained uncoated. From literature, it was learned that a spiro-TTB layer has a water contact angle of 85°, which makes the surface hydrophilic [47]. On the other hand, for example spiro-OMeTAD, has a water contact angle of only 27° [47]. The relatively high water contact angle of spiro-TTB does explain the difficulties we encountered with the precursor solution being swept away. Note that with a water contact angle above 90°, a surface is classified as hydrophobic, and under 90° classified as hydrophilic.

A possible solution was found in another research on PSCs where a similar problem was encountered (spin-coating on top of a hydrophobic PTAA layer) [136]. They dealt with the issue by firstly wetting the surface with the solvent DMF. In our case, 150 μl DMF was spin-coated on top of the spiro-TTB at a low rotation speed of 500 rpm for 30 s. After this, the deposition of the PVK layer worked according to our normal spin-coating procedure resulting in the film shown in Fig. 6.7.

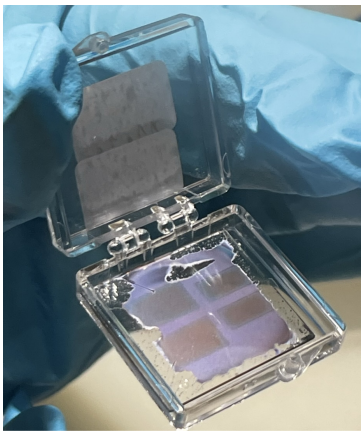

Figure 6.7: Image of a device right after spin-coating and annealing of the $MAPbI_3$ layer. DMF was spread on top of the spiro-TTB layer prior to $MAPbI_3$ spin-coating.

After completion and testing of the devices depicted in table 6.2, it was found in comparable research that spiro-based molecules, such as spiro-TTB and spiro-OMeTAD, readily dissolve in DMF [47]. Therefore, dissolution of spiro-based molecules in DMF, may lead to the spiro-based HTL being washed off during the spin-coating of perovskite [47]. DMF is the most commonly used solvent in PVK precursor solutions and was used in our recipe as well. In addition, we even spread more DMF on the spiro-TTB layer prior to spin-coating of the $MAPbI_3$ layer. Therefore, it is very probable that part or maybe all of the underlying spiro-TTB layer was washed off in our devices. Solutions for this problem suggested by the cited literature were thermal evaporation of the PVK layer or using orthogonal solvents for the PVK precursor solution (GBL and DMSO were used) [47].

Before we learned that at least part of the spiro-TTB layer was washed off, the devices were completed as intended and the solar simulator was used to carry out light and dark J-V curve measurements. The results for four cells each belonging to one of the configurations of table 6.2, are shown in Fig. 6.8. Whether it was a small cell (0.16 cm^2) or large cell (0.36 cm^2) is indicated. It can be clearly observed that none of these cells show the J-V curve of a working solar cell, both under illumination and in the dark. Again, the linear relation between J and V indicates that the cells seem to act like resistors. Considering that most of the devices share similar J-V characteristics, only a small selection of the different cells are shown in Fig. 6.8.

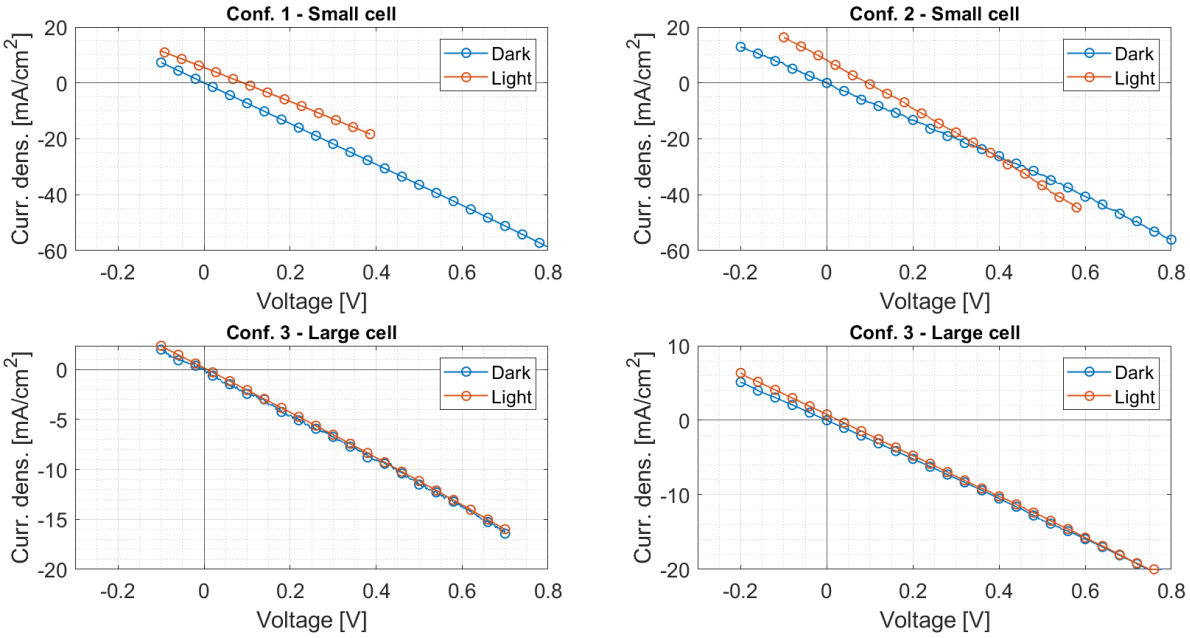

Figure 6.8: Dark J-V curves (blue) and light J-V curves (red) for four cells of the first spin-coated devices (see table 6.2). Top left: configuration 1, small cell. Top right: configuration 2, small cell. Bottom left: configuration 3, large cell. Bottom right: configuration 3, large cell. Note that y-axes show different values.

The fact that the spiro-TTB is completely or partly washed off, implies that there is practically no extraction of light generated holes possible. In addition, from the TRMC results of the spiro-TTB/PVK bi-layer (subsection 5.2.5, Fig. 5.12) we learned that there is probably no extraction of holes, but rather an enhanced recombination at interface trap states.

A difference can be seen when comparing the light to the dark measurement for configuration 1 and 2. The light J-V curve passes through the first quadrant, whereas the dark J-V curve goes through the origin. This observation indicates that a small light response occurred under illumination, however, with a high series resistance and a low shunt resistance. Even though we used a lower deposition rate for the back electrodes, it could still be possible that there are current pathways from the back electrode to the front leading to shorting of the cell. We should mention that there may be other unidentified causes for the observed behaviour.

Based on the fabrication and results of the spin-coated devices of table 6.2, we set a few goals for the fabrication of the next batch. These goals are:

- Increase the thickness of the PVK absorber layer. Hence, spin-coating with a higher concentrated pre-

cursor solution.

- Introduce a buffer layer between C60 and Ag. For this reason, a recipe for BCP was developed (subsection 5.2.1).
- Find a suitable interface/seed layer underneath the $MAPbI_3$ layer to prevent washing away of the HTL, and to enable us to carry out the spin-coating procedure.

6.2.2. Looking for a suitable interface for spin-coating of $MAPbI_3$

In order to find a solution for the problem where the solvent of the PVK precursor solution washes away the spiro-TTB layer, we decided to look for a suitable interface (or seed layer) that could function as an underlying layer for $MAPbI_3$. This solution was preferred over looking for an orthogonal solvent and with that adjustment of our spin-coating procedure.

Eventually, it was found that MoO_x could function as an underlying layer, and a dark brown PVK layer could be obtained by carrying out our usual spin-coating procedure. In addition, since we wanted to increase the thickness of the PVK layer in our devices, the higher concentrated precursor solution was used (0.77 mol/L). The higher concentration should result in a thickness around 500 nm (see table 4.7). Note that the spin-coating of $MAPbI_3$ for these devices, corresponds to 'batch 4' in table 4.5 of section 4.2. In between C60 and the silver back electrode, 4 nm BCP was deposited to function as a buffer layer. Note that these were the first devices containing a BCP layer. Two devices with the same configuration were fabricated, as can be seen in table 6.3.

Table 6.3: Configuration of devices with a spin-coated PVK absorber layer. Front electrode, HTL, PVK absorber layer, ETL, BL and back electrode are indicated.

Nr.	**Front electr.**	**HTL**	**PVK**	**ETL**	**BL**	**Back electr.**
1	ITO (200 nm)	MoO_x (10 nm)	$MAPbI_3$	C60 (20 nm)	BCP (4 nm)	Ag (150 nm)

Fig. 6.9 depicts dark and light J-V curves, measured on each of the four cells of a device with a configuration, as shown in table 6.3. Note that each cell has been given a name. Small cell 1 and large cell 1 show resistive behaviour both under illumination and in the dark. These results show a similar trend as the J-V curves shown

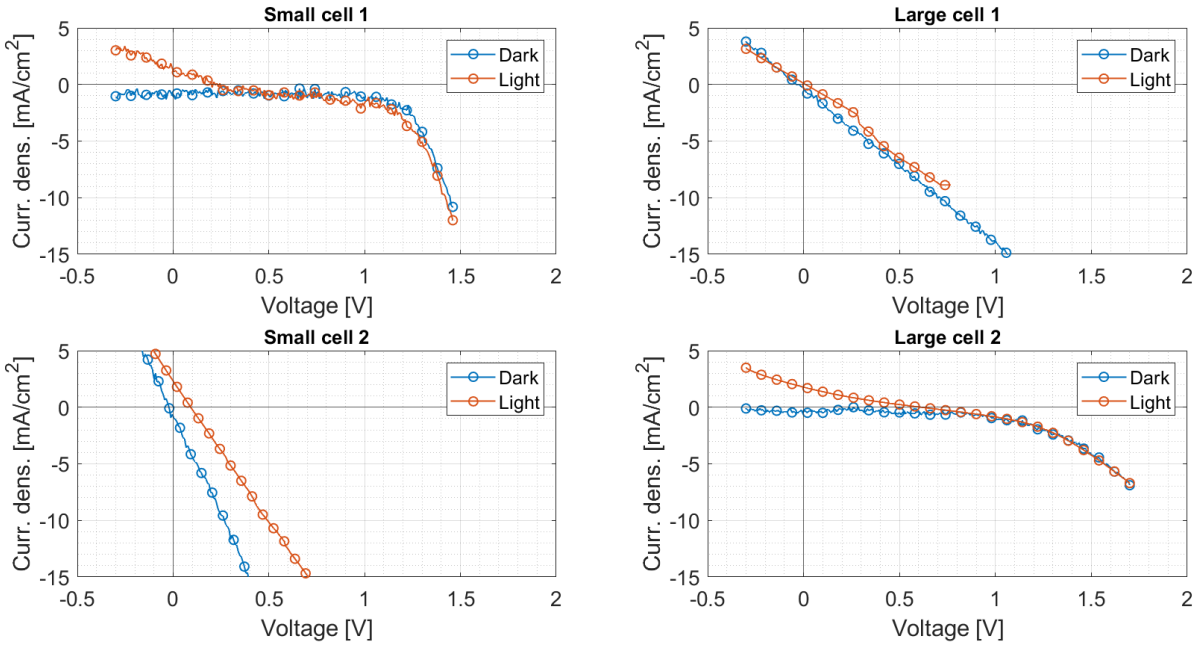

Figure 6.9: Dark J-V curves (blue) and light J-V curves (red) for the four cells on the device with configuration: ITO (200 nm)/MoO_x (10 nm)/$MAPbI_3$/C60 (20 nm)/BCP (4 nm)/Ag (150 nm). Two cells with active area 0.16 cm^2 (left) and two cells with active area 0.36 cm^2 (right).

in Fig. 6.8. For the other two cells (small cell 1 and large cell 2) some interesting observations can be done. Firstly, the dark J-V curves show diode behaviour typical of a solar cell in the dark. The exponential decrease in current seems to be stronger for small cell 1 compared to large cell 2. This result could indicate that R_s is relatively high for large cell 2 compared to small cell 1. Secondly, small cell 1 and large cell 2 exhibit a clear S-shaped characteristic under illumination. An S-shaped J-V curve is indicative of a charge transport problem [50]. When we attribute values to important solar cell parameters, we find for small cell 1 and large cell 2, a J_{sc} of 1.1 and 1.8 mA/cm^2, and a V_{oc} of 0.16, and 0.61 V respectively. Several possible explanations of the occurrence of the S-shaped J-V curve under illumination will be given at the end of this chapter.

The spin-coated $MAPbI_3$ layer used in the devices presented in this subsection corresponds to 'batch 4' in table 4.5 of section 4.2. We recall here that for this specific batch of $MAPbI_3$, many characterisation measurements were carried out (see section 4.2). It was found that properties such as thickness, crystallinity and absorption were all as desired. However, based on the PL and TRMC signal, we concluded that in this $MAPbI_3$ film the non-radiative recombination of electrons and holes is very high (see subsection 4.2.2). Therefore, this batch does probably not possess good electronic properties. For this reason, we decided to fabricate one more set of PSCs with hopefully a better PVK absorber layer. Moreover, until this point we tried to use thermal evaporation as much as possible for the fabrication of different device layers. However, it was argued that a good result could possibly be obtained if we used a spin-coated layer of spiro-OMeTAD at the hole transport side.

6.2.3. Diode behaviour and S-shaped J-V curves

Based on the results of the devices with a 10 nm MoO_x layer between the ITO and the PVK absorber layer, it was decided to consider some more possibly interesting device architectures. Table 6.4 gives an overview on the different configurations. The numbers in the table will be used to refer to a certain configuration. This set of devices are the final ones fabricated and studied.

Configuration 1 and 2 were fabricated to investigate the effect of different MoO_x thicknesses. Configuration 3 was fabricated to repeat the first set of spin-coated devices, but this time with a BCP layer and more experience measuring with the solar simulator setup. Configurations 4 and 5 were fabricated to investigate the function of spiro-TTB underneath the MoO_x layer, and therefore it not being washed off. Configurations 6-8 incorporate, spin-coating of the hole transport material spiro-OMeTAD, which was not used before in a device. Again we are varying the thickness of the MoO_x layer (table 6.4). Images of the fabricated devices can be seen in Fig. 6.10.

Note that the spin-coating of $MAPbI_3$ for these devices corresponds to 'batch 5' in table 4.5 of section 4.2. The higher concentrated precursor solution was used.

Table 6.4: Configuration of devices with a spin-coated PVK absorber layer. Front electrode, HTL, PVK absorber layer, ETL, BL and back electrode are indicated.

Nr.	**Front electr.**	**HTL 1 (spiro)**	**HTL 2 (MoO_x)**	**PVK**	**ETL**	**BL**	**Back electr.**
1	ITO (200 nm) w/ sub. heat.	-	MoO_x (5 nm)	$MAPbI_3$	C60 (20 nm)	BCP (4 nm)	Ag (150 nm)
2	ITO (200 nm) w/ sub. heat.	-	MoO_x (15 nm)	$MAPbI_3$	C60 (20 nm)	BCP (4 nm)	Ag (150 nm)
3	ITO (200 nm)	Spiro-TTB (20 nm)	-	$MAPbI_3$	C60 (20 nm)	BCP (4 nm)	Ag (150 nm)
4	ITO (300 nm)	Spiro-TTB (20 nm)	MoO_x (5 nm)	$MAPbI_3$	C60 (20 nm)	BCP (4 nm)	Ag (150 nm)
5	ITO (300 nm)	Spiro-TTB (20 nm)	MoO_x (15 nm)	$MAPbI_3$	C60 (20 nm)	BCP (4 nm)	Ag (150 nm)
6	ITO (200 nm)	Spiro-OMeTAD	-	$MAPbI_3$	C60 (20 nm)	BCP (4 nm)	Ag (150 nm)
7	ITO (200 nm)	Spiro-OMeTAD	MoO_x (5 nm)	$MAPbI_3$	C60 (20 nm)	BCP (4 nm)	Ag (150 nm)
8	ITO (200 nm)	Spiro-OMeTAD	MoO_x (15 nm)	$MAPbI_3$	C60 (20 nm)	BCP (4 nm)	Ag (150 nm)

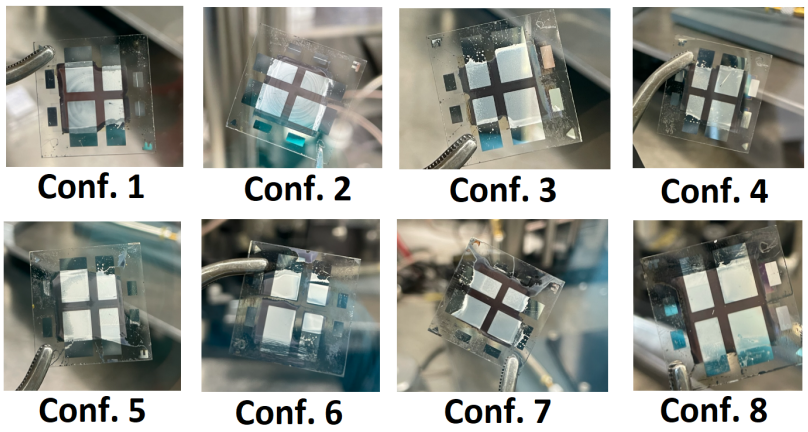

Figure 6.10: Images of the final eight devices with a spin-coated PVK layer. Configuration numbers are indicated (see table 6.4).

Dark and light J-V curves for each of the eight configurations of table 6.4 will be presented in the following paragraphs. For each device, measurements on all four cells are given, consisting of two cells with an active area of 0.16 cm^2 and two cells with an active area of 0.36 cm^2. Relevant observations and parameters will be discussed briefly. Afterwards, a comparison is made and possible explanations for the observed behaviour are given in subsection 6.2.4.

1. ITO w/ sub. heat. (200 nm)/MoO_x (5 nm)/$MAPbI_3$/C60 (20 nm)/BCP (4 nm)/Ag (150 nm)

Dark and light J-V curves measured on four cells of the device with 5 nm MoO_x on the hole transport side are shown in Fig. 6.11. Note that each cell has been given a name. Small cell 1, small cell 2 and large cell 2 exhibit an S-shaped characteristic under illumination with a J_{sc} of 4.6, 4.4 and 3.6 mA/cm^2, and a V_{oc} of 0.58, 0.21 and 0.42 V respectively. The dark J-V curves for the same cells, show diode behaviour typical of a solar cell in the dark. However, these dark curves do not show strong exponential behaviour. This observation is in line with the S-shaped curve under illumination and indicates that R_s is relatively high. Large cell 1 shows resistive behaviour both under illumination and in the dark. In general, all cells are characterised by a relatively high R_s and relatively low R_{sh}.

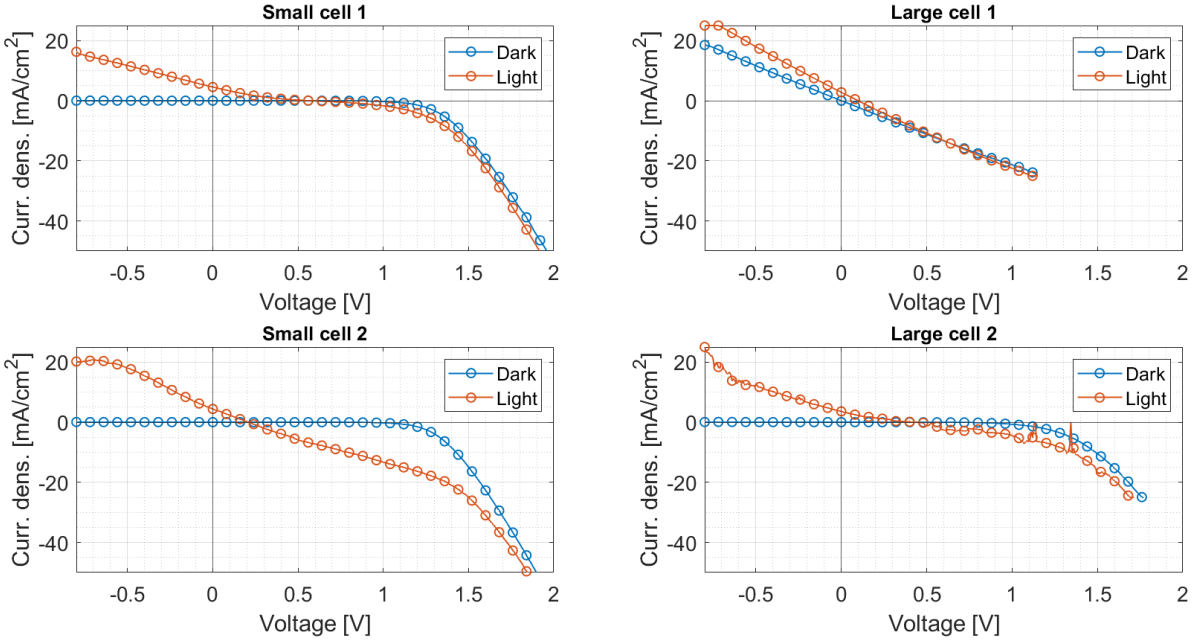

Figure 6.11: Dark J-V curves (blue) and light J-V curves (red) for the four cells on the device with configuration: ITO (200 nm) w/ sub. heat./MoO_x (5 nm)/$MAPbI_3$/C60 (20 nm)/BCP (4 nm)/Ag (150 nm). Two cells with active area 0.16 cm^2 (left) and two cells with active area 0.36 cm^2 (right).

2. ITO w/ sub. heat. (200 nm)/ MoO_x (15 nm)/$MAPbI_3$/C60 (20 nm)/BCP (4 nm)/Ag (150 nm)

Dark and light J-V curves measured on four cells of the device with 15 nm MoO_x on the hole transport side are shown in Fig. 6.12. Small cell 1, small cell 2 and large cell 2 exhibit a clear S-shaped characteristic under illumination with a J_{sc} of 2.9, 2.0 and 2.2 mA/cm^2, and a V_{oc} of 0.51, 0.31 and 0.58 V respectively. The dark J-V curves for these cells show diode behaviour typical of a solar cell in the dark. However, these dark curves do not show strong exponential behaviour. This observation is in line with the S-shaped curve under illumination and indicates that R_s is relatively high. Large cell 1 shows resistive behaviour both under illumination and in the dark. All cells are characterised by a relatively high R_s and relatively low R_{sh}.

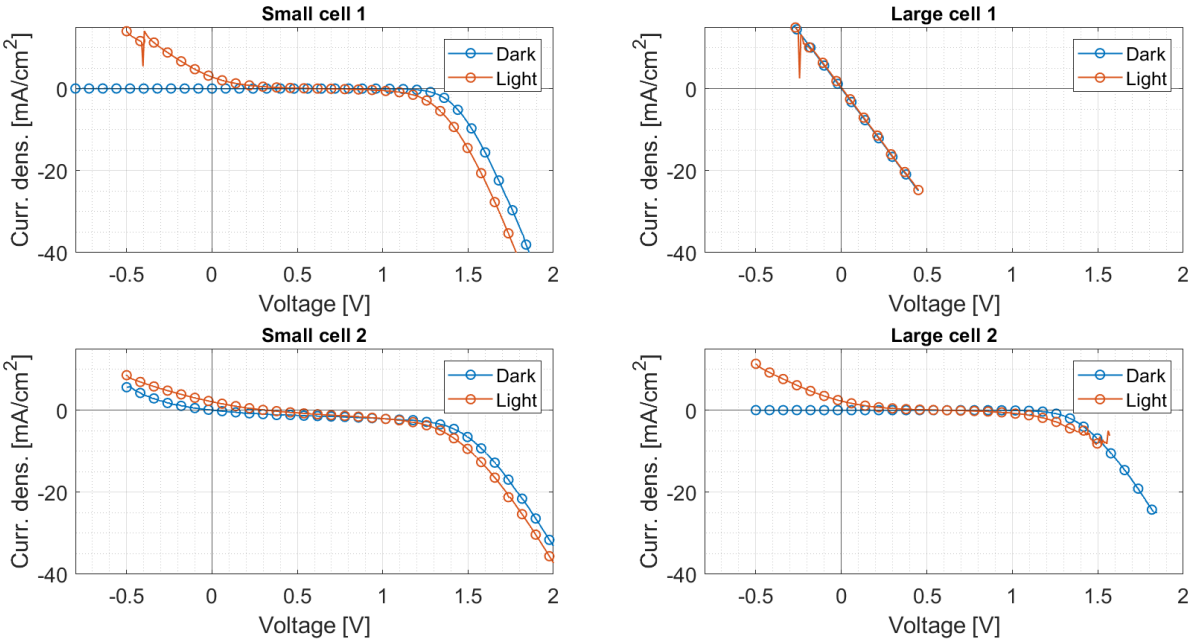

Figure 6.12: Dark J-V curves (blue) and light J-V curves (red) for the four cells on the device with configuration: ITO (200 nm) w/ sub. heat./MoO_x (15 nm)/$MAPbI_3$/C60 (20 nm)/BCP (4 nm)/Ag (150 nm). Two cells with active area 0.16 cm^2 (left) and two cells with active area 0.36 cm^2 (right).

3. ITO (200 nm)/Spiro-TTB (20 nm)/$MAPbI_3$/C60 (20 nm)/BCP (4 nm)/Ag (150 nm)

Dark and light J-V curves measured on four cells of the device with 20 nm spiro-TTB on the hole transport side are shown in Fig. 6.13. For small cell 2 and both large cells, the J-V curves show a similar trend. It can be observed that these cells show limited diode behaviour, but are characterised by a relatively high R_s and relatively low R_{sh}. If we attribute values to the short circuit current density and open circuit voltage, we find for small cell 2, large cell 1, and large cell 2, a J_{sc} of 5.0, 4.3 and 5.7 mA/cm^2, and a V_{oc} of 0.26, 0.20 and 0.29 V respectively. Small cell 1 shows resistive behaviour both under illumination and in the dark.

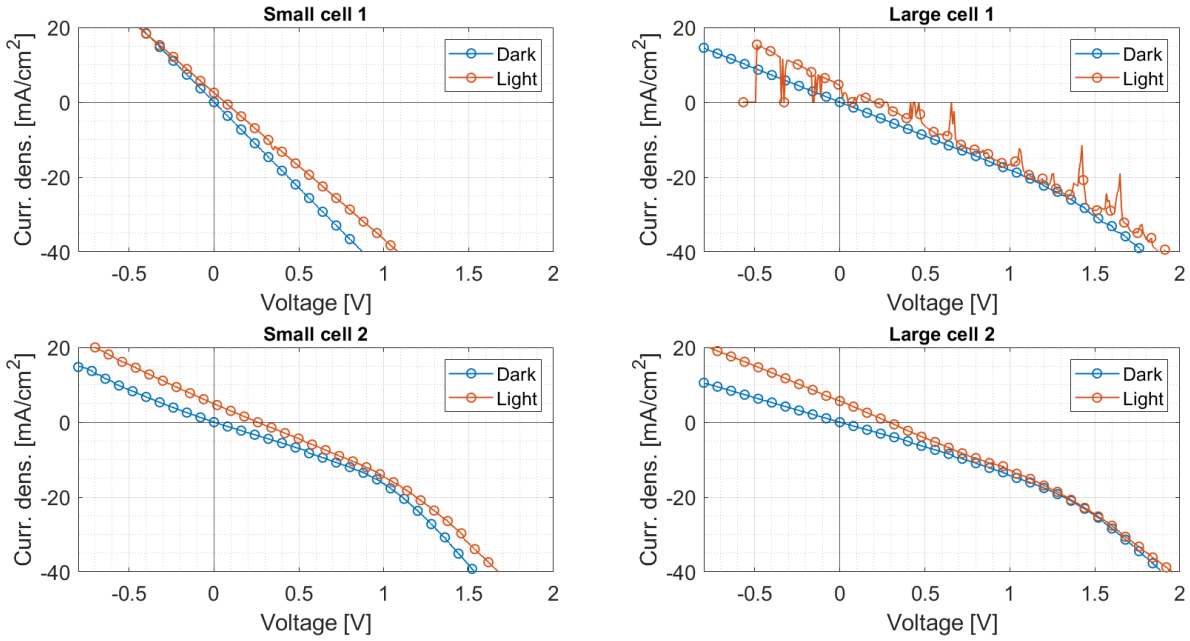

Figure 6.13: Dark J-V curves (blue) and light J-V curves (red) for the four cells on the device with configuration: ITO (200 nm)/Spiro-TTB (20 nm)/$MAPbI_3$/C60 (20 nm)/BCP (4 nm)/Ag (150 nm). Two cells with active area 0.16 cm^2 (left) and two cells with active area 0.36 cm^2 (right).

4. ITO (300 nm)/Spiro-TTB (20 nm)/MoO_x (5 nm)/$MAPbI_3$/C60 (20 nm)/BCP (4 nm)/Ag (150 nm)

Dark and light J-V curves measured on four cells of the device with 20 nm spiro-TTB and 5 nm MoO_x on the hole transport side are shown in Fig. 6.14. Small cell 2 and large cell 2 exhibit a clear S-shaped characteristic under illumination with a J_{sc} of 5.0 and 3.6 mA/cm^2, and a V_{oc} of 0.38 and 0.24 V respectively. The dark J-V curves for these two cells do show diode behaviour typical of a solar cell in the dark. However, for voltages below zero, the current increases which indicates that R_{sh} is relatively low. In addition, no strong exponential behaviour is observed, which means that R_s is relatively high. Small and large cell 1 show resistive behaviour both under illumination and in the dark. All cells are characterised by a relatively high R_s and relatively low R_{sh}.

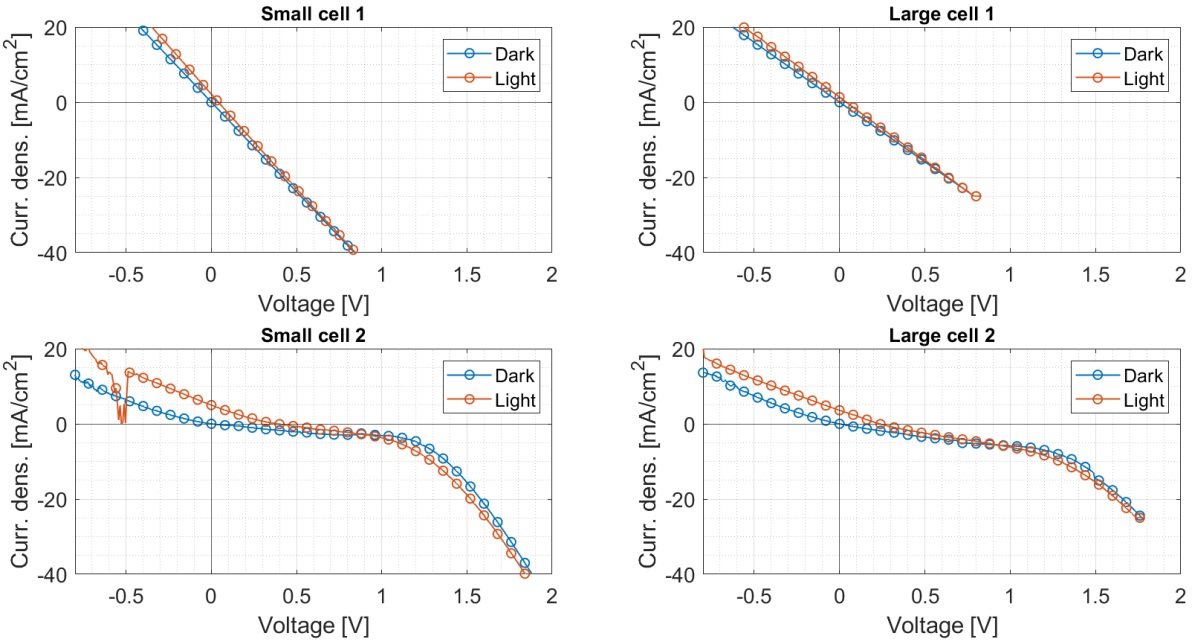

Figure 6.14: Dark J-V curves (blue) and light J-V curves (red) for the four cells on the device with configuration: ITO (300 nm)/Spiro-TTB (20 nm)/MoO_x (5 nm)/$MAPbI_3$/C60 (20 nm)/BCP (4 nm)/Ag (150 nm). Two cells with active area 0.16 cm^2 (left) and two cells with active area 0.36 cm^2 (right).

5. ITO (300 nm)/Spiro-TTB (20 nm)/MoO_x (15 nm)/$MAPbI_3$/C60 (20 nm)/BCP (4 nm)/Ag (150 nm)

Dark and light J-V curves measured on four cells of the device with 20 nm spiro-TTB and 15 nm MoO_x on the hole transport side are shown in Fig. 6.15. Small cell 1, small cell 2 and large cell 2 exhibit a clear S-shaped characteristic under illumination with a J_{sc} of 4.8, 5.8 and 3.9 mA/cm^2, and a V_{oc} of 0.69, 0.68 and 0.61 V respectively. The dark J-V curves for the same cells show diode behaviour typical of a solar cell in the dark. However, these dark curves do not show strong exponential behaviour. This observation is in line with the S-shaped curve under illumination and indicates that R_s is relatively high. Large cell 1 shows resistive behaviour both under illumination and in the dark. All cells are characterised by a high R_s and relatively low R_{sh}.

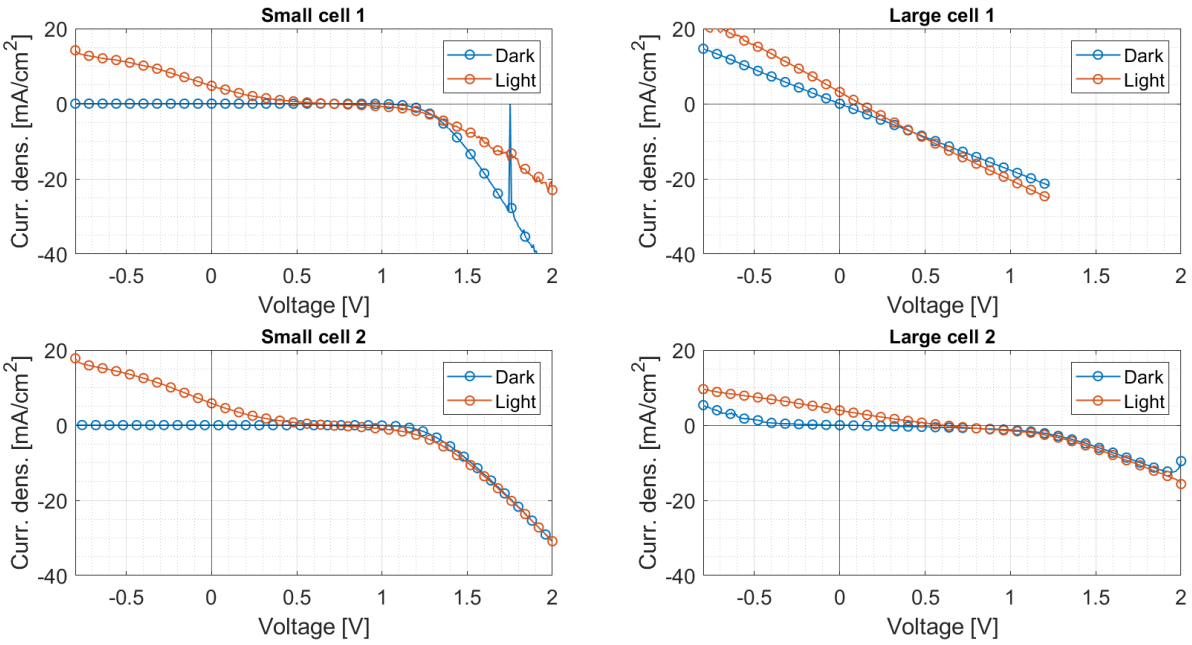

Figure 6.15: Dark J-V curves (blue) and light J-V curves (red) for the four cells on the device with configuration: ITO (300 nm)/Spiro-TTB (20 nm)/MoO_x (15 nm)/$MAPbI_3$/C60 (20 nm)/BCP (4 nm)/Ag (150 nm). Two cells with active area 0.16 cm^2 (left) and two cells with active area 0.36 cm^2 (right).

6. ITO (200 nm)/Spiro-OMeTAD/$MAPbI_3$/C60 (20 nm)/BCP (4 nm)/Ag (150 nm)

Dark and light J-V curves measured on four cells of the device with spiro-OMeTAD on the hole transport side are shown in Fig. 6.16. The dark J-V curve for large cell 1 does seem to show some diode behaviour, however, the measurement is noisy and we cannot give a clear explanation of what we observe. For small cell 1, small cell 2 and large cell 2, the J-V curves show a similar trend. It can be observed that these cells show diode behaviour, but are characterised by a relatively high R_s and relatively low R_{sh}. If we attribute values to the short circuit current density and open circuit voltage, we find for small cell 1, small cell 2, and large cell 2, a J_{sc} of 4.6, 9.2 and 6.3 mA/cm^2, and a V_{oc} of 0.17, 0.34 and 0.36 V respectively.

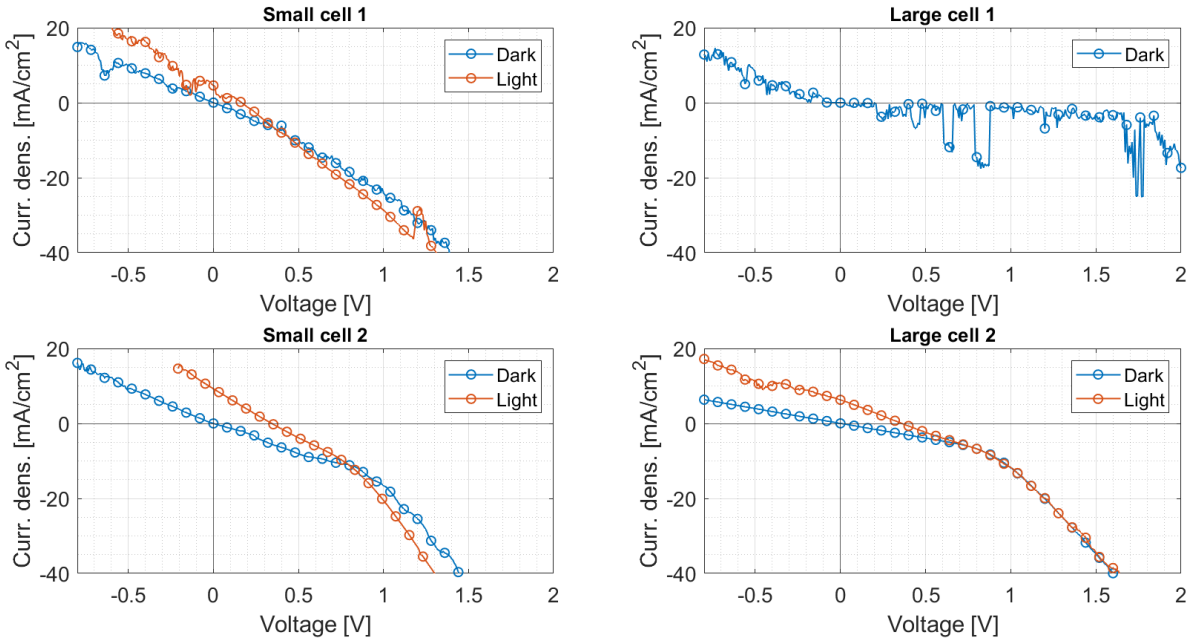

Figure 6.16: Dark J-V curves (blue) and light J-V curves (red) for the four cells on the device with configuration: ITO (200 nm)/Spiro-OMeTAD/$MAPbI_3$/C60 (20 nm)/BCP (4 nm)/Ag (150 nm). Two cells with active area 0.16 cm^2 (left) and two cells with active area 0.36 cm^2 (right).

7. ITO (200 nm)/Spiro-OMeTAD/MoO_x (5 nm)/$MAPbI_3$/C60 (20 nm)/BCP (4 nm)/Ag (150 nm)

Dark and light J-V curves measured on four cells of the device with spiro-OMeTAD and 5 nm MoO_x on the hole transport side are shown in Fig. 6.17. The light J-V curves for small cell 1 and large cell 1 are not showing an S-shape, instead, they show the shape of a J-V curve for a solar cell with a relatively high R_s and relatively low R_{sh}. If we attribute values to the short circuit current density and open circuit voltage, we find for small cell 1 and large cell 1, a J_{sc} of 10.0 and 6.4 mA/cm^2, and a V_{oc} of 0.67 and 0.41 V respectively. For small cell 1 and large cell 2 diode behaviour is observed with a relatively high R_s and relatively low R_{sh}. The dark J-V curve for small cell 2 shows diode behaviour typical of a solar cell in the dark. However, the dark curve does not show strong exponential behaviour. This observation indicates that R_s is relatively high. Large cell 2 shows resistive behaviour under dark conditions.

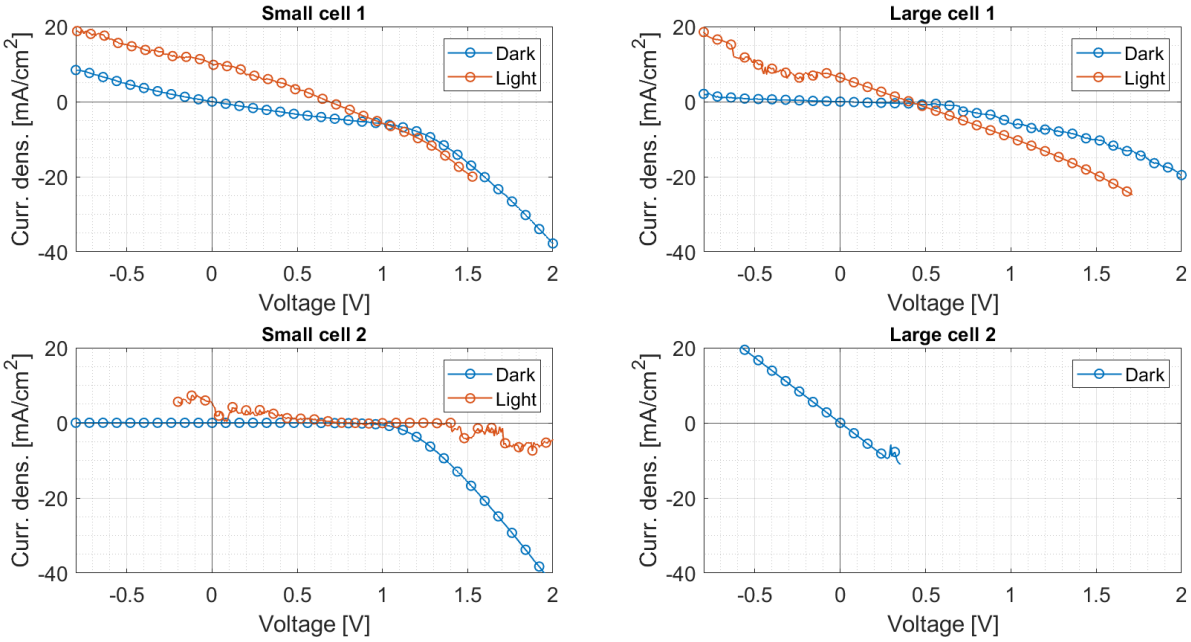

Figure 6.17: Dark J-V curves (blue) and light J-V curves (red) for the four cells on the device with configuration: ITO (200 nm)/Spiro-OMeTAD/MoO_x (5 nm)/$MAPbI_3$/C60 (20 nm)/BCP (4 nm)/Ag (150 nm). Two cells with active area 0.16 cm^2 (left) and two cells with active area 0.36 cm^2 (right).

8. ITO (200 nm)/Spiro-OMeTAD/MoO_x (15 nm)/$MAPbI_3$/C60 (20 nm)/BCP (4 nm)/Ag (150 nm)

Dark and light J-V curves measured on four cells of the device with spiro-OMeTAD and 15 nm MoO_x on the hole transport side are shown in Fig. 6.18. Small cell 1, small cell 2 and large cell 2 seem to show a bit of an S-shaped characteristic under illumination with a J_{sc} of 5.4, 7.4 and 8.7 mA/cm^2, and a V_{oc} of 0.76, 0.44 and 0.79 V respectively. The dark J-V curves for small cell 1 and large cell 2 show diode behaviour typical of a solar cell in the dark. However, these dark curves do not show strong exponential behaviour. This observation indicates that R_s is relatively high. The dark J-V curve for small cell 2 shows diode behaviour typical of a solar cell in the dark. However, for voltages below zero, the current increases which indicates that R_{sh} is relatively low. Large cell 1 shows resistive behaviour under illumination and some limited diode behaviour in the dark. All cells are characterised by a relatively high R_s and relatively low R_{sh}.

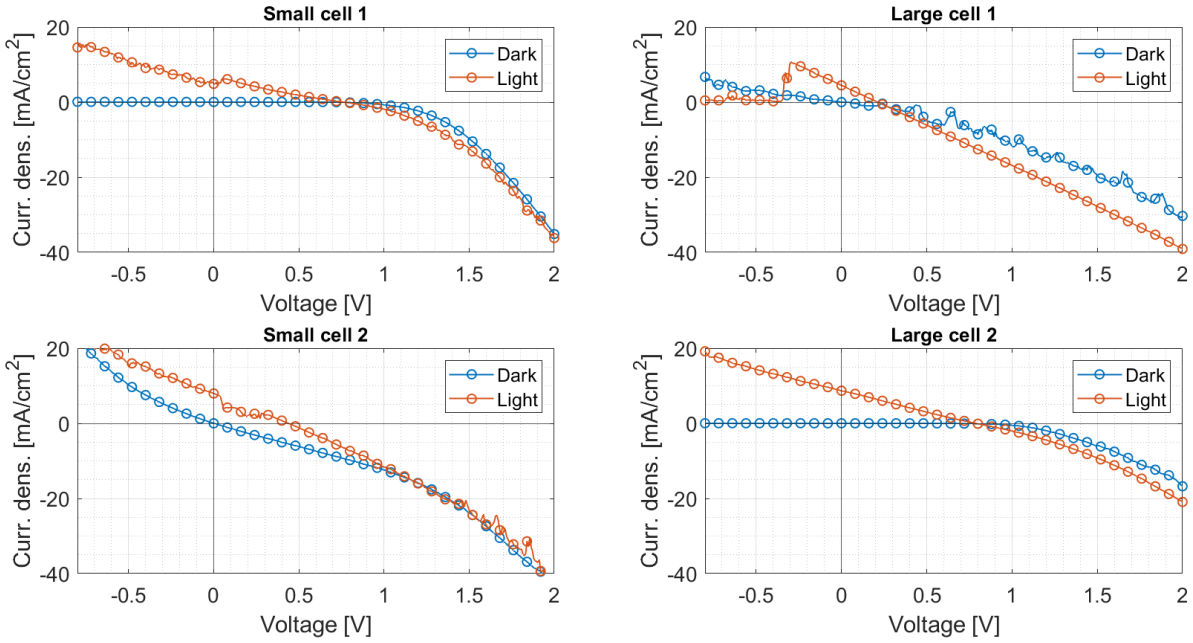

Figure 6.18: Dark J-V curves (blue) and light J-V curves (red) for the four cells on the device with configuration: ITO (200 nm)/Spiro-OMeTAD/MoO_x (15 nm)/$MAPbI_3$/C60 (20 nm)/BCP (4 nm)/Ag (150 nm). Two cells with active area 0.16 cm^2 (left) and two cells with active area 0.36 cm^2 (right).

6.2.4. Comparison and explanations of observed J-V characteristics

An overview of relevant solar cell parameters and observations for the cells with configurations of table 6.4 is depicted in table 6.5. The materials used on the hole transport side, J_{sc}, V_{oc} and observations such as S-shape, diode behaviour in the dark, poor diode behaviour and resistor are given. Moreover, the best performing cell for each configuration of table 6.4 is shown in Fig. 6.19 to allow for easier comparison.

It is relatively easy to measure whether a perovskite solar cell works well. On the other hand, finding the problem in case a cell performs badly, is a lot harder [137]. PSCs that behave far from ideal often show an S-shaped J-V curve under illumination [137]. There are many reports of S-shaped behaviour in all kinds of (perovskite) solar cells [50]. In general, the underlying physical effect resulting in S-shaped J-V curves is a problem with the extraction of charge carriers at an interface. Note that for PSCs, there is not yet a complete description of the causes for the occurrence of the S-shape [137],[138].

Most of the PSCs studied in the former subsection exhibited J-V characteristics dominated by S-shapes. In order to find a possible explanation for the S-shapes, several known causes from literature are considered. Firstly, a mismatch in the energy band alignment between two adjacent layers. This mismatch creates an energy barrier for either a hole or an electron, and could lead to the build up of charge at an interface. Note that this mismatch could occur at any interface in the device such as the PVK/TL interface or the TL/electrode interface [50],[139]. Secondly, high non-radiative recombination at the an interface due to the presence of many trap states. Thirdly, the presence of a layer with a poor hole or electron mobility. Such a layer would get an insulating character [139]. Finally, a difference in electron and hole mobility in the transport layers by at

least two orders of magnitude [139]. This difference has been observed to be the cause of the S-shape in organic solar cells [139]. For more information on the occurrence of S-shapes in J-V curves see Ch.2 subsection 2.3.2.

Table 6.5: Overview of HTL(s), J_{sc}, V_{oc}, observations (S-shape, clear S-shape, diode in dark, poor diode, resistor and no clear measurement) are given for each cell of the eight configurations of table 6.4

Nr.	HTL(s)	Small cell 1	Small cell 2	Large cell 1	Large cell 2
1	MoO_x (5 nm)	V_{oc} = 0.58 V J_{sc} = 4.6 mA/cm^2 Clear S-shape Diode in dark	V_{oc} = 0.21 V J_{sc} = 4.4 mA/cm^2 S-shape Diode in dark	Resistor	V_{oc} = 0.42 V J_{sc} = 3.6 mA/cm^2 S-shape Diode in dark
2	MoO_x (15 nm)	V_{oc} = 0.51 V J_{sc} = 2.9 mA/cm^2 Clear S-shape Diode in dark	V_{oc} = 0.31 V J_{sc} = 2.0 mA/cm^2 Clear S-shape Diode in dark	Resistor	V_{oc} = 0.58 V J_{sc} = 2.2 mA/cm^2 Clear S-shape Diode in dark
3	Spiro-TTB (20 nm)	Resistor	V_{oc} = 0.26 V J_{sc} = 5.0 mA/cm^2 Poor diode	V_{oc} = 0.20 V J_{sc} = 4.2 mA/cm^2 Poor diode	V_{oc} = 0.29 V J_{sc} = 5.7 mA/cm^2 Poor diode
4	Spiro-TTB (20 nm)/MoO_x (5 nm)	Resistor	V_{oc} = 0.38 V J_{sc} = 5.0 mA/cm^2 Clear S-shape Diode in dark	Resistor	V_{oc} = 0.24 V J_{sc} = 3.6 mA/cm^2 Clear S-shape Diode in dark
5	Spiro-TTB (20 nm)/MoO_x (15 nm)	V_{oc} = 0.69 V J_{sc} = 4.8 mA/cm^2 Clear S-shape Diode in dark	V_{oc} = 0.68 V J_{sc} = 5.8 mA/cm^2 Clear S-shape Diode in dark	Resistor	V_{oc} = 0.61 V J_{sc} = 3.9 mA/cm^2 Clear S-shape Diode in dark
6	Spiro-OMeTAD	V_{oc} = 0.17 V J_{sc} = 4.6 mA/cm^2 Poor diode	V_{oc} = 0.34 V J_{sc} = 9.2 mA/cm^2 Poor diode	No clear measurement	V_{oc} = 0.36 V J_{sc} = 6.3 mA/cm^2 Poor diode
7	Spiro-OMeTAD/MoO_x (5 nm)	V_{oc} = 0.67 V J_{sc} = 10.0 mA/cm^2 Decent light J-V	No clear light J-V Diode in dark	V_{oc} = 0.41 V J_{sc} = 6.4 mA/cm^2 Decent light J-V	Resistor
8	Spiro-OMeTAD/MoO_x (15 nm)	V_{oc} = 0.76 V J_{sc} = 5.4 mA/cm^2 S-shape Diode in dark	V_{oc} = 0.44 V J_{sc} = 7.4 mA/cm^2 S-shape	Resistor	V_{oc} = 0.79 V J_{sc} = 8.7 mA/cm^2 S-shape Diode in dark

The given causes for the occurrence of S-shapes (mismatch in energy band alignment, interface trap states, insulating layer and different mobilities) could be attributed to every interface (or layer) in our device. In order to assess which interface and or layer is (mostly) responsible for the S-shape, we first list several observations about the occurrence of the S-shapes in our measurements:

1. The S-shape is only observed in configurations that contain a MoO_x layer. To elaborate, devices with MoO_x, spiro-TTB/MoO_x and spiro-OMeTAD/MoO_x on the hole transport side have all shown at least one S-shaped J-V curve.
2. The S-shape is not observed in devices containing only spiro-TTB or spiro-OMeTAD. These devices are characterised by a resistor characteristic, but do show some diode behaviour with a high R_s and low R_{sh}.
3. The S-shape becomes more evident with a thicker MoO_x layer. In order to see this in the J-V curves, configuration 1 is compared to 2, 5 to 6, and 7 to 8 (see Fig. 6.19).
4. The S-shape is most evident in devices with only MoO_x on the hole transport side and least evident for devices with spiro-OMeTAD/MoO_x on the hole transport side.

Based on these observations, we conclude that it is most probable that the presence of the MoO_x layer and its contact with the $MAPbI_3$ is causing the S-shaped J-V curves. Note that the reason to implement this layer in our devices was to function as seed layer for spin-coated $MAPbI_3$. Considering the possible explanations for S-shaped behaviour in relation to our MoO_x layer, we can make the following arguments:

- Based on findings in literature, a possible mismatch in energy band alignment between the MoO_x layer and PVK is considered the most probable cause for the occurrence of the S-shape [57],[140]. In litera-

ture it was found that when MoO_3 was used directly on $MAPbI_3$, their energy levels changed after they made contact leading to a barrier for hole extraction [57]. Note that since we are working with MoO_x (x < 3), with the exact oxidation state unknown, we are not sure how the bands align with $MAPbI_3$. Based on these two arguments, it is likely that the S-shape is caused by a mismatch in energy bands. If this is true, it explains the observation that the S-shape seems most profound for thicker MoO_x layers, since it is easier to overcome the energy barrier if the layer is thinner. In other research, where MoO_x was used as hole selective contact in a heterojunction silicon solar cell, it was found that indeed a mismatch in band alignment was the cause of the S-shape and a more profound S-shape was found for thicker MoO_x layers [140].

- The presence of trap states at the interface between perovskite and MoO_x is another likely reason for the S-shape. In literature it was found that a chemical reaction (MoO_3 to MoO_2) at the MoO_3/PVK interface could occur leading to an enhanced surface recombination [57]. In addition, based on the comparison of the PL intensity of a neat $MAPbI_3$ layer to a bi-layer of MoO_x/PVK, we concluded that the strong quenching could possibly be attributed to a large trap state density at the interface (see subsection 5.2.5).
- The MoO_x layer having a low hole mobility which could make it function as an insulating layer or make it differ two orders of magnitude with the electron mobility in the ETL, is probably not the cause for the S-shape behaviour. In general, MoO_x has a relatively high hole mobility [54]. Although it is a possibility, there is no reason to assume that our MoO_x exhibits a low hole mobility. If the hole mobility in MoO_x is two orders of magnitude lower than the electron mobility in C60 could not be found in literature.

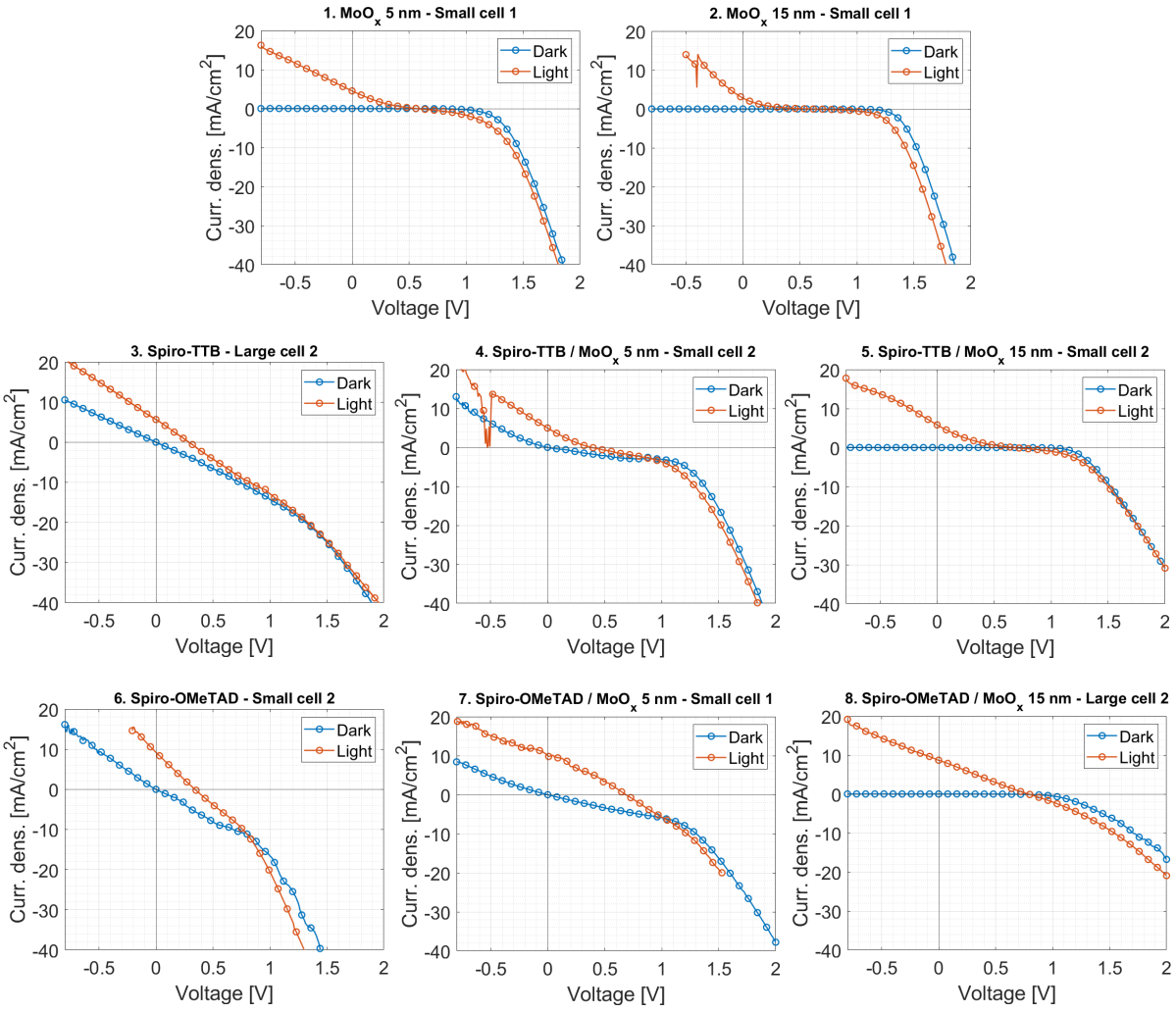

Figure 6.19: Dark J-V curves (blue) and light J-V curves (red) for the best performing cell of each configuration of table 6.4. Configuration number, HTL(s) and large/small cell are indicated.

For devices with only spiro-TTB or spiro-OMeTAD on the hole transport side, spin-coating of the $MAPbI_3$ layer could have possibly washed off (part of) the HTL. For this reason, the J-V curves for these devices seem to follow a similar trend as the first spin-coated devices (see Fig. 6.8) and are characterised by a high R_s and low R_{sh}. However, different than for the first spin-coated devices, this time the devices seem to show at least some diode behaviour. This result may have been due to the implementation of the BCP layer and/or to more experience carrying out J-V characterisation with the solar simulator.

Considering the electron transport side, it does seem likely that the corresponding layers (C60, BCP and Ag) are functioning properly and facilitate the transport of light generated electrons from the PVK absorber layer all the way to the silver electrode. This statement is based on several results obtained during this work. For example, from the TRMC results on the bi-layer of $MAPbI_3$/C60 we learned that electrons are probably extracted effectively (subsection 5.2.5). In addition, once we started using BCP in our devices, the J-V curves started showing something different than only resistive behaviour. Possibly, BCP molecules bonded with silver atoms and thereby suppress diffusion of silver atoms towards other device layers [69]. It could also be possible that BCP improved the contact between C60 and silver to a good ohmic contact [68]. On the other hand, optimisation is required on aspects such as thickness and deposition rate for C60, BCP and Ag layer. From a different perspective, it may be possible that the poor performance of the PSCs can (partly) be attributed to malfunctions at the electrons transport side, however, based on the results there is no evidence for that.

Considering the equivalent circuit for a solar cell, it is evident that our cells are subjected to a relatively high R_s and relatively low R_{sh} (see Fig. 6.19). There are several possible explanations causing the high series resistance. Firstly, a relatively poor lateral conductivity of the ITO contact indicated by the values measured for the sheet resistance (subsection 5.1.2, table 5.2). Secondly, a low mobility in the ETL, HTL and PVK absorber layer, which could be the consequence of a high defect density. In addition, a non-optimal thickness for specific layers with a low mobility enhances the series resistance. Finally, a large contact resistance with the electrodes [25]. In order to find the exact causes and contributions to R_s, further characterisation of individual layers and bi-layers is needed. An example could be measuring the resistivity of transport layers. The relatively low R_{sh} could possibly be caused by internal currents due to filling of pinholes by the metal electrode. In addition, due to possible mismatches in energy band alignment between the PVK and transport layers, it could be possible that a transport layer loses its electron or hole blocking character leading to a lower R_{sh} [50].

Although none of the devices worked as we hoped, small cell 1 on device with configuration 7 of table 6.4 showed the most decent J-V curve under illumination. This device with Spiro-OMeTAD and 5 nm MoO_x on the hole transport side had a J_{sc} of 10.0 mA/cm^2 and a V_{oc} of 0.67 V. Note that a very good functioning PSC is expected to have a J_{sc} around 24 mA/cm^2 and a V_{oc} around 1.08 V [45].

7

Conclusion and Recommendations

7.1. Conclusion

The main objective of this thesis project was to develop and optimise the various device layers forming a PSC and demonstrate a working perovskite device. The methodology used to attempt this objective is twofold: (1) development (and stacking) of all required layers that form a PSC, i.e. TCO front contact, HTL, PVK absorber layer, ETL, possibly a buffer layer and metallic back electrode, and (2) investigation of the J-V characteristics to assess the device operation.

We have fabricated devices with eleven different inverted p-i-n architectures, and with active areas of 0.16 cm^2 and 0.36 cm^2. The different materials used in this project are: ITO as front electrode, spiro-TTB, spiro-OMeTAD and MoO_x as hole transport layer, $MAPbI_3$ and $FA_xCs_{1-x}Pb(I_yBr_{1-y})_3$ as perovskite absorber layer, C60 as electron transport layer, BCP as buffer layer, and silver and aluminium as metallic back electrode. Furthermore, three different techniques have been used to fabricate the different device layers: RF sputtering for ITO, spin-coating for spiro-OMeTAD and $MAPbI_3$, and thermal evaporation for spiro-TTB, MoO_x, $FA_xCs_{1-x}Pb(I_yBr_{1-y})_3$, C60, BCP, silver and aluminium.

Before we conclude the development and testing of devices, we first reflect on several smaller research goals that were set to support the main goal. The following conclusions can be drawn:

- For $FA_xCs_{1-x}Pb(I_yBr_{1-y})_3$ deposited by sequential layer thermal evaporation, the uniformity and tooling factors were optimised to grow layers with a correct precursor ratio resulting in a high crystallinity and high absorptance. However, it was quite difficult to fabricate layers with thicknesses desired for PSCs. Additionally, the thermal evaporation process did not always seem to have a high reproducibility, which led to a steep learning curve. After spending much time optimising the ratio between the set thicknesses for the different precursors, perovskite could no longer be obtained due to a problem with the PbI_2 precursor. For this reason, the optimisation process was limited. Furthermore, no clear effect of post-annealing on the PVK thin films could be detected for the temperatures and times tested in this work. This observation could possibly be explained by a different effect that annealing can have on samples with different (non-optimal) precursor ratios. We conclude that the thermally evaporated PVK thin films are not yet of high enough quality that would be desired for application in a device.
- We managed to fabricate spin-coated $MAPbI_3$ layers with a desired thickness for device application. This result was achieved by increasing the concentration of the precursor solution. In addition, our $MAPbI_3$ films possess an appropriate bandgap, good diffractogram and high absorptance. However, based on the small crystal size determined with SEM, and poor device performance, further improvement is needed to enhance the PVK quality in order to achieve a high device performance.
- Transport, buffer, and contact layers were successfully fabricated, mostly via thermal evaporation processes. On top of existing deposition recipes for aluminium, C60, and MoO_x, new deposition recipes were successfully developed for silver, BCP, and spiro-TTB. We managed to fabricate thin films, while using deposition rates and thicknesses comparable to similar research. It is encouraging to note that we can produce thin layers of many different materials relatively easily via thermal evaporation.

- From spectrophotometry measurements, it can be concluded that the HTLs spiro-TTB and MoO_x exhibit very low parasitical absorption losses, whereas usage of spin-coated spiro-OMeTAD introduces relatively high parasitic absorption losses. Furthermore, an optical model to fit spectroscopic ellipsometry data has been successfully developed for spiro-TTB thin films. The model allows us to determine the thickness and optical properties with a relatively low mean squared error.
- From TRMC and PL measurements, we learned that the electronic properties of neat $MAPbI_3$ thin films may vary a lot between different batches, indicating that the reproducibility could be limited. In addition, TRMC measurements indicated that C60 effectively extracts electrons when deposited on top of $MAPbI_3$, whereas spiro-TTB did not show to possess any hole extracting abilities when deposited on top of $MAPbI_3$. Furthermore, strong quenching of the steady-state PL signal was observed for several PVK/TL combinations ($MAPbI_3$ with C60, spiro-OMeTAD, MoO_x). This result can be attributed to extraction of either electrons or holes and/or enhanced non-radiative recombination at the interface. Quenching was not observed for a bi-layer of PVK and spiro-TTB.
- A method was successfully developed to accurately determine the ITO sheet resistance by taking into account correction factors applicable to the dimensions of the layer. The lowest sheet resistance among our ITO depositions, was determined to be 24.5 $\Omega/\square$ for a 300 nm thick ITO layer fabricated with substrate heating. On the other hand, ITO layers fabricated with substrate heating were found to have a lower transmittance and poorer crystallinity than their counterpart without substrate heating.

When we consider the development and testing of devices, perovskite solar cells with dark diode characteristics were fabricated after several attempts. However, under illumination, the device performance is far from the specifications of a properly functioning cell and is limited by a low light response. Possible explanations as to why our cells are showing a poor performance are based on measured J-V curves and are supported by observations made during the fabrication process. The J-V curve results encountered during this project are categorised below. For each J-V curve observation, possible explanations are summarised:

- An ohmic response, characterised by a linear relation between current density and voltage. This resistor-like behaviour was observed for several architectures, including all cells with a thermally evaporated $FA_xCs_{1-x}Pb(I_yBr_{1-y})_3$ absorber layer and some cells with a spin-coated $MAPbI_3$ layer. A possible explanation for this resistive behaviour, is the presence of shorts in the cell due to pinholes which are possibly filled with thermally evaporated metal. This argument is supported by the fact that the deposition rates may have been too high during the fabrication of the back electrodes which were used in some of these cells. In addition, the ohmic behaviour was observed to a lesser extent for cells with a BCP layer in between the ETL and back electrode, which could indicate that the ohmic response is suppressed by implementation of an extra layer underneath the back electrode. Furthermore, the devices with a thermally evaporated PVK layer appeared to contain a PVK layer of inferior quality due to suboptimal precursor ratios and technical setbacks. For devices with a spin-coated $MAPbI_3$ layer that showed resisitive behaviour, issues were encountered during the spin-coating of $MAPbI_3$ with a spiro-TTB film as the underlying layer (due to the poor hydrophilicity of spiro-TTB). In addition, it turned out that our spin-coating procedure may wash off the spiro-TTB layer. Based on the above mentioned limiting factors for both device types, it is no surprise that these cells did not show the expected solar cell behaviour.
- S-shaped J-V curves under illumination and diode behaviour in the dark. To overcome the spin-coating issues on top of spiro-TTB, MoO_x was used as an underlying layer for $MAPbI_3$. Meanwhile, BCP was deposited in between C60 and silver to act as a buffer layer. The dark J-V curves for these devices showed diode behaviour typical of a solar cell in the dark. Under illumination, the J-V curves exhibited clear S-shapes which are indicative of an issue regarding the extraction of charge carriers at an interface. The S-shapes were only observed for devices where spin-coating of $MAPbI_3$ was carried out on top of MoO_x. From these observations, we conclude that the S-shapes are most likely caused by a transport issue at the MoO_x/PVK interface. This transport issue is possibly due to a mismatch in energy band alignment and/or a high trap state density enhancing non-radiative recombination.
- Parasitic resistances are evident in the measured J-V curves for all cells. It is observed that our cells are subject to a relatively high R_s and relatively low R_{sh}. The high series resistance is possibly related to a relatively poor lateral conductivity of the ITO contact, low mobility in the ETL, HTL and PVK absorber layer (possibly due to a high defect density), non-optimal thickness for specific layers with low mobility,

and a large contact resistance with the electrodes. The low shunt resistance could possibly be caused by internal currents due to the presence of pinholes, and a possible mismatch in energy band alignment of the PVK layer with a transport layer, whereby the transport layer loses its electron or hole blocking property.

The most promising J-V curve was obtained for a cell with architecture ITO (200 nm)/Spiro-OMeTAD/MoO_x (5 nm)/$MAPbI_3$/C60 (20 nm)/BCP (4 nm)/Ag (150 nm). This cell exhibited a short circuit current density of 10.0 mA/cm^2 and an open circuit voltage of 0.67 V. Same as for all other cells, a relatively high R_s and relatively low R_{sh} were detected.

7.2. Recommendations

Based on the results and insights obtained during the experimental work conducted for this thesis, a comprehensive set of recommendations can be given. First of all, when analysing the different device architectures fabricated in this work, the following experiments could be interesting to confirm or refute the possible explanations given in the previous section for the observed device behaviour:

- Structural characterisation of a quartz/MoO_x/spin-coated $MAPbI_3$ sample. XRD and SEM can be used to determine the crystallinity and crystal size to draw a comparison with neat $MAPbI_3$ thin films. Moreover, profilometry should be used to confirm that the same thickness can be achieved as for a neat film. In general, it could be interesting to characterise how the PVK film changes when deposited in a device (on top of glass/ITO/HTL) compared to a neat single layer.
- Verify the presence of pinholes and their size and density. Since we suspect that the parasitic resistances and the ohmic response could (partly) be caused by pinholes, it is important to confirm their presence in the HTL, PVK absorber layer and ETL. SEM and metallurgical microscopy could possibly be used for this.
- Further investigate the diffusion of silver into underlying device layers by using grazing incidence X-ray diffraction (GXRD) or X-ray photoelectron spectroscopy (XPS). If the presence of silver in underlying device layers can be detected, a comparison between devices with or without BCP and for different deposition rates of silver could be made. In addition, this experiment could be informative since it has been proven that the diffusion of silver into the PVK layer contributes to its degradation.
- Determine the band alignment of MoO_x with XPS to investigate the possibility that a mismatch with the PVK layer leads to the occurrence of s-shaped J-V curves.
- Resistivity measurements on different device layers or stack of layers to identify possible causes for the high series resistance.

The above mentioned experiments could provide us with insights that may assist the further development of our PSCs. On the other hand, it might be more beneficial to introduce several major changes along with some minor adjustments to the device architecture and fabrication process. The following adjustments are recommended:

- Develop devices with a thermally evaporated and spin-coated perovskite layer in parallel, using the same perovskite in both: $FA_xCs_{1-x}Pb(I_yBr_{1-y})_3$. Once the right materials and corresponding fabrication have been identified, devices with a spin-coated PVK layer could function as a baseline for the development of fully thermally evaporated devices. In this case, a comparison between the two device types can be made. Furthermore, any suggested changes to the device can be tested on a spin-coated version which is faster to produce.
- Develop a suitable spin-coating procedure for the fabrication of $FA_xCs_{1-x}Pb(I_yBr_{1-y})_3$ thin films by using an orthogonal solvent that allows for the deposition of uniform and pinhole-free perovskite films while preserving the properties of the underlying layer. A spin-coating procedure that makes use of an anti-solvent could possibly have a beneficial effect in limiting the pinhole formation.
- Avoid using the spiro-TTB precursor that was used in this work. The bandgap energy did not coincide with values reported in literature and TRMC results proved that spiro-TTB does not extract holes. We

suspect that the precursor used might have needed doping, as is common practice for hole transport materials.

- Avoid using MoO_x. Since we suspect that the presence of the MoO_x layer is responsible for the s-shaped J-V characteristics, it is not advisable to keep using this material. It could potentially be used as buffer layer between the ITO and HTL.
- Consider investigating different hole transport materials, such as PTAA, PEDOT:PSS, TaTm and NiO_x.
- Spiro-OMeTAD can probably function well as a hole transport material in PSCs. However, the rotation speed during spin-coating should be optimised to obtain an adequate thickness with high uniformity. If the spin-coating of spiro-OMeTAD is carried out directly on top of ITO, UV-Ozone treatment of the samples is advised to obtain a higher wettability. Annealing of other device layers fabricated on top of spiro-OMeTAD should be done cautiously to prevent destroying the spiro-OMeTAD layer.
- Initially, we recommend using the same materials on the electron transport side (C60, BCP and Ag) as used in this work. Note that it is relevant to investigate the role of the back electrode and its deposition procedure in the occurrence of the ohmic behaviour. At a later stage, the thickness and possibly several deposition parameters should be optimised for the C60, BCP and Ag layer.
- Start using high temperature post-deposition annealing directly after fabrication of the ITO layer. Annealing could reduce the sheet resistance while increasing the transparency. At a later stage, thickness, annealing temperature and duration, and oxygen flow during RF sputtering could be optimised to obtain an ITO layer of very high quality.
- Optimise the measurement procedure of the solar simulator. Once a properly working cell is obtained, a consistent measurement procedure should be developed, including measurements in both forward and reverse scanning direction. Note that at the start of this work, J-V curves have been recorded with varying voltage ranges, step sizes and scanning directions. At the end, a more consistent procedure was used, however, J-V curves were still subject to change when carrying out the same measurement on the same cell at different times. This observation may be attributed to the cell's functionality or to the measurement procedure.

A

Appendix

A.1. Different device architectures

A.1.1. Devices with thermally evaporated perovskite

Schematics of the architectures of PSCs with a thermally evaporated PVK absorber layer fabricated during this project are shown in Fig. A.1-A.4.

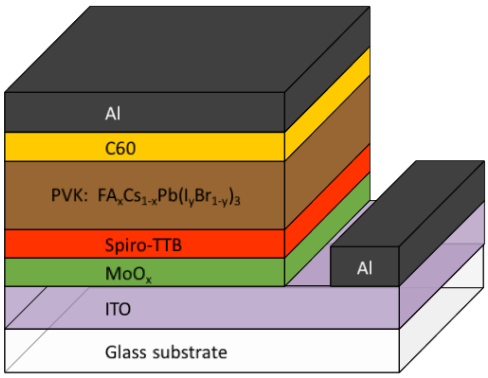

Figure A.1: ITO/MoO_x/Spiro-TTB/$FA_xCs_{1-x}Pb(I_yBr_{1-y})_3$/C60/Al

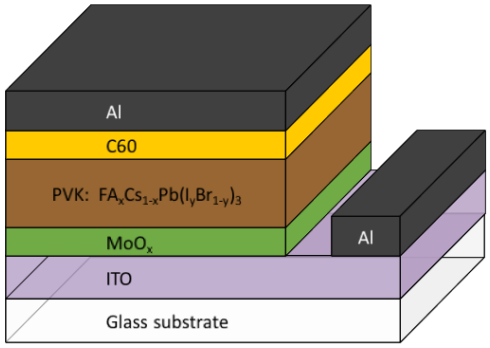

Figure A.2: ITO/MoO_x/$FA_xCs_{1-x}Pb(I_yBr_{1-y})_3$/C60/Al

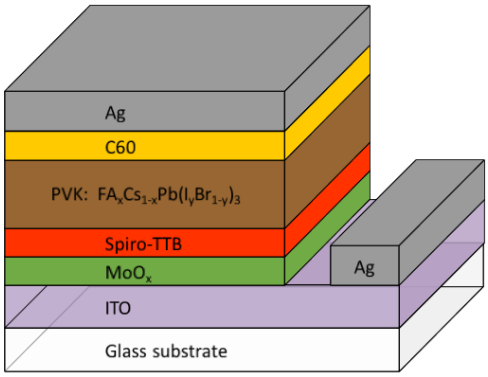

Figure A.3: ITO/MoO_x/Spiro-TTB/$FA_xCs_{1-x}Pb(I_yBr_{1-y})_3$/C60/Ag

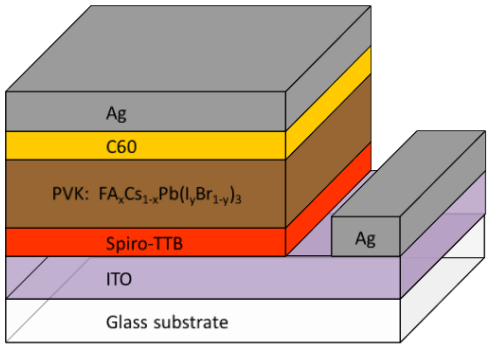

Figure A.4: ITO/Spiro-TTB/$FA_xCs_{1-x}Pb(I_yBr_{1-y})_3$/C60/Ag

A.1.2. Devices with spin-coated perovskite

Schematics of the architectures of PSCs with a spin-coated PVK absorber layer fabricated during this project are shown in Fig. A.5-A.11.

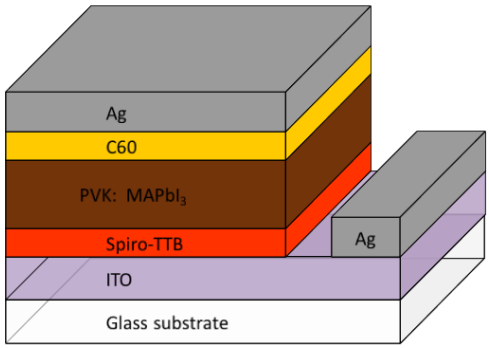

Figure A.5: ITO/Spiro-TTB/$MAPbI_3$/C60/Ag

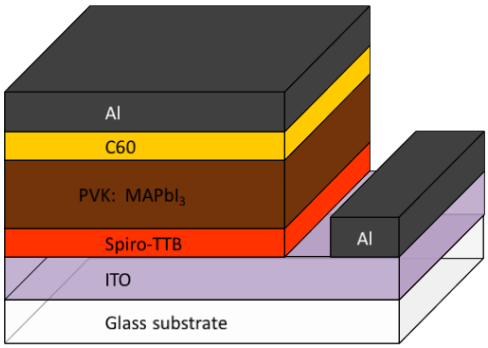

Figure A.6: ITO/Spiro-TTB/$MAPbI_3$/C60/Al

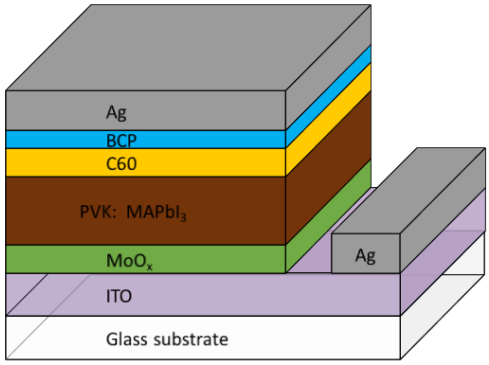

Figure A.7: ITO/MoO_x/$MAPbI_3$/C60/BCP/Ag

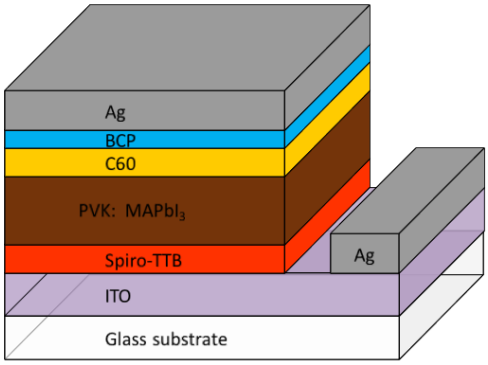

Figure A.8: ITO/Spiro-TTB/$MAPbI_3$/C60/BCP/Ag

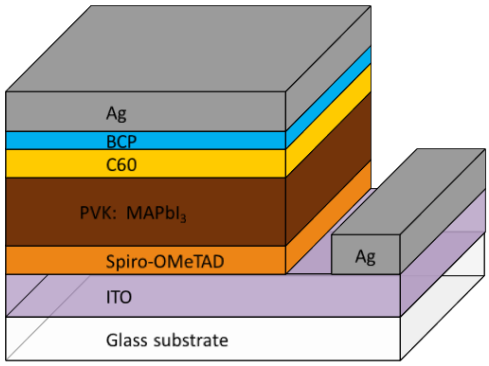

Figure A.9: ITO/Spiro-OMeTAD/$MAPbI_3$/C60/BCP/Ag

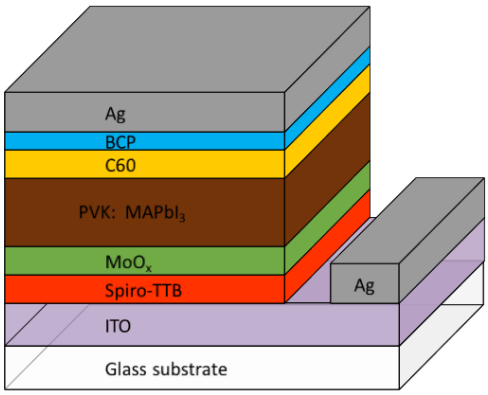

Figure A.10: ITO/Spiro-TTB/MoO_x/$MAPbI_3$/C60/BCP/Ag

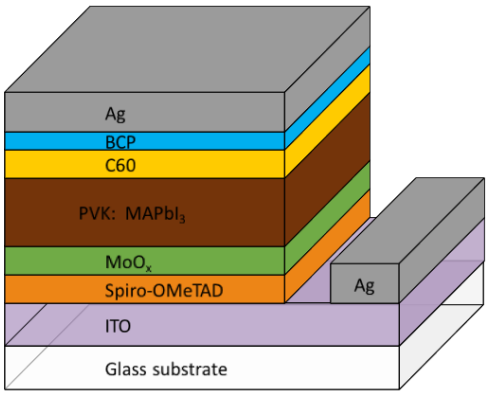

Figure A.11:
ITO/Spiro-OMeTAD/MoO_x/$MAPbI_3$/C60/BCP/Ag

A.2. Matlab script to calculate nominal thicknesses for thermally evaporated PVK

```
clear all
clc

%Constants
rho_PbI2 = 6.16;      % Density of PbI2 in [g/cm^3]
rho_FAI  = 2.31;      % Density of FAI in [g/cm^3]
rho_CsBr = 4.44;      % Density of CsBr in [g/cm^3]
MM_PbI2  = 461.01;    % Molar mass of PbI2 in [g/mol]
MM_FAI   = 171.97;    % Molar mass of FAI in [g/mol]
MM_CsBr  = 212.81;    % Molar mass of CsBr in [g/mol]

%Desired molar ratio between precursors n_PbI2:n_FAI:n_CsBr
n_PbI2   = 1;
n_FAI    = 0.85;
n_CsBr   = 0.15;

%Total target thickness
t_target_total = 100;         % [nm]

%System of equations and solving n = t*rho/MM
syms t_PbI2 t_FAI t_CsBr
eqn1 = (t_PbI2*rho_PbI2/MM_PbI2)/(t_FAI*rho_FAI/MM_FAI) == n_PbI2/n_FAI;
eqn2 = (t_PbI2*rho_PbI2/MM_PbI2)/(t_CsBr*rho_CsBr/MM_CsBr) == n_PbI2/n_CsBr;
%eqn3 = (t_FAI*rho_FAI/MM_FAI)/(t_CsBr*rho_CsBr/MM_CsBr) == n_FAI/n_CsBr; % Extra equation to solve the system
eqn3 = t_PbI2+t_FAI+t_CsBr == t_target_total;
sol = solve([eqn1, eqn2, eqn3], [t_PbI2, t_FAI, t_CsBr]);

% Real desired thicknesses to fulfill desired molar ratio
% t_actual_PbI2 = (double(sol.t_PbI2)/(double(sol.t_PbI2)+double(sol.t_FAI)+double(sol.t_CsBr)));
% t_actual_FAI = (double(sol.t_FAI)/(double(sol.t_PbI2)+double(sol.t_FAI)+double(sol.t_CsBr)));
% t_actual_CsBr = (double(sol.t_CsBr)/(double(sol.t_PbI2)+double(sol.t_FAI)+double(sol.t_CsBr)));

t_actual_PbI2 = (double(sol.t_PbI2));
t_actual_FAI = (double(sol.t_FAI));
t_actual_CsBr = (double(sol.t_CsBr));

% Tooling factor of sources TF = t_actual/t_sensor
TF_S1 = 0.394; %0.394 for the 100 nm PbI2, 0.344 for the 300 nm PbI2
TF_S2 = 0.833; % SEM
TF_S3 = 0.922; % Determined on 100 nm of CsBr

% Sensor thicknesses for setting in evaporator in nm

t_sensor_PbI2 = t_actual_PbI2/TF_S1    % [nm]
t_sensor_FAI = t_actual_FAI/TF_S2      % [nm]
```

```
t_sensor_CsBr = t_actual_CsBr/TF_S3    % [nm]
```

A.3. Deposition recipe for aluminium and C60

C60 deposition

1. Set QCM values for C60:
    - Acoustic impedance: $0.5650 \cdot 10^5$ g/cm^{2}s
    - Material density: 1.65 g/cm^3
    - TF: 120%
2. Rotation to 10 rpm and switch on power supply 3
3. Ramp up current to 29 A in 480 s
4. Manually open shutter, deposit until target thickness is reached, manually close shutter
5. Ramp down current to 0 A in 700 s
6. Turn off power supply 3 and rotation to 0 rpm

Aluminium deposition

1. Set QCM values for Al:
    - Acoustic impedance: $17.1 \cdot 10^5$ g/cm^{2}s
    - Material density: 2.70 g/cm^3
    - TF: 184%
2. Rotation to 15 rpm and switch on power supply 2
3. Ramp up current to 39 A in 700 s
4. Manually open shutter, deposit until target thickness is reached, manually close shutter
5. Ramp down current to 0 A in 1000 s
6. Turn off power supply 2 and rotation to 0 rpm

A.4. Diffractogram and spectrophotometry spectra for a quartz substrate

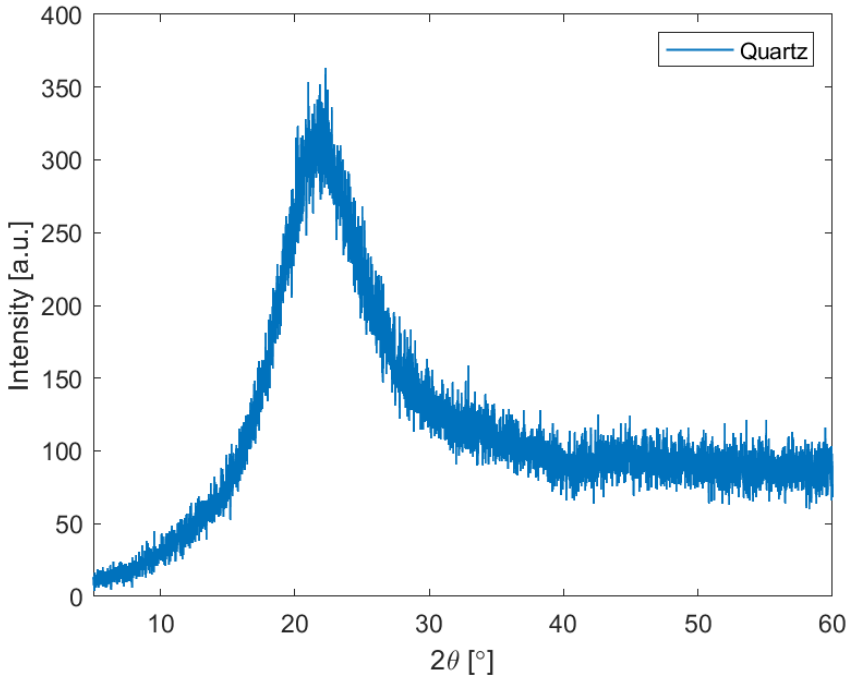

Figure A.12: Diffractogram of a quartz substrate showing the amorphous phase.

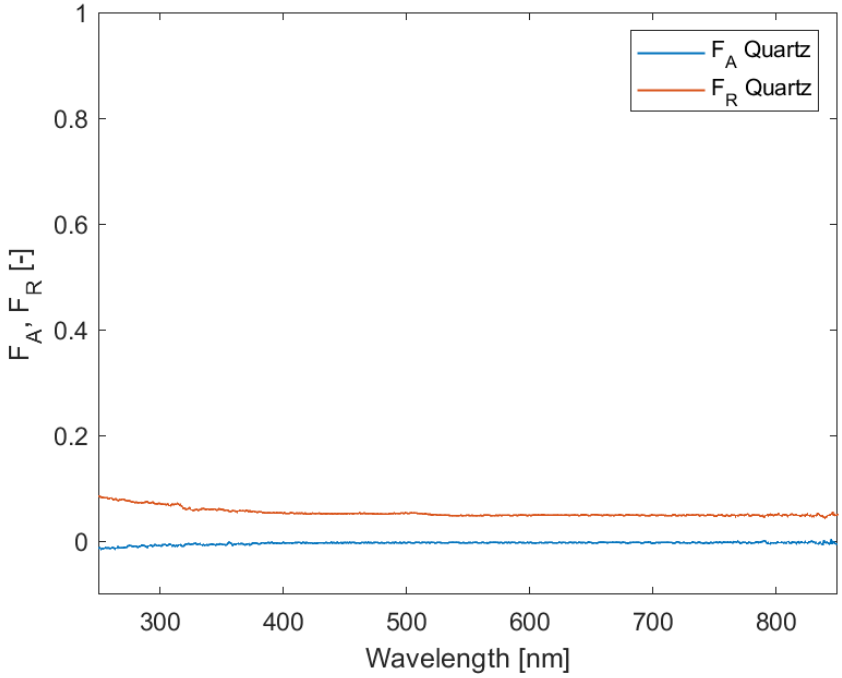

Figure A.13: F_A and F_R as a function of wavelength for a quartz substrate. F_R calculated from measurement of F_A and F_T.

A.5. Correction factors and Matlab code four-point probe method

Table A.1: 4.5324·CF for the calculation of the sheet resistance depending on the dimensions of a sample [104].

d/S	a/d = 1	a/d = 2	a/d = 3	a/d = 4
1.0			0.9988	0.994
1.25			1.2467	1.2248
1.5		1.4788	1.4893	1.4893
1.75		1.7196	1.7238	1.7238
2.0		1.9454	1.9475	1.9475
2.5		2.3532	2.3541	2.3541
3.0	2.4575	2.7000	2.7005	2.7005
4.0	3.1137	3.2246	3.2248	3.2248
5.0	3.5098	3.5749	3.5750	3.5750
7.5	4.0095	4.0361	4.0362	4.0362
10.0	4.2209	4.2357	4.2357	4.2357
15.0	4.3882	4.3947	4.3947	4.3947
20.0	4.4516	4.4553	4.4553	4.4553
40.0	4.5120	4.5129	4.5129	4.5129
∞	4.5324	4.5324	4.5324	4.5324

```
clear all
close all
clc
%% Cubic interpolation for a small cell 0.16 cm^2
% Small cell: d/s = 4
% Small cell: a/d = 1.875
aoverd = [1 2 3 4];  % Different values from table for a/d
CF_at_four = [3.1137 3.2246 3.2248 3.2248]; % Correction factors at d/s=4 for the different a/d values
xx = 1:0.005:4; % Vector for a/d values
IV = spline(aoverd, CF_at_four, xx); % To make a plot
plot(xx,IV)
hold on
plot(aoverd,CF_at_four)

CF_SC = spline(aoverd, CF_at_four, 1.875); %To calculate the correcting factor at a/d = 1.875

%% Cubic interpolation for big cell 0.36 cm^2
% Big cell: d/s = 6
% Big cell: a/d = 1.5833333....
DoverS = [3 4 5 7.5 10.0 15.0 20.0 40.0]; % Different d/s values
aoverd_een = [2.4575 3.1137 3.5098 4.0095 4.2209 4.3882 4.4516 4.5120]; %Values from table
aoverd_twee = [2.7000 3.2246 3.5749 4.0361 4.2357 4.3947 4.4553 4.5129];
aoverd_drie = [2.7005 3.2248 3.5750 4.0362 4.2357 4.3947 4.4553 4.5129];
aoverd_vier = [2.7005 3.2248 3.5750 4.0362 4.2357 4.3947 4.4553 4.5129];

W = spline(DoverS, aoverd_een, 6);
R = spline(DoverS, aoverd_twee, 6);
Y = spline(DoverS, aoverd_drie, 6);
P = spline(DoverS, aoverd_vier, 6);

CF_at_six = [W R Y P]; % First cubic interpolation to find value for d/s = 6

CF_BC = spline(aoverd, CF_at_six, 9.5/6); % Second cubic interpolation to find value for a/d = 1/583...
```

A.6. Development of ellipsometry model for spiro-TTB

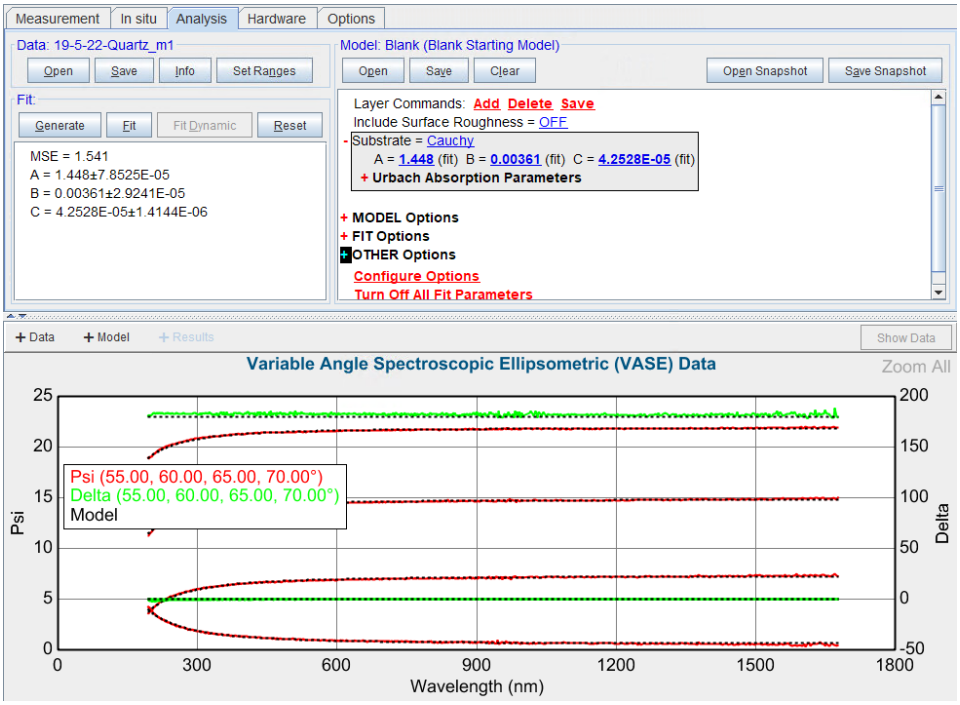

Figure A.14: SE model for quartz only.

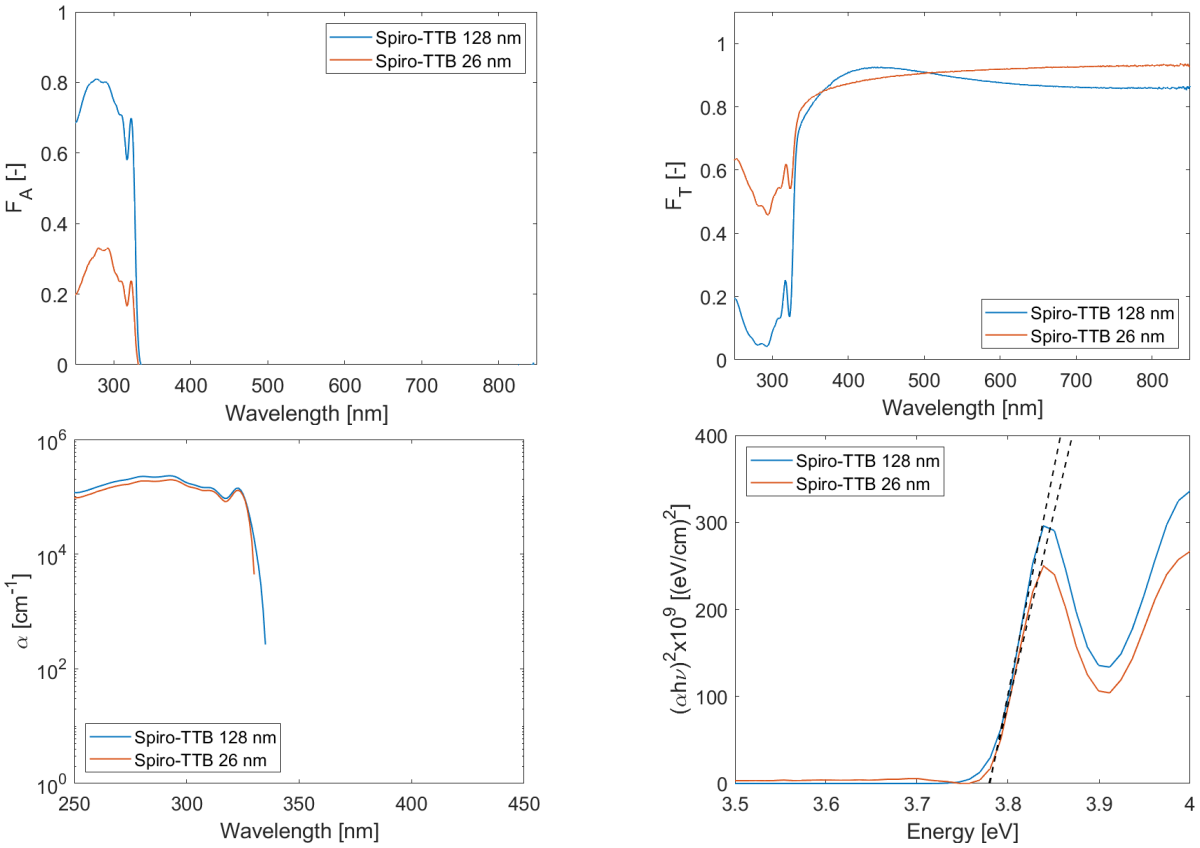

Figure A.15: F_A (top left), F_R (top right) and α (bottom left) as a function of wavelength for two spiro-TTB layers of 128 nm (blue) and 26 nm (red). Tauc plot for 128 nm (blue) and 26 nm (red) spiro-TTB layer (bottom right), linear part is extended to the x-axis (black).

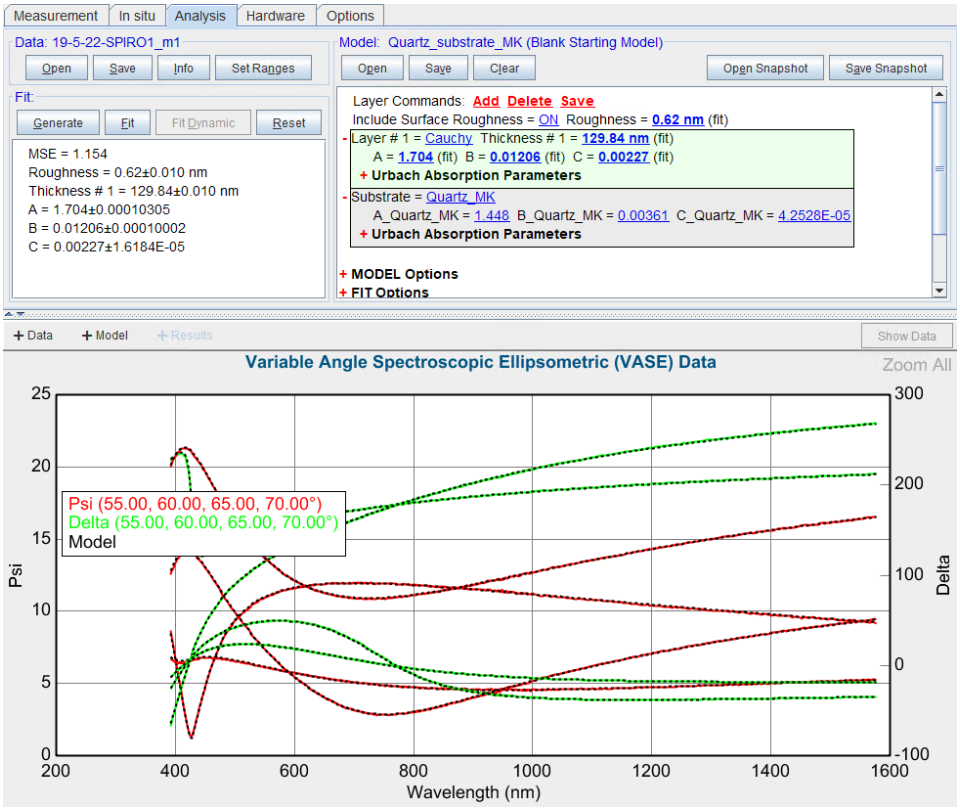

Figure A.16: Cauchy model for 128 nm spiro-TTB on quartz.

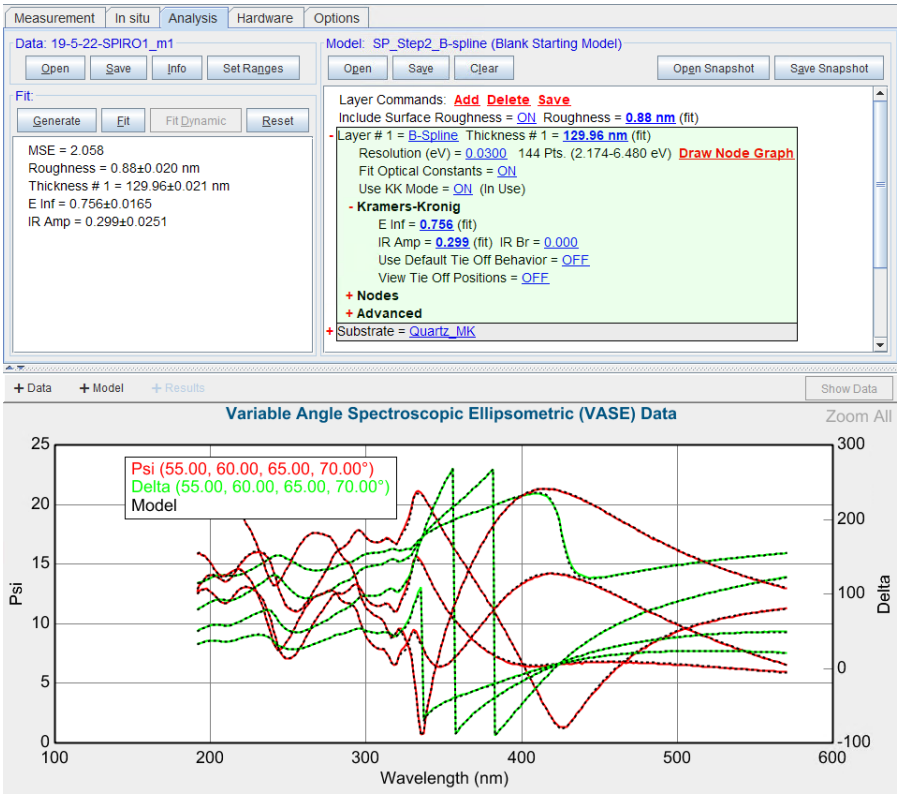

Figure A.17: B-spline model for 128 nm spiro-TTB on quartz.

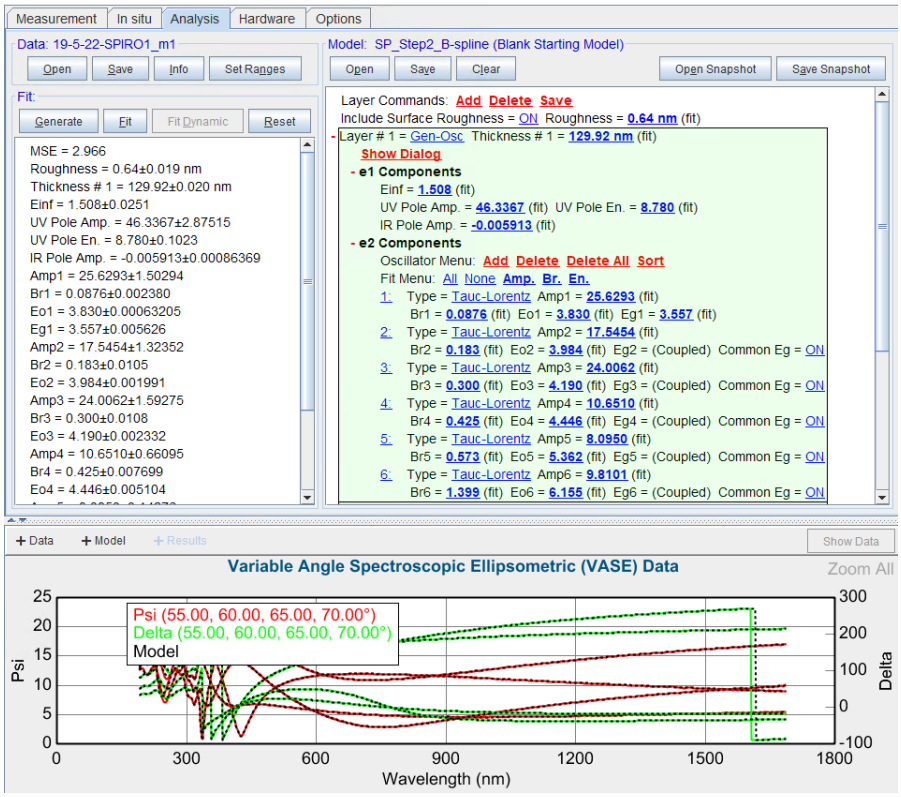

Figure A.18: Generic oscillator model for 128 nm spiro-TTB on quartz.

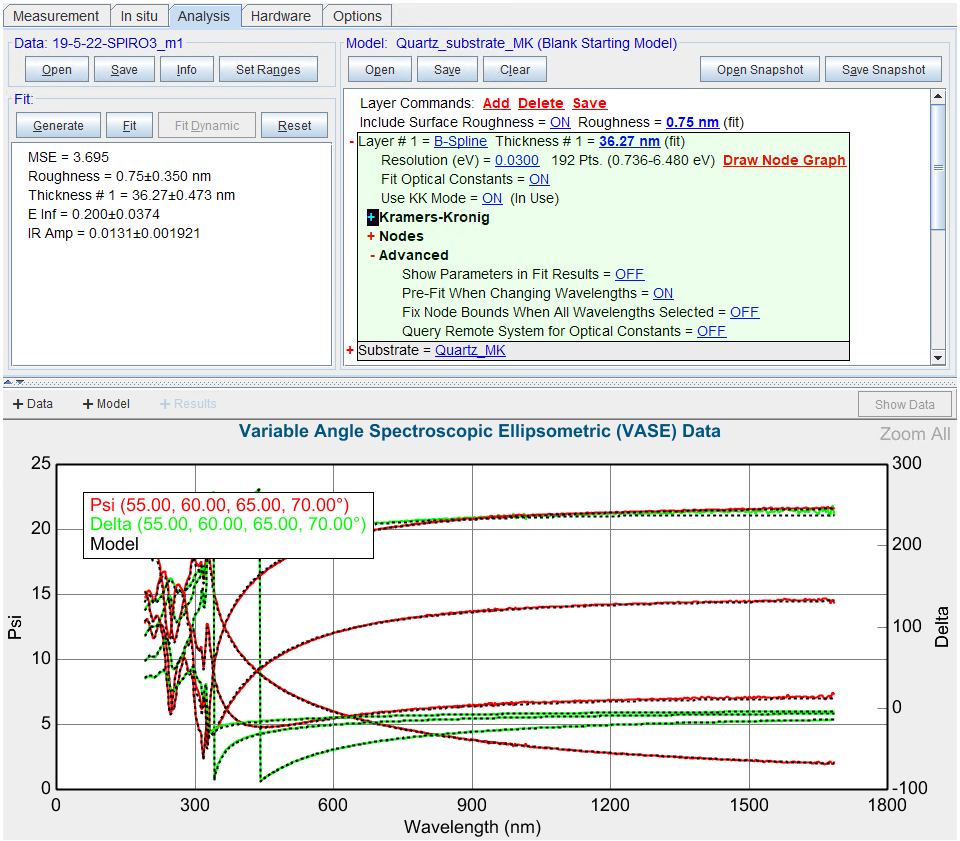

Figure A.19: B-spline model for 26 nm spiro-TTB on quartz.

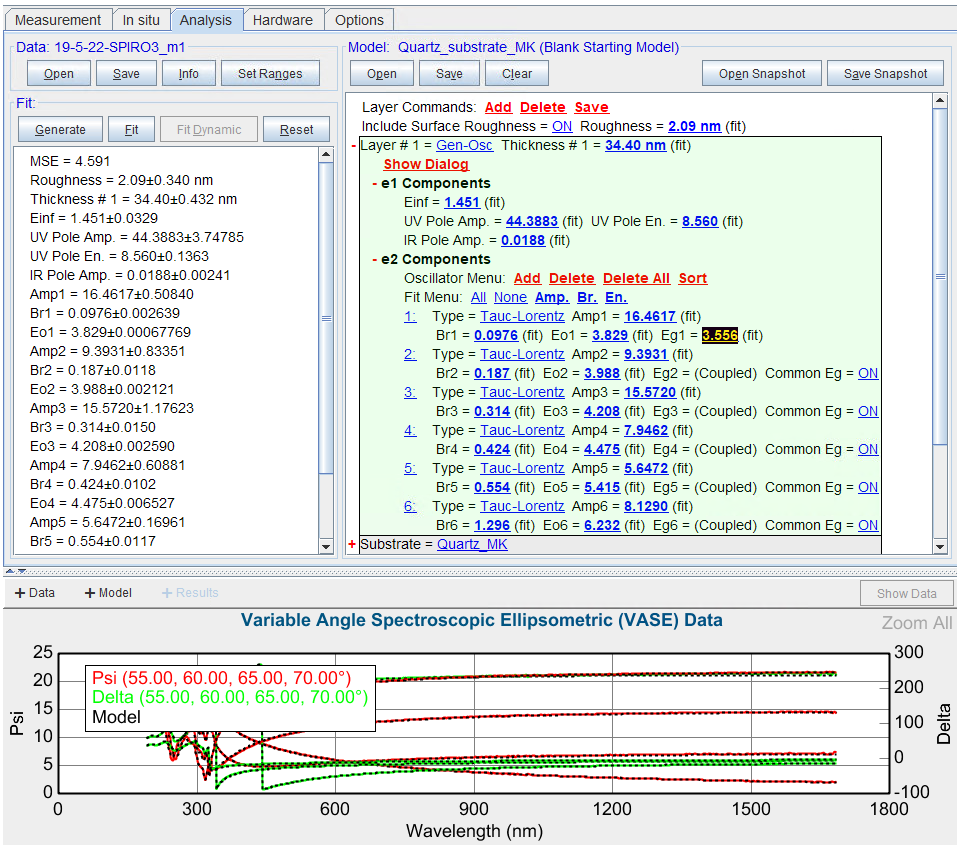

Figure A.20: Generic oscillator model for 26 nm spiro-TTB on quartz.

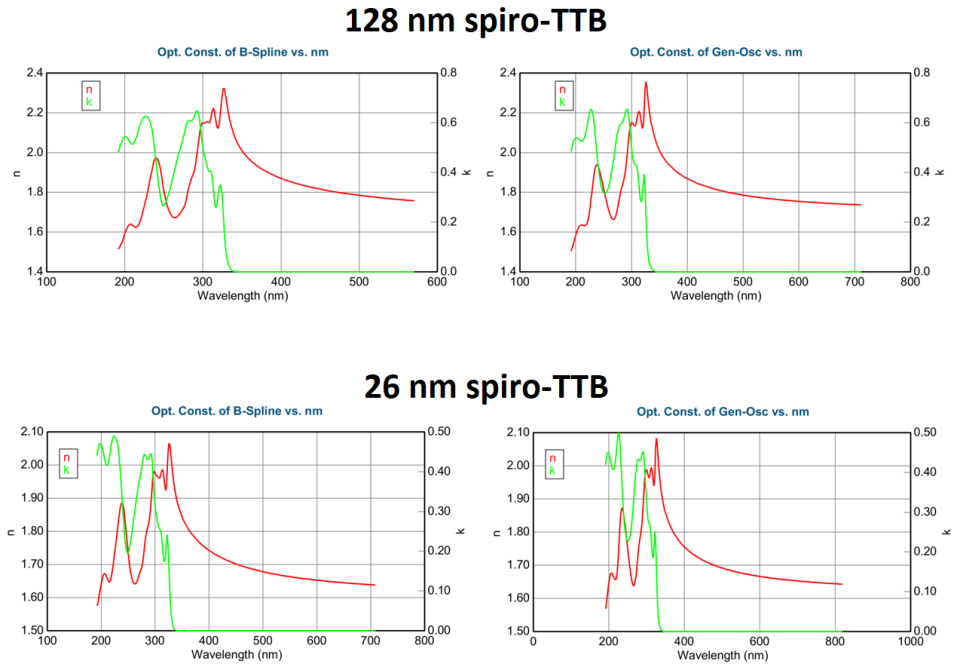

Figure A.21: Top left: n and k data for 128 nm spiro-TTB with b-spline model. Top right: n and k data for 128 nm spiro-TTB with generic oscillator model. Bottom left: n and k data for 26 nm spiro-TTB with b-spline model. Bottom right: n and k data for 26 nm spiro-TTB with generic oscillator model.

Bibliography

[1] U.S. Department of Energy, "International energy outlook", Energy Information Administration, Tech. Rep., 2021.

[2] IPCC, "Climate change 2022: Mitigation of climate change", Intergovernmental Panel on Climate Change, Tech. Rep., 2022.

[3] VUK LTD, "ISO 50001 (enms) energy management systems", TUV NORD, Tech. Rep., 2014.

[4] Solar Energy Technologies Office, *How does solar work?*, Sep. 2020. [Online]. Available: https://www.energy.gov/eere/solar/how-does-solar-work.

[5] International Energy Agency, *Solar pv*, Nov. 2021. [Online]. Available: https://www.iea.org/reports/solar-pv.

[6] T. Saga, "Advances in crystalline silicon solar cell technology for industrial mass production", *NPG Asia Materials*, vol. 2, no. 3, pp. 96–102, Jul. 2010. DOI: 10.1038/asiamat.2010.82.

[7] Fraunhofer Institute for Solar Energy Systems, "Photovoltaics report", Fraunhofer ISE, Tech. Rep., 2022.

[8] W. Shockley and H. J. Queisser, "Detailed balance limit of efficiency of p-n junction solar cells", *Journal of Applied Physics*, vol. 32, no. 3, pp. 510–519, Mar. 1961. DOI: 10.1063/1.1736034.

[9] A. Richter, M. Hermle, and S. W. Glunz, "Reassessment of the limiting efficiency for crystalline silicon solar cells", *IEEE Journal of Photovoltaics*, vol. 3, no. 4, pp. 1184–1191, Oct. 2013. DOI: 10.1109/jphotov.2013.2270351.

[10] W. Liu, H. Li, B. Qiao, S. Zhao, Z. Xu, and D. Song, "Highly efficient CIGS solar cells based on a new CIGS bandgap gradient design characterized by numerical simulation", *Solar Energy*, vol. 233, pp. 337–344, Feb. 2022. DOI: 10.1016/j.solener.2022.01.054.

[11] A. Kojima, K. Teshima, Y. Shirai, and T. Miyasaka, "Organometal halide perovskites as visible-light sensitizers for photovoltaic cells", *Journal of the American Chemical Society*, vol. 131, no. 17, pp. 6050–6051, Apr. 2009. DOI: 10.1021/ja809598r.

[12] J.-H. Im, C.-R. Lee, J.-W. Lee, S.-W. Park, and N.-G. Park, "6.5% efficient perovskite quantum-dot-sensitized solar cell", *Nanoscale*, vol. 3, no. 10, p. 4088, 2011. DOI: 10.1039/c1nr10867k.

[13] H.-S. Kim, C.-R. Lee, J.-H. Im, K.-B. Lee, T. Moehl, A. Marchioro, S.-J. Moon, R. Humphry-Baker, J.-H. Yum, J. E. Moser, M. Grätzel, and N.-G. Park, "Lead iodide perovskite sensitized all-solid-state submicron thin film mesoscopic solar cell with efficiency exceeding 9%", *Scientific Reports*, vol. 2, no. 1, Aug. 2012. DOI: 10.1038/srep00591.

[14] M. Liu, M. B. Johnston, and H. J. Snaith, "Efficient planar heterojunction perovskite solar cells by vapour deposition", *Nature*, vol. 501, no. 7467, pp. 395–398, Sep. 2013. DOI: 10.1038/nature12509.

[15] H. Min, D. Y. Lee, J. Kim, G. Kim, K. S. Lee, J. Kim, M. J. Paik, Y. K. Kim, K. S. Kim, M. G. Kim, T. J. Shin, and S. I. Seok, "Perovskite solar cells with atomically coherent interlayers on SnO2 electrodes", *Nature*, vol. 598, no. 7881, pp. 444–450, Oct. 2021. DOI: 10.1038/s41586-021-03964-8.

[16] S. Prathapani, P. Bhargava, and S. Mallick, "Electronic band structure and carrier concentration of formamidinium-cesium mixed cation lead mixed halide hybrid perovskites", *Applied Physics Letters*, vol. 112, no. 9, p. 092 104, Feb. 2018. DOI: 10.1063/1.5016829.

[17] K. P. Bhandari and R. J. Ellingson, "An overview of hybrid organic–inorganic metal halide perovskite solar cells", in *A Comprehensive Guide to Solar Energy Systems*, Elsevier, 2018, pp. 233–254. DOI: 10.1016/b978-0-12-811479-7.00011-7.

[18] D. Li, D. Zhang, K.-S. Lim, Y. Hu, Y. Rong, A. Mei, N.-G. Park, and H. Han, "A review on scaling up perovskite solar cells", *Advanced Functional Materials*, vol. 31, no. 12, p. 2 008 621, Dec. 2020. DOI: 10.1002/adfm.202008621.

[19] T. Soto-Montero, W. Soltanpoor, and M. Morales-Masis, "Pressing challenges of halide perovskite thin film growth", *APL Materials*, vol. 8, no. 11, p. 110 903, Nov. 2020. DOI: 10.1063/5.0027573.

[20] A. T. Sabu Thomas, Ed., *Perovskite Photovoltaics*. Elsevier, 2018. DOI: 10.1016/c2016-0-03790-7.

[21] A. Smets, K. Jager, O. Isabella, R. van Swaaij, and M. Zeman, *Solar Energy*. UIT Cambridge LTD, Feb. 2016, 488 pp., ISBN: 1906860327. [Online]. Available: https://www.ebook.de/de/product/25115410/arno_smets_klaus_jager_olindo_isabella_rene_van_swaaij_miro_zeman_solar_energy.html.

[22] D. Neamen, *Semiconductor Physics and Devices: Basic Principles*. MCGRAW HILL BOOK CO, Jan. 2011, 784 pp., ISBN: 0073529583. [Online]. Available: https://www.ebook.de/de/product/13620453/donald_neamen_semiconductor_physics_and_devices_basic_principles.html.

[23] L. Tous, "Nickel/copper plated contacts as an alternative to silver screen printing for the front side metallization of industrial high efficiency silicon solar cells", PhD thesis, KU Leuven, Jan. 2014.

[24] D. Naemen, *Semiconductor Physics and Devices*, L. Neyens, Ed. Mc Graw Hill, 2012.

[25] C. Honsberg and S. Bowden, *A collection of resources for the photovoltaic educator*, 2019. [Online]. Available: https://www.pveducation.org/.

[26] J. Cubas, S. Pindado, and C. de Manuel, "Explicit expressions for solar panel equivalent circuit parameters based on analytical formulation and the lambert w-function", *Energies*, vol. 7, no. 7, pp. 4098–4115, Jun. 2014. DOI: 10.3390/en7074098.

[27] Analog Devices, *Activity: Characteristics of photovoltaic solar cells*, May 2015. [Online]. Available: https://wiki.analog.com/_detail/university/courses/.

[28] S. F. Hoefler, G. Trimmel, and T. Rath, "Progress on lead-free metal halide perovskites for photovoltaic applications: A review", *Monatshefte für Chemie - Chemical Monthly*, vol. 148, no. 5, pp. 795–826, Mar. 2017. DOI: 10.1007/s00706-017-1933-9.

[29] A. M. A. Leguy, P. Azarhoosh, M. I. Alonso, M. Campoy-Quiles, O. J. Weber, J. Yao, D. Bryant, M. T. Weller, J. Nelson, A. Walsh, M. van Schilfgaarde, and P. R. F. Barnes, "Experimental and theoretical optical properties of methylammonium lead halide perovskites", *Nanoscale*, vol. 8, no. 12, pp. 6317–6327, 2016. DOI: 10.1039/c5nr05435d.

[30] M. Shirayama, H. Kadowaki, T. Miyadera, T. Sugita, M. Tamakoshi, M. Kato, T. Fujiseki, D. Murata, S. Hara, T. N. Murakami, S. Fujimoto, M. Chikamatsu, and H. Fujiwara, "Optical transitions in hybrid perovskite solar cells: Ellipsometry, density functional theory, and quantum efficiency analyses", *Physical Review Applied*, vol. 5, no. 1, p. 014 012, Jan. 2016. DOI: 10.1103/physrevapplied.5.014012.

[31] A. Zekry, I. Yahyaoui, and F. Tadeo, "Generic analytical models for organic and perovskite solar cells", in *2019 10th International Renewable Energy Congress (IREC)*, IEEE, Mar. 2019. DOI: 10.1109/irec.2019.8754574.

[32] D. Kiermasch, P. Rieder, K. Tvingstedt, A. Baumann, and V. Dyakonov, "Improved charge carrier lifetime in planar perovskite solar cells by bromine doping", *Scientific Reports*, vol. 6, no. 1, Dec. 2016. DOI: 10.1038/srep39333.

[33] D. Wang, M. Wright, N. K. Elumalai, and A. Uddin, "Stability of perovskite solar cells", *Solar Energy Materials and Solar Cells*, vol. 147, pp. 255–275, Apr. 2016. DOI: 10.1016/j.solmat.2015.12.025.

[34] G. Niu, X. Guo, and L. Wang, "Review of recent progress in chemical stability of perovskite solar cells", *Journal of Materials Chemistry A*, vol. 3, no. 17, pp. 8970–8980, 2015. DOI: 10.1039/c4ta04994b.

[35] Y.-H. Chiang, M. Anaya, and S. D. Stranks, "Multisource vacuum deposition of methylammonium-free perovskite solar cells", *ACS Energy Letters*, vol. 5, no. 8, pp. 2498–2504, Jun. 2020. DOI: 10.1021/acsenergylett.0c00839.

[36] L. Gil-Escrig, C. Momblona, M.-G. La-Placa, P. P. Boix, M. Sessolo, and H. J. Bolink, "Vacuum deposited triple-cation mixed-halide perovskite solar cells", *Advanced Energy Materials*, vol. 8, no. 14, p. 1 703 506, Feb. 2018. DOI: 10.1002/aenm.201703506.

[37] T. Leijtens, B. Lauber, G. E. Eperon, S. D. Stranks, and H. J. Snaith, "The importance of perovskite pore filling in organometal mixed halide sensitized TiO2-based solar cells", *The Journal of Physical Chemistry Letters*, vol. 5, no. 7, pp. 1096–1102, Mar. 2014. DOI: 10.1021/jz500209g.

[38] G. Xing, N. Mathews, S. Sun, S. S. Lim, Y. M. Lam, M. Grätzel, S. Mhaisalkar, and T. C. Sum, "Long-range balanced electron- and hole-transport lengths in organic-inorganic CH3NH3PbI3", *Science*, vol. 342, no. 6156, pp. 344–347, Oct. 2013. DOI: 10.1126/science.1243167.

[39] Ossila, *Perovskites and perovskite solar cells: An introduction*, Jun. 2018. [Online]. Available: https://www.ossila.com/en-eu/pages/perovskites-and-perovskite-solar-cells-an-introduction.

[40] I. Mora-Sero, "How do perovskite solar cells work?", *Joule*, vol. 2, no. 4, pp. 585–587, Apr. 2018. DOI: 10.1016/j.joule.2018.03.020.

[41] K. Rakstys, C. Igci, and M. K. Nazeeruddin, "Efficiency vs.stability: Dopant-free hole transporting materials towards stabilized perovskite solar cells", *Chemical Science*, vol. 10, no. 28, pp. 6748–6769, 2019. DOI: 10.1039/c9sc01184f.

[42] P. Lopez-Varo, J. A. Jiménez-Tejada, M. Garcia-Rosell, S. Ravishankar, G. Garcia-Belmonte, J. Bisquert, and O. Almora, "Device physics of hybrid perovskite solar cells: Theory and experiment", *Advanced Energy Materials*, vol. 8, no. 14, p. 1 702 772, Feb. 2018. DOI: 10.1002/aenm.201702772.

[43] C.-S. Jiang, M. Yang, Y. Zhou, B. To, S. U. Nanayakkara, J. M. Luther, W. Zhou, J. J. Berry, J. van de Lagemaat, N. P. Padture, K. Zhu, and M. M. Al-Jassim, "Carrier separation and transport in perovskite solar cells studied by nanometre-scale profiling of electrical potential", *Nature Communications*, vol. 6, no. 1, Sep. 2015. DOI: 10.1038/ncomms9397.

[44] R. Ji, Z. Zhang, C. Cho, Q. An, F. Paulus, M. Kroll, M. Löffler, F. Nehm, B. Rellinghaus, K. Leo, and Y. Vaynzof, "Thermally evaporated methylammonium-free perovskite solar cells", *Journal of Materials Chemistry C*, vol. 8, no. 23, pp. 7725–7733, 2020. DOI: 10.1039/d0tc01550d.

[45] Z. Chen, B. Turedi, A. Y. Alsalloum, C. Yang, X. Zheng, I. Gereige, A. AlSaggaf, O. F. Mohammed, and O. M. Bakr, "Single-crystal MAPbI3 perovskite solar cells exceeding 21% power conversion efficiency", *ACS Energy Letters*, vol. 4, no. 6, pp. 1258–1259, May 2019. DOI: 10.1021/acsenergylett.9b00847.

[46] J. Li, H. A. Dewi, H. Wang, J. H. Lew, N. Mathews, S. Mhaisalkar, and A. Bruno, "Design of perovskite thermally co-evaporated highly efficient mini-modules with high geometrical fill factors", *Solar RRL*, vol. 4, no. 12, p. 2 000 473, Oct. 2020. DOI: 10.1002/solr.202000473.

[47] C. Wang, J. Hu, C. Li, S. Qiu, X. Liu, L. Zeng, C. Liu, Y. Mai, and F. Guo, "Spiro-linked molecular hole-transport materials for highly efficient inverted perovskite solar cells", *Solar RRL*, vol. 4, no. 3, p. 1 900 389, Nov. 2019. DOI: 10.1002/solr.201900389.

[48] G. M. Arumugam, S. K. Karunakaran, C. Liu, C. Zhang, F. Guo, S. Wu, and Y. Mai, "Inorganic hole transport layers in inverted perovskite solar cells: A review", *Nano Select*, vol. 2, no. 6, pp. 1081–1116, Jan. 2021. DOI: 10.1002/nano.202000200.

[49] T. Golubev, D. Liu, R. Lunt, and P. Duxbury, "Understanding the impact of c60 at the interface of perovskite solar cells via drift-diffusion modeling", *AIP Advances*, vol. 9, no. 3, p. 035 026, Mar. 2019. DOI: 10.1063/1.5068690.

[50] R. Saive, "S-shaped current–voltage characteristics in solar cells: A review", *IEEE Journal of Photovoltaics*, vol. 9, no. 6, pp. 1477–1484, Nov. 2019. DOI: 10.1109/jphotov.2019.2930409.

[51] S.-E. Chiang, J.-R. Wu, H.-M. Cheng, C.-L. Hsu, J.-L. Shen, C.-T. Yuan, and S. H. Chang, "Origins of the s-shape characteristic in j-v curve of inverted-type perovskite solar cells", *Nanotechnology*, vol. 31, no. 11, p. 115 403, Dec. 2019. DOI: 10.1088/1361-6528/ab5a02.

[52] S. Li, Y.-L. Cao, W.-H. Li, and Z.-S. Bo, "A brief review of hole transporting materials commonly used in perovskite solar cells", *Rare Metals*, vol. 40, no. 10, pp. 2712–2729, May 2021. DOI: 10.1007/s12598-020-01691-z.

[53] B. T. Feleki, C. H. L. Weijtens, M. M. Wienk, and R. A. J. Janssen, "Thin thermally evaporated organic hole transport layers for reduced optical losses in substrate-configuration perovskite solar cells", *ACS Applied Energy Materials*, vol. 4, no. 4, pp. 3033–3043, Mar. 2021. DOI: 10.1021/acsaem.0c02653.

[54] F. Jannat, S. Ahmed, and M. A. Alim, "Performance analysis of cesium formamidinium lead mixed halide based perovskite solar cell with MoOx as hole transport material via SCAPS-1d", *Optik*, vol. 228, p. 166 202, Feb. 2021. DOI: 10.1016/j.ijleo.2020.166202.

[55] E. Bobeico, L. V. Mercaldo, P. Morvillo, I. Usatii, M. D. Noce, L. Lancellotti, C. Sasso, R. Ricciardi, and P. D. Veneri, "Evaporated MoOx as general back-side hole collector for solar cells", *Coatings*, vol. 10, no. 8, p. 763, Aug. 2020. DOI: 10.3390/coatings10080763.

[56] D. M. Torres-Herrera, P. M. Moreno-Romero, D. Cabrera-German, H. J. Cortina-Marrero, M. Sotelo-Lerma, and H. Hu, "Thermal co-evaporated MoOx:au thin films and its application as anode modifier in perovskite solar cells", *Solar Energy*, vol. 206, pp. 136–144, Aug. 2020. DOI: 10.1016/j.solener.2020.05.105.

[57] S. Wang, T. Sakurai, W. Wen, and Y. Qi, "Energy level alignment at interfaces in metal halide perovskite solar cells", *Advanced Materials Interfaces*, vol. 5, no. 22, p. 1 800 260, Jul. 2018. DOI: 10.1002/admi.201800260.

[58] K. Mahmood, S. Sarwar, and M. T. Mehran, "Current status of electron transport layers in perovskite solar cells: Materials and properties", *RSC Advances*, vol. 7, no. 28, pp. 17 044–17 062, 2017. DOI: 10.1039/c7ra00002b.

[59] G. Yang, H. Tao, P. Qin, W. Ke, and G. Fang, "Recent progress in electron transport layers for efficient perovskite solar cells", *Journal of Materials Chemistry A*, vol. 4, no. 11, pp. 3970–3990, 2016. DOI: 10.1039/c5ta09011c.

[60] K.-M. Lee, C.-C. Chen, L.-C. Chen, S. H. Chang, K.-S. Chen, S.-C. Yeh, C.-T. Chen, and C.-G. Wu, "Thickness effects of thermally evaporated c60 thin films on regular-type CH3nh3pbi3 based solar cells", *Solar Energy Materials and Solar Cells*, vol. 164, pp. 13–18, May 2017. DOI: 10.1016/j.solmat.2017.02.003.

[61] N. Klipfel, A. O. Alvarez, H. Kanda, A. A. Sutanto, C. Igci, C. Roldán-Carmona, C. Momblona, F. Fabregat-Santiago, and M. K. Nazeeruddin, "C60 thin films in perovskite solar cells: Efficient or limiting charge transport layer?", *ACS Applied Energy Materials*, vol. 5, no. 2, pp. 1646–1655, Jan. 2022. DOI: 10.1021/acsaem.1c03060.

[62] A. Smets, *Tco-part 1*, 2017. [Online]. Available: https://ocw.tudelft.nl/course-lectures/tco-part-1/.

[63] A. Stadler, "Transparent conducting oxides - an up-to-date overview", *Materials*, vol. 5, no. 12, pp. 661–683, Apr. 2012. DOI: 10.3390/ma5040661.

[64] P. P. Edwards, A. Porch, M. O. Jones, D. V. Morgan, and R. M. Perks, "Basic materials physics of transparent conducting oxides", *Dalton Transactions*, no. 19, p. 2995, 2004. DOI: 10.1039/b408864f.

[65] N. Shibayama, H. Kanda, T. W. Kim, H. Segawa, and S. Ito, "Design of BCP buffer layer for inverted perovskite solar cells using ideal factor", *APL Materials*, vol. 7, no. 3, p. 031 117, Mar. 2019. DOI: 10.1063/1.5087796.

[66] P. P. Rajbhandari and T. P. Dhakal, "Low temperature ALD growth optimization of ZnO, TiO, and al2o3 to be used as a buffer layer in perovskite solar cells", *Journal of Vacuum Science and Technology A*, vol. 38, no. 3, p. 032 406, May 2020. DOI: 10.1116/1.5139247.

[67] R. Chen, B. Long, S. Wang, Y. Liu, J. Bai, S. Huang, H. Li, and X. Chen, "Efficient and stable perovskite solar cells using bathocuproine bilateral-modified perovskite layers", *ACS Applied Materials and Interfaces*, vol. 13, no. 21, pp. 24 747–24 755, May 2021. DOI: 10.1021/acsami.1c03637.

[68] C. Chen, S. Zhang, S. Wu, W. Zhang, H. Zhu, Z. Xiong, Y. Zhang, and W. Chen, "Effect of BCP buffer layer on eliminating charge accumulation for high performance of inverted perovskite solar cells", *RSC Advances*, vol. 7, no. 57, pp. 35 819–35 826, 2017. DOI: 10.1039/c7ra06365b.

[69] J. Troughton, M. Neophytou, N. Gasparini, A. Seitkhan, F. H. Isikgor, X. Song, Y.-H. Lin, T. Liu, H. Faber, E. Yengel, J. Kosco, M. F. Oszajca, B. Hartmeier, M. Rossier, N. A. Lüchinger, L. Tsetseris, H. J. Snaith, S. D. Wolf, T. D. Anthopoulos, I. McCulloch, and D. Baran, "A universal solution processed interfacial bilayer enabling ohmic contact in organic and hybrid optoelectronic devices", *Energy and Environmental Science*, vol. 13, no. 1, pp. 268–276, 2020. DOI: 10.1039/c9ee02202c.

[70] M. Imran, H. Cokun, F. H. Isikgor, L. Bichen, N. A. Khan, and J. Ouyang, "Highly efficient and stable inverted perovskite solar cells with two-dimensional ZnSe deposited using a thermal evaporator for electron collection", *Journal of Materials Chemistry A*, vol. 6, no. 45, pp. 22 713–22 720, 2018. DOI: 10.1039/c8ta08306a.

[71] Best Technology, *How do ultrasonic cleaners work?*, Jul. 2013. [Online]. Available: https://www.besttechnologyinc.com/precision-cleaning-systems/how-do-ultrasonics-work/.

[72] Ossila, *Uv ozone cleaner*, 2022. [Online]. Available: https://www.ossila.com/en-eu/products/uv-ozone-cleaner.

[73] T. Hu, F. Zhang, Z. Xu, S. Zhao, X. Yue, and G. Yuan, "Effect of UV–ozone treatment on ITO and post-annealing on the performance of organic solar cells", *Synthetic Metals*, vol. 159, no. 7-8, pp. 754–756, Apr. 2009. DOI: 10.1016/j.synthmet.2008.11.024.

[74] M. F. Albab, "Development of c60 transport layer and optical analysis of perovskite absorber material", Master's thesis, Delft University of Technology, Delft, 2021.

[75] A. Sarangan, "Thin-film optics", in *Nanofabrication*, CRC Press, Oct. 2016, pp. 99–125. DOI: 10.1201/9781315370514-4.

[76] K. Wasa, M. Kitabatake, and H. Adachi, "Thin film processes", in *Thin Film Materials Technology*, Elsevier, 2004, pp. 17–69. DOI: 10.1016/b978-081551483-1.50003-4.

[77] M. Ohring, *Materials Science of Thin Films*. Elsevier, 2002. DOI: 10.1016/b978-0-12-524975-1.x5000-9.

[78] Nanoscience Instruments, *Quartz crystal microbalance (qcm)*, Jan. 2019. [Online]. Available: https://www.nanoscience.com/techniques/quartz-crystal-microbalance/.

[79] A. Yurgens, *Lab demophysical evaporation of metals*, Nov. 2004.

[80] N. Ariel-Sternberg, *Tooling factor calibration standard operating procedure*, May 2017.

[81] K. S. S. Harsha, *Principles of Physical Vapor Deposition of Thin Films*. Elsevier, 2006.

[82] A. Rockett, *Section 1 evaporation*, University of Illinois, 1997.

[83] Ossila, *Spin coating: Complete guide to theory and techniques*, 2022. [Online]. Available: https://www.ossila.com/en-eu/pages/spin-coating#introduction-to-spin-coating.

[84] F. W. Low, C. W. Lai, N. A. Samsudin, Y. Yusoff, S. M. Goh, C. F. Chau, M. Shakeri, N. Amin, and S. K. Tiong, "Chapter 5 - graphene and its derivatives, synthesis route, and mechanism for photovoltaic solar cell applications", in *Sustainable Materials for Next Generation Energy Devices*, K. Y. Cheong and L.-C. Chen, Eds., Elsevier, 2021, pp. 103–132.

[85] M. Saleem, *Overview of magnetron sputtering system*, Lahore University of Management Sciences.

[86] S. Canossa, *Xrd data interpretation*, Delft University of Technology, Delft, The Netherlands, 2018.

[87] X. Liu, *X-ray powder diffraction interpretation*, Delft University of Technology, Delft, The Netherlands, 2018.

[88] C. Stan, C. Beavers, M. Kunz, and N. Tamura, "X-ray diffraction under extreme conditions at the advanced light source", *Quantum Beam Science*, vol. 2, no. 1, p. 4, Jan. 2018. DOI: 10.3390/qubs2010004.

[89] A. Höpe, "Diffuse reflectance and transmittance", in *Experimental Methods in the Physical Sciences*, Elsevier, 2014, pp. 179–219. DOI: 10.1016/b978-0-12-386022-4.00006-6.

[90] Perkin Elmer, *Applications and use of integrating spheres with the lambda 650 and 850 uv/vis and lambda 950 uv/vis/nir spectrophotometers*, Perkin Elmer, Shelton, United States, 2004.

[91] A. Fernández-García, F. Sutter, L. Martínez-Arcos, C. Sansom, F. Wolfertstetter, and C. Delord, "Equipment and methods for measuring reflectance of concentrating solar reflector materials", *Solar Energy Materials and Solar Cells*, vol. 167, pp. 28–52, Aug. 2017. DOI: 10.1016/j.solmat.2017.03.036.

[92] Sphere Optics, "Integrating sphere design and applications", Sphere Optics, Tech. Rep., 2007.

[93] J. Tauc, R. Grigorovici, and A. Vancu, "Optical properties and electronic structure of amorphous germanium", *physica status solidi (b)*, vol. 15, no. 2, pp. 627–637, 1966. DOI: 10.1002/pssb.19660150224.

[94] E. M. Hutter, M. C. Gélvez-Rueda, A. Osherov, V. Bulović, F. C. Grozema, S. D. Stranks, and T. J. Savenije, "Direct–indirect character of the bandgap in methylammonium lead iodide perovskite", *Nature Materials*, vol. 16, no. 1, pp. 115–120, Oct. 2016. DOI: 10.1038/nmat4765.

[95] R. Ye, *Physical methods in chemistry and nanoscience*, A. R. Barron, Ed. Connexions, 2012.

[96] Edinburgh Instruments, *Fls980 photoluminescence spectrometer*, Edinburgh Instruments Ltd, Livingston, United Kingdom, 2015.

[97] E. Hutter, "Revealing the fate of photo-generated charges in metal halide perovskites", PhD thesis, 2018. DOI: 10.4233/UUID:F8E21539-BD26-4694-B170-6D0641E4C31A.

[98] Nanoscience Instruments, *Scanning electron microscopy*, May 2018. [Online]. Available: https://www.nanoscience.com/techniques/scanning-electron-microscopry/.

[99] A. Ilitchev, *How do you make an electron beam?*, May 2019. [Online]. Available: https://www.thermofisher.com/blog/microscopy/electron-source-fundamentals/.

[100] Montana State Univsersity, *Scanning electron microscope*, Feb. 2022. [Online]. Available: https://physics.montana.edu/ical/old-content/instrumentation/sem.html.

[101] Nanoscience Instruments, *Stylus profilometry*, Jul. 2018. [Online]. Available: https://www.nanoscience.com/techniques/optical-profilometry/.

[102] H. Fujiwara, R. W. Collins, T. Tiwald, J. N. Hilfiker, N. Hong, and J. Sun, *Spectroscopic Ellipsometry for Photovoltaics*, H. Fujiwara and R. W. Collins, Eds. Springer International Publishing, 2018. DOI: 10.1007/978-3-319-75377-5.

[103] Ossila, *Sheet resistance: A guide to theory*, 2022. [Online]. Available: https://www.ossila.com/en-eu/pages/sheet-resistance-theory.

[104] *Four probes measurement*, PVMD.

[105] ——, *I-v curves: A guide to measurement*, 2022. [Online]. Available: https://www.ossila.com/en-eu/pages/iv-curves-measurement.

[106] J. Feng, Y. Jiao, H. Wang, X. Zhu, Y. Sun, M. Du, Y. Cao, D. Yang, and S. (Liu, "High-throughput large-area vacuum deposition for high-performance formamidine-based perovskite solar cells", *Energy and Environmental Science*, vol. 14, no. 5, pp. 3035–3043, 2021. DOI: 10.1039/d1ee00634g.

[107] K. I. Hassoon, M. S. Mohammed, and G. D. Salman, "Characerization of pbi2 thin films prepared by fast vacuum thermal evaporation", *Digest Journal of Nanomaterials and Biostructures*, 2019.

[108] S. Weber, T. Rath, B. Kunert, R. Resel, T. Dimopoulos, and G. Trimmel, "Dependence of material properties and photovoltaic performance of triple cation tin perovskites on the iodide to bromide ratio", *Monatshefte für Chemie - Chemical Monthly*, vol. 150, no. 11, pp. 1921–1927, Oct. 2019. DOI: 10.1007/s00706-019-02503-6.

[109] Y. Kumar, E. Regalado-Pérez, A. M. Ayala, N. Mathews, and X. Mathew, "Effect of heat treatment on the electrical properties of perovskite solar cells", *Solar Energy Materials and Solar Cells*, vol. 157, pp. 10–17, Dec. 2016. DOI: 10.1016/j.solmat.2016.04.055.

[110] A. Ummadisingu and M. Grätzel, "Revealing the detailed path of sequential deposition for metal halide perovskite formation", *Science Advances*, vol. 4, no. 2, Feb. 2018. DOI: 10.1126/sciadv.1701402.

[111] P. F. Ndione, Z. Li, and K. Zhu, "Effects of alloying on the optical properties of organic-inorganic lead halide perovskite thin films", *Journal of Materials Chemistry C*, vol. 4, no. 33, pp. 7775–7782, 2016, ISSN: Suppl. DOI: 10.1039/c6tc02135b.

[112] P. Fan, D. Gu, G.-X. Liang, J.-T. Luo, J.-L. Chen, Z.-H. Zheng, and D.-P. Zhang, "High-performance perovskite CH3nh3pbi3 thin films for solar cells prepared by single-source physical vapour deposition", *Scientific Reports*, vol. 6, no. 1, Jul. 2016. DOI: 10.1038/srep29910.

[113] Y. Zhang, Y. Ma, I. Shin, Y. K. Jung, B. R. Lee, S. Wu, J. H. Jeong, B. H. Lee, J. H. Kim, K. H. Kim, and S. H. Park, "Lead acetate assisted interface engineering for highly efficient and stable perovskite solar cells", *ACS Applied Materials and Interfaces*, vol. 12, no. 6, pp. 7186–7197, Jan. 2020. DOI: 10.1021/acsami.9b19691.

[114] Y. Wang, Y. Zhang, P. Zhang, and W. Zhang, "High intrinsic carrier mobility and photon absorption in the perovskite ch3nh3pbi3", *Physical Chemistry Chemical Physics*, vol. 17, no. 17, pp. 11 516–11 520, 2015. DOI: 10.1039/c5cp00448a.

[115] C. Dreessen, D. Pérez-del-Rey, P. P. Boix, and H. J. Bolink, "Radiative and non-radiative losses by voltage-dependent in-situ photoluminescence in perovskite solar cell current-voltage curves", *Journal of Luminescence*, vol. 222, p. 117 106, Jun. 2020. DOI: 10.1016/j.jlumin.2020.117106.

[116] D. Choi, S.-J. Hong, and Y. Son, "Characteristics of indium tin oxide (ITO) nanoparticles recovered by lift-off method from TFT-LCD panel scraps", *Materials*, vol. 7, no. 12, pp. 7662–7669, Nov. 2014. DOI: 10.3390/ma7127662.

[117] V. S. Reddy, K. Das, A. Dhar, and S. K. Ray, "The effect of substrate temperature on the properties of ITO thin films for OLED applications", *Semiconductor Science and Technology*, vol. 21, no. 12, pp. 1747–1752, Nov. 2006. DOI: 10.1088/0268-1242/21/12/043.

[118] N. M. Ahmed, F. A. Sabah, H. Abdulgafour, A. Alsadig, A. Sulieman, and M. Alkhoaryef, "The effect of post annealing temperature on grain size of indium-tin-oxide for optical and electrical properties improvement", *Results in Physics*, vol. 13, p. 102 159, Jun. 2019. DOI: 10.1016/j.rinp.2019.102159.

[119] C. Han, L. Mazzarella, Y. Zhao, G. Yang, P. Procel, M. Tijssen, A. Montes, L. Spitaleri, A. Gulino, X. Zhang, O. Isabella, and M. Zeman, "High-mobility hydrogenated fluorine-doped indium oxide film for passivating contacts c-si solar cells", *ACS Applied Materials and Interfaces*, vol. 11, no. 49, pp. 45 586–45 595, Nov. 2019. DOI: 10.1021/acsami.9b14709.

[120] Y. Zhong, Y. Shin, C. Kim, B. Lee, E. Kim, Y. Park, K. Sobahan, C. Hwangbo, Y. Lee, and T. Kim, "Optical and electrical properties of indium tin oxide thin films with tilted and spiral microstructures prepared by oblique angle deposition", *Journal of Materials Research*, vol. 23, no. 9, pp. 2500–2505, Sep. 2008. DOI: 10.1557/jmr.2008.0312.

[121] M. Nisha, S. Anusha, A. Antony, R. Manoj, and M. Jayaraj, "Effect of substrate temperature on the growth of ITO thin films", *Applied Surface Science*, vol. 252, no. 5, pp. 1430–1435, Dec. 2005. DOI: 10.1016/j.apsusc.2005.02.115.

[122] S. Svanström, T. J. Jacobsson, G. Boschloo, E. M. J. Johansson, H. Rensmo, and U. B. Cappel, "Degradation mechanism of silver metal deposited on lead halide perovskites", *ACS Applied Materials and Interfaces*, vol. 12, no. 6, pp. 7212–7221, Jan. 2020. DOI: 10.1021/acsami.9b20315.

[123] B. R. Patil, M. Ahmadpour, G. Sherafatipour, T. Qamar, A. F. Fernandez, K. Zojer, H.-G. Rubahn, and M. Madsen, "Area dependent behavior of bathocuproine (BCP) as cathode interfacial layers in organic photovoltaic cells", *Scientific Reports*, vol. 8, no. 1, Aug. 2018. DOI: 10.1038/s41598-018-30826-7.

[124] J. Avila, L. Gil-Escrig, P. P. Boix, M. Sessolo, S. Albrecht, and H. J. Bolink, "Influence of doped charge transport layers on efficient perovskite solar cells", *Sustainable Energy and Fuels*, vol. 2, no. 11, pp. 2429–2434, 2018, ISSN: Suppl. DOI: 10.1039/c8se00218e.

[125] S. Pfuetzner, J. Meiss, A. Petrich, M. Riede, and K. Leo, "Improved bulk heterojunction organic solar cells employing c70 fullerenes", *Applied Physics Letters*, vol. 94, no. 22, p. 223 307, Jun. 2009. DOI: 10.1063/1.3148664.

[126] F. Sahli, J. Werner, B. A. Kamino, M. Bräuninger, R. Monnard, B. Paviet-Salomon, L. Barraud, L. Ding, J. J. D. Leon, D. Sacchetto, G. Cattaneo, M. Despeisse, M. Boccard, S. Nicolay, Q. Jeangros, B. Niesen, and C. Ballif, "Fully textured monolithic perovskite/silicon tandem solar cells with 25.2% power conversion efficiency", *Nature Materials*, vol. 17, no. 9, pp. 820–826, Jun. 2018. DOI: 10.1038/s41563-018-0115-4.

[127] A. Dhar, G. Ahmad, D. Pradhan, and J. N. Roy, "Performance analysis of c-si heterojunction solar cell with passivated transition metal oxides carrier-selective contacts", *Journal of Computational Electronics*, vol. 19, no. 2, pp. 875–883, Mar. 2020. DOI: 10.1007/s10825-020-01483-9.

[128] J. A. Raiford, R. A. Belisle, K. A. Bush, R. Prasanna, A. F. Palmstrom, M. D. McGehee, and S. F. Bent, "Atomic layer deposition of vanadium oxide to reduce parasitic absorption and improve stability in n–i–p perovskite solar cells for tandems", *Sustainable Energy and Fuels*, vol. 3, no. 6, pp. 1517–1525, 2019. DOI: 10.1039/c9se00081j.

[129] L. Wagner, P. Schygulla, J. P. Herterich, M. Elshamy, D. Bogachuk, S. Zouhair, S. Mastroianni, U. Würfel, Y. Liu, S. M. Zakeeruddin, M. Grätzel, A. Hinsch, and S. W. Glunz, "Revealing fundamentals of charge extraction in photovoltaic devices through potentiostatic photoluminescence imaging", *Matter*, vol. 5, no. 7, pp. 2352–2364, Jul. 2022. DOI: 10.1016/j.matt.2022.05.024.

[130] E. M. Hutter, T. Kirchartz, B. Ehrler, D. Cahen, and E. von Hauff, "Pitfalls and prospects of optical spectroscopy to characterize perovskite-transport layer interfaces", *Applied Physics Letters*, vol. 116, no. 10, p. 100 501, Mar. 2020. DOI: 10.1063/1.5143121.

[131] Y. Kato, L. K. Ono, M. V. Lee, S. Wang, S. R. Raga, and Y. Qi, "Silver iodide formation in methyl ammonium lead iodide perovskite solar cells with silver top electrodes", *Advanced Materials Interfaces*, vol. 2, no. 13, p. 1 500 195, Jul. 2015. DOI: 10.1002/admi.201500195.

[132] D. Wang, R. Q. Liu, X. Tan, Q. Liu, H. R. Nan, S. L. Sang, F. Chen, and W. Huang, "Amplified spontaneous emission properties of solution processed CsPbBr perovskite thin films doped with large-group ammonium cations", *Optical Materials Express*, vol. 10, no. 4, p. 981, Mar. 2020. DOI: 10.1364/ome.384158.

[133] B. Li, Y. Zhang, L. Fu, T. Yu, S. Zhou, L. Zhang, and L. Yin, "Surface passivation engineering strategy to fully-inorganic cubic cspbi3 perovskites for high-performance solar cells", *Nature Communications*, vol. 9, no. 1, Mar. 2018. DOI: 10.1038/s41467-018-03169-0.

[134] D. Yao, C. Zhang, N. D. Pham, Y. Zhang, V. T. Tiong, A. Du, Q. Shen, G. J. Wilson, and H. Wang, "Hindered formation of photoinactive fapbi3 phase and hysteresis-free mixed-cation planar heterojunction perovskite solar cells with enhanced efficiency via potassium incorporation", *The Journal of Physical Chemistry Letters*, vol. 9, no. 8, pp. 2113–2120, Apr. 2018. DOI: 10.1021/acs.jpclett.8b00830.

[135] Y. Jiang, S. He, L. Qiu, Y. Zhao, and Y. Qi, "Perovskite solar cells by vapor deposition based and assisted methods", *Applied Physics Reviews*, vol. 9, no. 2, p. 021 305, Jun. 2022. DOI: 10.1063/5.0085221.

[136] B. P. Finkenauer, Y. Gao, X. Wang, Y. Tian, Z. Wei, C. Zhu, D. J. Rokke, L. Jin, L. Meng, Y. Yang, L. Huang, K. Zhao, and L. Dou, "Mechanically robust and self-healable perovskite solar cells", *Cell Reports Physical Science*, vol. 2, no. 2, S19, Feb. 2021, ISSN: Suppl. DOI: 10.1016/j.xcrp.2020.100320.

[137] M. Koopmans and J. A. Koster, "A comprehensive numerical study of the implications of s-shaped JV characteristics in perovskite solar cells", in *Proceedings of the nanoGe Fall Meeting 2018*, Fundacio Scito, Jun. 2018. DOI: 10.29363/nanoge.nfm.2018.107.

[138] D. G. Lee, M.-c. Kim, S. Wang, B. J. Kim, Y. S. Meng, and H. S. Jung, "Effect of metal electrodes on aging-induced performance recovery in perovskite solar cells", *ACS Applied Materials and Interfaces*, vol. 11, no. 51, pp. 48 497–48 504, Dec. 2019. DOI: 10.1021/acsami.9b14619.

[139] W. Tress, *Organic Solar Cells*. Springer International Publishing, 2014. DOI: 10.1007/978-3-319-10097-5.

[140] C. Battaglia, S. M. de Nicolas, S. D. Wolf, X. Yin, M. Zheng, C. Ballif, and A. Javey, "Silicon heterojunction solar cell with passivated hole selective moox contact", *Applied Physics Letters*, vol. 104, no. 11, p. 113 902, Mar. 2014. DOI: 10.1063/1.4868880.